GYROFLUID MODELS OF PLASMA TURBULENCE

William Douglass Dorland

A DISSERTATION
PRESENTED TO THE FACULTY
OF PRINCETON UNIVERSITY
IN CANDIDACY FOR THE DEGREE
OF DOCTOR OF PHILOSOPHY

RECOMMENDED FOR ACCEPTANCE
BY THE DEPARTMENT OF
ASTROPHYSICAL SCIENCES

November, 1993

To my wife Sarah, with love.

Abstract

TURBULENCE IN MAGNETIZED PLASMA in the presence of density, velocity, and temperature gradients is studied numerically and analytically with an extended fluid model. Interactions between plasma waves and plasma particles are considered in the low-frequency limit ($\omega \ll eB/m_i c$). The unique feature of the model is a set of fluid closure relations for the moments of the electrostatic gyrokinetic equation. The resulting set of "gyrofluid" equations contains approximate models that describe Landau damping and its inverse ($\omega \sim k_\parallel v_{ti}$), the usual finite-Larmor-radius effects ($k_\perp \rho_i \sim 1$), and a new, nonlinear perpendicular phase-mixing effect ($\propto k_\perp^2 |\Phi_{\vec{k}} \vec{k} \times \vec{k'}|$) due to the finite Larmor radii. The equations are investigated linearly both locally and nonlocally, analytically and numerically. Nonlinearly, a local weak-turbulence calculation is carried out for electron drift-wave turbulence. A nonlinear, three-dimensional gyrofluid code is described for the study of the turbulent transport resulting from pressure gradients in a plasma embedded in a strong, sheared magnetic field. Thermal transport properties are measured and compared to existing particle simulation results and to modern magnetic fusion tokamak experiments. It is found that the gyrofluid model compares favorably with gyrokinetic particle simulations, lending credence to the various approximations employed. Physics results from gyrofluid simulations indicate that the thermal transport associated with pressure gradients in a simple (sheared but without curvature) magnetic-field geometry is not sufficient to explain the anomalous transport observed in magnetic confinement fusion devices. However, it is found that the interaction between the fluctuations and the self-generated flows often dominate the nonlinear dynamics, even when the flows themselves are not large compared to the turbulent fluctuations. It is expected that this interplay, previously ignored for turbulence characteristic of the core plasma in a thermonuclear fusion reactor, will persist in the presence of curvature and magnetic drifts. Finally, it is noted that the inclusion of toroidal drift resonances could destabilize the system further, making this turbulence relevant to existing experiments.

Contents

Figures

Acknowledgements

I will remember my years at Princeton happily. Though it is difficult to transform oneself from a student into a scientist, I was aided by many friends and teachers to whom I owe much appreciation. Because I cannot list them all, I would like to salute a few special individuals. First, I am sure that I could not have found a better advisor anywhere. I owe more than simple thanks to Dr. Greg Hammett for sharing his insights with me, and for his patience, understanding, interest, and thoughtfulness. To my wife Sarah I also owe more than can be expressed here; she has made me happier than anyone has a right to be, and I look forward to a lifetime of love together with her. I hope that I can always be as loving, understanding, and supportive as she has been for me.

To my family I give my appreciation for their support and love over the years. I couldn't have even gotten close without them. [Mom, I suppose now that I have finished the 21^{st} grade, I can start giving back some of the more tangible kinds of support that you have always provided me. I hope you'll forgive me for dedicating three otherwise productive years to the study of greasy Greek sandwiches.]

I would also like to thank Dr. John Krommes and Dr. Charles Karney for reading my thesis carefully and making many useful suggestions.

To Dr. Liu Chen I owe appreciation as well for serving as my co-advisor early in this process. His encouragement, insights, and excitement about physics inspired me to learn more plasma physics from the beginning of my graduate studies. Thanks also to Dr. Taik Soo Hahm, who helped me to derive and to understand the material that constitutes Chap. 5.

I am grateful to my fellow gyrofluid schemers Mike Beer and Steve Smith[1] for many wonderful conversations and for their willingness to explain to me many

[1] May your hair always be long.

ideas that I otherwise might not have grasped.

I offer a special thanks to Robert Santoro, who made Chap. 7 of this thesis possible by generously sharing his time, energy, and ideas (and his particle code!). Thanks, too, to Scott Parker and John Reynders for many hours of useful benchmarks and discussions. I look forward to publishing our results together soon.

To Ms. Barbara Sarfaty I offer my heartfelt appreciation for her loyalty to graduate students in general, and for her kindness to me in particular. She is a special treasure of the fusion community.

I owe my next thanks to Dr. Tom Stix for encouraging me to explore my interests in plasma physics and in science policy. Thanks also are due to Dr. Frank von Hippel, Dr. Rush Holt, and Dr. Robert Kaita for helping me to discover more about the world of politics and ideas.

To Mehmet Artun I offer thanks for many hours of entertainment and amazement. I look forward to more ski trips, strawberry desserts, and chicken dinners with him in the future.

To Sandy MacAulay and Spencer Kelly(?) I offer thanks for encouraging me to come to Princeton, and to Mike Montgomery and Chris Zuiker, I say thanks for many years of pleasant home life.

To David Coster, I owe a very special thanks for introducing me to Africa. I will never forget my experiences there. Oh, and thanks for occasional computer tips.

To Peter Liu I owe thanks for all those Wednesday nights at Ronald's Residence and for many hours of good conversations.

This work was supported by U. S. Department of Energy Contract No. DE-AC02-76CH03073. Numerical computations were carried out the National Energy Research Supercomputer Center. I also would like to thank the TFTR project for supporting this work which is ultimately aimed at developing quantitative tools for understanding tokamak turbulence. Finally, thanks also to the Numerical Tokamak Project for additional support.

Chapter 1

Introduction

UNDERSTANDING THE ROLE OF TURBULENCE in thermonuclear plasma dynamics has been the goal of much research in the magnetic confinement fusion (MCF)[1] community. Many approaches to the subject have been suggested and investigated, with widely varying degrees of sophistication and effectiveness. In this thesis, I propose and begin to explore extended fluid models for plasma turbulence that (given the essential insights found in HAMMETT and PERKINS, 1990) are straightforward, efficient, and capable of producing results immediately relevant to present and future MCF experiments. Their unique utility ultimately rests on two pillars: economy and accuracy. Accordingly, most of this thesis is dedicated to deriving the models in detail (so the numerous approximations are clearly spelled out) and to benchmarking the resulting predictions and performance with accepted references and techniques from the literature. After making the case for the speed and reliability of this extended fluid approach relative to accepted techniques, I attempt to illuminate the importance of the interplay between turbulent fluctuations and larger-scale plasma flows (enhanced by the correct adiabatic electron response [DORLAND *et al.*, 1990]) in a strongly turbulent, three-dimensional system.

Advances in technology often lead directly to advances in scientific understanding. Today, the explosion of computational power available to scientists is

[1]For readers interested in learning more about the current problems and recent progress in MCF, good references include CORDEY *et al.*, 1992; CALLEN *et al.*, 1992; WESSON, 1987; and LIDSKY, 1983. For an easy-reading, optimistic description of MCF research, I suggest HEPPENHEIMER, 1984.

making possible direct simulations of problems long thought unassailable. Workstations now on the market are as fast as the first Cray supercomputers, and massively-parallel teraflop computers are just around the corner. Nevertheless, three-dimensional simulations of turbulence characteristic of magnetized thermonuclear plasma remain sufficiently intransigent to force one to take advantage of improved physics algorithms. For example, the gyrokinetic equation [Frieman and Chen, 1982] allows one to eliminate superfluous fast time scales without compromising the description of the low-frequency turbulence. Gyrofluid models (presented here) allow one to replace the remaining two dimensions of velocity space with a few moments, so that numerical realizations of the turbulence are less time-consuming to produce. Finally, efficient coordinate systems [Roberts and Taylor, 1965; Cowley *et al.*, 1991; Beer *et al.*, 1993] allow one to simulate the smallest relevant volume of real space by taking advantage of the short perpendicular[2] correlation lengths observed in tokamak turbulence while still allowing for long parallel wavelengths and rapid parallel motions. By thus reducing the required numerical computations as much as possible, one may contemplate performing realistic simulations of tokamak turbulence. However, whenever one reduces one's description of a physical phenomenon, one must carefully check to make sure that the new model continues to describe the important physical effects.

We [Dorland and Hammett, 1993] have spent much time working out FLR models that would be generalizable to toroidal geometry and studying the validity of the fluid closures for drift-type turbulence. Many nonlinear simulations were performed and presented over the three-year period [Dorland *et al.*, 1990; Dorland *et al.*, 1992c; Hammett *et al.*, 1992b; Dorland and Hammett, 1991; Dorland *et al.*, 1992a; Dorland *et al.*, 1992b; Hammett *et al.*, 1992a; Beer *et al.*, 1992; Dorland *et al.*, 1993a; Beer *et al.*, 1993] with variations of the models presented here providing us with a fair amount of experience and insights relevant to plasma turbulence simulations in general. The remainder of this chapter and Chaps. 2–4 draw heavily from Dorland and Hammett, 1993. Chapter 5 and App. D build upon work first presented in Dorland *et al.*, 1992a. Chapter 6 is largely taken from Dorland *et al.*, 1993b; much of the material in Chap. 8 was presented first in Dorland *et al.*, 1992b.

[2]Here "perpendicular" and "parallel" refer to spatial directions with respect to the strong magnetic field.

1.1 Overview

Nonlinear problems in plasma physics have been investigated numerically with a tremendous variety of techniques. These techniques may be very broadly classified into particle simulations, in which many particle trajectories are evolved in time according to simple physical laws, and fluid simulations, in which a few moments of the distribution function are evolved according to somewhat more complicated relations. The conventional wisdom was that problems that intrinsically involve wave-particle interactions and/or finite-Larmor-radius (FLR) effects, often referred to as kinetic effects, could not be adequately addressed with fluid techniques, since for these processes the details of the distribution function seemed to matter a great deal in the analysis [Kotschenreuther *et al.*, 1991]. However, as has been recently shown [Kadomtsev and Pogutse, 1985; Hazeltine *et al.*, 1987; Hammett and Perkins, 1990; Aydemir, 1991; Hammett *et al.*, 1992c; Chang and Callen, 1992a; Chang and Callen, 1992b; Dorland and Hammett, 1993], many kinetic effects can be included in fluid theories when derived with such details in mind. Furthermore, many authors [Hasegawa and Mima, 1977; Dupree and Tetreault, 1978; Lee and Diamond, 1986; Cowley *et al.*, 1991] often utilize fluid theories in nonlinear analyses because of the relative simplicity and occasional insights afforded by the reduced dynamics described by fluid equations. Finally, numerical solutions of fluid equations may be found by using the relatively vast and well-understood array of simulation techniques developed in the computational-fluid-dynamics and plasma-physics communities.

Even in the long mean-free-path limit, fluid equations provide solutions to initial-value problems that are as accurate as n^{th}-order Taylor-series approximations in time where n is the number of fluid moments ($\int dv\, f v^n$) being evolved; that is, a given solution is accurate for a finite time $T \propto \sqrt{n}$. Kinetic models such as those found in Hammett and Perkins, 1990 provide the correct long-time (low-frequency) behavior. In this context, the correspondence between n^{th}-order Hermite expansions and n fluid moments discussed in Smith and Hammett, 1993 and Hammett *et al.*, 1993 strongly suggests that the solutions one obtains converge to the exact solutions in the limit of increasing numbers of fluid moments, though the convergence may be slow for certain problems (such as the nonlinear plasma echo problem [Davidson, 1972; O'Neil and Gould, 1968; Hammett

et al., 1993; SMITH and HAMMETT, 1993] and the ultra-marginal stability limit of ITG turbulence [MATTOR and DIAMOND, 1988; MATTOR, 1992].)

The long-term goal of this work is to derive "gyrofluid" equations (so called because they are derived by taking moments of the gyrokinetic equation and include models of kinetic effects[3] that are missing from traditional fluid equations) with sufficiently accurate models of kinetic effects to simulate the general class of plasma "microturbulence" that is believed to be responsible for anomalous transport in tokamaks. In this class of microturbulence one finds a broad range of instabilities that are covered by the gyrokinetic ordering [FRIEMAN and CHEN, 1982]. This includes not only the usual trapped-electron-driven drift waves and variants, but also the ion-temperature-gradient (ITG) instability [RUDAKOV and SAGDEEV, 1961; COPPI *et al.*, 1967] or longer wavelength modes with magnetohydrodynamic (MHD)-type effects, such as the drift-resistive-ballooning mode [GUZDAR *et al.*, 1993].

The goals of this thesis, however, are to develop effective fluid models of important "kinetic" effects, to test the performance of these models (against the more fundamental particle simulations and analytic theory) in a simple geometry, and to use the gyrofluid equations to investigate realistic problems. It is thus sufficient to look at electrostatic perturbations in a sheared slab geometry and assume that the electron dynamics are adiabatic. [A nonadiabatic electron model is presented in App. F and has been implemented in the gyrofluid code described in Chap. 6.] Linearly, these equations contain only slab ITG instabilities and stable electron drift waves, but will eventually be extended to encompass the broader range of turbulence spanned by the gyrokinetic ordering. The extension to include the toroidal drift resonance necessary for the toroidal version of the ITG instability has been carried out [WALTZ *et al.*, 1992; BEER and HAMMETT, 1992], and we [HAMMETT *et al.*, 1993] have plans to extend these equations to include the effects of collisions, trapped particles, and fully electromagnetic perturbations.

[3]Sometimes these equations are called "gyro-Landau-fluid" equations to emphasize the wave-particle effects as well as gyroradius effects.

1.2 Relation to Previous Work

Many authors have considered the ITG instability with a variety of approaches and assumptions. I do not attempt to review the literature on the subject here in detail. Instead, I follow a few threads that lead to the work presented here through the tangle.

1.2.1 FLR Models

Many authors have considered the problem of including FLR effects in fluid equations for ITG studies. Hamaguchi and Horton [Hamaguchi and Horton, 1990; Hamaguchi and Horton, 1992b] developed a "minimum" FLR model and investigated its behavior analytically and numerically using a three-dimensional sheared-slab code that I have used as a starting platform for my numerical studies. Lee and Tang [Lee and Tang, 1988] presented fluid equations with a more complete set of FLR effects for analytical investigations of nonlinear conservation properties and mode coupling, but like the equations of Hamaguchi and Horton, they are valid only in the long-wavelength limit ($k_\perp \rho \ll 1$, where $k_\perp$ is a typical wavenumber perpendicular to the magnetic field and ρ is the ion gyroradius) and in the absence of magnetic shear. Brizard [Brizard, 1992] has gone quite a bit further, deriving a set of gyrofluid equations in general geometry and including finite-β effects (β is the ratio of the plasma pressure P to the magnetic pressure, $B^2/8\pi$), though he assumed that the total distribution function may be considered to be bi-Maxwellian, leading him to overestimate the FLR averaging effects (see Sec. 2.4) and to leave higher moments such as the heat fluxes unspecified. The higher moments, however, are in general non-neglible, and must be carefully handled; by neglecting these heat fluxes, one neglects wave-particle effects such as phase mixing.

Similon [Similon, 1981] developed better FLR models that, unlike the aforementioned formulations, are linearly exact to all orders in $k_\perp \rho$ for a shearless slab geometry. However, his formulation neglected the effects of temperature gradients (because he was concentrating on the electron drift wave) and contained inaccuracies of order $(k_\perp \rho)^2$ in the nonlinear and shear terms (see Sec. 2.4.1 below). The FLR model employed by Waltz *et al.*, 1992 has some similarities to Similon's work (extended to include temperature gradients and the toroidal curvature drive), though

it also contains inaccuracies of order $(k_\perp\rho)^2$ from $\mathbf{E}\times\mathbf{B}$ nonlinearities and shear. The FLR models developed in this thesis regain second-order accuracy for small $k_\perp\rho$ even when nonlinearities and magnetic shear effects are included. They are also all well behaved at large $k_\perp\rho$, much as the Padé approximation $\exp(-x^2)\approx 1/(1+x^2)$ is both second-order accurate for small x *and* well behaved for large x [unlike the Taylor-series approximation $\exp(-x^2)\approx 1-x^2$]. The improved accuracy for nonlinearities and shear is gained at the expense of losing rigorous higher-order accuracy for the shearless linear limit, unless an equal number of parallel velocity moments and perpendicular velocity moments are kept [such as in the "4+4"model presented in App. A]. My model is related to Similon's, except that I have taken advantange of the significant simplification of the nonlinear terms obtained if one takes *guiding-center* fluid moments (in guiding-center coordinates), rather than attempting to transform the gyrokinetic equation back to particle coordinates first (also noted independently by Brizard [Brizard, 1992]).

1.2.2 Nonlinear Phase Mixing

A unique feature of the FLR model presented here is its inclusion of a nonlinear FLR-induced phase-mixing effect that arises from the FLR-corrected nonlinear $J_0(k_\perp\rho)\mathbf{E}\times\mathbf{B}$ drift. [After deriving a fluid model of this effect, the work of Lehnert, 1989 came to my attention. Lehnert, 1989 pointed out that this phase mixing is present in the original kinetic equation in "higher-order orbit theory" than he had so far considered, but did not describe a way to include the effect in fluid equations.] One may understand the origin of the nonlinear phase-mixing with a simple physical picture. High-energy particles gyroaverage gradients in the potential more strongly than low-energy particles and hence drift more slowly. This spread in drift velocities leads to phase mixing, a collisionless damping process. Nonlinear gyrokinetic particle simulations automatically include this effect, but its significance has not been widely appreciated (excepting Lehnert's work) and its effect has been ignored in previous fluid simulations. This "FLR phase mixing" leads to a hyperviscosity-like damping approximately proportional to $k_\perp^2|\Phi_{\vec{k}}\vec{k}\times\vec{k'}|$. Because it is proportional to Φ, it only appears nonlinearly. It provides a physics-based collisionless damping mechanism at high $k_\perp\rho$ that is potentially just as important

as the usual "polarization-drift" nonlinearity.[4] It may provide an important sink for saturation in a nonlinear, turbulent system.

1.2.3 Related Advances

A more complete gyrofluid plasma model would merge the FLR and kinetic models presented here; the toroidal resonance models of WALTZ *et al.*, 1992 and BEER and HAMMETT, 1992; the fully electromagnetic, general geometry results of BRIZARD, 1992 along with the electromagnetic generalizations of the fluid-kinetic closures that have been linearly investigated by Chang and Callen [CHANG and CALLEN, 1992a; CHANG and CALLEN, 1992b] and by Hedrick and Leboeuf [HEDRICK and LEBOEUF, 1992]; and the collisional effects considered by Chang and Callen [CHANG and CALLEN, 1992a; CHANG and CALLEN, 1992b]. Such a model would allow one to understand better the nonlinear dynamics of fusion plasmas by making possible comprehensive numerical simulations within this extended fluid paradigm.

1.2.4 Particle Simulations

Gyrofluid simulations are complementary to gyrokinetic particle simulations [LEE, 1983; LEE, 1987; PARKER and LEE, 1992], as each method will likely prove to have different strengths and weaknesses. Already, it has proven tremendously useful to cross-check and benchmark the gyrokinetic and gyrofluid codes. Because the gyrofluid equations are derived from the gyrokinetic equation, gyrokinetic particle simulations are more fundamental and potentially more accurate. On the other hand, the reduced dimensionality of the gyrofluid equations (from five to three) makes numerical solutions less recalcitrant. Though it is too early to make quantitative statements concerning the relative efficiency of the two methods for the general case, the comparisons described in Chap. 7 indicate that the gyrofluid equations yield predictions for the saturation level and thermal flux comparable

[4] FLR phase mixing terms appear at the same order in $k_\perp \rho$ as the polarization nonlinearity. However, the mode-coupling coefficients are quite different. FLR phase mixing equalizes fluctuations on surfaces of constant potential and therefore represents a previously unnoticed type of coupling in Fourier space. In concrete terms, one may consider the differences introduced by the appearance of the absolute values by inspecting the FLR phase-mixing operator presented in Chap. 2.5.

to gyrokinetic particle simulations using about 10-20% of the total CPU time for a turbulent, three-dimensional, sheared-slab simulation. This estimate may vary depending on the number of particles used and the grid resolution desired. Also, optimization of either code could change this result significantly.[5] For simulations of sheared-slab turbulence in which sheared-velocity flows are suppressed, the gyrofluid approach presently produces comparable results in about 1% of the total CPU time.

1.2.5 Velocity-Space Nonlinearities

As they stand, fluid models of kinetic effects may not be efficient for some types of problems, especially those in which strongly non-Maxwellian features characterize the distribution function. For such problems, it is necessary to keep a large number of fluid moments to describe the detailed shape of the distribution function, in which case the fluid approach may lose its efficiency advantages [Hammett *et al.*, 1993]. For example, Smith and Hammett, 1993 have recently found that the standard nonlinear plasma echo phenomenon can be reproduced with the fluid equations using the phase-mixing closure of Hammett and Perkins, 1990 if the parallel nonlinearities are retained in a fairly large set of equations [Hammett *et al.*, 1993]. It was found that ten parallel velocity moments are needed even for an echo that occurs fairly quickly. Non-Maxwellian features could also result in a given problem if particle trapping in a single electrostatic wave were important, or if (as in the usual quasilinear theory) velocity-space plateaus were created. However, one ordinarily does not expect such effects to be important in ITG turbulence or for most other types of tokamak microturbulence. The relevant velocity-space nonlinearity [$\propto E_\parallel \partial F_1/\partial v_\parallel$ in Eq. (2.1)] is smaller by a factor of $\varepsilon \equiv \rho/L$ (the gyrokinetic expansion parameter) than the other nonlinear term in Eq. (2.1). That is,

$$\frac{\dfrac{\partial}{\partial v_\parallel}\left(\dfrac{e}{m}F_1\hat{\mathbf{b}}\cdot\nabla J_0\Phi\right)}{\nabla\cdot F_1 J_0 \mathbf{v}_E} \sim \frac{k_\parallel \rho}{k_\perp \rho} \sim \varepsilon.$$

The ordering assumes that the velocity-space gradients of the distribution function are of order $1/v_t$, and consequently that terms of this size are small. In a strongly

[5] It is worth noting that the particle code with which I am most familiar [Santoro and Lee, 1990] multitasks very efficiently on the Cray C-90, so that very good wall-clock turnaround times may be achieved when the machine is dedicated to one user.

turbulent plasma with many interacting modes, each with different resonant particle velocities, it is unlikely that stronger velocity-space gradients can persist. HORTON *et al.*, 1980 found in an early numerical investigation of ITG turbulence that (within a simple fluid model) the associated fluid terms were small compared to the $\mathbf{E} \times \mathbf{B}$ nonlinearities and could be neglected. Thus, the present general approach may be broadly applicable to many outstanding problems in plasma physics.

One may legitimately question the validity of this ordering, however. The consequences of the velocity-space nonlinearity for the predicted heat flux in the context of existing gyrofluid simulations (that do not include terms that follow from the velocity-space nonlinearity) should be carefully investigated. A straightforward numerical test might employ gyrokinetic particle simulations, since it is easy to switch off the velocity-space nonlinearity for the purposes of comparison. Recently, just such a study was carried out by SYDORA, 1993. In this study, "good" to "excellent" agreement was found between gyrokinetic simulations performed with and without the velocity-space nonlinearity. However, the diagnostics reported measured the saturation level and the thermal flux of two- and three-dimensional electrostatic, sheared-slab ITG turbulence, and not the rate of entropy production. The full role of the velocity-space interactions has not yet been definitively demonstrated. I have made no attempt to include velocity-space effects in the gyrofluid models presented in this thesis. If particle simulations show that the velocity-space nonlinearity plays an essential role in the dynamics, this point will have to be revisited.

1.2.6 Sheared Rotational Flows

Nonlinear numerical studies have found evidence for robust sheared-flow generation in turbulence characteristically found in the edge of tokamak plasmas [HASEGAWA and WAKATANI, 1987; CARRERAS and LYNCH, 1991; GUZDAR *et al.*, 1993]. Two mechanisms have been put forth to explain this generation: the turbulent Reynold's stress [DIAMOND and KIM, 1986]; and a toroidal effect pointed out by STRINGER, 1969 and WINSOR, 1969. Furthermore, results such as these are often invoked to explain the "L–H" transition to regimes of improved confinement widely observed in tokamak discharges. However, little attention has been paid to the possibility of the generation of sheared velocity flows in the core of the tokamak. Indeed, Diamond and Kim argued that Landau damping would likely restrict the spectral width of the

turbulence to scales small compared to the typical scale lengths of the plasma and thus not generate sheared flows except near the edge of the device where steeper gradients or limiter interactions could play a decisive role [DIAMOND and KIM, 1986]. In Chap. 8, I discuss the role of nonlinearly generated sheared-velocity flows in ITG turbulence in conditions characteristic of the core of a tokamak discharge.

Related Simulations. HASEGAWA and WAKATANI, 1987 reported the self-generation of a radial electric field (with the associated velocity shear) in their simulations of electrostatic turbulence. By using a basic model applicable to resistive drift-wave and resistive interchange instabilities, they were able to explain the "self-organization" by the conservation of potential enstrophy and angular momentum. CARRERAS and LYNCH, 1991 investigated resistive pressure-gradient-driven turbulence and also found the strong generation of sheared velocity flows, which played a significant role in determining the level of the resulting turbulence. They argued that a broad spectrum of modes would on average cancel one another out with respect to the generation of large-scale structures and therefore could not generate sheared flows except near the limiter, where the unique edge conditions break the overall symmetry. GUZDAR *et al.*, 1993 have investigated nonlinear drift-resistive-ballooning modes, and report significant sheared-flow stabilization driven by both Reynolds stress and the Stringer–Winsor terms.

Sheared flows have not been widely discussed in the particle-simulation community for about a decade. In general, the importance of $k_\parallel = 0$ modes was noted in very early three-dimensional equilibrium particle simulations. Over time, however, their estimated importance was discounted until eventually it has become a widespread practice to suppress such modes altogether. The more detailed chronology of ideas presented below supports this interpretation of the literature.

Twenty years ago, OKUDA and DAWSON, 1973 observed $k_\parallel = 0$, zero-frequency modes generated nonlinearly in three-dimensional particle simulations. The plasma they studied was in thermal equilibrium (no density or temperature gradients) in an unsheared magnetic field. They noted that these modes were damped only by collisional effects and that "since this zero-frequency motion can always exist in a plasma, it is clear that this mode can play a very important role for plasma transport." However, their attention was focused primarily on radial convection as-

sociated with these modes rather than on rotational modes associated with gradients in the poloidally and toroidally symmetric electrostatic potential $\Phi(r)$ (sometimes referred to as "ambipolar modes"). Later 3D studies [CHENG and OKUDA, 1977] also emphasized the radial convection aspect of the zero-frequency modes, termed "convective cells". CHENG and OKUDA, 1978b noted that convective cells were not observed in the presence of strong magnetic shear, although this was attributed to the stabilization of the electron drift-wave turbulence that would have otherwise generated the convective cells. Small-amplitude convective cells were observed in the 3D toroidal particle simulations of CHENG and OKUDA, 1978a, generated by charge separation associated with the bounce motion of trapped particles.

Interest in zero-frequency modes waned as it became widely felt that convective cells would be less relevant in the presence of magnetic shear, which limits the radial extent over which $k_\parallel = 0$ for most modes. However, the poloidally and toroidally symmetric ($k_y = 0, k_z = 0$) component of Φ has $k_\parallel = 0$ everywhere. While it is true that $\Phi(r)$ does not cause radial transport, it can produce sheared perpendicular rotation that can interact strongly with the turbulence. This important role of the only remaining component of Φ that satisfies $k_\parallel = 0$ globally was not widely appreciated at that time.

At least one study did note this possibility. Soon after the work of CHENG and OKUDA, 1977, LEE *et al.*, 1978 found in $2\frac{1}{2}$-dimensional simulations of electron-drift-wave turbulence that nonlinearly self-generated, sheared rotational flows were the principal nonlinear stabilization mechanism. In that paper, the importance of the radially-dependent Doppler shift was noted and an estimate of the saturation level based on this consideration was presented. Drift-kinetic electrons were pushed along with the full-dynamics ions. (No further assumptions were made about the nature of the electron response.) In later papers this early unambiguous result indicative of an important role for ambipolar modes in the presence of magnetic shear was not properly generalized to three-dimensional simulations with an assumed adiabatic electron response.

A model of adiabatic electrons was put forth by OKUDA *et al.*, 1978 and elaborated upon by LEE *et al.*, 1980. The original model consisted of replacing the electron dynamical equations with the assumption of a Boltzmann response in Poisson's equation, without explicit consideration of the electron response for the

case when $k_\parallel = 0$. In the latter expanded 2D model, two electron responses were allowed for the $k_\parallel \propto k_y = 0$ mode, the high- and low-electron-mobility models. In the high-electron-mobility model, the electron contribution to Poisson's equation was taken to be equal to the flux-surface-averaged total ion density. The authors reported that this model effectively suppressed the ambipolar modes. The low-electron-mobility model, in which $n_e(x, k_y = 0, t)$ was taken to be $n_e(x, k_y = 0, t = 0)$, was reported to allow charge buildup and the ambipolar modes. Thus, there was some awareness of the importance of the $k_\parallel = 0$ modes for nonlinear saturation along with some ambiguity about how to treat the adiabatic electron response in only two dimensions, where $k_y = 0$ implies $k_\parallel = 0$. [In three dimensions $k_\parallel = k_z + k_y(B_y/B_z)$, so there are many $k_y = 0$ modes with $k_\parallel \neq 0$. Only in this setting can one consistently treat the $k_y = 0$ part of the adiabatic electron response, including many components with $k_\parallel = 0$ and the one component with $k_\parallel = 0$.]

A few years later, in a 2D gyrokinetic particle-simulation study [Lee *et al.*, 1984], the practice of systematically removing the $\Phi(x, k_y = 0)$ modes that give rise to sheared $\mathbf{E} \times \mathbf{B}$ flows surfaced. The authors explained their reasons: "We have also suppressed all the $k_y = 0$ potentials in the code by letting $\Phi(k_y = 0) = 0$, in order to eliminate the nonlinearly generated ambipolar drifts [Lee *et al.*, 1978]. This is because they exist only in the region where $k_\parallel = 0$, and therefore are not expected to play a dominant role in tokamaks." However, this reasoning does not apply to the poloidally and toroidally symmetric component of Φ. Later studies [Lee and Tang, 1988] continued to suppress the $k_y = 0$ components of Φ, perhaps in part due to the ambiguity of whether $k_y = 0$ should really mean $k_\parallel$ is exactly zero in the two-dimensional systems (as discussed in the previous paragraph).

In three dimensions, one must consider the $\Phi(k_y = 0, k_z = 0)$ mode separately [rather than just the $\Phi(k_y = 0)$ component]. In this setting the ambiguity with respect to the purely adiabatic electron response is removed (assuming one is not considering stochastic magnetic field lines). However, the practice of suppressing the $\Phi(k_y = 0)$ component used in the 2D simulations has apparently evolved into the present practice of suppressing $\Phi(k_y = 0, k_z = 0)$ in 3D ITG simulations with the tautological result that sheared flows are not observed [Lee *et al.*, 1993]. The intuition behind this practice is partly valid, in the sense that the strong dominance of sheared rotation otherwise observed in sheared-slab simulations is probably

non-representative of the dynamics in a toroidal device. Two points may be made here. First, rather than suppress the sheared flows artificially, one should investigate the physical mechanisms that would damp sheared rotational flows in the geometry of interest. One such neoclassical mechanism (termed "banana-orbit averaging") has been identified in the toroidal gyrofluid simulations of BEER *et al.*, 1993 and described in more detail by HAMMETT *et al.*, 1993. Second, there is a consistent way of treating the 3D strictly adiabatic electron response and that is to take $\delta n_e(x, k_y = 0, k_z = 0) = 0$. One then finds radially varying electric fields related to the ion polarization drift. Until after the first presentation of our gyrofluid equations [DORLAND *et al.*, 1990], which contained this adiabatic electron response (described in more detail in Chap. 8), no one emphasized the critical role of the correct adiabatic electron response in generating shear flows in microturbulence simulations. Recently, however, several presentations on this topic have been made [WONG *et al.*, 1991; DORLAND *et al.*, 1992b; BEER *et al.*, 1992; DIMITS, 1992; WALTZ, 1993].

1.3 Motivation and Outline

One of the early proposed reasons for the improved confinement of the Supershot regime [BELL *et al.*, 1989] was the reduction of $L_n/L_T \equiv \eta_i$, with a commensurate reduction of ITG turbulence. Here L_n is the scale length of the background density gradient and L_T is the scale length of the background temperature gradient. However, analysis of the Tokamak Fusion Test Reactor (TFTR) [HAWRYLUK *et al.*, 1987] density perturbation experiments and other TFTR transport studies brought into question the reigning concept of marginal η_i stability and showed that existing transport estimates based on fluid models of slab ITG turbulence were too high by a couple of orders of magnitude [ZARNSTORFF *et al.*, 1991; HORTON *et al.*, 1992]. [Recently, Kotschenreuther has shown that impurity effects can significantly reduce the linear growth rates even when η_i is large [KOTSCHENREUTHER, 1993], reviving interest in the marginality assumption.] At about the same time, Kotschenreuther pointed out that existing gyrokinetic [KOTSCHENREUTHER *et al.*, 1991] and fluid [HAMAGUCHI and HORTON, 1990] estimates of ITG heat transport differed by at least an order of magnitude [KOTSCHENREUTHER *et al.*, 1991]. The gyrofluid model presented below can resolve this disagreement, as one can recover

Kotschenreuther's gyrokinetic results by retaining kinetic effects and the results of Hamaguchi and Horton by neglecting them. The kinetic effects addressed are phase mixing (parallel and perpendicular) and FLR averaging. Although the slab ITG mode is now understood to be probably too weak to explain the measured thermal transport, it appears that the addition of toroidal drive to the ITG mode may raise it back to a level consistent with the core measurements. The theoretically predicted thermal transport rate is probably still too small in the outer half of the plasma where other instabilities presumably dominate [HORTON *et al.*, 1992]. Ultimately, one would prefer to simulate the nonlinear ITG dynamics in a more realistic geometry. WALTZ *et al.*, 1992 and BEER and HAMMETT, 1992 employed models similar to the present model in a toroidal setting. Beer's toroidal `ITGC` code [BEER *et al.*, 1992; BEER *et al.*, 1993; HAMMETT *et al.*, 1993] is a modified version of the code presented in Chap. 6.

The derivation of the gyrofluid equations is presented in Chap. 2. Section 2.1 is a brief review of the gyrokinetic Vlasov-Poisson system, the starting point of the gyrofluid derivation. The basic parallel phase-mixing model is described in HAMMETT and PERKINS, 1990 and in HAMMETT *et al.*, 1992c. This physically-motivated phase-mixing model includes wave-particle effects such as Landau damping and its inverse, processes that are very important in drift-wave physics. In Sec. 2.3 I generalize the closure to describe the effects of anisotropic temperature fluctuations, so as to include FLR effects (linear and nonlinear) more easily. Two gyrofluid models of FLR averaging that are more useful than the usual Taylor-series expansions of the gyroaveraging operators for numerical investigations are developed in Sec. 2.4. These models remain robust approximations for $k_\perp \rho \geq 1$, where the Taylor-series expressions fail. The more accurate "$\Gamma_0^{1/2}$" model (Section 2.4.2) may be easily added to existing spectral codes, while the "Padé" model (Sec. 2.4.4) could improve the accuracy of finite-difference codes. Both models take into account the gyroaveraging of the shear pointed out by Bakshi [BAKSHI *et al.*, 1977] and Linsker [LINSKER, 1981] and recover the adiabatic ion response in the $k_\perp \rho \gg 1$ limit. A new, nonlinear FLR phase-mixing model is described in Sec. 2.5.

Linear results are presented in Chaps. 3 and 4. The problem of deciding how many moments it is necessary to retain for the present problem is discussed, in the local limit (Chap. 3) and in the presence of magnetic shear (Chap. 4). I

have utilized the gyrokinetic integral eigenmode code of Linsker [LINSKER, 1981] extensively to benchmark the linear performance of the kinetic models.

In Chap. 5, I compare the nonlinear gyrokinetic and gyrofluid equations analytically. Weak-turbulence analyses show that the agreement is very good in the drift wave limit, where the most unstable modes are non-resonant, but the resulting beat waves are resonant. The comparison is less favorable in the regime characterized by resonant unstable waves.

In Chap. 6 I describe the numerical code `ITG` that simulates sheared-slab ITG turbulence using gyrofluid equations. In addition to describing some of the details of my particular code, I discuss issues related to boundary conditions and geometry generic to microturbulence simulations. Then, in Chap. 7 I show comparisons between my gyrofluid simulations and R. A. Santoro's gyrokinetic particle simulations [SANTORO and LEE, 1990] in a variety of settings. A simple two-dimensional system (without magnetic shear and with a single $k_\parallel$) that may be described by a straightforward three-mode-coupling theory is studied. Then, two- and three-dimensional simulation results in the presence of magnetic shear are compared. The agreement is in general good, lending credence to the general gyrofluid method.

The simulations described in Chap. 7 do not allow sheared $\mathbf{E} \times \mathbf{B}$ flows. The implications of the inclusion of the self-consistent evolution of sheared $\mathbf{E} \times \mathbf{B}$ flows are examined in Chap. 8. It is shown that these flows are very important and should not be neglected, although their effects in a simple sheared-slab geometry are probably greater than in a toroidal system where natural damping mechanisms exist to regulate the flows more strongly.

Chapter 9 contains a summary of the results presented in this thesis and a discussion of useful related work that needs to be undertaken. In the appendices several extensions to the basic gyrofluid model derived in Chap. 2 are presented, including non-adiabatic electrons, imposed sheared velocity flows, multiple ion species, and higher-moment representations. Also, the numerical convergence of the code and models is investigated. Finally, sample input files that generate gyrofluid dispersion relations (using a symbolic algebra program *Maple* [CHAR *et al.*, 1991]) and control my code `ITG` are presented.

Chapter 2

Derivation of the Gyrofluid Equations

THE STARTING POINT OF THE DERIVATION of the gyrofluid equations is the nonlinear electrostatic gyrokinetic equation [Frieman and Chen, 1982; Lee, 1983; Dubin *et al.*, 1983; Lee, 1987]. Fluid equations are generated by taking velocity-space moments of this equation directly. Conceptually, one could begin with the Vlasov equation, generate a set of moments including the stress tensor, heat-flux tensor, and so on, and then take the low-frequency ($\omega \ll eB/m_i c$) limit of the fluid equations. However, since the turbulence of interest is well characterized by the gyrokinetic ordering, it is natural to take advantage of the strong magnetic field to simplify the kinetic equation first and then to take the moments. This course has the sizable advantage of retaining the FLR effects ($k_\perp \rho \sim 1$) relatively easily. "Gyroviscous cancellations" are recovered automatically with comparatively little effort, even for $k_\perp \rho \sim 1$. Also, parallel and perpendicular dynamics (linear and nonlinear) naturally separate, as is appropriate for a collisionless system. The resulting equations are similar to the CGL double-adiabatic equations [Chew *et al.*, 1956].

In this chapter, I shall consider turbulence in the electrostatic limit and ignore the effects of non-adiabatic electrons. If electromagnetic perturbations are retained in the derivation below, the reduced MHD equations can be recovered [Hahm *et al.*, 1988; Brizard, 1992] by taking $k_\perp \rho \sim \varepsilon$ and ignoring the kinetic phase-mixing model. It is straightforward to add non-adiabatic electrons, velocity

gradients, or toroidal effects to the present model, thereby extending the class of instabilities that can be modeled beyond the sheared-slab ITG mode.

2.1 The Gyrokinetic-Poisson System

The usual gyrokinetic ordering [FRIEMAN and CHEN, 1982] is $\omega/\Omega \sim \rho/L \sim k_\parallel \rho \sim F_1/F_0 \sim e\Phi/T_e \sim \varepsilon \ll 1$ and $k_\perp \rho \sim 1$, where ω is a typical frequency of the fluctuation spectrum, Ω is the ion cyclotron frequency ($eB/m_i c$), ρ is the ion Larmor radius, L is a typical scale length of the system, $k_\parallel$ and $k_\perp$ are typical parallel and perpendicular wavenumbers of the fluctuation spectrum, and Φ is the electrostatic potential.

The nonlinear, electrostatic gyrokinetic equation [FRIEMAN and CHEN, 1982; LEE, 1983; DUBIN *et al.*, 1983; LEE, 1987] governing the dynamics of the ion distribution function may be written in conservative form as:[1]

$$\frac{\partial F}{\partial t} + \nabla \cdot \Big(F(v_\parallel \hat{\mathbf{b}} + J_0 \mathbf{v}_E) \Big) - \frac{\partial}{\partial v_\parallel} \left(\frac{e}{m} F \hat{\mathbf{b}} \cdot \nabla J_0 \Phi \right) = 0, \tag{2.1}$$

where $F(\mathbf{R}, v_\parallel, v_\perp, t)$ is the gyrophase-independent part of the distribution function; that is, it is the density of guiding centers at position $\mathbf{R}$ with parallel velocity $v_\parallel$ and perpendicular velocity $v_\perp$. The distribution function F includes both the equilibrium F_0 and fluctuating F_1 components, but excludes the gyrophase-dependent part of the distribution, given (to the same order in ε) by

$$\tilde{f}(\mathbf{R}, v_\parallel, v_\perp, \alpha, t) = -\left(\frac{e\Phi(\mathbf{X}, t)}{T_i} - \left\langle \frac{e\Phi(\mathbf{X}, t)}{T_i} \right\rangle_\alpha \right) F_0, \tag{2.2}$$

where the particle position $\mathbf{X} \equiv \mathbf{R} + \rho$ is related to the guiding-center position $\mathbf{R}$ and the gyroradius vector ρ (that depends on the gyrophase α). Averaging over the gyrophase angle α (while holding $\mathbf{R}$ fixed) is denoted by $\langle \cdots \rangle_\alpha$. The total distribution function $f(\mathbf{R}, v_\parallel, v_\perp, \alpha, t) = F + \tilde{f}$, where $\tilde{f}$ represents an adiabatic response around the gyro-orbit and is related to the polarization drift [DUBIN and KROMMES, 1983].

The $\mathbf{E} \times \mathbf{B}$ velocity is given by $\mathbf{v}_E \equiv (c/B)\, \hat{\mathbf{b}} \times \nabla \Phi$. J_0 is a linear operator that carries out the gyro-averaging operation. It is simply a Bessel function in

[1] A brief derivation of Eqs. (2.1) and (2.4) is presented in App. C.

Fourier space:

$$J_0(\frac{k_\perp v_\perp}{\Omega}) = \frac{1}{2\pi}\int_0^{2\pi} d\alpha\, \exp\left(i\frac{k_\perp v_\perp}{\Omega}\cos\alpha\right) = \sum_{n=0}^{\infty}\frac{1}{(n!)^2}\left(i\frac{k_\perp v_\perp}{2\Omega}\right)^{2n}$$

$$= \sum_{n=0}^{\infty}\frac{1}{(n!)^2}\left(\frac{v_\perp}{2\Omega}\right)^{2n}\nabla_\perp^{2n}. \tag{2.3}$$

In real space, the Bessel function is an operator that may not commute with other operators that appear in the analysis. It is therefore important to keep track of what has been gyroaveraged (and therefore what is being operated upon by a given J_0) at each point in the derivation. J_0 operates only on Φ in Eq. (2.1).

Note that this ordering retains the physics of strong turbulence even though the fluctuating quantities are ordered small, since their derivatives may be $O(1)$. That is, although $F_1/F_0 \sim \varepsilon$, $(\nabla_\perp F_1)/(\nabla_\perp F_0) \sim 1$, thus retaining the dominant $\mathbf{E}\times\mathbf{B}$ nonlinearity.

This equation is closed by the quasineutrality constraint $n_i(\mathbf{x}) = n_e(\mathbf{x})$, which when written in terms of the guiding-center quantities becomes

$$\bar{n}_i - n_{i0}(1-\Gamma_0)\frac{e\Phi}{T_i} = n_e, \tag{2.4}$$

in which $\Gamma_n(b) = I_n(b)e^{-b}$ and $I_n(b) = i^{-n}J_n(ib)$ is the modified Bessel function. The contribution to the local particle density, $\bar{n}_i(\mathbf{x})$, comes from the gyrophase-*independent* part of the guiding-center distribution function F,

$$\bar{n}_i(\mathbf{x}) = \int d^3v\, J_0 F = \int d^3v\, (F_0 + J_0 F_1). \tag{2.5}$$

In this expression, J_0 operates on the distribution function (though F_0 is slowly varying so $J_0F_0 \approx F_0$). The second term on the left-hand side of Eq. (2.4) (usually called the "polarization density") is the contribution to the local particle density from $\tilde{f}$, the gyrophase-*dependent* part of the distribution function.

One can use the same fluid equations derived below for the ions to describe the electron dynamics, usually also assuming $k_\perp\rho_e \ll 1$. However, in this chapter I shall consider only the adiabatic part of the electron response, so Eq. (2.4) becomes

$$\bar{n}_i - n_{i0}(1-\Gamma_0)\frac{e\Phi}{T_i} = n_{e0}\left[1 + \frac{|e|}{T_e}(\Phi - \langle\!\langle\Phi\rangle\!\rangle)\right]. \tag{2.6}$$

The $\langle\langle\Phi\rangle\rangle$ term on the right-hand side represents the flux-surface average of the electrostatic potential, and must be included to prevent non-physical radial particle transport, as discussed in more detail in Chap. 8. Throughout this thesis, these equations are studied in the commmonly used "sheared-slab" approximation described in more detail in Chaps. 2.6 and 6. It is sufficient at this point to note that the sheared-slab model is essentially a right parallelepiped, in which the x direction corresponds to the radial direction in a torus, the y direction corresponds to the poloidal direction, and the z direction corresponds to the toroidal direction. Therefore, the flux-surface average of a quantity (such as the potential) is given by

$$\langle\langle\Phi\rangle\rangle \equiv \frac{1}{L_y L_z}\int_0^{L_y} dy \int_0^{L_z} dz\,\Phi.$$

2.2 General Gyrofluid Equations

Because the moment averages are performed in guiding-center coordinates, n is the density of guiding centers, $mnu_\parallel$ is the momentum of guiding centers, etc. Specifically,

$$\begin{aligned}
n &\equiv \int F\,d^3v,\\
nu_\parallel &\equiv \int F v_\parallel\,d^3v,\\
p_\parallel &\equiv m\int F(v_\parallel-u_\parallel)^2\,d^3v,\\
q_\parallel &\equiv m\int F(v_\parallel-u_\parallel)^3\,d^3v,\\
R_\parallel &\equiv m\int F(v_\parallel-u_\parallel)^4\,d^3v,\\
p_\perp &\equiv (m/2)\int F v_\perp^2\,d^3v,\\
q_\perp &\equiv (m/2)\int F v_\perp^2(v_\parallel-u_\parallel)\,d^3v,\\
R_\perp &\equiv (m/2)\int F v_\perp^2(v_\parallel-u_\parallel)^2\,d^3v,\\
s_\perp &\equiv (m/2)\int F v_\perp^2(v_\parallel-u_\parallel)^3\,d^3v.
\end{aligned} \tag{2.7}$$

Upon using these definitions and the relations $p_{\parallel,\perp} \equiv nT_{\parallel,\perp}$, one may derive the following general fluid equations by taking various integrals of the form $\int d^3v\, v_\perp^{2j} v_\parallel^\ell \ldots$ over Eq. (2.1):

$$\frac{\partial n}{\partial t} + \nabla \cdot \left(n u_\parallel \hat{\mathbf{b}} + n \left\langle J_0 \right\rangle \mathbf{v}_E \right) = 0, \tag{2.8}$$

$$\frac{\partial (n u_\parallel)}{\partial t} + \nabla \cdot \left((\frac{p_\parallel}{m} + n u_\parallel^2) \hat{\mathbf{b}} + n \left\langle v_\parallel J_0 \right\rangle \mathbf{v}_E \right) + \frac{e}{m} \hat{\mathbf{b}} \cdot n \left\langle J_0 \right\rangle \nabla \Phi = 0, \tag{2.9}$$

$$\frac{\partial (p_\parallel + m n u_\parallel^2)}{\partial t} + \nabla \cdot \left((q_\parallel + 3 p_\parallel u_\parallel + m n u_\parallel^3) \hat{\mathbf{b}} + n \left\langle m v_\parallel^2 J_0 \right\rangle \mathbf{v}_E \right) + 2e \hat{\mathbf{b}} \cdot n \left\langle v_\parallel J_0 \right\rangle \nabla \Phi = 0, \tag{2.10}$$

$$\frac{\partial (q_\parallel + 3 u_\parallel p_\parallel + m n u_\parallel^3)}{\partial t} + \nabla \cdot \left((R_\parallel + 4 u_\parallel q_\parallel + 6 u_\parallel^2 p_\parallel + m n u_\parallel^4) \hat{\mathbf{b}} + n \left\langle m v_\parallel^3 J_0 \right\rangle \mathbf{v}_E \right) + 3e \hat{\mathbf{b}} \cdot n \left\langle v_\parallel^2 J_0 \right\rangle \nabla \Phi = 0, \tag{2.11}$$

$$\frac{\partial p_\perp}{\partial t} + \nabla \cdot \left((q_\perp + n u_\parallel T_\perp) \hat{\mathbf{b}} + n \left\langle \tfrac{1}{2} m v_\perp^2 J_0 \right\rangle \mathbf{v}_E \right) = 0, \tag{2.12}$$

$$\frac{\partial (q_\perp + n u_\parallel T_\perp)}{\partial t} + \nabla \cdot \left((R_\perp + 2 u_\parallel q_\perp + n u_\parallel^2 T_\perp) \hat{\mathbf{b}} + n \left\langle \tfrac{1}{2} m v_\perp^2 v_\parallel J_0 \right\rangle \mathbf{v}_E \right) + \frac{e}{m} \hat{\mathbf{b}} \cdot \nabla n \left\langle \tfrac{1}{2} m v_\perp^2 J_0 \right\rangle \Phi = 0, \tag{2.13}$$

where $\langle \cdots \rangle \equiv \int d^3v\, F \cdots / \int d^3v\, F$. These equations are the exact, nonlinear evolution equations for the first few moments of the electrostatic gyrokinetic equation in the collisionless limit. They express the conservation of density, parallel momentum, parallel and perpendicular energy, and so on. However, their utility is limited unless closure approximations are specified. In this case, one must make two distinct closure assumptions.

First, one must close the usual fluid hierarchy that results from the linear parallel convection term [$\nabla \cdot (F v_\parallel \hat{\mathbf{b}})$ in the gyrokinetic equation]. Because of this term, the time evolution of each fluid moment is driven in part by the gradient of the next-higher parallel velocity moment. It has been shown [Hammett and Perkins, 1990; Hammett *et al.*, 1992c] that collisionless phase mixing (and thus Landau damping) may be modeled by approximating this single term in the highest moment equations retained (*e.g.*, $R_\parallel, R_\perp$). Note that in the present case one finds expressions for $R_\parallel$ and $R_\perp$, which appear in Eqs. (2.11) and (2.13), respectively. No dissipation is introduced by this closure into the evolution equations for the

lower moments, which therefore remain exact nonlinear expressions. Later in this particular derivation, however, I do neglect the higher-order parallel nonlinearities, as noted above.

Second, one must close each of the FLR terms $\langle \cdots J_0 \rangle$ that arise from the gyroaveraging process. The gyroaveraging operator J_0 depends in general upon all even powers of $v_\perp$, as is evident from Eq. (2.3). Thus, $\langle J_0 \rangle$ is in general a function of all $v_\perp^{2j}$ moments of the distribution function. I shall approximate these higher moments in terms of lower moments whose time evolution is followed. Furthermore, the nonlinear part of the $J_0 \mathbf{v}_E \cdot \nabla$ term in Eq. (2.1) is responsible for perpendicular FLR phase mixing analogous to the parallel phase mixing that arises from the $v_\parallel \nabla_\parallel$ term. The closure approximations for the various $\langle \cdots J_0 \rangle$ terms may be chosen to model this collisionless damping process. To my knowledge, all previous fluid closure approximations for the FLR terms have missed this effect.

Closure approximations for the various parallel and FLR terms are discussed in the next several sections. The final gyrofluid equations are given in Chap. 2.6.

2.3 Parallel Phase-Mixing Closure

The parallel phase-mixing model outlined in HAMMETT and PERKINS, 1990 is immediately appropriate for the parallel fluid moments (such as $R_\parallel$), but does not directly address the effects of anisotropic temperature perturbations, which for $k_\perp \rho \sim 1$ are as important as the parallel temperature fluctuations and should be treated on an equal footing. Note that $T_\perp$ appears linearly in Poisson's equation and nonlinearly in the density equation at the same order as each of the other terms retained. Rather than using only one equation to express the evolution of the total temperature $T = (2T_\perp + T_\parallel)/3$ and trying to correct for the difference between $T_\perp$ and $T_\parallel$ with an approximate stress tensor, I choose to evolve two separate equations for the parallel and perpendicular temperatures. This route allows one to find the nonlinear FLR corrections ($\propto T_\perp$) easily and bypasses the tedious algebra associated with the gyroviscous corrections. Because the perpendicular temperature evolution equation includes the same kind of parallel resonance term as is found in each of the other equations, one expects to find a similarity in the parallel phase-mixing closures. In fact, the underlying kinetic equation guarantees the connection between

the parallel moments ($n, u_\parallel, T_\parallel$ and $q_\parallel$) and the perpendicular moments ($T_\perp, q_\perp, R_\perp$ and $s_\perp$) that we exploit in Chap. 2.4.

The closure prescription in HAMMETT and PERKINS, 1990 is to approximate the highest moments that occur in the fluid hierarchy with the Maxwellian part of each plus a small correction due to the perturbed part of the distribution function, chosen to reproduce the linear response function $R(\zeta) = -\tilde{n}/(n_0 e\Phi/T_0)$ (where T_0 is the background temperature) in the low- and high-frequency limits. However, examination of Eqs. (2.8–2.13) reveals that linearly when $k_\perp \rho \ll 1$ the perpendicular moment fluctuations are decoupled from the density perturbations. Rather than trying to solve for the closure of the FLR terms and the phase-mixing terms all at once, one may take advantage of this decoupling and consider the problem in a slightly different light.

2.3.1 Linear Propagator

Consider a simple one-dimensional, homogeneous system in the absence of particle interactions. Linearly, the perturbed distribution function evolves according to

$$\frac{\partial F_1}{\partial t} + v\frac{\partial F_1}{\partial z} = \delta(t) g(z, v), \tag{2.14}$$

where g is a perturbation assumed to occur at time $t = 0$. It is convenient to define the kinetic linear propagator $\mathcal{L}$, whose inverse can be represented in Fourier space as

$$\mathcal{L}_k^{-1} \equiv -i\omega + ikv, \tag{2.15}$$

so $F_{1k} = \mathcal{L}_k g_k$ (one must use the Landau prescription for the singularity on the real axis). For the moment, consider the case in which $g_k(v)$ is Maxwellian with a perturbation only in the density. Previously [HAMMETT and PERKINS, 1990], the case in which $g \propto vF_M(v) \propto E_\parallel \partial F_M/\partial v_\parallel$ was considered, as is appropriate for an electric-field term in the usual Landau-damping problem. Here I show that one finds the same closure coefficients for the case in which the initial perturbation $g \propto F_M(v)$. [The correspondence between the two viewpoints in both the fluid and kinetic descriptions is discussed in more detail in HAMMETT *et al.*, 1992c.] This is not a coincidence; rather, it is related to the fact that the solution to Eq. (2.14), $F_{1k} = F_M(v)e^{ik(z-vt)}$, contains products of F_M and all powers of the velocity v^n as

time goes on:

$$F_M(v)e^{-ikvt} \simeq F_M(v)[1 - ikvt - (kt)^2\frac{v^2}{2} + \cdots].$$

The density response in the frequency domain[2] is simply

$$\frac{n_{1k}}{n_0} = \frac{1}{n_0}\int d^3v\, F_1 = \frac{1}{n_0}\int d^3v\, F_M\mathcal{L}_k = -\frac{i\zeta}{\omega}Z(\zeta), \tag{2.16}$$

in which $\zeta \equiv \omega/\sqrt{2}|k_\parallel|v_t$, $v_t \equiv \sqrt{T/m}$ and $Z(\zeta)$ is the usual plasma dispersion function [Fried and Conte, 1961]. One may recast the closure scheme in Hammett and Perkins, 1990 in terms of the lowest moments of the linear propagator. From this viewpoint, the generalization to anisotropic temperature fluctuations will be simple.

For simplicity, consider a two-moment fluid model, n and $u_\parallel$, of the same system. The linearized fluid equations written in nondimensional units [see Eqs. (2.61) and (2.62)] are

$$\frac{\partial n}{\partial t} + \nabla_\parallel u_\parallel = \delta(t)S(z), \tag{2.17}$$

$$\frac{\partial u_\parallel}{\partial t} + \nabla_\parallel p_\parallel = 0, \tag{2.18}$$

in which $S(z) \equiv \int dv\, g(z,v)$.

In linearized, nondimensional variables (indicated in this paragraph with tildes for clarity), $\tilde{p}_\parallel = \tilde{n} + \tilde{T}_\parallel$. That is, in dimensional units $p_\parallel = nT_\parallel$ so that upon linearizing

$$p_{\parallel 0} + p_{\parallel 1} = n_0T_{\parallel 0} + n_1T_{\parallel 0} + n_0T_{\parallel 1} + n_1T_{\parallel 1},$$

one is led to

$$\tilde{p}_\parallel \equiv \frac{p_{\parallel 1}}{p_{\parallel 0}} = \tilde{n} + \tilde{T}_\parallel.$$

If one does not wish to solve equations for higher moments to describe non-Maxwellian perturbations, one may approximate their effects by allowing $\tilde{T}_\parallel$ to be non-zero. Thus,

$$\tilde{p}_\parallel = \tilde{n} + \tilde{T}_\parallel, \qquad \tilde{T}_\parallel = -\mu\nabla_\parallel\tilde{u}_\parallel, \tag{2.19}$$

[2] In the time domain, a density perturbation initially proportional to e^{ikz} evolves according to

$$n_1(z,t) = n_1(t=0)\frac{e^{ikz}}{\sqrt{2\pi v_t^2}}\int dv\, e^{-ikvt}e^{-v^2/(2v_t^2)} = n_1(z,t=0)e^{ikz}e^{-k^2v_t^2t^2/2}.$$

The density perturbation rapidly phase-mixes away, even though $F_1(t)$ remains finite.

and kinetic theory is to be used to find the appropriate closure relation for μ. [In general, $\tilde{T}_\parallel$ could also be a function of $\tilde{n}$, but in comparing to kinetic theory one finds that the coefficient analogous to μ is zero.] With the insight gained from HAMMETT and PERKINS, 1990, one may assume the form of the collisionless "diffusion" coefficient μ for this simple fluid model to be

$$\mu \equiv \mu_1 \frac{\sqrt{2}}{|k_\parallel|}$$

in Fourier space, which corresponds to an integral operator in real space [HAMMETT and PERKINS, 1990]. The dimensionless parameter μ_1 is $O(1)$ and remains to be determined.

Upon using Eq. (2.18) to find $u_\parallel$ and substituting the result into Eq. (2.17), one is led to

$$\left[-i\omega + \frac{ik_\parallel^2}{\omega + i\mu_1\sqrt{2}|k_\parallel|} \right] n = S.$$

One may use this to define the linear propagator for density, $n = \mathcal{L}_n S$. The quantity $\mathcal{L}_n$ may be rewritten in the form

$$\mathcal{L}_n = \frac{i\zeta}{\omega} \left(\frac{\zeta + i\mu_1}{\zeta^2 + i\mu_1\zeta - 1/2} \right) \equiv -\frac{i\zeta}{\omega} Z_2(\zeta). \tag{2.20}$$

The closure coefficient μ_1 is determined by requiring that this expression match the zeroth moment of the kinetic propagator [Eq. (2.16)] in the "adiabatic" ($\zeta \ll 1$) limit. One finds that $\mu_1 = \sqrt{\pi}/2$. In this closure scheme, one finds that the "fluid" limit ($\zeta \gg 1$) of the fluid approximation to the propagator is automatically well-behaved since the closure term is neglible in this limit. The resulting function $Z_2(\zeta)$ is a two-pole approximation to the plasma dispersion function $Z(\zeta)$, as shown in Fig. (2.1).

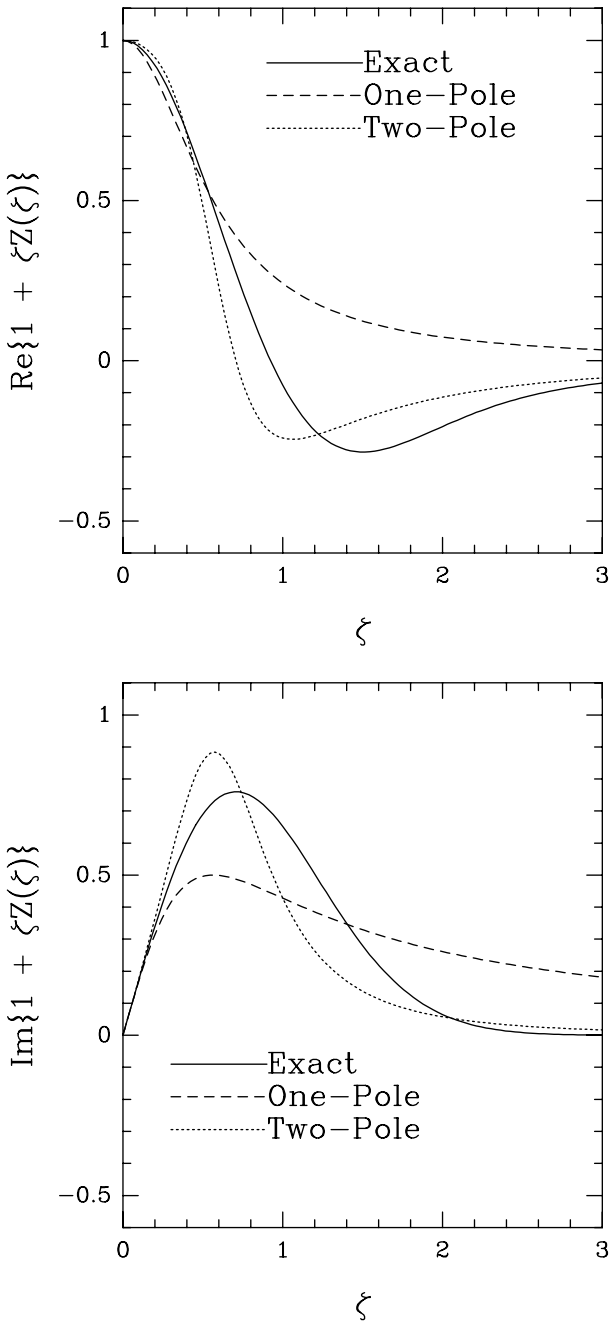

Figure 2.1: $1 + \zeta Z(\zeta)$ for one- and two-pole models of parallel phase mixing.

2.3.2 Anisotropic Temperature Fluctuations

Since this formalism makes no reference to the presence of the electric field, it generalizes easily to the case of fluctuations of the perpendicular temperature (which are decoupled from the potential fluctuations in the $k_\perp \rho \ll 1$ limit). To isolate the closure terms for the perpendicular moments, it is useful to consider the case in which $g(z, v_\parallel, v_\perp)$ in Eq. (2.14) is bi-Maxwellian with a perturbation in $T_\perp$ only, not in n. That is,

$$g(z, v_\parallel, v_\perp) = F_m(v_\parallel, v_\perp) \left[1 + \left(\frac{m v_\perp^2}{2 T_{\perp 0}} - 1 \right) S_\perp(z) \right].$$

Upon taking the $v_\perp^2$ and $v_\parallel v_\perp^2$ moments of Eq. (2.14), one is led to equations describing the perpendicular pressure and parallel flow of perpendicular temperature ($q_\perp$) [c.f. Eqs. (2.12) and (2.13)]. Upon linearizing, transforming to non-dimensional variables [Eqs. (2.61) and (2.62)], and using Eqs. (2.17) and (2.18) (but ignoring the initial density perturbation) to eliminate several terms, one is led to expressions that describe the evolution of perpendicular temperature and $q_\perp$:

$$\frac{\partial T_\perp}{\partial t} + \nabla_\parallel q_\perp = \delta(t) S_\perp(z), \tag{2.21}$$

$$\frac{\partial q_\perp}{\partial t} + \nabla_\parallel T_\perp + \nabla_\parallel \delta R_\perp = 0. \tag{2.22}$$

[To obtain these equations, I took

$$\tilde{R}_\perp = \tilde{n} + \tilde{T}_\perp + \tilde{T}_\parallel + \delta \tilde{R}_\perp$$

and noted that the parallel temperature has been taken to be isotropic so that the third term on the RHS is identically zero.] As before, one approximates the irreducible component of the highest moment in terms of the lower moments. That is,

$$\delta R_\perp \simeq -\mu \nabla_\parallel q_\perp. \tag{2.23}$$

The quantity of interest is now the linear propagator for the perpendicular temperature fluctuation (written here in the transform space),

$$\mathcal{L}_T^{-1} \equiv -i\omega + \frac{i k_\parallel^2}{\omega + i \mu_1 \sqrt{2} |k_\parallel|},$$

which may be expressed as

$$\mathcal{L}_T = -\frac{i\zeta}{\omega} Z_2(\zeta).$$

It is now easily shown that one should choose μ exactly as before. Since the kinetic linear propagator $\mathcal{L}$ is independent of $v_\perp$, the second perpendicular moment of $\mathcal{L}^{-1}$ is exactly the same as was found in Eq. (2.16) (in non-dimensional units). This is not surprising, since the underlying kinetic resonance is the same for the hierarchy of parallel moments $(n, u_\parallel, \ldots)$ as for the hierarchy of perpendicular moments $(T_\perp, q_\perp, \ldots)$. Equation (2.23), with $\mu = \sqrt{\pi/2}/|k_\parallel|$, provides the closure for $R_\perp$ in Eq. (2.13).

Keeping the evolution equations for n coupled moments leads in this way to n-pole Padé approximants for the plasma dispersion function. For analytic investigations, it is usually convenient to keep an equal number of parallel and perpendicular moments, as all of the Z-function approximations that appear are then the same, allowing greatly simplified bookkeeping.

2.3.3 Moment Reduction Scheme

In HAMMETT *et al.*, 1992c we presented a 1-moment model, "the simplest possible fluid model of phase mixing". That model was Eq. (2.17) with the closure approximation $u_\parallel = -(\nu_1/|k_\parallel|)\nabla_\parallel n$ and $\nu_1 = \sqrt{2/\pi}$. Note that this same expression for $u_\parallel$ can be obtained by taking the $k_\parallel v_t \gg \omega$ limit of Eq. (2.18) [with the closure for $p_\parallel$ given by Eq. (2.19)]. One may use this fact to generalize the 1-moment model to include some additional adiabatic and FLR effects.

In its current form, the 1-moment model makes no reference to the electric field, so it will not recover the adiabatic limit ($\omega \ll k_\parallel$) where the density should be proportional to Φ, $n = -\Phi$. The problem is that Φ appears explicitly only in the $\partial u_\parallel/\partial t$ equation, so a closure approximation in a lower moment equation will not include the effects of Φ unless the closure is modified in some way. One way to do this is to go back to Eq. (2.18) and include the electrostatic potential on the right-hand side. With Eq. (2.19), Eq. (2.18) then becomes

$$\frac{\partial u_\parallel}{\partial t} + \nabla_\parallel n + \mu_1 \sqrt{2}|k_\parallel| u_\parallel = -\nabla_\parallel \Phi.$$

Taking the large $k_\parallel$ limit of this equation leads to a new closure approximation for $u_\parallel$ that includes the effect of the electric potential, $u_\parallel = -(\nu_1/|k_\parallel|)\nabla_\parallel(n+\Phi)$. Inserting this closure into Eq. (2.17) causes the density to relax to the adiabatic limit. This mends the deficiency with a result that might have been anticipated, since one expects to recover the adiabatic response in the zero-frequency limit.

This procedure can be generalized to derive an $n-1$ moment closure from an n-moment closure. The basic idea is that by taking the high-$k_\parallel$ limit of the n^{th} fluid moment equation, the $\partial/\partial t$ becomes negligible and one obtains a frequency-independent closure approximation for the n^{th} moment that can be used in the $n-1$ moment equation. Physically, this is related to the fact that phase mixing is most important for $\omega \ll k_\parallel v_t$, which is where the closure can be determined. The opposite limit, $\omega \gg k_\parallel v_t$, is the cold-plasma limit where the highest moment can be ignored and the choice of closure is not too important.

For example, the 2-moment closure for $p_\parallel$ in Eq. (2.19) can be derived by taking the large $k_\parallel$ limit ($k_\parallel v_t \gg \omega, \omega_*$) of the 3-moment equation for $T_\parallel$, Eq. (2.72). In turn, the 3-moment closure for $q_\parallel$ used in Eq. (2.72) can be derived by taking the large $k_\parallel$ limit of the 4-moment equation for $q_\parallel$, Eq. (2.66). Likewise, upon taking the high $k_\parallel$ limit of Eq. (2.68), one is led to the closure approximation

$$q_\perp = -\frac{1}{\sqrt{2}D_\perp|k_\parallel|}\nabla_\parallel\left(T_\perp + \frac{1}{2}\hat{\nabla}_\perp^2\Psi\right),$$

where $\hat{\nabla}_\perp^2\Psi \approx \nabla_\perp^2\Phi$ includes FLR-related adiabatic terms in the $T_\perp$ dynamics described in detail in Sec. 2.4. This closure for $q_\perp$ is used in the "3+1" model of Eqs. (2.70–2.73), which uses 3 parallel moments but only 1 perpendicular moment. In App. A, I present an 8-moment gyrofluid model, which I refer to as the "4+4" model since it contains 4 parallel moments ($n, u_\parallel, T_\parallel$, and $q_\parallel$) and 4 perpendicular moments ($T_\perp, q_\perp, R_\perp$, and $s_\perp$). Each of the lower-moment models can easily be obtained from this "4+4" set.

One caveat should be mentioned. The $n \to n-1$ moment reduction procedure outlined in this section is apparently not general. In particular, I have not been able to generate an n-moment closure with this reduction property valid for $n > 4$.

2.3.4 Parallel Phase-Mixing Closure Summary

It is convenient to collect together the results obtained thus far for the 4+2 gyrofluid model and to write them in dimensional units. One implements the parallel phase-mixing closure in Eqs. (2.11) and (2.13) by approximating the highest two full moments, $R_\parallel$ and $R_\perp$, in terms of the lower moments. It is useful first to write each in terms of its reducible components plus an irreducible correction:

$$R_\parallel \equiv \frac{3p_\parallel^2}{mn} + r_\parallel \quad \text{and} \quad R_\perp \equiv \frac{p_\parallel p_\perp}{mn} + r_\perp. \tag{2.24}$$

One then linearizes, and approximates the irreducible part so as to reproduce the low- and high-frequency limits of the lowest moments of the linear propagator. The closure approximation has a simple form in wave-number space. That is,

$$r_\parallel \equiv -D_\parallel \frac{\sqrt{2}v_t}{|k_\parallel|} ik_\parallel q_\parallel + \beta_\parallel \frac{p_{\parallel 0}}{m} T_{\parallel 1} \quad \text{and} \quad r_\perp \equiv -D_\perp \frac{\sqrt{2}v_t}{|k_\parallel|} ik_\parallel q_\perp. \tag{2.25}$$

The constants $D_\parallel, D_\perp$, and $\beta_\parallel$ are

$$D_\parallel \equiv \frac{2\sqrt{\pi}}{3\pi - 8}, \qquad \beta_\parallel \equiv \frac{32 - 9\pi}{3\pi - 8}, \qquad D_\perp \equiv \frac{\sqrt{\pi}}{2}, \tag{2.26}$$

exactly as found in Hammett and Perkins, 1990 and Hammett *et al.*, 1992c. Figs. (2.1) and (2.2) show the real and imaginary parts of the local kinetic response function for a Maxwellian $F_0, R(\zeta) = 1 + \zeta Z(\zeta)$ compared with the gyrofluid approximations.

In these figures, the argument of the plasma dispersion function is real. The approximations to the collisionless response in all but the one-pole models are reasonable, improving as more moments are kept. Each reproduces the most important qualitative features of the response. The one-pole model is the roughest, for while it is correct at $\zeta = 0$ and $\zeta = \infty$ and gives damping for intermediate values of ζ, the real part of the response function has the wrong sign for $\zeta > 1$.

Most importantly, this approach eliminates the singularities that are present at resonances in the collisionless limit of most previous fluid equations. These closure relations are linearly exact for some distribution that is close to Maxwellian [Hammett and Perkins, 1990] (but only approximate in the case that the equilibrium distribution function is Maxwellian). It is therefore not surprising that Landau damping and its inverse, ion Compton scattering, and other "kinetic" phenomena are described reasonably well by these few equations.

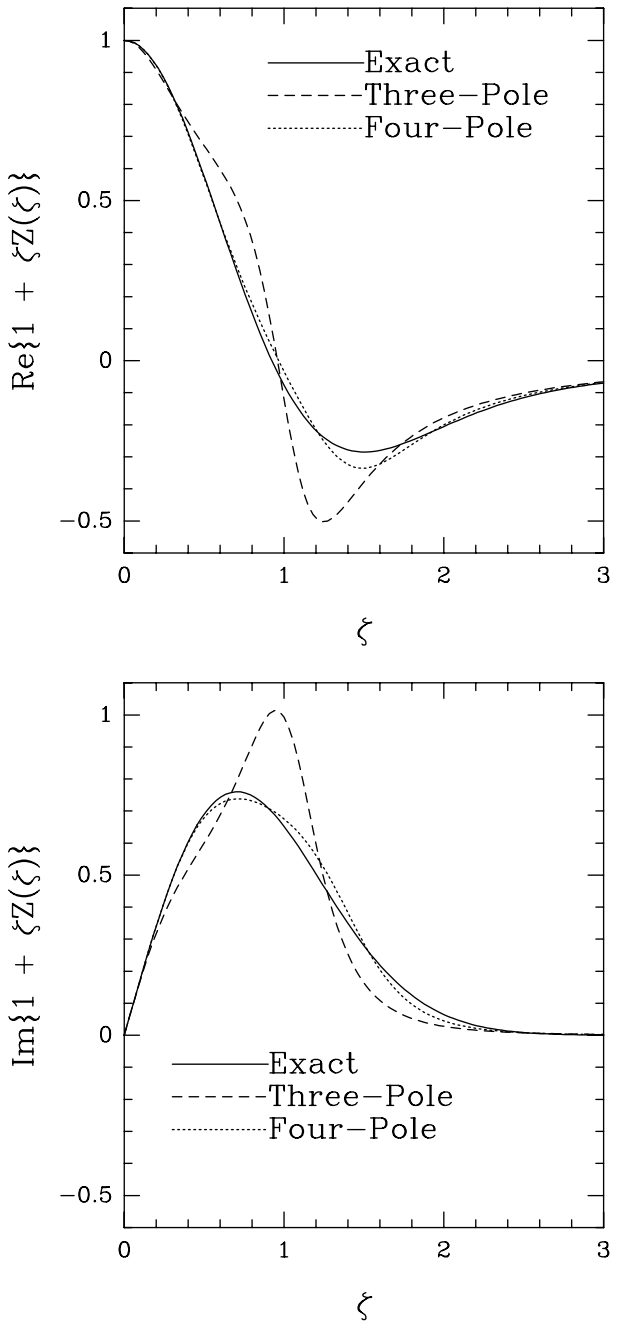

Figure 2.2: $1 + \zeta Z(\zeta)$ for three- and four-pole models of parallel phase mixing.

2.4 Finite-Larmor-Radius Effects

I shall now investigate the conventional (nondissipative) FLR effects buried in the various integrals involving J_0 in the fluid equations, Eqs. (2.8–2.13). (Collisionless dissipation induced by FLR gyrations will be considered in Sec. 2.5.) These integrals are of the form

$$\int d^3v\, v_\perp^{2j} v_\parallel^\ell F J_0 = n \left\langle v_\perp^{2j} v_\parallel^\ell J_0 \right\rangle . \tag{2.27}$$

Note that an exact, fully nonlinear (arbitrary F) evaluation of $\langle J_0 \rangle$ would require an infinite set of velocity-space moments, since J_0 contains all even powers of $v_\perp$; approximations are therefore necessary.

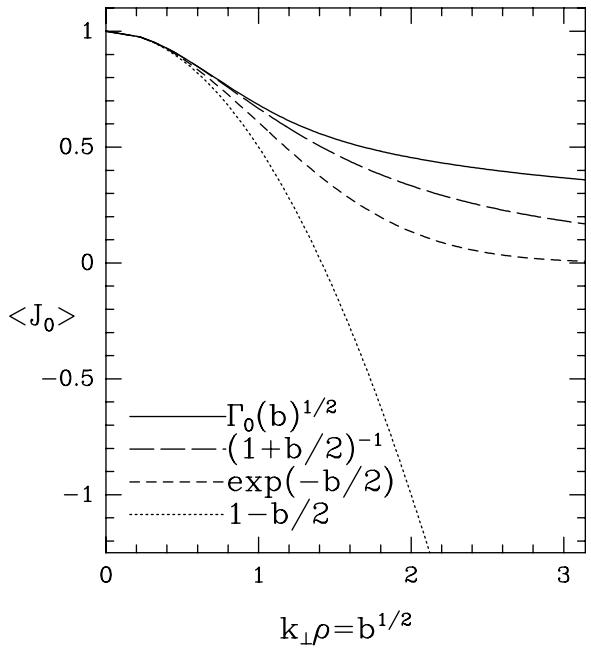

Figure 2.3: Comparison of FLR approximations to $\langle J_0 \rangle$.

The standard second-order Taylor-series expansion of J_0 yields $\langle J_0 \rangle \simeq 1 - b/2$, in which $b \equiv \rho_i^2 k_\perp^2$ and $\rho_i^2 \equiv \langle v_\perp^2 \rangle / (2\Omega) = T_\perp/(m\Omega)$. This approximation is equivalent to assuming that each of the perpendicular moments higher than $\langle v_\perp^2 \rangle$ is identically zero. In addition to the various J_0 integrals in the fluid equations where J_0 operates on Φ, one must also evaluate Eq. (2.5), in which J_0 operates on F itself.

A Taylor-series expansion of the J_0 in Eq. (2.5) yields

$$\bar{n} \equiv \int d^3v \, J_0 F = n + \nabla_\perp^2 \left(n \frac{T_\perp}{m 2\Omega^2} \right).$$

Upon expanding $nT_\perp$ in the last term into equilibrium and perturbed components in the gyrokinetic ordering (where, for example, $n_1 \ll n_0$ but $\nabla_\perp n_1 \sim \nabla_\perp n_0$), one is led to

$$\bar{n}_1 = \left(1 - \frac{b_0}{2} \right) n_1 - \frac{n_0}{T_{\perp 0}} \frac{b_0}{2} T_{\perp 1}, \tag{2.28}$$

where $b_0 \equiv k_\perp^2 T_{\perp 0}/(m\Omega^2)$. The Taylor-series approach provides the simplest second-order accurate model. It is useful for developing analytic understanding in the $k_\perp \rho \ll 1$ limit, but should be used cautiously because of the large errors introduced for $k_\perp \rho > 1$. The errors are particularly important in numerical simulations, since the typical grid needed to resolve the dynamics introduces large $k_\perp \rho$ values into the system. That is, the grid spacing in the direction of the background gradient must be $\Delta x \lesssim \rho$, which implies that the maximum $k_x \rho$ present is $\gtrsim \pi$. The Taylor-series approximation is egregiously wrong for such wavenumbers, since $1 - b/2 \approx -4$, while J_0 is bounded between -0.4 and 1. In Fig. (2.3), different expressions for $\langle J_0 \rangle$ are compared. The error in the Taylor-series approximation for the $\langle J_0 \rangle$ FLR terms is unacceptably large for $k_\perp \rho > \sqrt{2}$. The Taylor-series expansion of $\Gamma_0(b) \simeq 1 - b$ [which appears in the quasineutrality constraint, Eq. (2.4)] goes awry even sooner, as it is negative for $k_\perp \rho > 1$, whereas $\Gamma_0(b)$ is always positive. This can cause significant errors in the linear growth rates and eigenmode shapes, as demonstrated in Figs. (3.3–4.4), which will be discussed in Chapters 3 and 4.

Another way to carry out the various J_0 integrals [Hammett and Dorland, 1991; Brizard, 1992] is to assume that the total guiding-center F (including F_1) is always bi-Maxwellian (with perturbations in n, $T_\perp$, $u_\parallel$, and $T_\parallel$). This would imply, for example, that

$$\langle J_0 \rangle = e^{-b/2} = 1 + \frac{T_\perp}{2m\Omega^2} \nabla_\perp^2 + \frac{T_\perp^2}{8m^2\Omega^4} \nabla_\perp^4 + \cdots \tag{2.29}$$

and so on, where $b = b_0 + b_1 \propto T_{\perp 0} + T_{\perp 1}$ contains both equilibrium and perturbed parts of the $T_\perp$. The $\nabla_\perp^2$ operators above operate only on Φ in Eqs. (2.8–2.13). Upon applying the same assumption that F is always bi-Maxwellian to Eq. (2.5), where J_0 operates on F itself, one is led to

$$\bar{n}_1 = \int d^3v \, J_0 F - n_0 = e^{-b_0/2} n_1 + \frac{n_0}{T_{\perp 0}} \frac{\rho_0^2}{2} e^{-b_0/2} \nabla_\perp^2 T_{\perp 1}.$$

This "Maxwellian-total-F", or $\langle J_0 \rangle \approx \exp(-b/2)$, approximation reduces to the second-order Taylor-series approximation in the small-$k_\perp \rho$ limit, but it is better behaved for large $k_\perp \rho$. That is, it gives the reasonable result that $\langle J_0 \rangle \to 0$ as $k_\perp \rho \to \infty$. However, this approach does not match the kinetic linear dispersion relation very well for $k_\perp \rho \sim 1$ or larger [*e.g.,* see Fig. (3.3)]. The reason is that although the equilibrium F_0 is Maxwellian, the linear perturbation F_1 is quite non-Maxwellian in $v_\perp$. Indeed, the standard linear solution of Eq. (2.1) in an unsheared slab gives $F_1 \propto F_0 J_0(\alpha + v_\perp^2 \beta)$. Upon inserting this into Eq. (2.5), one obtains a linear dispersion relation with terms proportional to $\int d^3v \, (F_0/n_0) J_0^2 = \langle J_0^2 \rangle_0 = \Gamma_0(b_0)$. This is very different from the case in which the total F (including F_1) is assumed to be Maxwellian, where the $\langle J_0 \rangle = \exp(-b/2)$ in the fluid equations combines with another factor of $\exp(-b/2)$ in the $\bar{n}_i$ calculation to give terms proportional to $\exp(-b)$. Since the correct kinetic result, $\Gamma_0(b)$, has a much weaker b dependence at large b (asymptotically proportional to $1/\sqrt{b}$), the "Maxwellian-total-F" approximation results in too much gyroaveraging at large b. This major difference between $\langle J_0 \rangle^2$ and $\langle J_0^2 \rangle$ is part of what motivated the $\langle J_0 \rangle \approx \langle J_0^2 \rangle^{1/2} = \Gamma_0^{1/2}$ model considered below, which is linearly correct to all orders in $k_\perp \rho$ in the absence of magnetic shear and nonlinearly second-order accurate in its presence. Further motivation was provided by Similon's approach.

2.4.1 Similon and the Particle-Space Approach

Similon [SIMILON, 1981] derived a set of fluid equations for the nonlinear electron drift-wave problem. Since the quasineutrality constraint depends directly on the particle density $\bar{n} = \int d^3v \, J_0 F$ (plus the polarization part) and not on the guiding-center density $n = \int d^3v \, F$, he chose to perform the velocity averages in particle space rather than guiding-center space. That is, he operated on the gyrokinetic equation with J_0 before evaluating the moment integrals. This approach has the advantage of easily reproducing the proper kinetic linear dispersion relation in an unsheared slab. The primary disadvantages lie in the complexity of the nonlinear and shear terms evaluated in particle space.

Upon operating on Eq. (2.1) from the left with J_0 and keeping only the $\mathbf{E} \times$

B nonlinearity, one is led to

$$\frac{\partial(J_0F_1)}{\partial t} + \nabla\cdot\Big(v_\parallel J_0(F_1\hat{\mathbf{b}}) + F_0J_0^2\mathbf{v}_E + J_0(F_1J_0\mathbf{v}_E)\Big) - \frac{\partial}{\partial v_\parallel}\left(\frac{e}{m}F_0J_0(\hat{\mathbf{b}}\cdot\nabla J_0\Phi)\right) = 0. \tag{2.30}$$

One may then take moments of this equation, using the definitions

$$\bar{n}_1 \equiv \int d^3v\, J_0F_1, \qquad \bar{n}_0\bar{u}_{\parallel 1} \equiv \int d^3v\, J_0v_\parallel F_1,$$

and so on. Deferring the discussion of magnetic shear for the moment (so that $\hat{b} = \hat{z}$ and $J_0\nabla_\parallel - \nabla_\parallel J_0 = 0$), one may carry out the velocity-space averages by assuming that the equilibrium F_0 is Maxwellian with density and temperature gradients in the x direction. Upon utilizing the normalizations given in Eqs. (2.61) and (2.62), one finds the linear evolution equation for the particle-space perturbed density $\bar{n}$:

$$\frac{\partial\bar{n}}{\partial t} = -\nabla_\parallel\bar{u}_\parallel - \left[\Gamma_0 + \eta_i(\Gamma_0 - \Gamma_1)\nabla_\perp^2\right]\frac{\partial\Phi}{\partial y}. \tag{2.31}$$

Note that by operating on the gyrokinetic equation with J_0 before taking velocity-space integrals, one finds terms $\propto \Gamma_{0,1}$ from integrals such as $\int d^3v\, F_0J_0^2$, and thus reproduces the proper kinetic FLR behavior, unlike the "Maxwellian-total-F" model of the previous section. It is shown below how the guiding-center approach reproduces Eq. (2.31) with the appropriate transformations from guiding-center quantities $n, T_\perp, u_\parallel, q_\perp, \ldots$ to particle quantities $\bar{n}, \bar{u}_\parallel, \ldots$.

Unfortunately, the nonlinear term in Eq. (2.30) is quite complicated, since the leftmost gyroaveraging operator J_0 now operates on both the distribution function and the electrostatic potential, and

$$J_0(F_1J_0\mathbf{v}_E) \neq F_1J_0^2\mathbf{v}_E.$$

Similon approximated this term (on page 93 of his dissertation) by assuming that the $v_\perp$ dependence of F_1 was proportional to $F_0J_0(k_\perp v_\perp/\Omega)$, allowing him to develop a simple fluid model of FLR effects in the nonlinear $\mathbf{E}\times\mathbf{B}$ terms. However, errors of order $k_\perp^2\rho^2$ are introduced by this approximation. As is shown in the next section, one finds that by taking fluid moments in guiding-center space (delaying the second gyroaveraging operation to Poisson's equation) one can avoid having to take moments of quantities such as $J_0(F_1J_0\mathbf{v}_E)$, and thus can regain $k_\perp^2\rho^2$ accuracy.

A second complication in the particle-space approach arises from the fact that the gyroaveraging operator J_0 and the parallel derivative operator $\hat{\mathbf{b}}(\mathbf{x}) \cdot \nabla$ do not commute when the magnetic field is sheared. This introduces a gyro-averaging of $k_\parallel$ that may be important for some modes, as pointed out by Bakshi *et al.* [BAKSHI *et al.*, 1977] and Linsker [LINSKER, 1981]. In the usual sheared-slab model, where $\hat{b}(x) = \hat{z} + \hat{y}x/L_s$, one finds

$$J_0(\hat{b} \cdot \nabla \Phi) = \hat{b} \cdot \nabla (J_0 \Phi) + \frac{\rho^2}{2L_s} \frac{\partial^2 \Phi}{\partial x \partial y} + O(k_\perp^4 \rho^4),$$

upon using the small-b approximation for J_0. The fastest-growing modes typically have $k_\perp \rho \lesssim 1/2$ and an average $k_\parallel$ of order $k_y \rho / L_t$, so the shear-correction term is typically smaller than the lowest order $k_\parallel$ term by a factor of order L_T/L_s, which is usually small. However, as Linsker [LINSKER, 1981] has shown, this gyro-averaged shear effect can be quite important for other modes, particularly for narrow modes localized near the rational surface, where $k_\parallel \to 0$. Since there are modes with significant growth rates that satisfy this criterion, it is necessary to treat the gyro-averaging of the shear as accurately as other FLR corrections.

Similon noted the difficulty presented by the shear and pointed out that the expression

$$\int d^3v \, F_0 J_0 \hat{b} \cdot \nabla J_0 \Phi = n_0 \left\langle J_0 \hat{\mathbf{b}} \cdot \nabla J_0 \right\rangle_0 \Phi = \Gamma_0^{1/2} \hat{b} \cdot \nabla \Gamma_0^{1/2} \Phi$$

remained valid in the presence of shear. [This is proved most easily in Fourier space, where the x in $\hat{b}(x)$ becomes $-i\partial/\partial k_x$.] Though he used this identity for moments of the last term in Eq. (2.30), Similon ignored the effects of shear when taking moments of the $J_0(\hat{\mathbf{b}} \cdot \nabla v_\parallel F_1)$ term.

My approach is motivated in part by Similon's insights, though I improve upon his approach by taking moments of the gyrokinetic equation in guiding-center space, and also extend it to allow the presence of equilibrium and perturbed temperature gradients. The details of this approach are outlined in the next two sections.

2.4.2 Guiding-Center Approach

Equations (2.8–2.13) were derived by taking moments of the gyrokinetic equation directly, without first operating on it with a second J_0 as was done in the previous

section. The transformation from guiding-center fluid quantities to particle fluid quantities will be considered in the next section. Here, the focus is on how to approximate terms such as $\langle J_0 \rangle$ and to show how they lead to various linear and nonlinear FLR effects.

As an example, consider the following term from Eq. (2.8):

$$\nabla \cdot (n \langle J_0 \rangle \mathbf{v}_E). \tag{2.32}$$

From Eq. (2.3), one sees that in general $\langle J_0 \rangle$ is a function of all $v_\perp^{2\ell}$ moments of the guiding-center F. The following closure approximation allows one to express this in terms of just the lowest $\langle v_\perp^2 \rangle = T_\perp/m$ moment,

$$\langle J_0 \rangle \approx \Gamma_0^{1/2}(b) + \text{NLPM}, \tag{2.33}$$

where NLPM represents a model of nonlinear, FLR-induced phase mixing to be discussed in Chap. 2.5. This $\Gamma_0^{1/2}(b)$ approximation was motivated by the contrast between the "Maxwellian-total-F" model, which led to $\langle J_0 \rangle = \exp(-b/2)$, and Similon's real-space approach, in which (at least linearly in a shearless slab) two Bessel functions are combined before taking moments, leading to $\langle J_0^2 \rangle = \Gamma_0(b)$. In some sense, the $\langle J_0 \rangle \approx \langle J_0^2 \rangle^{1/2} = \Gamma_0^{1/2}(b)$ approximation anticipates the second gyroaveraging operation that will occur for the Poisson equation. Note that it is rigorous through second order in $k_\perp \rho$ (i.e., it matches the second-order Taylor series result $\langle J_0 \rangle = 1 - b/2$), and therefore agrees with the $\exp(-b/2)$ model through second order, while imposing less gyroaveraging than the exponential model for large b. The $\Gamma_0^{1/2}$ model has the added advantage of exactly reproducing the FLR effects in the local, linear (unsheared slab) kinetic dispersion relation.

Both the equilibrium and fluctuating components of the perpendicular temperature are "hidden" in the argument to the Bessel function, since $b \propto T_{\perp 0} + T_{\perp 1}$. Upon using the chain rule to carry out the divergence, one is led to

$$\nabla \cdot \left(n \Gamma_0^{1/2}(b) \mathbf{v}_E \right) = \underset{①}{(\nabla n) \cdot \Gamma_0^{1/2} \mathbf{v}_E} + \underset{②}{n (\nabla b) \frac{\partial \Gamma_0^{1/2}}{\partial b} \cdot \mathbf{v}_E} + \underset{③}{n \Gamma_0^{1/2} (\nabla \cdot \mathbf{v}_E)}. \tag{2.34}$$

Although $T_{\perp 1} \ll T_{\perp 0}$, $\nabla_\perp T_{\perp 1} \sim \nabla_\perp T_{\perp 0}$. Thus, while b may be replaced with b_0 in terms ① and ③, the gradient in ② produces two terms, proportional to ∇b_0 and ∇b_1. Because $\Gamma_0^{1/2}$ operates unambiguously on Φ, define $\Psi \equiv \Gamma_0^{1/2}(b_0)\Phi$ and $\mathbf{v}_\Psi \equiv$

$\Gamma_0^{1/2}(b_0)\mathbf{v}_E$. For notational convenience, I now introduce two modified Laplacian operators $\hat{\nabla}_\perp^2$ and $\hat{\hat{\nabla}}_\perp^2$:

$$\frac{1}{2}\hat{\nabla}_\perp^2\Gamma_0^{1/2} \equiv b\frac{\partial\Gamma_0^{1/2}}{\partial b}, \qquad \hat{\hat{\nabla}}_\perp^2\Gamma_0^{1/2} \equiv b\frac{\partial}{\partial b}\left(\Gamma_0^{1/2} + b\frac{\partial\Gamma_0^{1/2}}{\partial b}\right). \tag{2.35}$$

Note that as $b \to 0$, the operators $\hat{\nabla}_\perp^2, \hat{\hat{\nabla}}_\perp^2 \to \nabla_\perp^2$, as shown in Fig. (2.4).

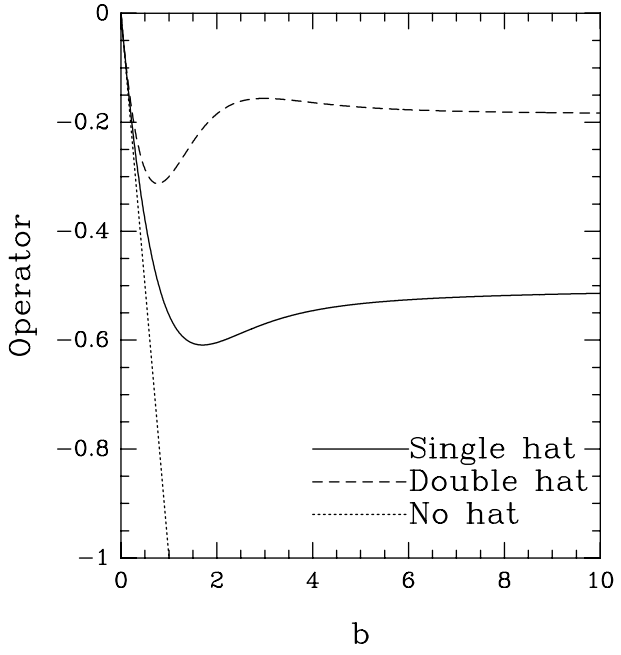

Figure 2.4: Fourier-transformed gyrofluid FLR operators compared to the usual Laplacian. Shown are $\rho^2\hat{\nabla}_\perp^2(b)$, $\rho^2\hat{\hat{\nabla}}_\perp^2(b)$, and $\rho^2\nabla_\perp^2(b)$. The gyrofluid operators are much less stiff than the Laplacian operator for large b.

In slab geometry, the divergence of $\mathbf{v}_E$ vanishes from Eq. (2.34), leaving

$$\nabla\cdot\left(n\Gamma_0^{1/2}(b)\mathbf{v}_E\right) = \left(\frac{\partial n_0}{\partial x}\hat{x} + \nabla n_1\right)\cdot\mathbf{v}_\Psi + \frac{n_0}{T_{\perp 0}}\left(\frac{\partial T_{\perp 0}}{\partial x}\hat{x} + \nabla T_{\perp 1}\right)\cdot\frac{\hat{\nabla}_\perp^2}{2}\mathbf{v}_\Psi,$$

in which n and $T_\perp$ have been separated into equilibrium and fluctuating parts as before. The last term on the right-hand side is a nonlinear FLR correction that appears quite naturally. In the small-$k_\perp\rho$ limit, $\Gamma_0^{1/2} = 1 - k_\perp^2\rho^2/2$; these terms reduce to the familiar Taylor-series expansion. However, in the large $k_\perp\rho$ limit,

since $\hat{\nabla}_\perp^2 \to -1/2$, this expression is much less stiff than the Taylor-series expansion. Upon using the normalizations given in Eqs. (2.61) and (2.62), one finds the equation for $\partial n/\partial t$ [Eq. (2.63)].

Consider now the $\langle (mv_\perp^2/2)J_0 \rangle$ term that appears in the perpendicular pressure equation, Eq. (2.12). If the $v_\perp$ dependence of F is close to Maxwellian (which is true at least for the linear F_0 component), then one can use the Maxwellian identity $(mv_\perp^2/2)F_\mathrm{M} = T_\perp \partial(T_\perp F_\mathrm{M})/\partial T_\perp$ to rewrite this in a form in which one can use Eq. (2.33):

$$n \left\langle \frac{mv_\perp^2}{2} J_0 \right\rangle \approx T_\perp \frac{\partial}{\partial T_\perp} \left(T_\perp \int d^3v F J_0 \right) \approx p_\perp \frac{\partial}{\partial b} (b\Gamma_0^{1/2}) + \mathrm{NLPM}.$$

(Again, NLPM represents a model of nonlinear, FLR-induced phase mixing to be discussed in Chap. 2.5.) In slab geometry, $\langle v_\perp^2 \rangle$ enters only through FLR corrections, so to maintain overall second-order accuracy it is only necessary to keep the lowest-order contribution $\langle (mv_\perp^2/2)J_0 \rangle \approx T_\perp$. The more robust expression above may be used to obtain higher-order accuracy in the linear limit (where $F = F_0$ is Maxwellian) along with an approximate treatment of nonlinear effects consistent with the form of the closures used in other terms. [The situation in toroidal geometry is more complicated. There, the $\langle v_\perp^2 \rangle$ moment enters through the ∇B drifts as well, so that the number of $\langle v_\perp^{2\ell} \rangle$ moments kept affects the accuracy of both the toroidal drift-resonance model [Waltz *et al.*, 1992; Beer and Hammett, 1992] and the FLR model.] Upon inserting this expression for $\langle (mv_\perp^2/2)J_0 \rangle$ into Eq. (2.12) and expanding in the gyrokinetic ordering as was done for the density equation, one arrives at the linear and nonlinear FLR terms found in Eq. (2.67).

Finally, I should also explicitly state how I approximate terms like $\langle v_\parallel J_0 \rangle$ and $\langle v_\parallel^3 J_0 \rangle$. My reasoning is as follows:

$$\begin{aligned} \langle v_\parallel J_0 \rangle &= \langle (u_\parallel + (v_\parallel - u_\parallel)) J_0 \rangle \\ &\approx (u_\parallel + \tfrac{1}{2} q_\perp \hat{\nabla}_\perp^2) \Gamma_0^{1/2}, \end{aligned} \tag{2.36}$$

where the heat flux $q_\perp$ results from the $\langle (v_\parallel - u_\parallel) v_\perp^2 \rangle$ moment and I have approximated the terms higher-order in $k_\perp \rho$ by analogy with Eq. (2.33). Similarly,

$$\begin{aligned} \langle v_\parallel^3 J_0 \rangle &= \left\langle \left((v_\parallel - u_\parallel)^3 + 3u_\parallel v_\parallel^2 - 3u_\parallel^2 v_\parallel + u_\parallel^3 \right) J_0 \right\rangle \\ &\approx (q_\parallel + 3u_\parallel p_\parallel) \Gamma_0^{1/2} + \text{higher-order nonlinear terms}. \end{aligned}$$

2.4.3 Guiding-Center → Particle-Space Transformation

It is not surprising to find that the simplicity gained in the evolution equations by writing the evolution equations in guiding-center space is somewhat offset by a more complicated quasineutrality condition. Next, the transformation from guiding-center moments $(n, T_\perp, \ldots)$ to the particle moments $(\bar{n}, \bar{u}_\parallel, \ldots)$ is developed. This is necessary because the quasineutrality equation, Eq. (2.4), depends directly on $\bar{n}$, not n. Along the way, one finds that this transformation shows that particle fluid equations [such as Eq. (2.31)] are linearly equivalent to the guiding-center fluid equations, Eqs. (2.63–2.67).

The (non-polarization part of the) perturbed particle density [defined in Eq. (2.5)] is $\bar{n}_1 \equiv \int d^3v\, J_0 F_1$. It is important to note that here, unlike in the evolution equations, the Bessel function operates on the distribution function.

Note that any linear solution of Eq. (2.1) in the absence of shear may be written as

$$F_1(\mathbf{x}, v_\parallel, v_\perp, t) = F_0(\mathbf{x}, v_\parallel, v_\perp) J_0\left(\frac{v_\perp}{\Omega} k_\perp\right) \left[\alpha(\mathbf{x}, v_\parallel, t) + \left(\frac{m v_\perp^2}{2T_{\perp 0}} - 1\right) \beta(\mathbf{x}, v_\parallel, t)\right]$$

$$= F_0 J_0 \alpha + T_{\perp 0} \frac{\partial F_0}{\partial T_{\perp 0}} J_0 \beta, \tag{2.37}$$

in which F_0 is the equilibrium distribution function, J_0 operates on α and β, and α and β are functions independent of $v_\perp$. The moments of α and β are determined self-consistently from the definitions of the guiding-center fluid quantities

$$\int d^3v\, F_1 \equiv n, \qquad \int d^3v\, \tfrac{1}{2} m v_\perp^2 F_1 \equiv p_\perp. \tag{2.38}$$

Upon substituting Eq. (2.37) into Eqs. (2.38) and using the normalizations given in Eqs. (2.61) and (2.62), one finds two equations in two unknowns:

$$n = \langle J_0 \rangle \langle \alpha \rangle + b \frac{\partial \langle J_0 \rangle}{\partial b} \langle \beta \rangle ,$$

$$p_\perp = \left[\left(1 + b\frac{\partial}{\partial b}\right) \langle J_0 \rangle\right] \langle \alpha \rangle + \left\{\left[1 + b\frac{\partial}{\partial b} + \frac{\partial}{\partial b}\left(b^2 \frac{\partial}{\partial b}\right)\right] \langle J_0 \rangle\right\} \langle \beta \rangle .$$

Given the *Ansatz* in Eq. (2.37), the transformation from the density of guiding centers to the density of particles is thus defined by $\langle J_0 \rangle$ [Eq. (2.33)]. The result of

the algebra is

$$\bar{n} = \frac{\Gamma_0^{1/2}}{D(b)} \left[N(b) n + \tfrac{1}{2} \hat{\nabla}_\perp^2 T_\perp \right], \tag{2.39}$$

in which

$$N(b) \equiv 1 + \hat{\hat{\nabla}}_\perp^{\,2} - \tfrac{1}{2} \hat{\nabla}_\perp^4 \tag{2.40}$$

and

$$D(b) \equiv N(b) + \tfrac{1}{4} \hat{\nabla}_\perp^4. \tag{2.41}$$

Note that $D(b) > 0$. Upon expanding Eq. (2.39) for small b, one can verify that it reproduces Eq. (2.28) and is therefore second-order accurate in $k_\perp \rho$. The guiding-center quasineutrality condition [Eq. (2.69)] may now be found by noting that $n_{e0} = n_{i0}$, substituting Eq. (2.39) into Eq. (2.6), and operating on the resulting equation from the left with $\Gamma_0^{1/2}$.

For the purpose of comparison, an equation describing the evolution of $\bar{n}$ must be found. To accomplish this, one combines Eq. (2.39) and the linear parts of Eqs. (2.63) and (2.67), yielding

$$\frac{\partial \bar{n}}{\partial t} = -\frac{\Gamma_0^{1/2}}{D(b)} \nabla_\parallel \left(N(b) u_\parallel + \tfrac{1}{2} \hat{\nabla}_\perp^2 q_\perp \right) - \left[\Gamma_0 + \eta_i (\Gamma_0 - \Gamma_1) \nabla_\perp^2 \right] \frac{\partial \Phi}{\partial y}. \tag{2.42}$$

Note that the coefficients of $\partial \Phi / \partial y$ in Eqs. (2.31) and (2.42) are exactly the same. A comparison of the parallel convection terms suggests that the transformation given in Eq. (2.39) may be generalized. This is the case, as the transformations

$$\bar{u}_\parallel \equiv \frac{\Gamma_0^{1/2}}{D(b)} \left(N(b) u_\parallel + \tfrac{1}{2} \hat{\nabla}_\perp^2 q_\perp \right), \tag{2.43}$$

$$\bar{p}_\parallel \equiv \frac{\Gamma_0^{1/2}}{D(b)} \left(N(b) p_\parallel + \tfrac{1}{2} \hat{\nabla}_\perp^2 r_\perp \right), \tag{2.44}$$

$$\bar{q}_\parallel \equiv \frac{\Gamma_0^{1/2}}{D(b)} \left(N(b) q_\parallel + \tfrac{1}{2} \hat{\nabla}_\perp^2 s_\perp \right) \tag{2.45}$$

are consistent with the observation made in Chap. 2.3 that the parallel phase-mixing closure for perpendicular temperature fluctuations had the same form as the closure for parallel temperature fluctations (i.e., a 3-moment closure for $p_\parallel$ has the same form as the 3-moment closure for $r_\perp$, and can be combined by the above transformations to give the same form for a 3-moment closure for $\bar{p}_\parallel$). If one ignores the nonlinear terms, which are unfortunately very complicated in particle

space, these transformations provide an alternate route to Eqs. (A.5–A.8) once Eqs. (2.63–2.66) are known. Specifically, one can find the linear 4+4 gyrofluid model by repeating the procedure in Sec. 2.4.1 for the parallel particle-space moments $\bar{n}, \bar{u}_\parallel, \bar{T}_\parallel$ and $\bar{q}_\parallel$, closing the resulting four equations as outlined in HAMMETT and PERKINS, 1990, and utilizing the transformations [Eqs. (2.39, 2.43–2.45)] along with Eqs. (2.63–2.66). The moment-reduction scheme outlined in Sec. 2.3.3 then uniquely determines the closures for models that retain fewer moments. While this gives one confidence that the linear FLR and parallel phase-mixing models have a degree of internal consistency, the complicated form of the nonlinear moments that arises in the particle-space derivation precludes one from taking full advantage of this route. It is more straightforward to develop accurate models of nonlinear terms by taking moments in guiding-center space.

2.4.4 Alternative FLR Models

It is perhaps not obvious why such an elaborate FLR model is necessary. Fig. (2.3) compares different approximations for $\langle J_0 \rangle$. Clearly, though valid in the small-b limit, the Taylor-series approximation is disastrously inaccurate for $b \geq 1$; other approximations are better. In particular, I have investigated the equations resulting from the $\langle J_0 \rangle = e^{-b/2}$ and $(1+b/2)^{-1}$ approximations and from an isotropic pressure model, each described briefly below.

4+0 Model. In our first foray [DORLAND *et al.*, 1990] into fluid FLR models, we considered an (even more) heuristic model that neglected the nonlinear FLR effects entirely and ignored the $T_\perp, q_\perp$, *etc.* fluctuations. The idea was to assume an isotropic temperature (background and fluctuations), so that $T_\perp = T_\parallel$. Since there are no equations for the evolution of the perpendicular moments, I refer to this model as either "4+0" or "3+0", depending upon the number of parallel moments retained. It must be stressed that this model is *not* directly related to the rest of the FLR models derived in this thesis and is not even second-order accurate in $k_\perp \rho_i$. On the other hand, of all the models shown in this thesis, the "3+0" most strongly favors the fluid equations typically found in the literature and may be obtained from the 4+0 model by using the method outlined in Sec. 2.3.3. Some nonlinear results (and deficiencies) from this type of model are presented in Sec. 7.1. The

model equations are

$$\frac{dn}{dt} + \nabla_\parallel u_\parallel + \left(1 + \eta_i \hat{\nabla}_\perp^2\right) \frac{\partial \Psi}{\partial y} = 0, \tag{2.46}$$

$$\frac{du_\parallel}{dt} + \nabla_\parallel \left(n + T + \Psi\right) = 0, \tag{2.47}$$

$$\frac{dT}{dt} + \nabla_\parallel (q_\parallel + 2u_\parallel) + \eta_i \frac{\partial \Psi}{\partial y} = 0, \tag{2.48}$$

$$\frac{dq_\parallel}{dt} + \nabla_\parallel (3 + \beta_\parallel) T + \sqrt{2} |k_\parallel| D_\parallel q_\parallel = 0. \tag{2.49}$$

Here $d/dt \to \partial/\partial t + \mathbf{v}_\Psi \cdot \nabla$, $\mathbf{v}_\Psi = \hat{\mathbf{b}} \times \nabla \Psi$, and $\Psi = \Gamma_0 \Phi$. No justification is offered for these equations other than to note that in the absence of magnetic shear these equations approximate the proper linear response with multipole approximations to the plasma dispersion function; they are presented to make contact with models found in the literature. In particular, the factor-of-two coefficient of the $u_\parallel$ term in the temperature evolution equation does not correspond to the usual 2/3 associated with the collisional Braginskii equations. In this model, the quasineutrality constraint is simply

$$\left(\tau + 1 - \Gamma_0\right) \Phi = n. \tag{2.50}$$

Total Maxwellian Model. One may recover the sheared-slab, electrostatic limit of Brizard's gyrofluid equations [Brizard, 1992] from Eqs. (2.63–2.69) by leaving $q_\parallel$ and $q_\perp$ unspecified, taking $\mathcal{N}_1 = \mathcal{N}_{21} = \mathcal{N}_{22} = 0, \Psi = e^{-b/2}\Phi, N(b) = D(b) = 1$, redefining

$$\tfrac{1}{2} \hat{\nabla}_\perp^2 e^{-b/2} \equiv b \frac{\partial e^{-b/2}}{\partial b},$$

$$\hat{\hat{\nabla}}_\perp^{\,2} e^{-b/2} \equiv b \frac{\partial}{\partial b} \left(e^{-b/2} + b \frac{\partial e^{-b/2}}{\partial b} \right),$$

and replacing the Γ_0 in term "7" of Eq. (2.69) with e^{-b}.

Padé Model. There also exists a simpler FLR model that is second-order accurate, well-behaved at large b, and straightforward to implement in a finite-difference code. Though I solve Eqs. (2.63–2.69) with a spectral method that handles the expressions involving the $\Gamma_0^{1/2}$ functions easily, it may be advantageous for some problems to use the Padé approximation $\langle J_0 \rangle = (1 + b/2)^{-1}$. I refer to this model

as the "Padé" model for this reason, though it should be noted that the $\Gamma_0^{1/2}$ model is also a Padé-like approximation to the full FLR effects in the presence of magnetic shear. The Padé model may be obtained from Eqs. (2.63–2.69) by taking $\Psi \equiv (1+b/2)^{-1}\Phi, N(b) = D(b) = 1$, redefining

$$\frac{1}{2}\hat{\nabla}_\perp^2(1+b/2)^{-1} \equiv b\frac{\partial(1+b/2)^{-1}}{\partial b},$$

$$\hat{\hat{\nabla}}_\perp^{\,2}(1+b/2)^{-1} \equiv b\frac{\partial}{\partial b}\left((1+b/2)^{-1} + b\frac{\partial(1+b/2)^{-1}}{\partial b}\right),$$

and replacing the Γ_0 in term "7" of Eq. (2.69) with $(1+b/2)^{-2}$ and the Γ_0 in term "8" of Eq. (2.69) with $(1+b)^{-1}$. Results from this approach are presented in Chap. 4.2.

2.5 FLR Phase Mixing

The phase-mixing process that underlies Landau damping is fundamentally due to the *distribution* of velocities of the particles freely streaming along the field lines. This spread in velocities causes neighboring particles to move apart, mixing away (damping) any density perturbations that arise, even in the asymptotically collisionless limit. In addition to the spread in parallel velocities of particles, there is also a spread in the *gyro-averaged* $\mathbf{E}\times\mathbf{B}$ drift velocities, which leads to phase mixing in the perpendicular direction. Physically, high-energy particles with large gyroradii will have a slower $\mathbf{E}\times\mathbf{B}$ drift than low-energy particles with small gyroradii; this spread in drift velocities leads to mixing. This process does not appear to be simply related to the usual stochastic perpendicular heating normally associated with large amplitude fluctuations [Ching, 1973; Dupree and Tetreault, 1978; Krommes, 1980; Hirshman, 1980]. Nonlinear FLR phase mixing is a complicated process that is difficult to reproduce accurately with fluid models, but the models presented below reproduce its essential qualitative features, providing a nonlinear damping process important at large $k_\perp\rho$ and mixing-length levels of Φ.

To illustrate the essence of this effect, consider first a simplified 1-dimensional problem, where a given electrostatic field varies in only one direction (such as would be the case for a long, thin eddy in the region away from one of the two regions of

curvature). Upon taking $\Phi = \Phi(y)$, so $\mathbf{v}_E = v_E(y)\hat{x}$, and assuming no gradients in the equilibrium F_0 and no parallel gradients, one can reduce Eq. (2.1) to

$$\frac{\partial F_1}{\partial t} + J_0(\frac{k_y v_\perp}{\Omega}) v_E \frac{\partial F_1}{\partial x} = 0. \tag{2.51}$$

Concentrate on a single Fourier mode of Φ, so the k_y in J_0 can be considered to be a fixed number and consider the response of this equation to an initial perturbation of the form $F_1(t=0) = \exp(ik_x x) F_{\rm M}(v)$, where $F_{\rm M}$ is a Maxwellian. The solution is

$$F_1 = e^{ik_x[x - J_0(k_y v_\perp/\Omega) v_E t]} F_{\rm M}(v).$$

Although F_1 oscillates in time, all velocity moments of F_1 will decay in time, just as in the parallel phase mixing discussed earlier. For example, consider the density response

$$n_{1k}(t) = e^{-ik_x x} \int d^3v\, F_1 = \int d^3v\, e^{-ik_x J_0(k_y v_\perp/\Omega) v_E t} F_{\rm M}(v). \tag{2.52}$$

Upon expanding J_0 in the small-$k_\perp\rho$ limit, one can evaluate this integral analytically:

$$\begin{aligned} n_{1k}(t) &\simeq \frac{n_0}{v_t^2} e^{-ik_x v_E t} \int_0^\infty dv_\perp\, v_\perp e^{ik_x (k_y^2 v_\perp^2/4\Omega^2) v_E t} e^{-v_\perp^2/(2v_t^2)} \\ &= n_0 e^{-ik_x v_E t} \frac{1}{1 - ik_x b v_E t/2}, \end{aligned} \tag{2.53}$$

where $b \equiv k_y^2 v_t^2/\Omega^2$ in this 1-D problem. [One could find an asymptotic representation of this integral without expanding in $k_\perp\rho$ by using the method of stationary phase. However, the Riemann–Lebesgue lemma [Bender and Orszag, 1978] guarantees that the integral goes to zero as $t \to \infty$; since the fluid equations generate an exponentially damped approximation, which is too strong in any case, greater detail is unnecessary.] From Eq. (2.53), one sees that the density decays in time though it has a long tail that decays like $1/t$, unlike the parallel phase-mixing case [Hammett *et al.*, 1992c] where initial density perturbations decay as $\exp(-k_\parallel^2 v_t^2 t^2/2)$, faster than exponential. The full J_0 effects on $n_{1k}(t)$ can be found by numerically integrating Eq. (2.52). The results are shown in Figs. (2.5–2.7). For $b > 1$, there is a rapid initial decay followed by a long tail containing several harmonic components with slowly decaying amplitudes.

Because of the details of the long tail, the temporal Fourier transform of the kinetic response is logarithmically divergent as ω tends to zero. Hence one is not

able to match the kinetic and fluid results in frequency space as before. However, one may choose the closure coefficients so that the qualitative features of the true solution are preserved, and can check the resulting estimate numerically for a wide range of parameters.

2.5.1 A 1-moment, 1-D Fluid Model

The fluid model of parallel phase mixing was based on a closure approximation for the $v_\parallel \nabla_\parallel$ kinetic term that introduced a damping rate of order

$$\nu_\parallel \approx |k_\parallel| v_t = |k_\parallel| \left\langle (v_\parallel - \langle v_\parallel \rangle)^2 \right\rangle^{1/2}.$$

Likewise, a fluid model of perpendicular FLR phase mixing comes from making a closure approximation for the $J_0 v_E \partial/\partial x$ term that introduces a damping term of order

$$\nu_\perp \approx |k_x| \left\langle (J_0 v_E - \langle J_0 v_E \rangle)^2 \right\rangle^{1/2} = |k_x v_E| [\Gamma_0(b) - e^{-b}]^{1/2}, \tag{2.54}$$

upon evaluating the averages $\langle \cdots \rangle$ over a Maxwellian. For small $k_\perp \rho$, this reduces to $\nu_\perp \approx |k_x v_E| b/2$, which reproduces the initial decay rate in Eq. (2.53).

This is illustrated by first developing a 1-moment fluid model of FLR phase mixing. Upon taking the density moment of Eq. (2.52), one obtains

$$\frac{\partial n}{\partial t} + \frac{\partial}{\partial x} \left(n \langle J_0 \rangle v_E \right) = 0.$$

Upon using a small-$k_y \rho$ approximation for the Bessel function, one finds

$$\frac{\partial n}{\partial t} + \left(1 - \frac{b}{2}\right) v_E \frac{\partial n}{\partial x} - \frac{k_x^2}{2m\Omega^2} n v_E \frac{\partial T_\perp}{\partial x} = 0. \tag{2.55}$$

At this point a closure approximation must be introduced for the unknown highest moments ($T_\perp$) in terms of the known lower moments (n). If one were to neglect $\partial T_\perp/\partial x$, then one would just get $n(t)$ oscillating at a frequency $\omega = k_x v_E (1 - b/2)$ with no damping. For short times, this actually is similar to the kinetic result $n_{1k}(t) \approx \exp(-ik_x v_E t)(1 + ik_x v_E b t/2) + \cdots$, but it misses the long-time damped behavor of Eq. (2.53). To correct this, one follows the same procedure used for parallel closures and includes a dissipative term in the closure approximation for $T_\perp$,

$$\frac{\partial n}{\partial t} + \left(1 - \frac{b}{2}\right) v_E \frac{\partial n}{\partial x} = -\nu_1 \frac{b}{2} |v_E k_x| \, n - \lambda_1 \frac{b}{2} v_E \frac{\partial n}{\partial x}. \tag{2.56}$$

The absolute value that appears in the first term on the right-hand side guarantees that that term is always dissipative. The second (reactive) term allows one to match the phase of the fluid approximation to that of the kinetic solution. The matching coefficients λ_1 and ν_1 are expected to be $O(1)$. Upon defining a relative squared error $\epsilon = (\int dt\, |n_f(t) - n_{1k}(t)|^2)/(\int dt\, |n_{1k}(t)|^2)$, where n_f is the fluid approximation from Eq. (2.56) and n_{1k} is the kinetic result from Eq. (2.53), one finds that a minimum value of $\epsilon = 0.17$ can be achieved with $(\nu_1, \lambda_1) = (0.4, 0.6)$.

One may extend this model to larger $k_\perp \rho$ by analogy with the results of Chap. 2.4, replacing the b's that appear in the closure terms on the right-hand side of Eq. (2.56) with the operator $-\hat{\nabla}_\perp^2 \Gamma_0^{1/2}$. (The $(1 - b/2)$ factor on the left-hand side becomes $\Gamma_0^{1/2}$ in accordance with Chap. 2.4.) A one-pole FLR phase-mixing operator $\mathcal{N}_1$ operating on some moment M is defined by

$$\mathcal{N}_1 M \equiv \nu_1 \left| \left[\frac{1}{2} \hat{\nabla}_\perp^2 \mathbf{v}_\Psi \right] \cdot \nabla \right| M - \lambda_1 \left[\frac{1}{2} \hat{\nabla}_\perp^2 \mathbf{v}_\Psi \right] \cdot \nabla M, \tag{2.57}$$

where $(\nu_1, \lambda_1) = (0.4, 0.6)$ as found in the small-b limit. The comparison between the 1-moment fluid model employing this $\mathcal{N}_1$ operator and the exact kinetic result from numerically integrating Eq. (2.52) is shown in Figs. (2.5–2.7). For small b, where the damping rate is small, the comparison is quite good. For b of order unity or larger, the agreement is not as good. Nevertheless, this is a significant improvement over past fluid models that ignored FLR phase mixing altogether and would have oscillated in Figs. 2.5–2.7 without any damping. Some fluid models in the past employed an *ad hoc* linear hyperviscosity term to provide damping at large $k_\perp \rho$. This model provides a physics-based nonlinear damping term with at least the proper qualitative scaling with Φ, b, and k_x.

2.5.2 Extension to more moments and 2-D

Rather than making a closure approximation for $T_\perp$ in Eq. (2.55), one can follow the dynamics for $T_\perp$ by taking the $v_\perp^2$ moment of Eq. (2.51). This requires a closure approximation for $\langle v_\perp^2 J_0 \rangle$, or at least of $\langle v_\perp^4 \rangle$ if the small-$k_\perp \rho$ expansion of J_0 is used. Upon following a path similar to that used to derive the 1-moment fluid model above, one finds the following two-moment model of FLR phase mixing:

$$\frac{dn}{dt} \quad + \quad \left[\tfrac{1}{2} \hat{\nabla}_\perp^2 \mathbf{v}_\Psi \right] \cdot \nabla T_\perp + \mathcal{N}_{21} T_\perp = 0,$$

$$\frac{dT_\perp}{dt} + \left[\tfrac{1}{2}\hat{\nabla}_\perp^2 \mathbf{v}_\Psi\right]\cdot\nabla n + \left[\hat{\hat{\nabla}}_\perp^{\,2}\mathbf{v}_\Psi\right]\cdot\nabla T_\perp + \mathcal{N}_{22}T_\perp = 0,$$

using the non-dimensional units of Eqs. (2.61-2.62), where $\mathcal{N}_{21}$ and $\mathcal{N}_{22}$ are given by

$$\begin{aligned}\mathcal{N}_{21} &= -\tfrac{1}{4}\nu_2\left|\left[\tfrac{1}{4}\hat{\nabla}_\perp^4\mathbf{v}_\Psi\right]\cdot\nabla\right| - \tfrac{1}{4}\lambda_2\left[\tfrac{1}{4}\hat{\nabla}_\perp^4\mathbf{v}_\Psi\right]\cdot\nabla,\\ \mathcal{N}_{22} &= \nu_2\left|\left[\tfrac{1}{2}\hat{\nabla}_\perp^2\mathbf{v}_\Psi\right]\cdot\nabla\right| - \lambda_2\left[\tfrac{1}{2}\hat{\nabla}_\perp^2\mathbf{v}_\Psi\right]\cdot\nabla.\end{aligned} \tag{2.58}$$

Choosing $(\nu_2,\lambda_2) = (1.6, 1.3)$ gives a relative squared error in the small-b limit of $\epsilon = (\int dt\,|n_f(t) - n_{1k}(t)|^2)/(\int dt\,|n_{1k}(t)|^2) = 0.06$, somewhat better than the 0.17 achieved by the 1-moment model. $\mathcal{N}_{21}$ represents closure approximations for higher-order terms in $\langle J_0\rangle$ of order $k_\perp^4\rho^4$. A comparison with the numerical kinetic solution of Eq. (2.52) for general b is shown in Figs. 2.5–2.7. Although the 2-moment model is formally more accurate than the 1-moment model for small b (and it recovers $\mathcal{O}(t)$ accuracy for the initial relaxation of a perturbation), one finds that in practice it is of accuracy comparable to that of the 1-moment model for general b. An improved model employing additional moments could probably be found at the cost of additional complexity.

So far I have been considering the FLR phase mixing caused by a given, static, 1-D $\Phi(y)$. The kinetic equation is reversible, and if at some time $\Phi(y)$ changed sign [or if $\Phi = \Phi(y)\cos\omega t$ were oscillatory], then F_1 would begin to "un-phase-mix" and eventually reconstruct the original density perturbation. [In fact, notice that the FLR phase-mixing model provides damping only nonlinearly and does not introduce any damping into the linear equations since the linear $J_0\mathbf{v}_E\cdot\nabla F_0$ terms are known and do not require any closure approximations.] In a turbulent nonlinear 2-D system, it seems unlikely that the 2-D convection paths given by the equipotential lines of $J_0\Phi(x,y)$ would ever exactly reverse to reconstruct the initial perturbation. This is even less likely in a turbulent 3-D system where the $v_\parallel$ of the particles would also have to be reversed to reconstruct the initial conditions. Nevertheless, the FLR phase-mixing process is very complicated, and it may be that in some cases (perhaps involving a few isolated modes) the model presented here may overestimate the amount of FLR phase mixing that is actually occuring. In nonlinear simulations one should therefore check the decorrelation times and

lengths, and also check the sensitivity of the simulations to the choice of ν and λ coefficients in the $\mathcal{N}_1$, $\mathcal{N}_{21}$, and $\mathcal{N}_{22}$ operators.

Briefly, I now outline one way to approximate terms like $|\hat{\nabla}_\perp^2 \mathbf{v}_E \cdot \nabla| M$ in general geometry. First, note that $\hat{\nabla}_\perp^2$ operates only on $\mathbf{v}_E$, so one can define an averaged velocity field $\mathbf{v} = \hat{\nabla}_\perp^2 \mathbf{v}_E$ using standard FFT's since the $\hat{\nabla}_\perp^2$ operator is evaluated most easily in k space. Since this is already a crude model of a fairly complicated process, it may be sufficient to approximate

$$|\mathbf{v} \cdot \nabla| \, M \simeq |v_x||\frac{\partial}{\partial x}|M + |v_y||\frac{\partial}{\partial y}|M - \langle |v_x||\frac{\partial}{\partial x}|M + |v_y||\frac{\partial}{\partial y}|M \rangle \tag{2.59}$$

where the volume average is subtracted off to ensure that the NLPM operators do not violate the conservation laws. Alternatively, one may rearrange this to be in explicitly conservative form:

$$|\mathbf{v} \cdot \nabla| \, M \simeq -\frac{\partial}{\partial x}\left(|v_x|\frac{1}{|k_x|}\frac{\partial M}{\partial x}\right) - \frac{\partial}{\partial y}\left(|v_y|\frac{1}{|k_y|}\frac{\partial M}{\partial y}\right). \tag{2.60}$$

The basic idea is to provide a fast numerical approximation by evaluating terms like $(1/|k_x|)\partial M/\partial x$ in k_x space where they are most easily evaluated, and then transform back to real space to multiply by $|v_x|$. [I use Eq. (2.59) in the `ITG` code, though I have tried both and found that the two approximations give almost the same answer.] This rough approximation will overestimate the FLR phase-mixing effect since it does not include "interference" terms inside the original absolute value. In the original kinetic equation, the $J_0 \mathbf{v}_E \cdot \nabla F_1$ nonlinearity vanishes if both Φ and F_1 have cylindrical symmetry (or, less restrictively, if $\nabla_\perp F_1 \| \nabla_\perp J_0 \Phi$), which may be related to the formation of long-lived coherent structures. The nonlinearity in Eq. (2.60) no longer satisfies this property exactly, though the nonlinear damping will be reduced for regions of the plasma that satisfy a kind of "square symmetry" where the two terms in Eq. (2.60) separately vanish. If a more accurate numerical implementation of $\mathcal{N}M$ is needed, one would probably have to map M onto a grid that followed the convection contours, use FFT's along each convection contour to evaluate the phase mixing from $|\mathbf{v} \cdot \nabla| M$, and then map the phase-mixed M back to the regular grid where the rest of the terms in the fluid equations are advanced in time.

FLR phase mixing is a difficult process to model accurately with fluid equations. The nonlinear simulations presented in later chapters are insensitive to the

exact details of the damping mechanism at high $k_\perp \rho$, especially if the turbulent spectrum is peaked at longer wavelengths with $k_\perp \rho \ll 1$. Furthermore, the model presented here does capture the essential qualitative features of FLR phase mixing with the proper physics-based scalings, providing nonlinear damping important at high $k_\perp$ and large Φ.

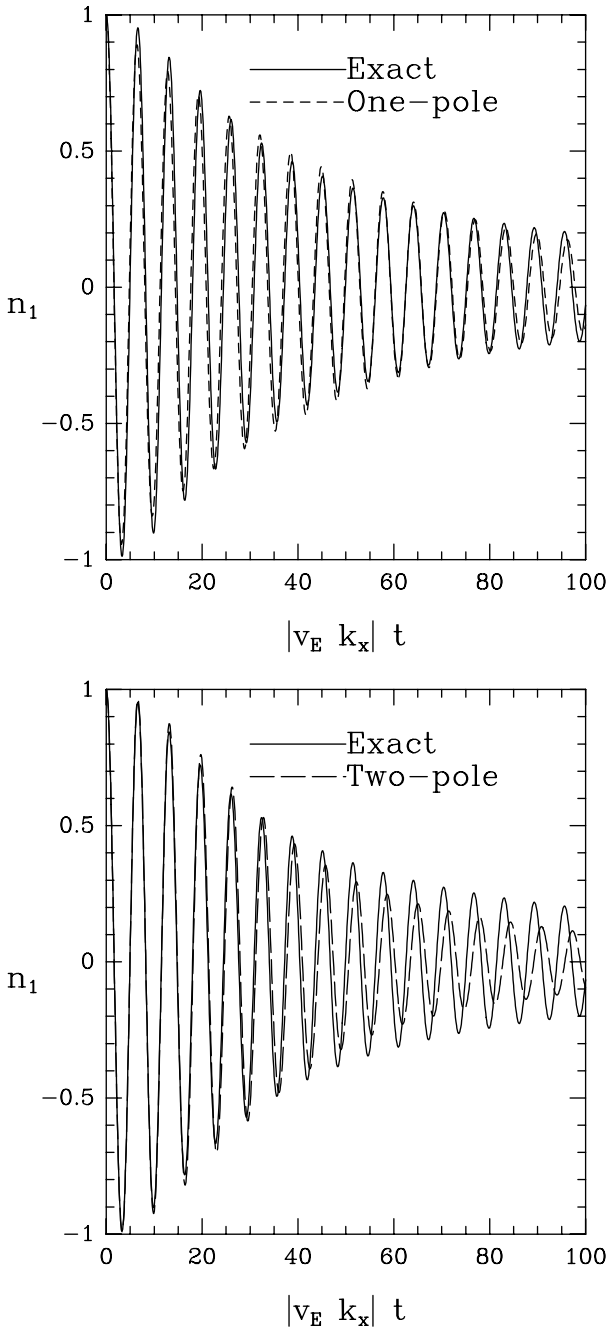

Figure 2.5: One- and two-pole FLR phase-mixing models, for $b = 0.1$.

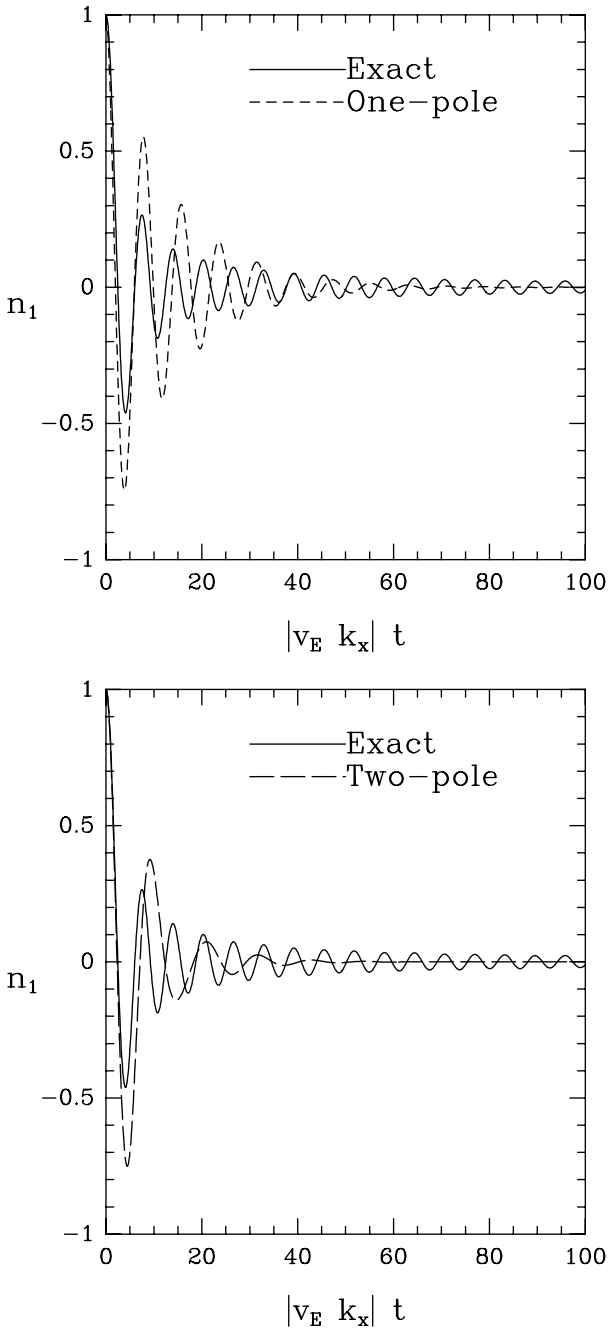

Figure 2.6: One- and two-pole FLR phase-mixing models, for $b = 1$.

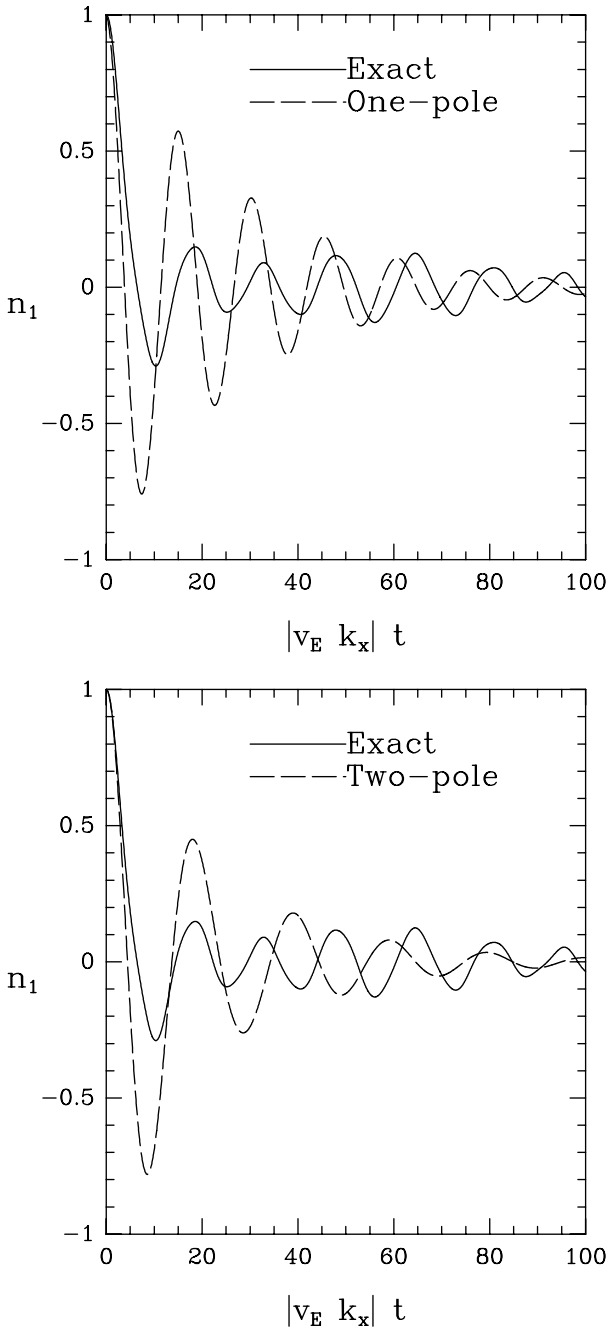

Figure 2.7: One- and two-pole FLR phase-mixing models, for $b = 10$.

2.6 Normalized Gyrofluid Equations

With the closure approximations specified, one may now complete the derivation of the nonlinear gyrofluid equations easily. The moments and the potential are separated into equilibrium and fluctuating components [$n = n_0 + n_1(t), \ldots$] and the normalizations used in Chap. 2.4 are utilized again. Specifically, the non-dimensional perturbed variables ($\tilde{n}, \tilde{u}_\parallel, \ldots$) are given in terms of the dimensional perturbed variables ($n_1, u_{\parallel 1}, \ldots$) by

$$\left(\frac{n_1}{n_0}, \frac{u_{\parallel 1}}{v_t}, \frac{T_{\parallel 1}}{T_i}, \frac{T_{\perp 1}}{T_i}, \frac{q_{\parallel 1}}{v_t p_{\parallel 0}}, \frac{q_{\perp 1}}{v_t p_{\perp 0}}, \frac{e\Phi_1}{T_i} \right) = \frac{\rho_i}{L_n} (\tilde{n}, \tilde{u}_\parallel, \tilde{T}_\parallel, \tilde{T}_\perp, \tilde{q}_\parallel, \tilde{q}_\perp, \tilde{\Phi}). \quad (2.61)$$

Upon normalizing (x, y, z, t) according to

$$\tilde{x} = \frac{x - x_0}{\rho_i}, \quad \tilde{y} = \frac{y}{\rho_i}, \quad \tilde{z} = \frac{z}{L_n}, \quad \text{and} \quad \tilde{t} = \frac{t v_t}{L_n}, \quad (2.62)$$

one is led to a simpler set of equations. The quantity x_0 is the position of a reference rational surface, taken to be at the center of the simulation domain. The following definitions are useful: $L_n^{-1} \equiv -\partial \ln n_0 / \partial x, v_t \equiv \sqrt{T_{0i}/m_i}$ and $\rho_i \equiv v_t/\Omega_i$. For convenience, the tildes over the linearized non-dimensional variables are dropped except where confusion might otherwise be generated. Thus, throughout most of this thesis ($n, u_\parallel, \ldots$) are the same as the non-dimensional variables ($\tilde{n}, \tilde{u}_\parallel, \ldots$) in Eq. (2.61) and should not be confused with the original dimensional moments defined and used in Eqs. (2.7–2.13).

The model is set in the usual sheared-slab geometry. In dimensionless units, this stipulation leads to

$$\nabla_\perp \equiv \hat{\mathbf{x}} \frac{\partial}{\partial x} + \hat{\mathbf{y}} \frac{\partial}{\partial y}, \qquad \hat{\mathbf{b}} \cdot \nabla \equiv \frac{\partial}{\partial z} + s x \frac{\partial}{\partial y}, \qquad s \equiv L_n / L_s.$$

Upon denoting the gyroaveraged potential $\Gamma_0^{1/2}(b_0)\Phi \equiv \Psi$, one may make further useful definitions:

$$\frac{d}{dt} = \frac{\partial}{\partial t} + \mathbf{v}_\Psi \cdot \nabla, \qquad \mathbf{v}_\Psi = \hat{z} \times \nabla \Psi.$$

If one neglects the parallel nonlinearities (which are higher-order in ε) but retains the $\mathbf{E} \times \mathbf{B}$ nonlinearities and the nonlinear FLR terms, one obtains a 4+2

gyrofluid model:

$$\frac{dn}{dt} + \underbrace{\left[\tfrac{1}{2}\hat{\nabla}_\perp^2 \mathbf{v}_\Psi\right]\cdot\nabla T_\perp}_{1} + \underbrace{\mathcal{N}_{21}T_\perp}_{5} + \hat{\mathbf{b}}\cdot\nabla u_\parallel + \left[1+\eta_{i\perp}\tfrac{1}{2}\hat{\nabla}_\perp^2\right]\frac{\partial\Psi}{\partial y} = 0, \tag{2.63}$$

$$\frac{du_\parallel}{dt} + \underbrace{\left[\tfrac{1}{2}\hat{\nabla}_\perp^2 \mathbf{v}_\Psi\right]\cdot\nabla q_\perp}_{1} + \underbrace{\mathcal{N}_{21}q_\perp}_{5} + \hat{\mathbf{b}}\cdot\nabla\left(T_\parallel + n + \Psi\right) = 0, \tag{2.64}$$

$$\frac{dT_\parallel}{dt} + \underbrace{\mathcal{N}_1 T_\parallel}_{5} + \hat{\mathbf{b}}\cdot\nabla(2u_\parallel + q_\parallel) + \eta_{i\parallel}\frac{\partial\Psi}{\partial y} = 0, \tag{2.65}$$

$$\frac{dq_\parallel}{dt} + \underbrace{\mathcal{N}_1 q_\parallel}_{5} + \hat{\mathbf{b}}\cdot\nabla(3 + \underbrace{\beta_\parallel}_{2})T_\parallel + \underbrace{\sqrt{2}|k_\parallel|\, D_\parallel q_\parallel}_{3} = 0, \tag{2.66}$$

$$\frac{dT_\perp}{dt} + \underbrace{\left[\tfrac{1}{2}\hat{\nabla}_\perp^2 \mathbf{v}_\Psi\right]\cdot\nabla n + \left[\hat{\hat{\nabla}}_\perp^{\,2}\mathbf{v}_\Psi\right]\cdot\nabla T_\perp}_{1} + \underbrace{\mathcal{N}_{22}T_\perp}_{5} + \hat{\mathbf{b}}\cdot\nabla q_\perp + \left[\tfrac{1}{2}\hat{\nabla}_\perp^2 + \eta_{i\perp}(1+\hat{\hat{\nabla}}_\perp^{\,2})\right]\frac{\partial\Psi}{\partial y} = 0, \tag{2.67}$$

$$\frac{dq_\perp}{dt} + \underbrace{\left[\tfrac{1}{2}\hat{\nabla}_\perp^2 \mathbf{v}_\Psi\right]\cdot\nabla u_\parallel + \left[\hat{\hat{\nabla}}_\perp^{\,2}\mathbf{v}_\Psi\right]\cdot\nabla q_\perp}_{1} + \underbrace{\mathcal{N}_{22}q_\perp}_{5} + \hat{\mathbf{b}}\cdot\nabla(T_\perp + \tfrac{1}{2}\hat{\nabla}_\perp^2\Psi) + \underbrace{\sqrt{2}|k_\parallel|\, D_\perp q_\perp}_{4} = 0. \tag{2.68}$$

Poisson's equation (assuming quasineutrality and adiabatic electrons) is

$$\tau(\Psi - \underbrace{\langle\!\langle\Psi\rangle\!\rangle}_{6}) = \underbrace{\frac{\Gamma_0}{D(b)}\left(N(b)n + \tfrac{1}{2}\hat{\nabla}_\perp^2 T_\perp\right)}_{7} + \underbrace{(\Gamma_0 - 1)}_{8}\Psi. \tag{2.69}$$

In these equations, $\tau \equiv T_{i0}/T_{e0}$, $\eta_i \equiv L_n/L_T$, and $L_T^{-1} \equiv -\partial \ln T_0/\partial x$. The argument of the Bessel functions is $b \equiv (k_x^2 + k_y^2)$. The modified perpendicular Laplacian operators $\hat{\nabla}_\perp^2$ and $\hat{\hat{\nabla}}_\perp^{\,2}$ are defined in Eqs. (2.35). The origins of the terms marked with underbraces are noted below.

(1) Nonlinear FLR terms that arise from the divergence of $\langle J_0\rangle$. The usual nonlinear terms are included in the definition of d/dt.

(2) The non-dissipative part of the $R_\parallel$ closure; $\beta_\parallel \equiv (32-9\pi)/(3\pi-8)$.

(3) The dissipative part of the $R_\parallel$ closure; $D_\parallel \equiv 2\sqrt{\pi}/(3\pi - 8)$.

(4) The $R_\perp$ closure; $D_\perp \equiv \sqrt{\pi}/2$.

(5) A model of nonlinear phase mixing. The operators are defined in Eqs. (2.57) and (2.59).

(6) In the absence of non-adiabatic electrons, the flux-surface-averaged potential must be explicitly subtracted to prevent non-physical electron transport across rational surfaces.

(7) With (8), the expression for the perturbed particle-space density. $N(b)$ and $D(b)$ are defined in Eqs. (2.40) and (2.41).

(8) The usual ion polarization density.

A simpler (but still reasonably accurate) set of equations consists of evolution equations for the density, parallel velocity, and parallel and perpendicular temperatures (the "3+1" model). In this model, the FLR phase mixing of the parallel velocity is modeled with a one-pole model rather than a two-pole model, and the closures for $q_\parallel$ and $q_\perp$ are found by taking the $k_\parallel v_t \gg \omega, \omega_*$ limit of Eqs. (2.66) and (2.68) respectively. The result is

$$\frac{dn}{dt} + \left[\tfrac{1}{2}\hat{\nabla}_\perp^2 \mathbf{v}_\Psi\right] \cdot \nabla T_\perp + \mathcal{N}_{21} T_\perp + \hat{\mathbf{b}} \cdot \nabla u_\parallel + \left[1 + \eta_{i\perp} \tfrac{1}{2}\hat{\nabla}_\perp^2\right] \frac{\partial \Psi}{\partial y} = 0, \tag{2.70}$$

$$\frac{du_\parallel}{dt} + \mathcal{N}_1 u_\parallel + \hat{\mathbf{b}} \cdot \nabla \left(T_\parallel + n + \Psi\right) = 0, \tag{2.71}$$

$$\frac{dT_\parallel}{dt} + \mathcal{N}_1 T_\parallel + \hat{\mathbf{b}} \cdot \nabla 2u_\parallel + \eta_{i\parallel} \frac{\partial \Psi}{\partial y} + \frac{3 + \beta_\parallel}{\sqrt{2} D_\parallel} |k_\parallel| T_\parallel = 0, \tag{2.72}$$

$$\begin{aligned} &\frac{dT_\perp}{dt} + \left[\tfrac{1}{2}\hat{\nabla}_\perp^2 \mathbf{v}_\Psi\right] \cdot \nabla n + \left[\hat{\hat{\nabla}}_\perp^{\,2} \mathbf{v}_\Psi\right] \cdot \nabla T_\perp + \mathcal{N}_{22} T_\perp \\ &+ \left[\tfrac{1}{2}\hat{\nabla}_\perp^2 + \eta_{i\perp}\left(1 + \hat{\hat{\nabla}}_\perp^{\,2}\right)\right] \frac{\partial \Psi}{\partial y} + \frac{1}{\sqrt{2} D_\perp} |k_\parallel| \left(T_\perp + \tfrac{1}{2}\hat{\nabla}_\perp^2 \Psi\right) = 0. \end{aligned} \tag{2.73}$$

Poisson's equation is not changed in this simpler model.

Chapter 3

Local Linear Analysis

IT IS USEFUL TO CONSIDER the local (shearless) limit as a partial check of the foregoing derivation. One can derive the local dispersion relation for the 4+2 model by Fourier transforming the linearized versions of Eqs. (2.63–2.69). The result is a polynomial in ω that may then be solved numerically. However, if equal numbers of parallel and perpendicular moments are kept, the dispersion relation may be factored into a form very similar to the familiar kinetic dispersion relation. For example, in dimensionless units, the dispersion relation for the 4+4 model (see App. A) is

$$1+\tau+\Gamma_0\left\{\left[1-\frac{k_y}{\omega}\left(1-\eta_i b(1-\frac{I_1}{I_0})\right)\right]\zeta Z_4(\zeta)\right.$$
$$\left.-\frac{k_y}{\omega}\eta_i\left[\zeta^2+(\zeta^2-\tfrac{1}{2})\zeta Z_4(\zeta)\right]\right\}=0. \qquad (3.1)$$

The only approximation to the usual kinetic result is $Z_4(\zeta)$, given in HAMMETT and PERKINS, 1990. It is a four-pole approximation to the plasma dispersion function $Z(\zeta)$. In the local limit, the $\Gamma_0^{1/2}$ FLR model is exact to all orders in $k_\perp\rho$ for $n+n$ models [in the presence of temperature gradients, $n \geq 3$]. With the aid of *Mathematica* [WOLFRAM, 1988] and *Maple* [CHAR *et al.*, 1991], I have derived the dispersion relations for each of the intermediate models (from 3+1 to 4+4). For example, one may use the *Maple* script in App. H to generate the 4+2 gyrofluid dispersion relation, including numerical roots for the parameters of interest. Except for the $n+n$ models, the dispersion relations cannot be easily factored into recognizable terms. Rather than delve into much unpleasant algebra here, I will instead rely upon Figs. (3.1–3.3) to show a few important features of the local limit.

In Fig. (3.1a), the 3+3 and 3+1 models are compared to one branch of the local linear dispersion relation for $\eta_i = 2$, $k_\parallel L_n = 0.1$, and $T_i = T_e$. Note that the agreement is good even for $k_y \rho_i \geq 1$, where linear FLR effects are important. The improvement that may be obtained with additional moments is shown in Fig. (3.1b). This kind of improvement, especially from the 3+1 to the 4+2 model, is quite typical of the local gyrofluid dispersion relations.

In Figure (3.2) I compare the gyrofluid model to kinetic results shown in a previous paper [DONG *et al.*, 1987]. The parameters are $k_\perp \rho = 0.71$, $k_\parallel L_n = 0.013$, and $T_i = T_e$. Above $\eta \simeq 3.4$, the kinetic analysis predicts no instability. The 3+3 gyrofluid dispersion relation closely matches this kinetic result, since Eq. (3.1) differs from Eq. (11) of DONG *et al.*, 1987 only in the plasma dispersion function. The limitations of the less accurate 3+1 gyrofluid model are made more apparent. While the 3+1 model reproduces the kinetic frequency with reasonable accuracy near $\eta_i = 2$, the real frequency does not match as well as η_i increases, and the second branch of the dispersion relation is overdamped. [For clarity, above $\eta_i = 3.5$ I show the branch of the 3+1 dispersion relation that corresponds to the marginally stable branch of the exact dispersion relation. There is another 3+1 branch that remains very slightly unstable, with a different real frequency.] Based on this high-$k_\perp \rho$, low-$k_\parallel L_n$ example, one might expect to see the shortcomings of the 3+1 model in the sheared system at high $k_\perp \rho$ near the rational surface. However, if one finds surprising results with the 3+1 model, one may easily check them with a more accurate gyrofluid model.

By considering the real and imaginary parts of the local dispersion separately, one may derive the ITG marginal stability curve (η_i *vs.* $k_y \rho_i$). The quantities ζ and ω are purely real exactly at marginal stability so the only imaginary terms in Eq. (3.1) at marginal stability result from Z_4 (the approximation to the plasma dispersion function). Upon requiring the real and imaginary parts of Eq. (3.1) to vanish independently, one is led to a marginal stability relation $\eta_{\rm crit}(b, \zeta_*)$ that is independent of the details of Z_4 as long as $\mathrm{Im}[Z_4]$ exists. This relation is

$$\eta_{\rm crit} = \frac{1 \pm \sqrt{1 + g(\zeta_*, b, \tau)}}{1 + 2b(1 - I_1/I_0)},$$

where

$$g(\zeta_*, b, \tau) = \frac{2[1 + 2b(1 - I_1/I_0)][1 + \tau][1 + \tau - \Gamma_0]}{(\zeta_* \Gamma_0)^2}.$$

The quantity g is smallest for large ζ_*. Thus, the 3+3 and 4+4 $\Gamma_0^{1/2}$ gyrofluid models recover the exact kinetic result [GALEEV *et al.*, 1963; KADOMTSEV and POGUTSE, 1970]

$$\eta_{\rm crit}(b) = \frac{2}{1 + 2b[1 - I_1(b)/I_0(b)]}.$$

Other FLR models perform less well, as evidenced by Fig. (3.3). Shown are marginal stability curves derived from the 3+1 $\Gamma_0^{1/2}$ and $e^{-b/2}$ models and the 3+0 model with Taylor-series approximations to $\langle J_0^2 \rangle$. The latter involves only three equations, for $\bar{n}, \bar{u}_\parallel$, and $\bar{T}_\parallel$. For $k_\perp \rho = 1$ the Taylor-series curve crosses the η axis, an unphysical result.

It is clear that the $\Gamma_0^{1/2}$ models more faithfully represent the linear physics than does the $e^{-b/2}$ model. Given the roughly comparable complexity of the two models — they are equally demanding to implement numerically — there is no reason to choose the less accurate FLR model. The Padé approximation, on the other hand, represents a clear improvement over the Taylor-series model, and is just slightly more difficult to implement in a finite-difference code, requiring only a standard tridiagonal solver.

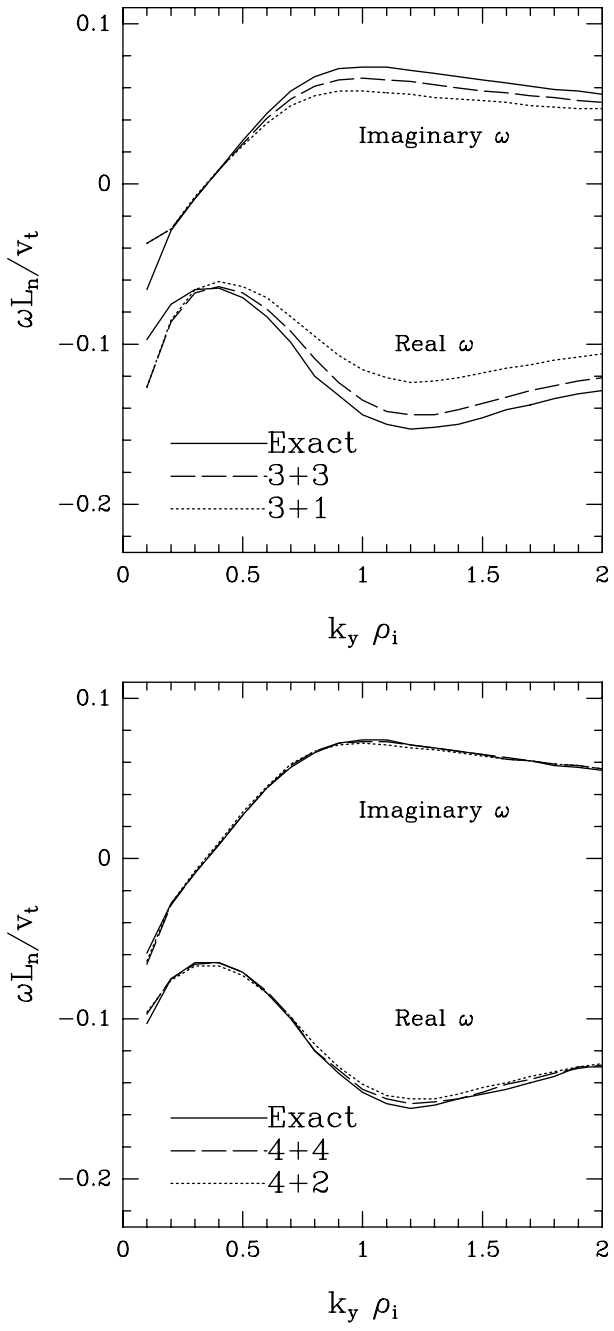

Figure 3.1: Unstable branch of the local dispersion relation for $\eta_i = 2$, $k_\parallel L_n = 0.1$, and $T_i = T_e$. Different curves represent results from retaining different numbers of moments.

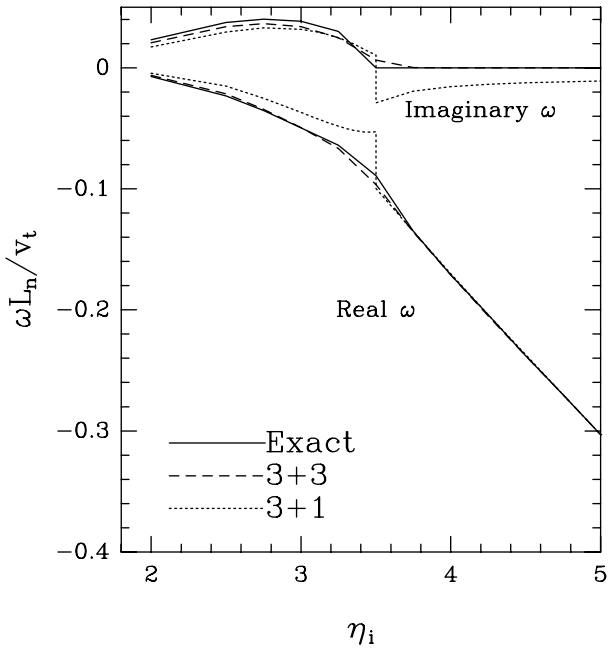

Figure 3.2: Local dispersion relation for $k_\perp \rho = 0.71$, $k_\parallel L_n = 0.013$, and $T_i = T_e$.

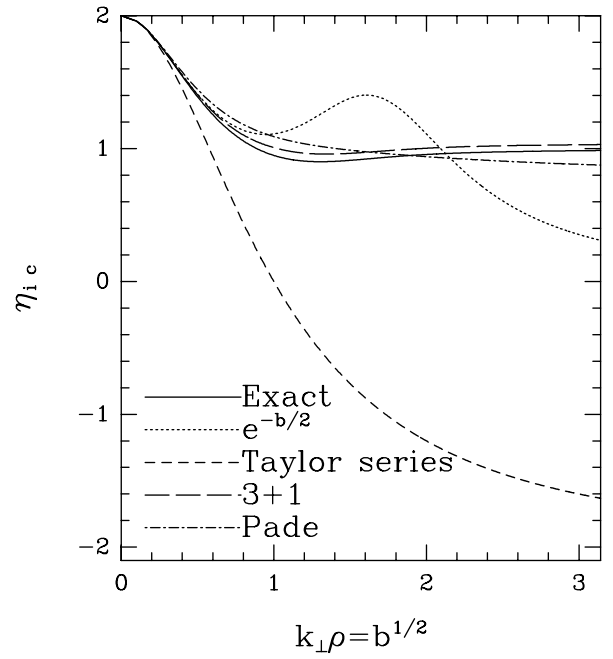

Figure 3.3: Marginal stability curves for different FLR models.

Chapter 4

Comparison with Linear Gyrokinetic Integral Code

In Chap. 3 I showed that in the absence of magnetic shear, the FLR and Landau-damping models yield dispersion relations that compare well with gyrokinetic theory. Here I include the effects of magnetic shear and show that the `ITG` code recovers gyrokinetic integral-code predictions [LINSKER, 1981] for the linear eigenmodes and eigenfrequencies.

4.1 Improper Gyroaveraging of the Shear

In Fig. (4.1) I compare the gyrofluid and gyrokinetic predictions for the fastest growing mode for the parameters $\eta_i = 3$, $L_s/L_n = 20$, $k_y\rho_i = 0.5$, and $\tau = 1$, in each case ignoring the proper gyroaveraging of the shear [LINSKER, 1981]. In Fig. (4.2) I show the corresponding eigenmodes for the various moments. The frequency (normalized to v_t/L_n) found with the gyrokinetic eigenvalue code is $\omega = -0.116 + 0.0635i$. The gyrofluid model predicts $\omega = -0.115 + 0.0635i$. In this case, complete inclusion of the magnetic shear alters the eigenmode only slightly and causes the frequency to shift to $\omega = -0.115 + 0.0655i$. Modes that are more strongly localized to the rational surface (e.g., for smaller η_i or smaller L_s/L_n) are more strongly affected [LINSKER, 1981]. As indicated in Chap. 2.4, it is not difficult to derive *linear* gyrofluid equations (describing the evolution of the real-space density, momentum, and so on) that neglect this gyroaveraging; the corresponding nonlinear

terms are in general intractable (see also the discussion in Chap. 2.4.1). The chief complications, however, are nonlinear FLR terms that may be negligible in the long-wavelength limit. Thus, if nonlinear simulations or analyses that include the full FLR effects indicate that the low-$k_\perp$ modes dominate the dynamics, it may be possible to use this simpler set of equations ($\bar{n}, \bar{u}_\parallel, \bar{T}_\parallel$, and $\bar{q}_\parallel$), which agrees well with the corresponding linear kinetic theory, as a rough model of the physics.

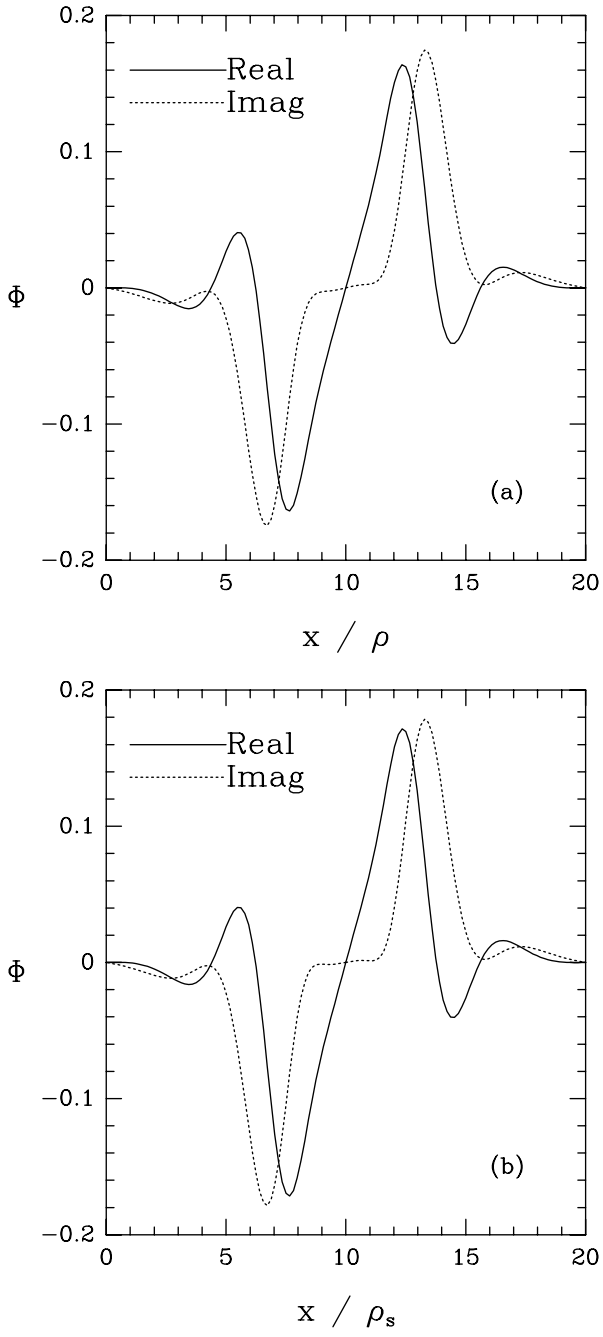

Figure 4.1: Electrostatic potential (arbitrary units) of the fastest growing mode for $\eta_i = 3$, $L_s/L_n = 20$, $k_y\rho_s = 0.5$, and $\tau = 1$. Numerical results from (a) gyrofluid initial-value code, and (b) gyrokinetic eigenvalue code, each ignoring Linsker's shear effect.

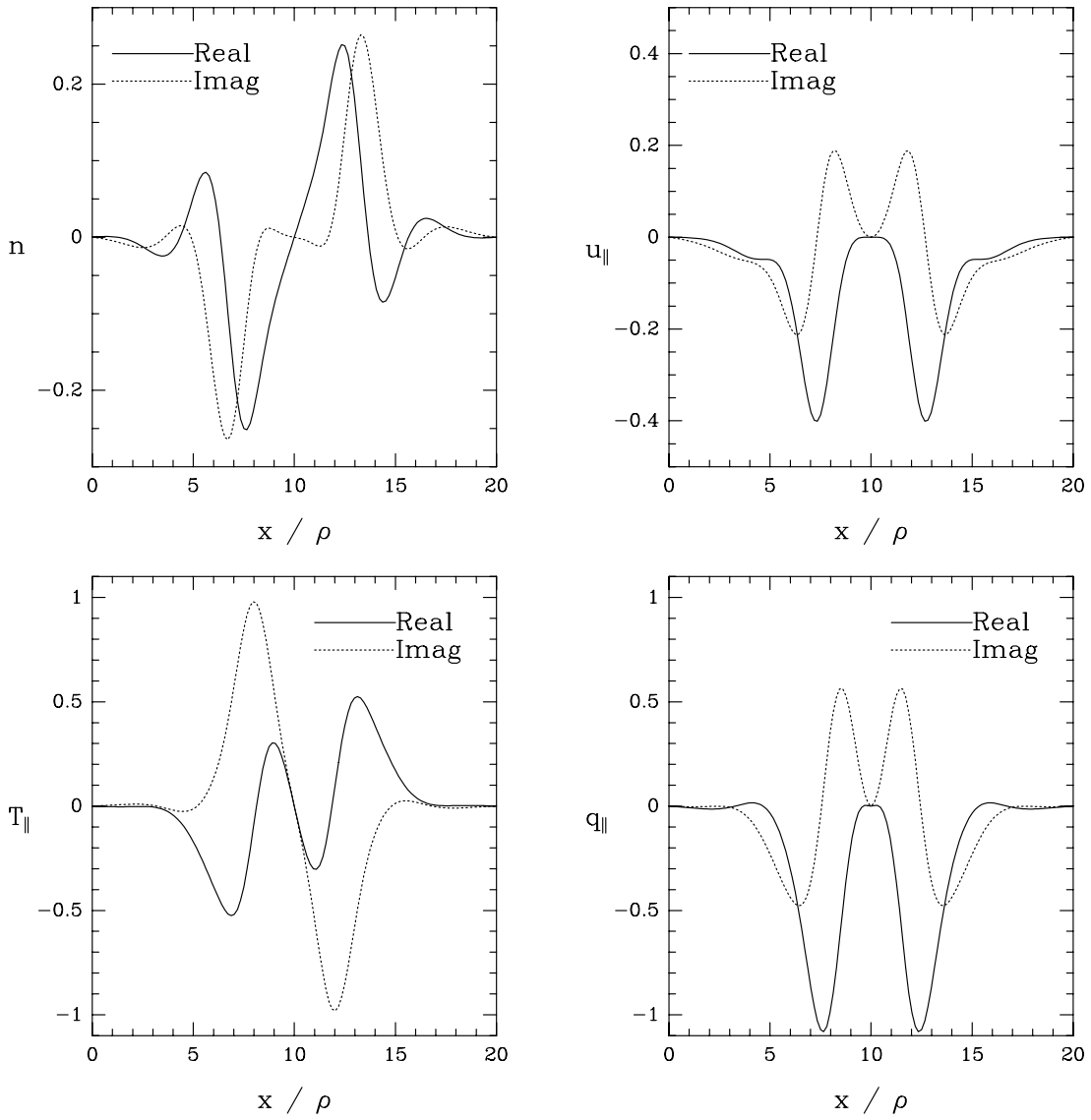

Figure 4.2: First four real-space moments (arbitrary units) of the fastest growing mode for $\eta_i = 3$, $L_s/L_n = 20$, $k_y\rho_s = 0.5$, and $\tau = 1$.

4.2 Padé FLR Model

While the Padé model (described in Chap. 2.4.4) does not perform quite as well as the $\langle J_0 \rangle = \Gamma_0^{1/2}$ model in the large $k_\perp \rho$ limit [Fig. (3.3)], it is nevertheless well-behaved and has the advantage that it may be easily incorporated into existing finite-difference codes. In Fig. (4.3) I compare the linear eigenmode obtained with

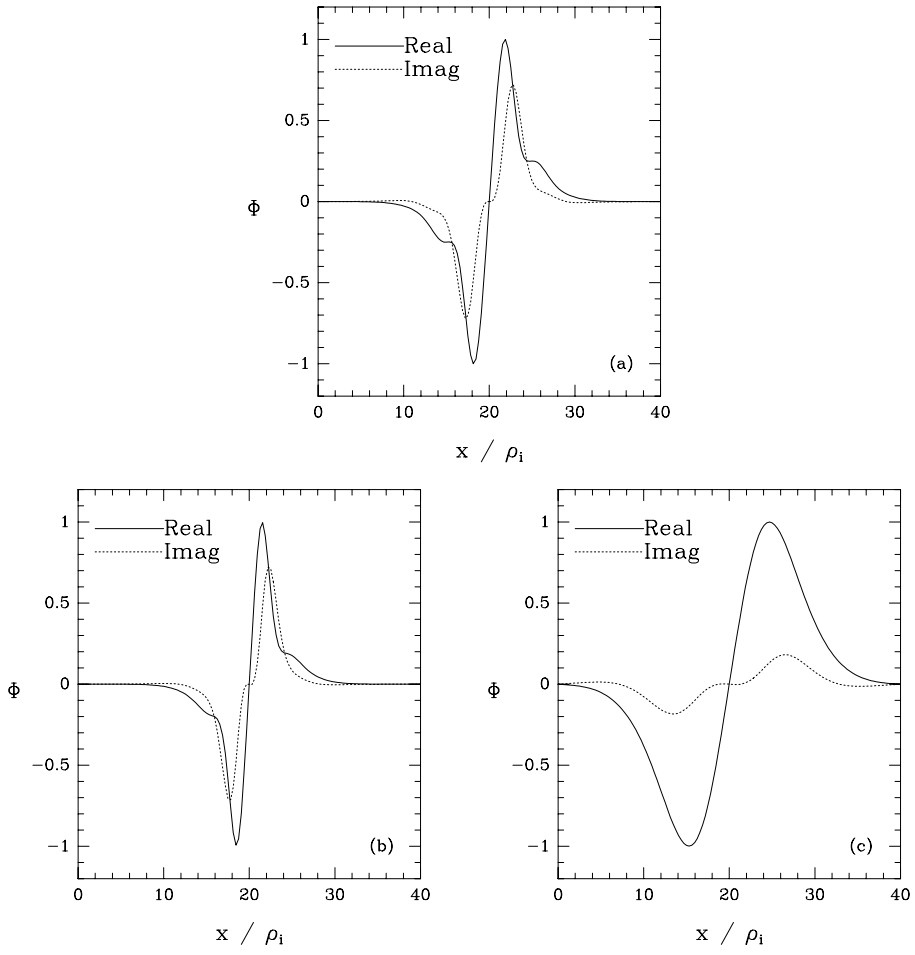

Figure 4.3: Electrostatic potential (arbitrary units) of the fastest-growing mode for $\eta_i = 2$, $L_s/L_n = 40$, $k_y \rho_i = 0.6$, and $T_i = T_e$. (a) Gyrokinetic model. (b) Gyrofluid (Padé 4+2) model. (c) Taylor-series model.

this model (including Linsker's shear effect) to the exact kinetic solution and to the 3+0 Taylor-series result for a typical case. The parameters are $\eta_i = 2$, $L_s/L_n = 40.0$, $k_y \rho_i = 0.6$, and $T_i = T_e$. The Taylor-series approximations for the FLR effects

predict a much wider mode than linear gyrokinetic theory. The gyrokinetic code finds $\omega = -0.049 + 0.039i$, and the 4+2 Padé model gives $\omega = -0.032 + 0.032i$. This level of error is typical of the Padé model. By way of comparison, the Taylor-series model yields $\omega = -0.170 + 0.050i$. While the Padé FLR model misses the real frequency by a sizable amount, it is nevertheless a substantial improvement over the Taylor-series equations. Again, if simulations or analysis show that the long-wavelength modes tend to dominate the saturated spectrum, the errors for the short-wavelength modes may be tolerable for the $\langle J_0 \rangle = (1 + b/2)^{-1}$ approximation.

4.3 Full Kinetic Model

One may improve upon the results of Sec. 4.2 by employing the more complicated $\Gamma_0^{1/2}$ FLR model, which is easily implemented in a spectral code. Here I compare this gyrofluid description of the linear dynamics to the corresponding gyrokinetic integral-code description [LINSKER, 1981].

4.3.1 Single-Mode Comparison

Several years ago, Bakshi [BAKSHI *et al.*, 1977] and Linsker [LINSKER, 1981] pointed out a "kinematic term" related to the gyroaveraging of $k_\parallel$ in systems with magnetic shear. All of the gyrofluid results presented below include this effect to second order in $k_\perp \rho$, sufficient accuracy to allow one to recover Linsker's Mode II [LINSKER, 1981], which he showed to exist only in the presence of the kinematic effect and to be unstable for $k_y \rho_i > 1$. I have found, however, that in practice this effect is usually not significant for the majority of linear ITG eigenmodes, as the radial modifications do not extend beyond a very few gyroradii from the rational surface and the frequency shifts are usually small.

Typical sheared-slab results from the 3+1 model are shown in Figs. (4.4) and (4.5). The parameters are $\eta_i = 2$, $L_s/L_n = 40$, $k_y \rho_i = 0.707$, and $T_i = T_e$. The frequency found with Linsker's gyrokinetic integral code is $\omega = -0.0674 + 0.0414i$; the 3+1 gyrofluid model yields $\omega = -0.0528 + 0.0318i$. Evolving the heat-flux moments as well (the 4+2 model) improves the frequency prediction to $\omega = -0.0674 + 0.0384i$. In Fig. 4.4(c) I show the result from a widely-used, particle-space

fluid model [HAMAGUCHI and HORTON, 1990]. The eigenmode is much broader than that found by either the gyrofluid or gyrokinetic codes, though qualitatively similar. The frequency predicted by this model, which uses a term $\propto \nabla_{\parallel}^2$ to model Landau damping and Taylor-series expansions for the FLR effects, is $\omega = -0.35 + 0.10i$.

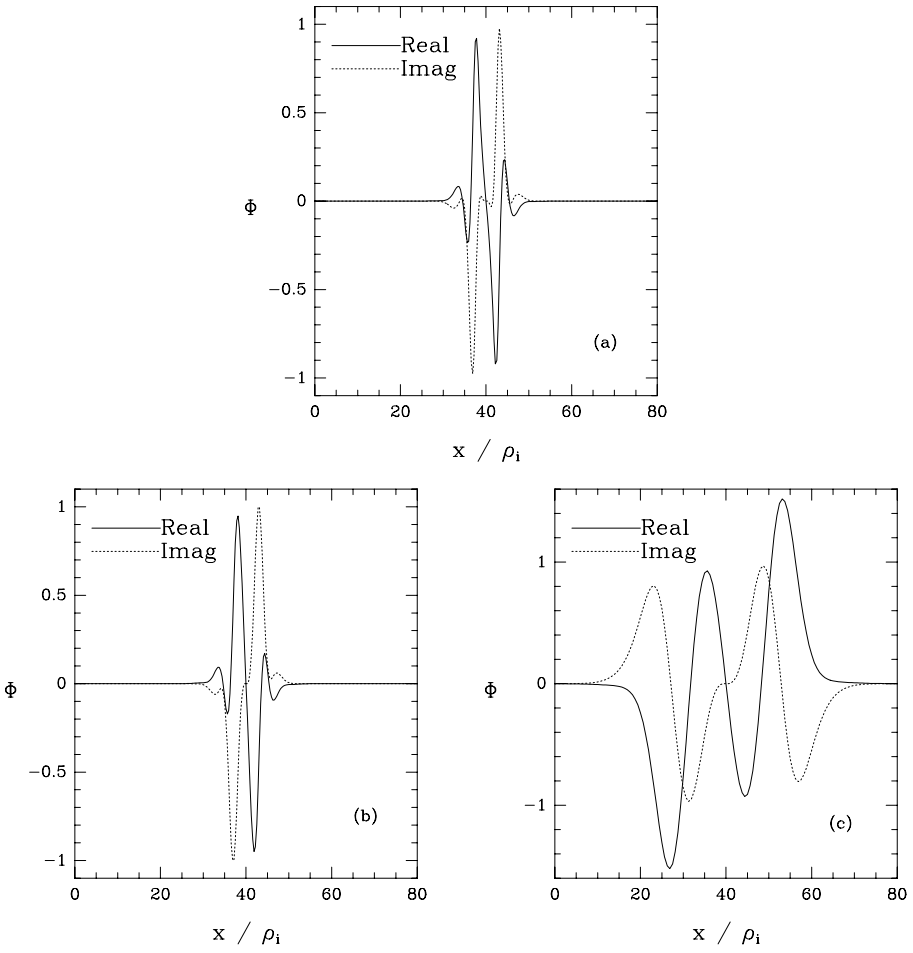

Figure 4.4: Electrostatic potential (arbitrary units) of the fastest-growing mode for $\eta_i = 2$, $L_s/L_n = 40$, $k_y\rho_i = 0.707$, and $T_i = T_e$. (a) Gyrofluid result. (3+1) (b) Gyrokinetic result. (c) Previous fluid model.

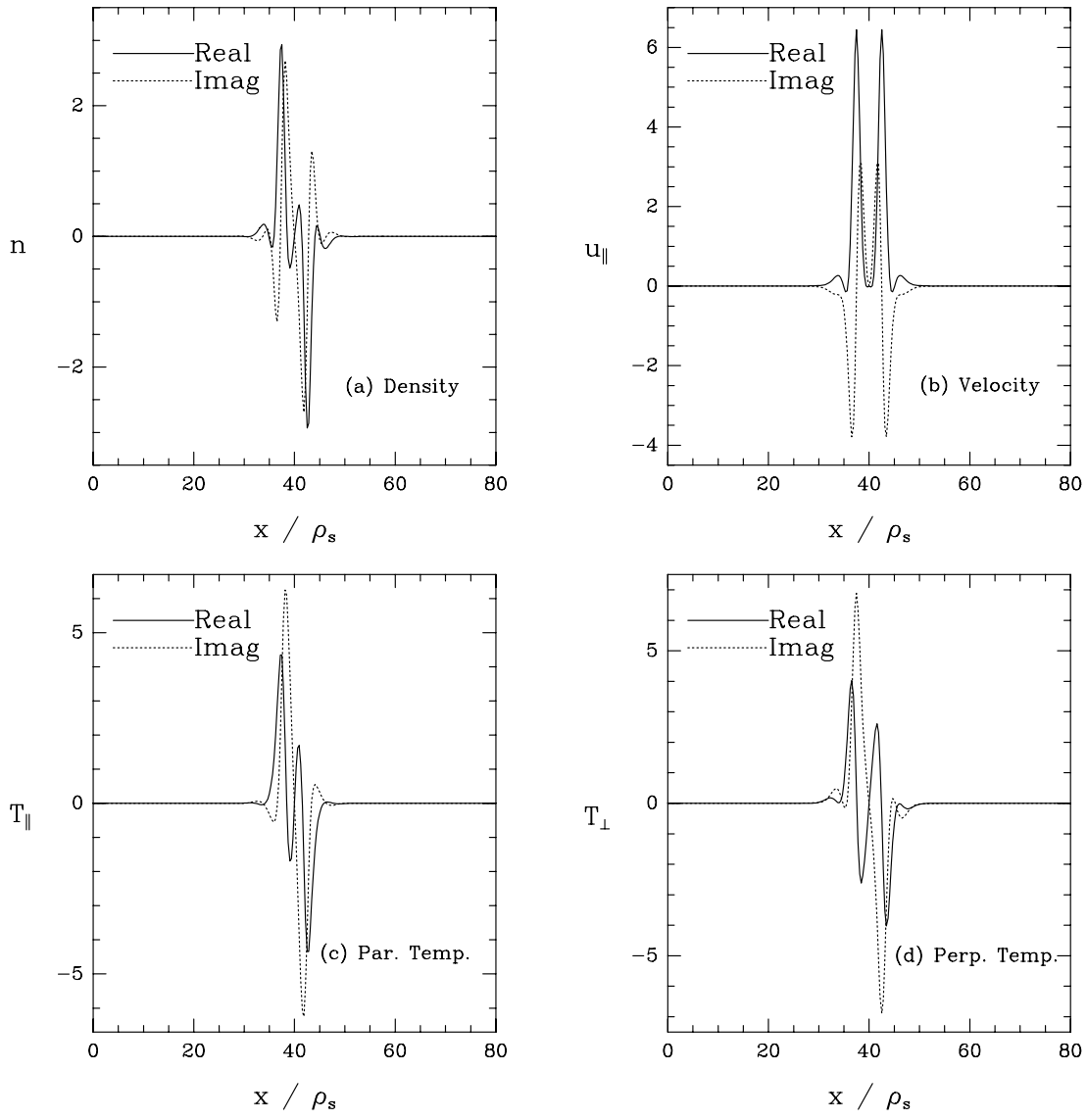

Figure 4.5: Gyrofluid moments of the fastest-growing mode for $\eta_i = 2$, $L_s/L_n = 40$, $k_y\rho_i = 0.707$, and $T_i = T_e$.

This comparison clearly indicates that Landau damping and FLR effects can dramatically affect the dynamics of the ITG mode. I have found that *both* kinetic effects affect the linear ITG eigenmodes strongly, even in the small $k_y\rho$ limit or away from marginal stability. This may be understood by investigating the ITG instability in the "fluid regime" ($\zeta \gg 1$). For example, consider Eq. (3.1) in the long-wavelength ($b \ll 1$), flat-density ($\eta_i \gg 1$) limit. Upon expanding

$$Z_4(\zeta) \simeq -\frac{1}{\zeta}\left(1 + \frac{1}{2\zeta^2}\right)$$

and taking $\eta_i\zeta_* \gg 1$, one is led to the dispersion relation

$$\omega^3 = \frac{\eta_i\omega_* k_\parallel^2 v_t^2}{2\tau}.$$

This equation has three roots, one of which must have $\mathrm{Im}[\omega] > 0$. However, the growth rate is an increasing function of $k_\parallel$,

$$\gamma \propto k_\parallel^{2/3},$$

so the fastest-growing modes challenge the fluid ordering $\omega \gg k_\parallel v_t$. Thus it appears that the fastest-growing modes satisfy $\omega \sim k_\parallel v_t$ in this limit. This trend remains in the presence of magnetic shear, where I find that fastest-growing eigenmodes tend to arrange themselves so that the volume-averaged fluid parameter $\langle k_\parallel v_t/\omega\rangle$ is never small. A good FLR model is needed even in the long-wavelength limit, since as $k_y\rho_i \to 0$ the linear eigenmodes develop more radial structure, so that $b \sim 1$. This tendency may be noted in Figs. (4.6–4.7), as the unstable modes for small $k_y\rho_i$ tend to have the character of $l = 3$ or $l = 4$, where l is the radial mode number.

4.3.2 Spectral Comparison

Primarily as a vehicle for showing the agreement between the gyrofluid and gyrokinetic codes for a range of the wave-number spectrum, here I discuss some simple linear estimates of the thermal diffusivity χ_i, defined by Eq. (B.2). Often attention is focused on the $l = 0$ mode in linear mixing-length[1] studies. However, there is no

[1]An excellent introduction to (and indictment of) mixing-length estimates of turbulence characteristics may be found in Bowman, 1992. He points out that mixing-length estimates of microturbulent saturation levels essentially predict that in a saturated state the $\mathbf{E}\times\mathbf{B}$ velocity

physical or mathematical reason to exclude other eigenmodes from a mixing-length type estimate, particularly if the fastest-growing or "largest" modes are not the $l = 0$ modes. For most of the parameter space in which I have benchmarked my code (low η_i and $\tau = 1$), I have found that other eigenmodes with comparable or larger average radial mode widths (despite the higher radial mode number) often have significantly larger growth rates than the fundamental mode. Figs. (4.6) and (4.7) illustrate this point.

First, a note on how to interpret these figures is in order. Since I solve the gyrofluid equations as an initial-value problem, the resulting eigenmode corresponds to the fastest-growing mode as long as the equations are evolved long enough to allow that mode to dominate. Thus, for each value of $k_y\rho_i$ the gyrofluid model yields a single solution. I have not recovered the other branches of the dispersion relation by performing a Fourier transform of the time series data.

Fig. (4.6) shows all of the branches of the linear dispersion relation for $\eta_i = 2, L_s/L_n = 40$, and $T_i = T_e$ that are at some point (for $0.1 < k_y\rho_i < 1.1$) fastest-growing for the 4+2 gyrofluid model or the integral gyrokinetic code [Linsker, 1981]. The gyrofluid equations successfully resolve the mode with the largest growth rate in each case. The $l = 0$ mode is not the fastest-growing mode until $k_y\rho_i > 1$; for most of the parameter space, the fastest-growing mode is of odd parity with an $l = 1$ character.

For $k_y\rho_i = 0.7$, the fastest-growing mode in Fig. (4.6) is odd, with average radial mode width of $\Delta_x = 1.9$, where the average radial mode width Δ_x is defined

---

should equal the diamagnetic velocity [Kadomtsev, 1965] [which is $O(1)$ in my units]. In practice, "mixing-length" estimates of thermal transport for plasmas often boil down to an argument that goes as follows. The temperature fluctuations are assumed to obey an equation that may be schematically represented as

$$\frac{\partial T}{\partial t} + \mathbf{v}_E \cdot \nabla T - \gamma_{\rm L} T = 0,$$

where $\gamma_{\rm L}$ represents the linear instability. The $\mathbf{E} \times \mathbf{B}$ nonlinearity is approximated as a diffusive term proportional to $|\Phi|^2$ with a diffusion coefficient D. In steady-state, the time derivative vanishes; as noted above, $|\Phi|^2 \sim 1$, leaving

$$D \sim \langle \frac{\gamma_{\rm L}}{k_\perp^2} \rangle,$$

where the details of the averaging procedure denoted by $\langle \ldots \rangle$ are more or less refined and the diffusion coefficient χ_i is assumed to correspond to D.

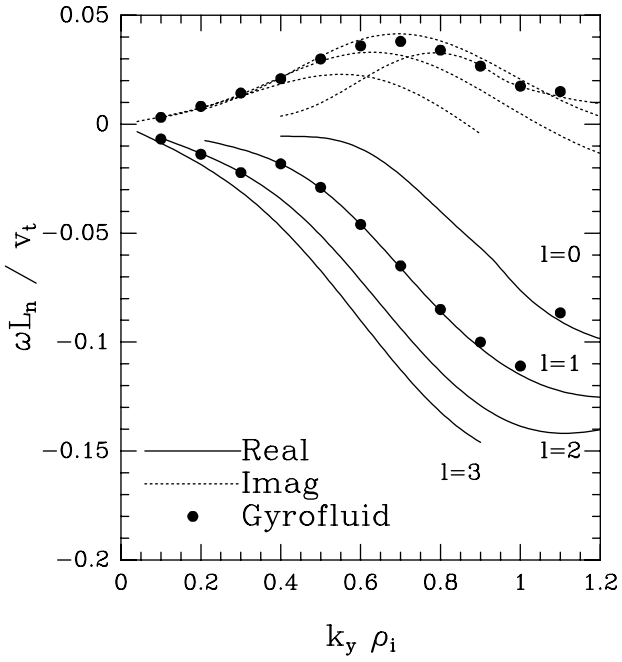

Figure 4.6: Linear dispersion relation for the first few radial eigenmodes for $\eta_i = 2$, $L_s/L_n = 40$, and $T_i = T_e$.

by [HAMAGUCHI and HORTON, 1990]

$$\Delta_x^2 \equiv \frac{\langle \Phi^2 \rangle}{\langle (\partial \Phi / \partial x) \rangle^2}. \tag{4.1}$$

Here the angle brackets indicate a volume average. For the same parameters, the $l = 0$ mode has $\Delta_x = 1.4$. Given the additional difference in growth rates, a simple mixing-length estimate ($\gamma \Delta_x^2$) of the transport from these two modes differs by a factor of three. At lower values of $k_y \rho_i$, for which the $l = 0$ growth rate is much smaller, the discrepancy can be greater than an order of magnitude. Even worse, an analysis that focused only on the $l = 0$ mode would incorrectly conclude that the system was only weakly unstable for $k_y \rho_i \leq 0.3$.

Figure (4.7) shows the same information for the same parameters, except that $\eta_i = 3$ and the 3+1 model is included. Also, the even- and odd-parity modes are shown on different panels for clarity. Again, the fastest-growing mode is odd for much of this region of parameter space, with the $l = 0$ mode becoming important only at high $k_y \rho_i$. There is no single dominant radial eigenmode structure for

the entire range of $k_y\rho_i$. Fig. (4.8a) shows that the $l = 0$ mode has the largest average radial mode width, yet the mixing-length estimate of χ_i given by $\gamma/\langle k_\perp^2 \rangle$ is largest for the $l = 1$ mode for most values of $k_y\rho_i$ in this region of parameter space [Fig. (4.8b)]. Again, I emphasize that my gyrofluid code picks out the fastest-growing mode for each set of parameters; it should be clear that all of the radial eigenmodes are present from Figs. (4.6) and (4.7).

One may also see from Figs. (4.7) and (4.8b) that for these parameters the peak of the mixing-length estimate of χ_i (at $k_\perp\rho_i \leq 0.4$) is downshifted 40% from the peak of the growth rate, which is at $k_\perp\rho_i \geq 0.6$. The downshift is more or less pronounced for different parameters, but indicates that the longer-wavelength modes are probably more important to transport than the simplest mixing-length arguments would suggest.

At least two others factors complicate a linear mixing-length estimate. First, there may be even longer-wavelength modes that are linearly damped or weakly unstable yet which nevertheless play an important role in determining the nonlinear thermal transport. Second, fundamentally nonlinear processes [COWLEY *et al.*, 1991] may determine the relevant scales, regulating small regions with steep gradients that could control the transport [BOWMAN, 1992]. Previous authors have commented at length on the shortcomings of mixing-length estimates of transport coefficients (for example, BOWMAN, 1992 or HAMAGUCHI and HORTON, 1990). Thus, I do not wish to emphasize the mixing-length estimates here. I present them primarily to show that the gyrofluid equations compare very favorably with linear gyrokinetic theory and to point out the potential hazards of concentrating one's linear analysis on a single unstable radial eigenmode. Having seen that the gyrofluid model performs satisfactorily in the linear regime, one may explore the nonlinear physics with more confidence.

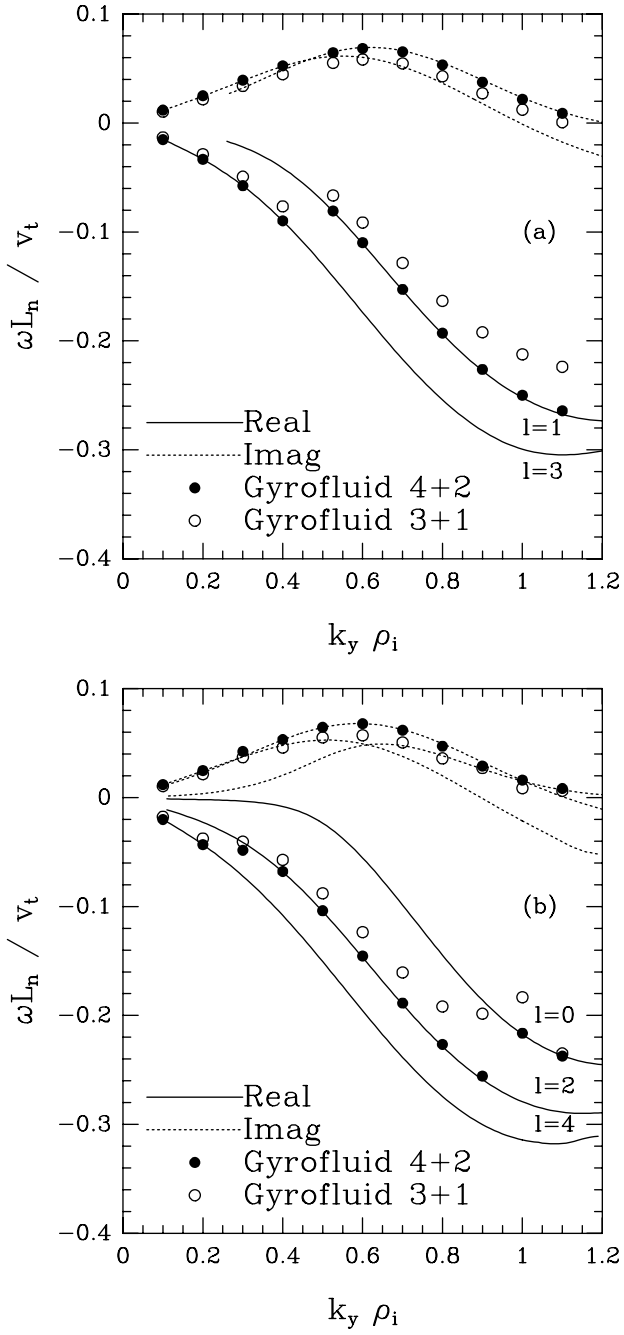

Figure 4.7: Linear dispersion relation for the first few radial eigenmodes for $\eta_i = 3$, $L_s/L_n = 40$, and $T_i = T_e$. (a) Odd parity. (b) Even parity.

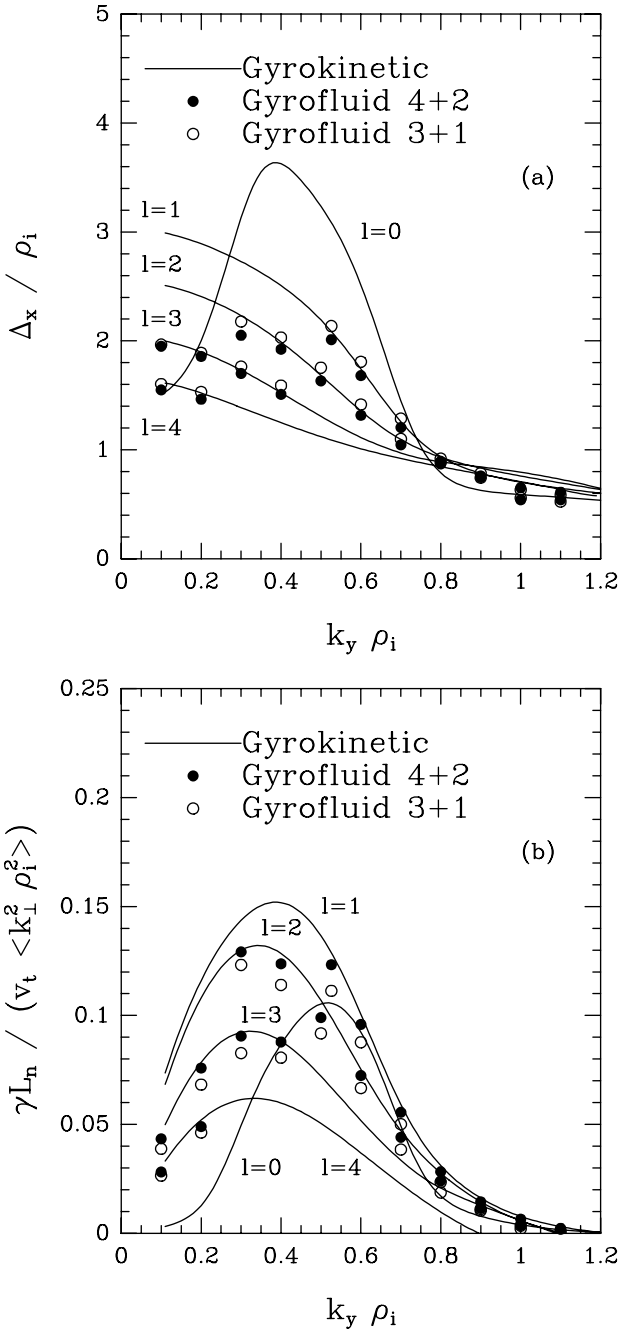

Figure 4.8: Mode widths and mixing-length estimates for $\eta_i = 3$, $L_s/L_n = 40$, and $T_i = T_e$. (a) Average mode width Δ_x. (b) Mixing-length χ_i, $\gamma/\langle k_\perp^2 \rangle$.

Chapter 5

Weak Turbulence Analysis

THE CLOSURE APPROXIMATIONS introduced for collisionless parallel dynamics in HAMMETT and PERKINS, 1990 and generalized in this thesis are chosen to match the linear kinetic response function. In the gyrokinetic regime, the terms that are approximated are linear; nevertheless, the equations cannot reproduce arbitrary nonlinear processes with a finite number of moments. For example, one can imagine a physical system in which the nonlinear $\mathbf{E} \times \mathbf{B}$ convection of heat flux (*e.g.,* $q_\parallel$) plays an important role in the dynamics; a three-moment gyrofluid model that approximated the heat-flux response in terms of density, momentum and temperature would describe such dynamics poorly. That is, even the description of the density evolution would be lacking, despite the fact that the density equation itself would have no terms reflecting the closure approximations. Similarly, if (as for ITG modes very near marginal stability) a linear instability satisfies $k_\parallel v_t \gg \omega$, the structure of the fluid hierarchy results in greater emphasis on the nonlinear convection of the higher-order moments, as shown below. Nonlinear scattering or absorption of energy that results from the interactions of high-order moments of the distribution function can probably be described with fluid equations only if a large number of moments are retained.

On the other hand, much of the intuition developed in the plasma-physics community regarding the turbulent behavior of plasma has derived from fluid models, which inevitably employ closure assumptions. Many nonlinear processes may be described rather well by a few moments of the distribution function. Physically, fine-scale velocity-space striations and structures probably play a minor role

in many systems of interest, since even a very weak collision rate is amplified by the diffusion-like part of the collision operator. [See, for example, the discussion in Chapter 12 of STIX, 1992 and references therein.] Turbulent scattering of particles tends to amplify this effect rather than to diminish it.

In this chapter, well-known properties of electron drift-wave turbulence are investigated with both gyrokinetic and gyrofluid equations with a weak-turbulence approach [SAGDEEV and GALEEV, 1969]. In each approach, I consider the simple, shearless slab geometry with an adiabatic electron response. Rather than exploring new physical regimes, the emphasis is on showing the areas of improved agreement with kinetic theory (compared to previous fluid theories [HORTON, 1984; SIMILON, 1981]), as well as the limitations of the gyrofluid approach. It is shown that the gyrofluid equations reproduce essentially nonlinear processes, such as "ion Compton scattering" (also known as nonlinear Landau damping) well in the drift-wave limit. For example, the gyrofluid equations correctly reproduce the shielded and bare components of ion Compton scattering, leading to a near (but not complete) cancellation of the scattering at long wavelengths. Furthermore, plasmon number is properly conserved and the transfer of energy from short to long perpendicular wavelengths is predicted. The more demanding "deeply resonant" limit [MATTOR, 1992] of ITG turbulence is also discussed. The limitations of the gyrofluid approach are made more apparent by his calculation. In particular, the importance of the nonlinear convection of high-order moments in this regime is demonstrated. An estimate [HAMMETT *et al.*, 1993] of the nonlinear accuracy afforded by a given number of moments is reviewed.

In Sec. 5.1, the assumptions and starting equations for these test problems are listed and briefly described. In Sec. 5.2.1, the kinetic version of the drift-wave calculation is reviewed to establish the context for the gyrofluid calculation described in Sec. 5.2.2. Then, the opposite limit (ITG turbulence very near marginal stability) is discussed in Sec. 5.3.

5.1 Starting Equations

Throughout this chapter the gyro-averaged potential is indicated with the same abbreviated notation as the gyro-averaged and velocity-space-averaged potential

when the context makes it clear which quantity is intended. That is,

$$\Psi = J_0\Phi, \text{ and } \Psi = \langle J_0 \rangle \Phi \equiv \Gamma_0^{1/2}\Phi.$$

Similarly, $\langle \cdots \rangle$ can imply either velocity-space averages or gyro-averages. Finally, the units and normalizations employed here and throughout this thesis are consistent with Eqs. (2.61) and (2.62). Where confusion would otherwise be generated, the full, unambiguous expressions are used.

Because I have assumed the electron response to be adiabatic, there is no positive growth rate in the electron drift-wave limit. Since my goal is to investigate the nonlinear response of the gyrofluid equations, this is not significant. Including a linear growth rate would change the principal result [Eq. (5.26)] only by modifying the linear growth rate $\gamma_{\mathbf{k}}$. Furthermore, I have not included the nonlinear phase-mixing terms in Eqs. (5.3–5.8). This is not a significant approximation in the weak-turbulence limit, since the nonlinear terms are ordered small and any dynamics described by the nonlinear phase-mixing terms may therefore be safely ignored. Hammett [HAMMETT, 1993] has shown that just as Landau damping is exponentially small for $\omega \gg |k_\parallel| v_t$, nonlinear phase mixing is exponentially small for $\omega \gg \mathbf{k} \cdot \mathbf{v}_E$.

Gyrokinetic Description. Consider the electrostatic gyrokinetic equation in the unsheared slab [FRIEMAN and CHEN, 1982; LEE, 1983; DUBIN *et al.*, 1983]:

$$\frac{\partial f}{\partial t} + v_\parallel \nabla_\parallel f + \frac{e}{m} \langle E_\parallel \rangle \frac{\partial f_0}{\partial v_\parallel} + \langle \mathbf{v}_E \rangle \cdot \nabla f_0 = - \langle \mathbf{v}_E \rangle \cdot \nabla f \tag{5.1}$$

Upon assuming $f_0 = f_M$ and the usual slab geometry, one may allow for background density and temperature gradients by writing

$$\frac{\partial f_0}{\partial x} = \left(\frac{1}{L_n} + (\frac{v^2}{2v_t^2} - \frac{3}{2}) \frac{1}{L_T} \right) f_0.$$

It will be useful later to have labels for the terms that arise from the temperature gradients. Hence, define

$$\theta_\parallel \equiv \left(\frac{v_\parallel^2}{2v_t^2} - \frac{1}{2} \right), \qquad \theta_\perp \equiv \left(\frac{v_\perp^2}{2v_t^2} - 1 \right).$$

The pressure gradients are then succintly described by ω_*^P:

$$\omega_*^P \equiv -k_y \left[1 + \eta_i(\theta_\parallel + \theta_\perp)\right].$$

The gyrokinetic quasineutrality constraint is[1]

$$\int d^3v \, J_0 f + (\Gamma_0 - 1)\Phi = \tau\Phi, \tag{5.2}$$

where I have assumed the electron response to be purely adiabatic. The proper self-consistent evolution of modes for which $k_\parallel = 0$ is ignored, in keeping with the usual weak-turbulence analysis [Sagdeev and Galeev, 1969]. It should be stressed that this oversight overlooks a potentially important physical mechanism for saturation discussed in more detail in Chap. 8. Also, nonlinear terms appear at the next-order expansion of Eqs. (5.2) and (5.1) that could appear at second order in the weak-turbulence theory [Krommes, 1993]. These terms were not considered here, and should be investigated further.

Gyrofluid Description. The gyrofluid analysis begins from the lowest six moments of Eq. (5.1), ignoring nonlinear phase mixing. For clarity, the starting equations are explicitly listed here:

$$\frac{\partial n}{\partial t} + \nabla_\parallel u_\parallel + \left[1 + \eta_{i\perp}\tfrac{1}{2}\hat{\nabla}_\perp^2\right]\frac{\partial \Psi}{\partial y} = -\mathbf{v}_\Psi \cdot \nabla n - \left[\tfrac{1}{2}\hat{\nabla}_\perp^2 \mathbf{v}_\Psi\right] \cdot \nabla T_\perp, \tag{5.3}$$

$$\frac{\partial u_\parallel}{\partial t} + \nabla_\parallel (n + T_\parallel + \Psi) = -\mathbf{v}_\Psi \cdot \nabla u_\parallel - \left[\tfrac{1}{2}\hat{\nabla}_\perp^2 \mathbf{v}_\Psi\right] \cdot \nabla q_\perp, \tag{5.4}$$

$$\frac{\partial T_\parallel}{\partial t} + \nabla_\parallel 2u_\parallel + \eta_i \frac{\partial \Psi}{\partial y} + \hat{\chi}|k_\parallel| T_\parallel = -\mathbf{v}_\Psi \cdot \nabla T_\parallel - \left[\tfrac{1}{2}\hat{\nabla}_\perp^2 \mathbf{v}_\Psi\right] \cdot \nabla r_\perp, \tag{5.5}$$

$$\frac{\partial T_\perp}{\partial t} + \nabla_\parallel q_\perp + \left[\tfrac{1}{2}\hat{\nabla}_\perp^2 + \eta_i(1 + \hat{\hat{\nabla}}_\perp^2)\right]\frac{\partial \Psi}{\partial y}$$
$$= -\left[(1 + \hat{\hat{\nabla}}_\perp^2)\mathbf{v}_\Psi\right] \cdot \nabla T_\perp - \left[\tfrac{1}{2}\hat{\nabla}_\perp^2 \mathbf{v}_\Psi\right] \cdot \nabla n, \tag{5.6}$$

$$\frac{\partial q_\perp}{\partial t} + \nabla_\parallel \left(r_\perp + T_\perp + \tfrac{1}{2}\hat{\nabla}_\perp^2 \Psi\right) = -\left[(1 + \hat{\hat{\nabla}}_\perp^2)\mathbf{v}_\Psi\right] \cdot \nabla q_\perp - \left[\tfrac{1}{2}\hat{\nabla}_\perp^2 \mathbf{v}_\Psi\right] \cdot \nabla u_\parallel, \tag{5.7}$$

$$\frac{\partial r_\perp}{\partial t} + \nabla_\parallel 2q_\perp + \eta_i \tfrac{1}{2}\hat{\nabla}_\perp^2 \frac{\partial \Psi}{\partial y} + \hat{\chi}|k_\parallel| r_\perp = -\left[(1 + \hat{\hat{\nabla}}_\perp^2)\mathbf{v}_\Psi\right] \cdot \nabla r_\perp - \left[\tfrac{1}{2}\hat{\nabla}_\perp^2 \mathbf{v}_\Psi\right] \cdot \nabla T_\parallel. \tag{5.8}$$

[1] A brief derivation of Eqs. (5.1) and (5.2) is presented in App. C.

The closure parameter $\hat{\chi}$ was found in Chap. 2 and is given by

$$\hat{\chi} \equiv \frac{3+\beta_\parallel}{\sqrt{2}D_\parallel} = 2\sqrt{\frac{2}{\pi}}.$$

The gyrofluid quasineutrality constraint is:

$$\bar{n} + (\Gamma_0 - 1)\Phi = \tau\Phi. \tag{5.9}$$

The particle density $\bar{n}$ is defined in Eq. (2.39).

It is instructive to compare these equations with the fluid model used by Lee and Diamond, 1986 to investigate ITG turbulence. Several improvements found in these equations could modify their results significantly. First (and foremost), Lee and Diamond, 1986 used a viscosity-based model for Landau-damping that has been shown to lead to difficulties of interpretation [Hammett and Perkins, 1990]. Lee and Diamond, 1986 correctly note the importance of the existence and form of the Landau-damping model with respect to their theory. They note that the saturation mechanism in their theory is the coupling of unstable pressure fluctuations to the stabilizing Landau-damping terms in the momentum equation. One would expect that the Landau-damping models used here would significantly modify this finding, since the damping appears in the temperature equations. Second, Eqs. (5.3–5.9) allow for anisotropic pressure fluctuations, shown to be important for describing the thermal flux in Chap. 7. Third, one may use Eqs. (5.3–5.8) along with Eq. (2.69) to describe the effect of ITG fluctuations and the associated self-generated sheared rotation in one self-consistent model. Finally, the present model consistently retains FLR effects to the same order and gives reasonable results for $k_\perp\rho \sim 1$.

The equations that follow are made particularly transparent by introducing gyrofluid equivalents of $\omega_*^P, v_\parallel$, *etc.*, to be indicated by a tilde. Thus, it is convenient to introduce the gyrofluid averaging operator $\mathcal{G}$:

$$\mathcal{G}(\cdots) \equiv \int d^3v \frac{(\cdots)J_0^2 f_0}{\omega - k_\parallel v_\parallel + i0^+} \left(\int d^3v \frac{J_0^2 f_0}{\omega - k_\parallel v_\parallel + i0^+} \right)^{-1}. \tag{5.10}$$

The needed quantities (for an $n+n$ gyrofluid model) are then obtained by replacing the plasma dispersion functions that appear in $\mathcal{G}(\cdots)$ with the multipole approximation Z_n. For example, Eqs. (5.3–5.9) ($n = 3$) yield the gyrofluid quantity $\tilde{v}_\parallel(\omega, k_\parallel)$

as follows:

$$\mathcal{G}(v_\parallel) = \frac{\omega}{k_\parallel \zeta}\left(\frac{1+\zeta Z(\zeta)}{Z(\zeta)}\right)$$

where $\zeta \equiv \omega/(\sqrt{2}|k_\parallel|)$, implying

$$\tilde{v}_\parallel \equiv \frac{\omega}{k_\parallel \zeta}\left(\frac{1+\zeta Z_3(\zeta)}{Z_3(\zeta)}\right).$$

In the same fashion,

$$\tilde{\theta}_\parallel \equiv \frac{\zeta + (\zeta^2 - \frac{1}{2})Z_3(\zeta)}{Z_3(\zeta)}, \qquad \tilde{\theta}_\perp \equiv -b\left(1 - \frac{I_1}{I_0}\right) \equiv -\hat{b},$$

$$\tilde{\omega}_*^P \equiv -k_y\left[1 + \eta_i(\tilde{\theta}_\parallel + \tilde{\theta}_\perp)\right]. \tag{5.11}$$

The three-pole approximation $Z_3(\zeta)$ is given by

$$Z_3 \equiv \frac{2\sqrt{\pi}i + 4\zeta - 2\sqrt{\pi}i\zeta^2}{2 - 3\sqrt{\pi}i\zeta - 4\zeta^2 + 2\sqrt{\pi}i\zeta^3}. \tag{5.12}$$

Fourier Representation. One may represent the various fields as

$$f(\vec{x},t) = \sum_{\vec{k}} \int d\omega\, f_{\vec{k},\omega} e^{i(\vec{k}\cdot\vec{x}-\omega t)},$$

$$\mathbf{v}_\Psi(\vec{x},t) = \sum_{\vec{k}} \int d\omega\, \hat{\mathbf{b}} \times \nabla \Psi_{\vec{k},\omega} e^{i(\vec{k}\cdot\vec{x}-\omega t)},$$

with $\Psi \equiv J_0\Phi$ and $\Psi_{-\vec{k},-\omega^*} \equiv \Psi^*_{\vec{k},\omega}$, $f_{-\vec{k},-\omega^*} \equiv f^*_{\vec{k},\omega}$ to ensure reality.

Following the standard approach, one Fourier transforms (and symmetrizes) the equations. For example, Eq. (5.1) becomes

$$-i\omega f_{\vec{k},\omega} + ik_\parallel v_\parallel f_{\vec{k},\omega} + ik_\parallel v_\parallel \Psi_{\vec{k},\omega} f_0 - i\omega_*^P \Psi_{\vec{k},\omega} f_0$$

$$= -\sum_{\vec{k}'} \int d\omega' \,(\vec{k}' \times \vec{k}\cdot\hat{\mathbf{b}})\left(\Psi_{\vec{k}',\omega'} f_{\vec{k}-\vec{k}',\omega-\omega'} - \Psi_{\vec{k}-\vec{k}',\omega-\omega'} f_{\vec{k}',\omega'}\right). \tag{5.13}$$

I shall investigate these equations in two limits: the drift-wave limit, in which I shall consider $\eta_i = 0$ and $\zeta, \zeta' \gg 1$; and the "deeply resonant" ITG limit, in which $\zeta, \zeta', \zeta'' \ll 1 \ll \zeta_*, \zeta_*', \zeta_*''$.

5.2 Drift Waves

5.2.1 Gyrokinetic Analysis

Linearly, one may ignore the RHS of Eq. (5.13). The solution of this equation is

$$f^{(1)}_{\vec{k},\omega} = -\frac{\omega^P_* - k_\parallel v_\parallel}{\omega - k_\parallel v_\parallel + i0^+}\Psi^{(1)}_{\vec{k},\omega} f_0. \tag{5.14}$$

The linear dispersion relation is obtained using Eq. (5.2), and may be used to define the dielectric function $\epsilon^{(1)}(\vec{k},\omega)$:

$$\left[(\tau + 1 - \Gamma_0) + \int d^3v\, J_0^2 \left(\frac{\omega^P_* - k_\parallel v_\parallel}{\omega - k_\parallel v_\parallel + i0^+}\right) f_0\right] \Phi_{\vec{k},\omega} \equiv \epsilon^{(1)}(\vec{k},\omega)\Phi_{\vec{k},\omega} = 0. \tag{5.15}$$

Virtual Modes Note that in Eq. (5.13) one needs expressions for $f_{\vec{k}-\vec{k}',\omega-\omega'}$ and $\Psi_{\vec{k}-\vec{k}',\omega-\omega'}$. One may proceed to second order by treating the nonlinearity on the RHS of Eq. (5.13) as a source term. That is, a beat wave is caused by linear modes at $\vec{k}$ and $\vec{k}'$ interacting:

$$\frac{\partial f^{(2)}_{\vec{k}-\vec{k}'}}{\partial t} + \cdots = -\left(\mathbf{v}_{\Psi_{\vec{k}}} \cdot \nabla f_{-\vec{k}'} + \mathbf{v}_{\Psi_{-\vec{k}'}} \cdot \nabla f_{\vec{k}}\right).$$

Upon using the convention that $\vec{k}'' = \vec{k} - \vec{k}'$, one finds that the distribution function at second order is given by

$$\begin{aligned} f^{(2)}_{\vec{k}'',\omega''} = &-\frac{\omega^{P\prime\prime}_* - k''_\parallel v_\parallel}{\omega'' - k''_\parallel v_\parallel + i0^+}\Psi^{(2)}_{\vec{k}'',\omega''} f_0 \\ &+ i\frac{(\vec{k}' \times \vec{k} \cdot \hat{\mathbf{b}})}{\omega'' - k''_\parallel v_\parallel + i0^+}\left(\Psi^{(1)}_{\vec{k},\omega} f^{(1)}_{-\vec{k}',-\omega'} - \Psi^{(1)}_{-\vec{k}',-\omega'} f^{(1)}_{\vec{k},\omega}\right). \end{aligned} \tag{5.16}$$

The expression for $\Phi^{(2)}_{\vec{k}'',\omega''}$ may be found by enforcing the quasineutrality constraint at second order:

$$\epsilon^{(1)}(\vec{k}'',\omega'')\Phi^{(2)}_{\vec{k}'',\omega''} = i\int d^3v\, J''_0 \frac{(\vec{k}' \times \vec{k} \cdot \hat{\mathbf{b}})}{\omega'' - k''_\parallel v_\parallel + i0^+}\left(\Psi^{(1)}_{\vec{k},\omega} f^{(1)}_{-\vec{k}',-\omega'} - \Psi^{(1)}_{-\vec{k}',-\omega'} f^{(1)}_{\vec{k},\omega}\right).$$

Upon substituting in for $f^{(1)}$ from Eq. (5.14), one finds

$$\epsilon^{(1)}(\vec{k}'',\omega'')\Phi^{(2)}_{\vec{k}'',\omega''} = -i\int d^3v\, J_0 J'_0 J''_0 \frac{(\vec{k}' \times \vec{k} \cdot \hat{\mathbf{b}})}{\omega'' - k''_\parallel v_\parallel + i0^+} f_0 \Phi^{(1)}_{\vec{k},\omega}\Phi^{(1)}_{-\vec{k}',-\omega'}$$

$$\times \left(\frac{\omega_*^{P\prime} - k_\parallel' v_\parallel}{\omega' - k_\parallel' v_\parallel + i0^+} - \frac{\omega_*^P - k_\parallel v_\parallel}{\omega - k_\parallel v_\parallel + i0^+} \right). \tag{5.17}$$

The induced potential in the drift-wave limit can be explicitly evaluated:

$$\epsilon^{(1)}(\vec{k}'', \omega'') \Phi^{(2)}_{\vec{k}'', \omega''}$$

$$= -i \left\langle J_0 J_0' J_0'' \right\rangle (\vec{k}' \times \vec{k} \cdot \hat{\mathbf{b}}) \left(\frac{\omega_*'}{\omega'} - \frac{\omega_*}{\omega} \right) \Phi^{(1)}_{\vec{k},\omega} \Phi^{(1)}_{-\vec{k}', -\omega'} \int \frac{f_0 dv_\parallel}{\omega'' - k_\parallel'' v_\parallel + i0^+}. \tag{5.18}$$

This expression matches the usual kinetic result [Sagdeev and Galeev, 1969] [c.f. also Eq. (10) of Chen *et al.*, 1977 in the appropriate limit of $\chi_e = 0$]. One further useful approximation for this expression may be derived by noting that the resonant denominator in the drift-wave limit implies that $\omega \sim \omega'$. Accordingly, one may use the definition of $\epsilon^{(1)}$ in Eq. (5.15) (upon noting that the resonant term is dominant) to find

$$\epsilon^{(1)}(\vec{k}'', \omega'') \simeq -\frac{\omega_*''}{\omega''} \zeta'' Z(\zeta'') \Gamma_0''. \tag{5.19}$$

Third Order. One may now complete Eq. (5.13) at third order:

$$-i\omega f^{(3)}_{\vec{k},\omega} + i k_\parallel v_\parallel f^{(3)}_{\vec{k},\omega} + i k_\parallel v_\parallel \Psi^{(3)}_{\vec{k},\omega} f_0 - i\omega_*^P \Psi^{(3)}_{\vec{k},\omega} f_0$$

$$= -\sum_{\vec{k}'} (\vec{k}' \times \vec{k} \cdot \hat{\mathbf{b}}) \left(\Psi^{(1)}_{\vec{k}',\omega'} f^{(2)}_{\vec{k}-\vec{k}', \omega-\omega'} - \Psi^{(2)}_{\vec{k}-\vec{k}', \omega-\omega'} f^{(1)}_{\vec{k}',\omega'} \right).$$

The solution is

$$f^{(3)}_{\vec{k},\omega} = -\frac{\omega_*^P - k_\parallel v_\parallel}{\omega - k_\parallel v_\parallel + i0^+} \Psi^{(3)}_{\vec{k},\omega} f_0$$

$$-i \sum_{\vec{k}'} \frac{(\vec{k}' \times \vec{k} \cdot \hat{\mathbf{b}})}{(\omega - k_\parallel v_\parallel + i0^+)} \left[\left(\frac{\omega_*^{P\prime} - k_\parallel' v_\parallel}{\omega' - k_\parallel' v_\parallel + i0^+} - \frac{\omega_*^{P\prime\prime} - k_\parallel'' v_\parallel}{\omega'' - k_\parallel'' v_\parallel + i0^+} \right) \Psi^{(1)}_{\vec{k}',\omega'} \Psi^{(2)}_{\vec{k}'',\omega''} f_0 \right.$$

$$\left. + i \frac{(\vec{k}' \times \vec{k} \cdot \hat{\mathbf{b}})}{(\omega'' - k_\parallel'' v_\parallel)} \left(\Psi^{(1)}_{\vec{k},\omega} f^{(1)}_{-\vec{k}', -\omega'} - \Psi^{(1)}_{-\vec{k}', -\omega'} f^{(1)}_{\vec{k},\omega} \right) \Psi^{(1)}_{\vec{k}',\omega'} \right].$$

Upon substituting into the third term on the RHS for $f^{(1)}$ and enforcing quasineutrality at third order,

$$(\tau + 1 - \Gamma_0) \Phi^{(3)}_{\vec{k},\omega} = \int d^3v \, J_0 f^{(3)}_{\vec{k},\omega},$$

one is led to

$$\epsilon^{(1)}(\vec{k},\omega)\Phi^{(3)}_{\vec{k},\omega} = -i\int d^3v \sum_{\vec{k}'} \frac{\vec{k}'\times\vec{k}\cdot\hat{\mathbf{b}}}{(\omega - k_\parallel v_\parallel + i0^+)} J_0 \Psi^{(1)}_{\vec{k}',\omega'}$$

$$\times\left[\left(\frac{\omega_*^{P\prime} - k'_\parallel v_\parallel}{\omega' - k'_\parallel v_\parallel + i0^+} - \frac{\omega_*^{P\prime\prime} - k''_\parallel v_\parallel}{\omega'' - k''_\parallel v_\parallel + i0^+}\right) f_0 \Psi^{(2)}_{\vec{k}'',\omega''}\right.$$

$$\left. + i\frac{(\vec{k}'\times\vec{k}\cdot\hat{\mathbf{b}})f_0}{(\omega'' - k''_\parallel v_\parallel + i0^+)}\left(\frac{\omega_*^{P\prime} - k'_\parallel v_\parallel}{\omega' - k'_\parallel v_\parallel + i0^+} - \frac{\omega_*^{P} - k_\parallel v_\parallel}{\omega - k_\parallel v_\parallel + i0^+}\right)\Psi^{(1)}_{-\vec{k}',-\omega'}\Psi^{(1)}_{\vec{k},\omega}\right]. \quad (5.20)$$

Eq. (5.20) is general; in the drift-wave limit, one can ignore the terms proportional to $k_\parallel v_\parallel$ and $k'_\parallel v_\parallel$. The first term of Eq. (5.20) $\propto \Psi^{(2)}$ is the "shielded" response, and the second term is the "bare" response. Upon combining the two parts using Eq. (5.19), one finds

$$\epsilon^{(1)}(\vec{k},\omega)\Phi^{(3)}_{\vec{k},\omega} = -\sum_{\vec{k}'}(\vec{k}'\times\vec{k}\cdot\hat{\mathbf{b}})^2$$

$$\times\left\{\left(\frac{\langle J_0 J'_0 J''_0\rangle^2}{\Gamma''_0} - \left\langle J_0^2 J_0'^2\right\rangle\right)\frac{\zeta''}{\omega''}Z(\zeta'')\frac{1}{\omega}\left(\frac{\omega'_*}{\omega'} - \frac{\omega_*}{\omega}\right)\right\}\Phi^{(1)}_{\vec{k},\omega}|\Phi^{(1)}_{\vec{k}',\omega'}|^2. \quad (5.21)$$

The shielded contribution therefore cancels the bare contribution in the $b = 0$ limit. The generalization of this expression for $\eta_i \neq 0$ may be found in Hahm and Tang, 1990.

5.2.2 Gyrofluid Analysis

Upon ignoring the RHS of Eqs. (5.3–5.8), one finds the linear dispersion relation, which in turn may be used to define the dielectric function $\epsilon^{(1)}(\vec{k},\omega)$:

$$\left[(\tau + 1 - \Gamma_0) + \Gamma_0\left(\frac{\tilde{\omega}_*^P - k_\parallel\tilde{v}_\parallel}{\omega - k_\parallel\tilde{v}_\parallel}\right)\right]\Phi_{\vec{k},\omega} \equiv \epsilon^{(1)}(\vec{k},\omega)\Phi^{(1)}_{\vec{k},\omega} = 0. \quad (5.22)$$

Note that $\tilde{v}_\parallel$ is complex and so there is no singularity in Eq. (5.22). This expression is equivalent to Eq. (3.1).

Virtual Modes. At this point in the gyrofluid version of the calculation, the algebra for the general case becomes somewhat tedious. Retaining all of the nonlinear FLR terms obscures the comparison unnecessarily; hence, for (only) the nonlinear terms, I will take $N(b) = D(b) = 1$ in the quasineutrality constraint. This is not a serious compromise, since the original equations are only rigorously valid for $k_\perp \rho < 1$ anyway. Other terms, if dropped, will be noted explicitly.

With this caveat in mind, one may find the induced potential $\Psi^{(2)}_{k''}$ following exactly the same steps as in the kinetic calculation. The virtual density perturbation (corresponding to $\int d^3v\, J_0'' f^{(2)}_{\vec{k}'',\omega''}$) is

$$\begin{aligned}\bar{n}^{(2)}_{\vec{k}'',\omega''} = &-\left(\frac{\tilde{\omega}_*^{P''} - k_\parallel'' \tilde{v}_\parallel''}{\omega'' - k_\parallel'' \tilde{v}_\parallel''}\right) \Gamma_0'' \Phi^{(2)}_{\vec{k}'',\omega''} - i \frac{(\vec{k}' \times \vec{k} \cdot \hat{\mathbf{b}})}{\omega'' - k_\parallel'' \tilde{v}_\parallel''} \Gamma_0^{1/2\,\prime\prime} \hat{\beta} \Psi^{(1)}_{\vec{k},\omega} \Psi^{(1)}_{-\vec{k}',-\omega'} \\ &\times \left[A_3(\xi', \xi'') \left(\frac{\tilde{\omega}_*^{P'} - k_\parallel' \tilde{v}_\parallel'}{\omega' - k_\parallel' \tilde{v}_\parallel'} + \frac{\eta_i \omega_*'}{2} \frac{\tilde{\theta}_\perp + \tilde{\theta}_\perp'' - \tilde{\theta}_\perp'}{\omega' - k_\parallel' \tilde{v}_\parallel'} \right) \right. \\ &\left. - A_3(\xi, \xi'') \left(\frac{\tilde{\omega}_*^{P} - k_\parallel \tilde{v}_\parallel}{\omega - k_\parallel \tilde{v}_\parallel} + \frac{\eta_i \omega_*}{2} \frac{\tilde{\theta}_\perp' + \tilde{\theta}_\perp'' - \tilde{\theta}_\perp}{\omega - k_\parallel \tilde{v}_\parallel} \right) \right]. \end{aligned} \tag{5.23}$$

Several new definitions have been used to keep the expression from becoming too unwieldy. The quantity ξ is used to refer to the frequency and wavenumber of a given mode; or put another way, $\xi = \{\zeta, \sigma(k_\parallel)\}$, where $\sigma(x) \equiv x/|x|$. The quantity $A_3(\xi, \xi')$ keeps track of the contributions from the various nonlinearities. It has the form

$$A_3(\xi, \xi'') \equiv 1 + \tilde{v}_\parallel \tilde{v}_\parallel'' + 2\tilde{\theta}_\parallel \tilde{\theta}_\parallel''.$$

The first term indicates the relative strength of the contributions from the nonlinearities in the density and perpendicular temperature equations. The second term is associated with the $u_\parallel$ and $q_\perp$ nonlinearities, and so on. As $\zeta \to \infty$, $A_3(\xi, \xi'') \to 1$. In this limit, only the nonlinearities in the n and $T_\perp$ equations contribute significantly. Previous authors [Similon, 1981; Horton, 1984; Mattor, 1992] have noted similar simplifications. In general, the quantity A_n has n terms, where n is the number of parallel and perpendicular moments. Finally, $\hat{\beta}$ keeps account of the FLR corrections:

$$\hat{\beta}(\vec{k}_\perp, \vec{k}'_\perp) \equiv 1 + \tfrac{1}{4}(\tilde{\theta}_\perp \tilde{\theta}'_\perp + \tilde{\theta}_\perp \tilde{\theta}''_\perp + \tilde{\theta}'_\perp \tilde{\theta}''_\perp).$$

Appropriately, $(\hat{\beta} - 1)$ is positive definite and symmetric with respect to interchanging $\vec{k}, \vec{k}'$.

In the drift-wave limit, with $\eta_i = 0$, a simple expression for $\Phi^{(2)}_{\vec{k}'',\omega''}$ may be found by enforcing the quasineutrality constraint at second order:

$$\epsilon^{(1)}(\vec{k}'',\omega'')\Phi^{(2)}_{\vec{k}'',\omega''} = -i\hat{\beta}(\Gamma_0\Gamma_0'\Gamma_0'')^{1/2}\frac{(\vec{k}'\times\vec{k}\cdot\hat{\mathbf{b}})}{\omega''-k_\parallel''\tilde{v}_\parallel''}\Phi^{(1)}_{\vec{k},\omega}\Phi^{(1)}_{-\vec{k}',-\omega'}\left(\frac{\omega_*'}{\omega'}-\frac{\omega_*}{\omega}\right). \quad (5.24)$$

This expression compares favorably with Eq. (5.18). As noted above, a useful approximation to $\epsilon^{(1)}(\vec{k}'',\omega'')$ is

$$\epsilon^{(1)}(\vec{k}'',\omega'') \simeq -\frac{\omega_*''}{\omega''}\zeta''Z_3(\zeta'')\Gamma_0''.$$

Third-Order Response. Again, the gyrofluid calculation parallels that of the gyrokinetic calculation very closely. The gyrofluid expression corresponding to Eq. (5.21) (the drift-wave limit) is:

$$\epsilon^{(1)}(\vec{k},\omega)\Phi^{(3)}_{\vec{k},\omega} =$$

$$\sum_{\vec{k}'}(\vec{k}'\times\vec{k}\cdot\hat{\mathbf{b}})^2\left\{\left[\Gamma_0\Gamma_0'(1-\hat{\beta})\right]\frac{\zeta''}{\omega''}Z_3(\zeta'')\frac{1}{\omega}\left(\frac{\omega_*'}{\omega'}-\frac{\omega_*}{\omega}\right)\right\}\Phi^{(1)}_{\vec{k},\omega}|\Phi^{(1)}_{\vec{k}',\omega'}|^2. \quad (5.25)$$

Note that $(1-\hat{\beta})\to 0$ in the $b=0$ limit, recovering the kinetic cancellation between the bare and shielded contributions at long wavelengths. This level of agreement between fluid and kinetic theory is a new result, presented here for the first time.

Wave-Kinetic Equation. One may now find the wave kinetic equation following the standard procedure [Sagdeev and Galeev, 1969]. First, define the plasmon number $N_{\vec{k}}(t)$ by

$$N_{\vec{k}} = \frac{\partial\epsilon_r^{(1)}(\vec{k},\omega)}{\partial\omega_{\vec{k}}}|\Phi_{\vec{k},\omega}|^2.$$

The wave-kinetic equation [Drummond and Pines, 1962] is found by making the random-phase approximation, multiplying Eq. (5.25)[2] by $\Phi^{(1)}_{-\vec{k},-\omega}\exp i(\tilde{\omega}-\omega)t$, integrating over $d\omega\,d\tilde{\omega}$ and taking the imaginary part:

$$\frac{1}{2}\frac{\partial N_{\vec{k}}}{\partial t} = \gamma_{\vec{k}}N_{\vec{k}} + \sum_{\vec{k}'}\delta(\vec{k},\vec{k}')N_{\vec{k}}N_{\vec{k}'}. \quad (5.26)$$

[2]Because I am only trying to show the correspondence between the gyrofluid and gyrokinetic descriptions, I have ignored some contributions to the wave-kinetic equation. In a more complete calculation, one should include terms proportional to $\Phi^{(2)}\Phi^{(2)}$ that can be found by multiplying Eq. (5.24) by $\Phi^{(2)}$ and treating it in a fashion similar to the terms retained in the present analysis. With this correction, Eq. (5.26) can be made energy-conserving.

The real part of Eq. (5.26) determines the eigenmode and the real frequency. The coupling coefficient δ is given by

$$\delta(\vec{k},\vec{k}') \equiv -(\vec{k}'\times\vec{k}\cdot\hat{\mathbf{b}})^2 \left\{ \left[\frac{\Gamma_0\Gamma_0'}{H(\vec{k})H(\vec{k}')}(1-\hat{\beta}) \right] \frac{\zeta''}{\omega''} \mathrm{Im}[Z_3(\zeta'')]\omega_*'' \right\},$$

where $H(\vec{k}) \equiv \omega_{\vec{k}}\partial\epsilon_r^{(1)}(\vec{k},\omega)/\partial\omega_{\vec{k}} = (\tau+1-\Gamma_0)$ and $\gamma_{\vec{k}}$ is the linear growth rate. This expression compares very well with Eqs. (14 – 17) of CHEN *et al.*, 1977, upon noting the approximation made there that $\omega \simeq \omega'$. In particular, two important features of this gyrofluid wave-kinetic equation should be noted. First, since $\delta(\vec{k},\vec{k}') = -\delta(\vec{k}',\vec{k})$, the number of plasmons is conserved by the nonlinear term. That is, since the phase velocity of the drift waves is much larger than the ion thermal velocity, the ions do not absorb an appreciable fraction of the wave action. Instead, the action is scattered. The direction of the scattering in k_y may be determined from Eq. (5.26). Rather than integrating this equation over wave-number space, note only that since $\delta > 0$ for $k_y < k_y'$, the wave action tends to be scattered to longer wavelengths. A more complete calculation (described in the preceding footnote) would allow a similar conclusion to be drawn for the wave energy.

In the regime of validity of this nonlinear analysis, solving Eqs. (5.3–5.9) for the saturated spectrum is equivalent to solving Eq. (5.26). Of course, more information (such as the resulting thermal flux) is immediately available from solving the primitive equations. However, direct solutions of Eq. (5.26) may be more desirable for some applications (and budgets). Finally, note that since the approximations made in the gyrofluid approach do not seriously compromise the results from the more complete kinetic calculation, numerical simulation of an instability such as this one using the computationally efficient gyrofluid equations should provide reliable insights into the corresponding turbulent behavior.

5.3 "Deeply Resonant" Limit

The agreement between the gyrofluid and the gyrokinetic results in the narrow weak-turbulence regime of ITG modes first studied by MATTOR and DIAMOND, 1988 is not as good as in the drift-wave limit [MATTOR, 1992]. The difficulty lies in the $\zeta, \zeta', \zeta'' \ll 1$ limit, where Eqs. (5.3–5.9) underestimate the damping due to

ion Compton scattering compared with the kinetic prediction. The implication for thermal transport is that the kinetic equations predict a χ_i that is smaller than the gyrofluid prediction by a factor of ζ^2 in this regime. Because this limit has received less attention in the literature, I shall first briefly review a few aspects of the linear theory.

5.3.1 Linear Properties.

The integral in Eq. (5.15) may be performed in terms of the plasma dispersion function. The ordering $\zeta = \mathcal{O}(\varepsilon)$, $\eta - \eta_c(b) = o(\varepsilon)$, and $1/\zeta_* = \mathcal{O}(\varepsilon)$ then allows one to solve the dispersion relation for the frequency and growth rate:

$$\omega \sim \frac{2(1+\tau)}{\Gamma_0 \eta \omega_*} k_\parallel^2, \qquad\qquad \gamma \sim \sqrt{2\pi}|k_\parallel| \frac{\eta - \eta_c}{\eta \eta_c}. \tag{5.27}$$

Upon comparing the magnitudes of these expressions, one finds that

$$\frac{\gamma}{\omega} \sim \frac{\sqrt{\pi}\Gamma_0(b)}{1+\tau} \frac{\eta - 0.9}{0.9} \zeta_*, \tag{5.28}$$

where I have used the fact that $\eta_c \simeq 0.9$. According to this expression, there exists a narrow region of parameter space within which $\gamma/\omega \leq 1$, possibly permitting a perturbation expansion. The window is quite narrow, however. For example, for a given set of physical parameters (η_i, τ) and for a given $k_y\rho$ one may estimate from this expression the value of $k_\parallel L_n$ for which the growth rate is equal to the frequency. One finds for $\eta_i = 0.93, \tau = 1, k_y\rho = 1.3$, the crossover point is $k_\parallel L_n \sim 0.0085$. The full linear dispersion relation yields for the same parameters $k_\parallel L_n \sim 0.0074$.

In Fig. (5.1) I examine this point more closely. Shown in Fig. (5.1a) are the real frequency and growth rates for the unstable modes for the parameters $\eta_i = 0.93, k_y\rho = 1.3, \tau = 1$ as $k_\parallel L_n$ is varied. Lower values of $k_y\rho$ are generally stable; higher values of η_i do not satisfy the basic ordering. This is the regime indicated by Mattor's ordering [Mattor, 1992]. The curves are taken from solutions of the full dispersion relation. However, Eqs. (5.27) and (5.28) capture the fundamental features fairly well. As $k_\parallel L_n$ increases, the growth rate increases linearly at first (as expected) but turns over around $k_\parallel L_n = 0.018$. Note that the growth rate curve is fairly flat over a wide range. The real frequency behaves as expected throughout this range of parameters. The validity of the weak-turbulence approximation is

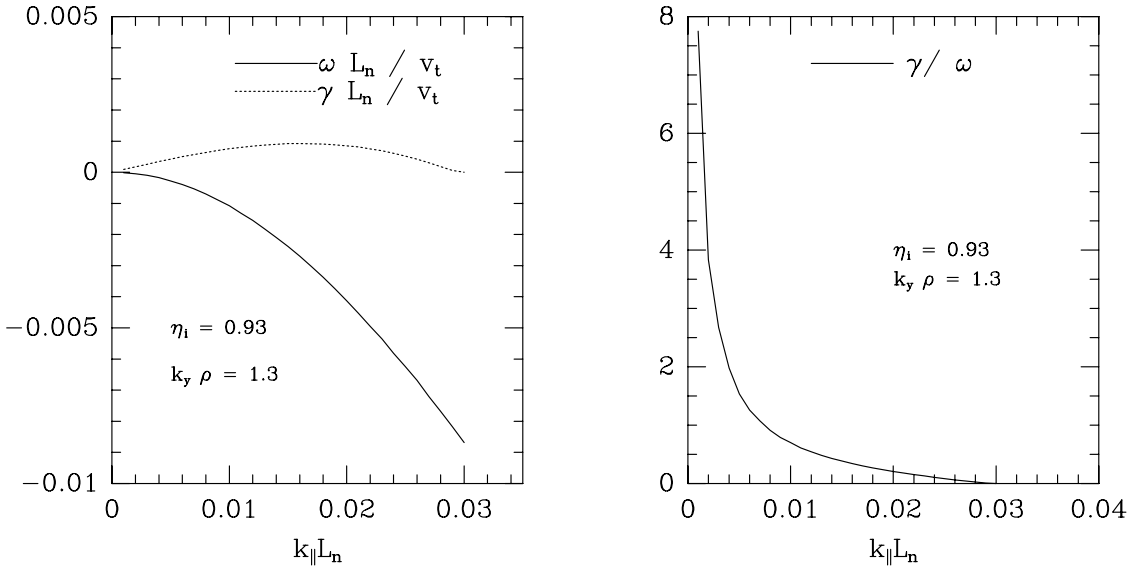

Figure 5.1: The validity of the weak-turbulence expansion for ITG turbulence is limited for $\eta_i = 0.93, k_y\rho = 1.3, \tau = 1$.

especially doubtful in light of the curve in Fig. (5.1b). One sees that although the fastest growing modes do satisfy the weak-turbulence ordering $\gamma/\omega < 1$, there are nearby modes with comparable growth rates that strongly violate the ordering. One may understand this scaling from Eq. (5.28) easily, as the factor of ζ_* causes the divergence as $k_\parallel L_n \to 0$. What might not have been clear without solving the full dispersion relation is that the growth rates for these modes are not as small (compared to the fastest growing modes) as one might have thought from the first-order expression for the growth rate. The warning here is that although some of the fluctuations have long growth times compared to their phase velocities, there are other fluctuations with comparable growth rates that spend a long time in phase with one another. As pointed out clearly in KADOMTSEV, 1965, one should consider a strong turbulence approach if this is the case. To date, strong turbulence theories of ITG turbulence [LEE and DIAMOND, 1986] have not recovered the kinetic reduction factor discussed by Mattor. (On the other hand, to my knowledge no attempt to include wave-particle effects such as ion Compton scattering has been made in a strong-turbulence theory of ITG turbulence.)

The strongest restriction imposed by the ordering assumed here is probably $\eta_i < 0.9 + \varepsilon$. Numerical solutions of the gyrokinetic (or gyrofluid) equations show

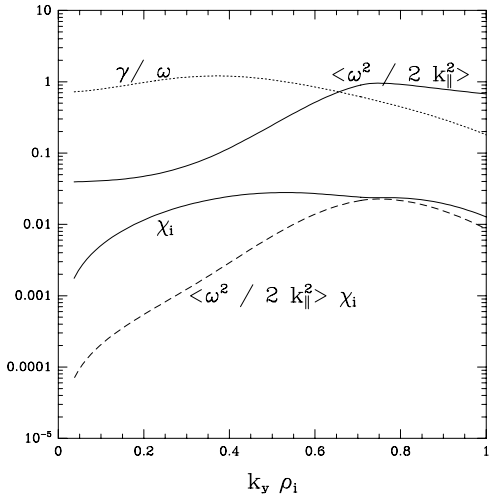

Figure 5.2: The validity of the weak-turbulence expansion for ITG turbulence is limited for $\eta_i = 2, L_s = 40 L_n$.

that for experimentally interesting parameters still somewhat near marginal stability ($\eta \sim 2, \tau \sim 1$), the fastest growing modes have either $\zeta \sim 1$ or $\gamma \sim \omega$ for a wide range of the k_y spectrum. For example, Figs. (5.2) and Fig. (4.6) together tell a typical story. For $k_y \rho_i > 0.5$, the growth rate is smaller than the frequency. Thus, one might expect that the results from the weak-turbulence analysis might be relevant. However, in this regime, $\langle \zeta \rangle = \bar{x} k_y / L_s \sim 1$, where $\bar{x}$ is defined by

$$\bar{x} \equiv \frac{\int dx\, x |\Phi^2|}{\int dx\, |\Phi^2|}.$$

Since the predicted reduction in χ_i from the kinetic analysis is proportional to $\langle \zeta \rangle^2 \sim 1$, the difference between a gyrofluid and a gyrokinetic calculation of χ will probably be small except very near marginal stability. Comparisons with gyrokinetic particle codes for parameters of experimental interest presented in Chap. 8 support this conclusion and at the same time provide a method to test the predictions of Mattor, 1992 directly. It would be interesting to compare nonlinear gyrokinetic and gyrofluid simulation results in the extreme marginal-stability limit to test the predictions of Mattor, 1992 numerically.

In any case, the analysis of Mattor, 1992 remains interesting, since many strong-turbulence theories begin with a weak-coupling expansion of the dynamical equations. Furthermore, the wave-particle interaction is a major source of wave dissipation within the present model (along with nonlinear phase-mixing); hence,

the details of the interaction between the nonlinear scattering and the dissipation are of interest.

5.3.2 Nonlinear Properties

Virtual Modes. Previously [MATTOR, 1992], the shielded contributions to the ion Compton-scattering rate were ignored on the grounds that the effect would be of order unity for the modes of interest, since in that analysis it was assumed that $k_\perp \rho \sim 1$. However, simulations indicate that the fluctuation spectrum has an appreciable component for $k_\perp \rho < 1$, where substantial cancellation between the shielded and bare potentials occurs. In fact, in a scenario in which the ion Compton scattering is predominant, its reduction at long wavelengths by turbulent shielding would actually determine the peak of the turbulent spectrum. Nevertheless, because I am interested primarily in examining the shortcomings of the gyrofluid equations, I shall follow Mattor and consider only the "bare" potential in this section.

As discussed in MATTOR, 1992, the essential differences between the kinetic and fluid approaches are not related to FLR effects. Hence, in what follows I have taken $b = 0$.

The appropriate second-order density perturbation may therefore be found from Eq. (5.16) by neglecting $\Phi^{(2)}$ and integrating over velocity space,

$$n^{(2)}_{\vec{k}'',\omega''} = \int dv\, f^{(2)}_{\vec{k}'',\omega''} = -i \int dv\, \frac{(\vec{k}' \times \vec{k} \cdot \hat{\mathbf{b}})}{\omega'' - k''_\parallel v_\parallel + i0^+} \Phi^{(1)}_{\vec{k},\omega} \Phi^{(1)}_{-\vec{k}',-\omega'} f_0$$
$$\times \left(\frac{\omega_*^{P\prime} - k'_\parallel v_\parallel}{\omega' - k'_\parallel v_\parallel + i0^+} - \frac{\omega_*^P - k_\parallel v_\parallel}{\omega - k_\parallel v_\parallel + i0^+} \right). \tag{5.29}$$

This integral may evaluated in terms of plasma dispersion functions. In the limit $\zeta, \zeta', \zeta'' \ll 1 \ll \zeta_*, \zeta'_*, \zeta''_*$, one finds

$$n^{(2)}_{\vec{k}'',\omega''} = i(\vec{k}' \times \vec{k} \cdot \hat{\mathbf{b}}) \Phi^{(1)}_{\vec{k},\omega} \Phi^{(1)}_{-\vec{k}',-\omega'}$$
$$\times \frac{1}{2} \left[\frac{\omega_*^{P\prime}}{k'_\parallel k''_\parallel} \left(\frac{Z(\zeta'') - Z(\zeta')\,\sigma(k'_\parallel k''_\parallel)}{\zeta'' - \zeta'\,\sigma(k'_\parallel k''_\parallel)} \right) - \frac{\omega_*^P}{k_\parallel k''_\parallel} \left(\frac{Z(\zeta'') - Z(\zeta)\,\sigma(k_\parallel k''_\parallel)}{\zeta'' - \zeta\,\sigma(k_\parallel k''_\parallel)} \right) \right]. \tag{5.30}$$

The comparable expression for the second-order perturbed guiding-center density obtained from the gyrofluid equations may be found from Eq. (5.23) in the

long-wavelength limit (so that $\bar{n} = n$),

$$n^{(2)}_{\vec{k}'',\omega''} = -i(\vec{k}' \times \vec{k} \cdot \hat{\mathbf{b}})\Phi^{(1)}_{\vec{k},\omega}\Phi^{(1)}_{-\vec{k}',-\omega'}$$
$$\times \left[\tilde{\omega}_*^{P'}\frac{A_3(\xi',\xi'')}{(\omega'' - k_\parallel''\tilde{v}_\parallel'')(\omega' - k_\parallel'\tilde{v}_\parallel')} - \tilde{\omega}_*^{P}\frac{A_3(\xi,\xi'')}{(\omega'' - k_\parallel''\tilde{v}_\parallel'')(\omega - k_\parallel\tilde{v}_\parallel)}\right].$$

In the present limit, this expression reduces to

$$n^{(2)}_{\vec{k}'',\omega''} = i\frac{\pi}{2}(\vec{k}' \times \vec{k} \cdot \hat{\mathbf{b}})\Phi^{(1)}_{\vec{k},\omega}\Phi^{(1)}_{-\vec{k}',-\omega'}\left[\frac{\tilde{\omega}_*^{P'}}{k_\parallel' k_\parallel''}A_3(\xi',\xi'')\sigma(k_\parallel' k_\parallel'') - \frac{\tilde{\omega}_*^{P}}{k_\parallel k_\parallel''}A_3(\xi,\xi'')\sigma(k_\parallel k_\parallel'')\right].$$

Finally, upon expanding the A_3 functions in this limit, one is led to

$$n^{(2)}_{\vec{k}'',\omega''} = i(\vec{k}' \times \vec{k} \cdot \hat{\mathbf{b}})\Phi^{(1)}_{\vec{k},\omega}\Phi^{(1)}_{-\vec{k}',-\omega'}$$
$$\times \left[\frac{\tilde{\omega}_*^{P'}}{k_\parallel' k_\parallel''}\left(\frac{3\pi}{4}\sigma(k_\parallel' k_\parallel'') - 1\right) - \frac{\tilde{\omega}_*^{P}}{k_\parallel k_\parallel''}\left(\frac{3\pi}{4}\sigma(k_\parallel k_\parallel'') - 1\right)\right]. \tag{5.31}$$

Upon comparing Eqs. (5.30) and (5.31) one may understand the shortcomings with the gyrofluid model in this limit [MATTOR, 1992]. If the primary and beat waves are aligned so that $\sigma(k_\parallel k_\parallel'') = \sigma(k_\parallel' k_\parallel'') = 1$, the gyrofluid approximation does not err badly since the expression

$$\frac{Z(\zeta'') - Z(\zeta)}{\zeta'' - \zeta} = \mathcal{O}(1).$$

However, for any other alignment of the wave vectors, the gyrofluid prediction is too small by a factor $\sim 1/\zeta$.

The essential problem is that in this limit, *all* of the nonlinear terms contribute strongly to the second-order perturbation. This may be seen by examining the A_3 factors:

$$A_3(\xi',\xi'') = 1 - \frac{2}{\pi}\sigma(k_\parallel')\sigma(k_\parallel'') + \frac{1}{2}.$$

The terms are all $\mathcal{O}(1)$. Including more moments extends this series; it nevertheless probably does not converge in the $\zeta, \zeta', \zeta'' = 0$ limit for a finite number of moments. In Sec. (5.2.2), I showed that in the high-frequency ($\zeta, \zeta' \to \infty$) limit the gyrofluid model performs adequately. One would like to know for what order of ζ the gyrofluid approximation begins to perform well. In this context it is instructive to compare the corresponding expressions for the doubly-resonant integral:

$$I_{\mathrm{GF}}(\xi,\xi') \equiv A_3(\xi,\xi')Z_3(\zeta)Z_3(\zeta') \propto \frac{A_3(\xi,\xi')}{(\omega - k_\parallel\tilde{v}_\parallel)(\omega' - k_\parallel'\tilde{v}_\parallel')},$$

$$I_{\rm GK} \equiv \frac{Z(\zeta) - Z(\zeta')\,\sigma(k_\parallel k'_\parallel)}{\zeta - \zeta'\,\sigma(k'_\parallel k_\parallel)} \propto \int dv\, \frac{f_0}{(\omega - k_\parallel v_\parallel)(\omega' - k'_\parallel v'_\parallel)},$$

for $\sigma(k_\parallel k'_\parallel) = -1$.

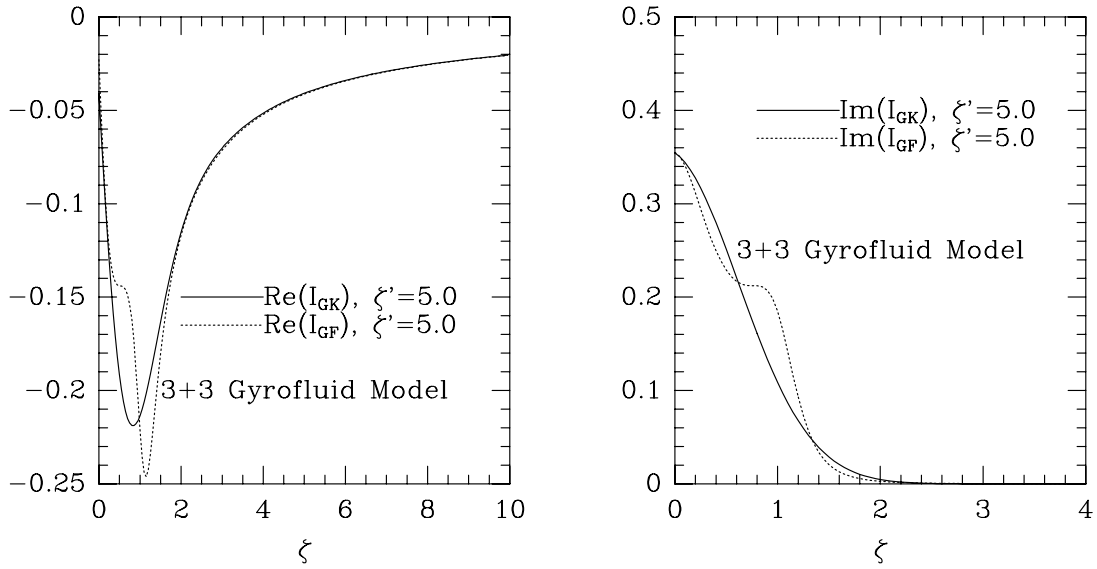

Figure 5.3: Comparison of gyrofluid and gyrokinetic second-order nonlinear response *vs.* ζ for $\zeta' = 5.0$. In this limit, the agreement is as good as the 3-pole approximation to the Z-function.

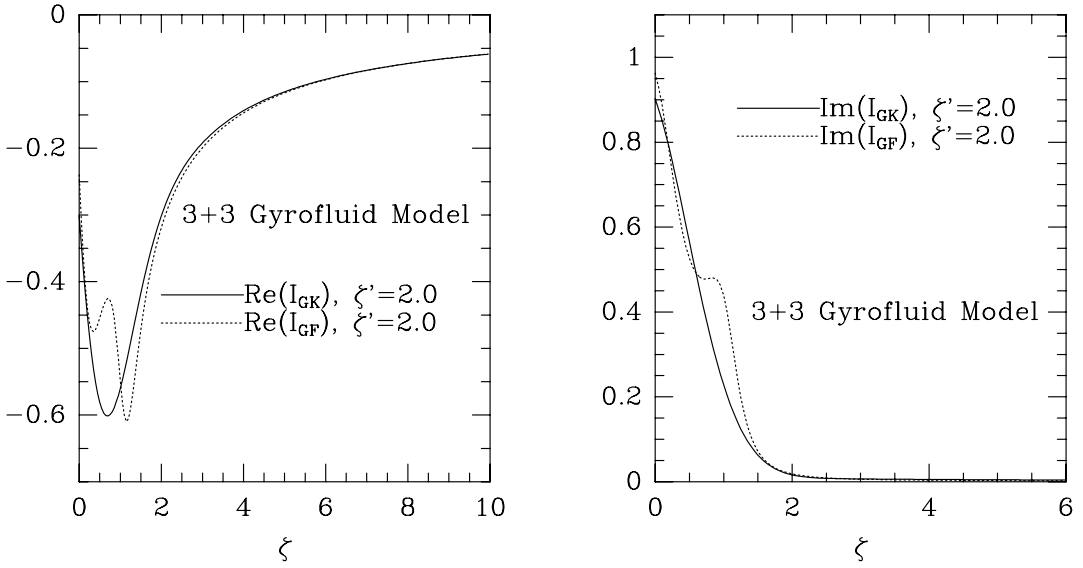

Figure 5.4: Comparison of gyrofluid and gyrokinetic second-order nonlinear response *vs.* ζ for $\zeta' = 2.0$. Note the discrepancy at low frequency, especially in the imaginary part.

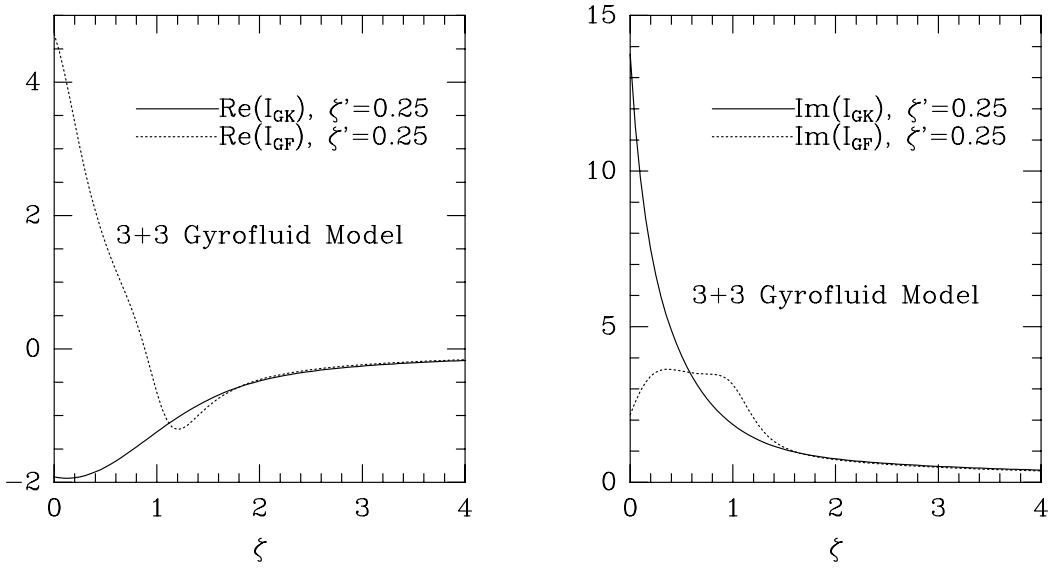

Figure 5.5: Comparison of gyrofluid and gyrokinetic second-order nonlinear response *vs.* ζ for $\zeta' = 0.25$. The discrepancy at low frequency is large as the doubly-resonant limit is approached.

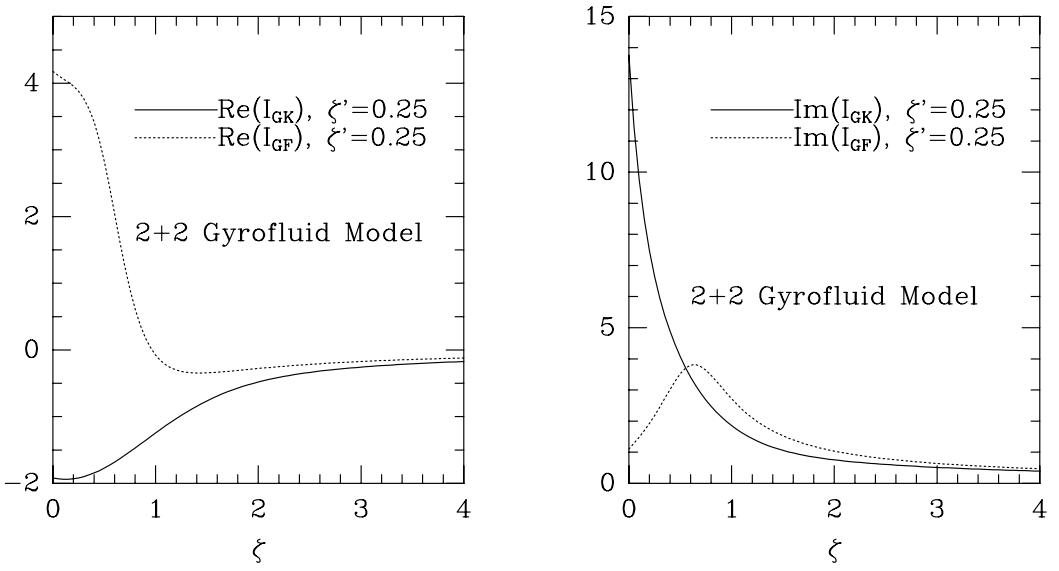

Figure 5.6: Comparison of gyrofluid and gyrokinetic second-order nonlinear response *vs.* ζ for $\zeta' = 0.25$. The 2+2 equations do not agree as well for large ζ.

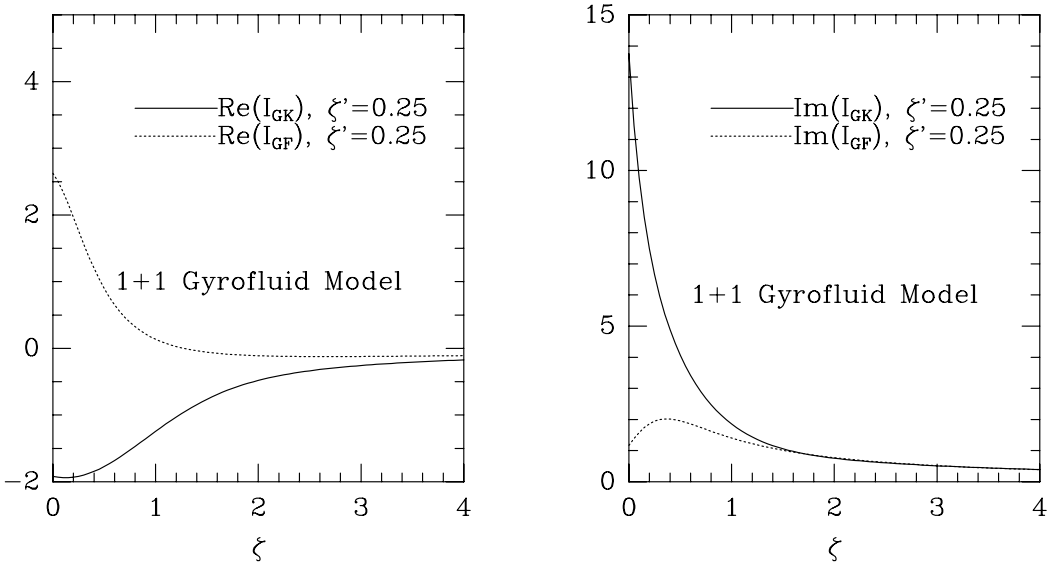

Figure 5.7: Comparison of gyrofluid and gyrokinetic second-order nonlinear response *vs.* ζ for $\zeta' = 0.25$. The 1+1 model is reasonable for large ζ.

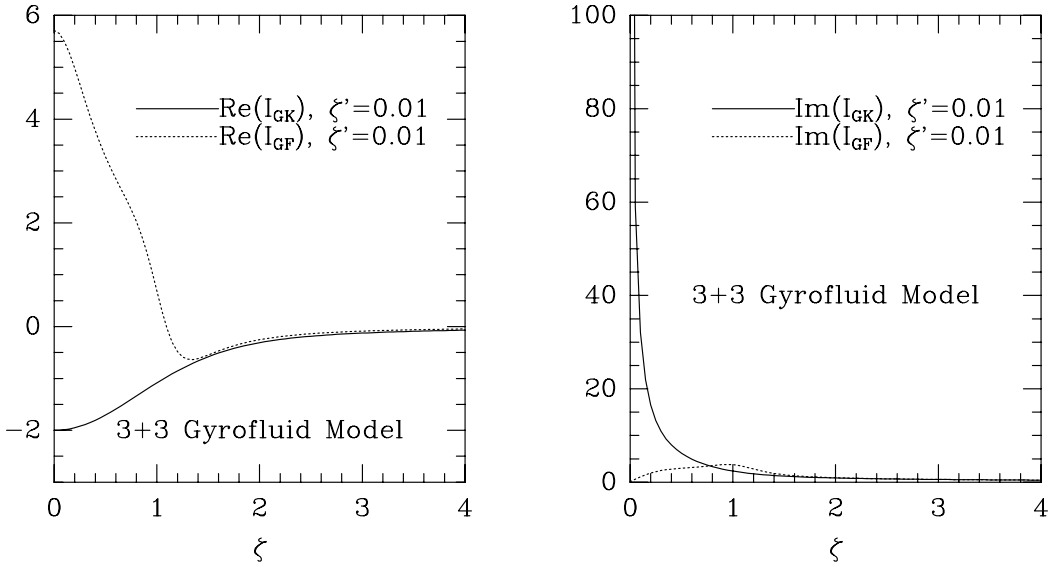

Figure 5.8: Comparison of gyrofluid and gyrokinetic second-order nonlinear response *vs.* ζ for $\zeta' = 0.01$. The error for small ζ, ζ' is very large.

In Figs. (5.3)–(5.8) I show a few slices of the $I_{\rm GK}$ and $I_{\rm GF}$ functions. In general, it is difficult to see clear improvement as one retains more moments with this primitive approach. However, one may see that even if $\zeta' \ll 1$, the agreement between the gyrofluid and gyrokinetic expressions is reasonable above $\zeta \sim 1$. More study is needed to quantify the deficiency in the low-frequency limit, and to estimate its impact in a sheared, three-dimensional setting. As noted by MATTOR, 1992, the error in the third-order response is larger.

Additional Moments. I have carried through this analysis with two-, four-, six- (shown here), and eight-moment models to check to see if adding moments improves the agreement with the kinetic result. The quantity A_4 in the $\zeta = 0$ limit is

$$A_4(\xi', \xi'') = 1 - \frac{2}{\pi}\sigma(k_\parallel')\sigma(k_\parallel'') + \frac{1}{2} - \frac{(3\pi - 8)}{2\pi}\sigma(k_\parallel')\sigma(k_\parallel'').$$

SMITH and HAMMETT, 1993 have studied the one-dimensional nonlinear plasma-echo problem and have made further progress in interpreting the terms represented by the A_n functions and in understanding the relationship between linear Landau damping and the nonlinear coupling of the fluid moments. It would be interesting to apply their insights to the ion Compton-scattering problem. In particular, they found that one must retain roughly $(k_\parallel v_t t_2)^2$ moments to reproduce the plasma echo, where t_2 is the time between the initial perturbations. Based upon Figs. (5.3)–(5.8), one might expect that a similar result could be found for the ion Compton-scattering problem.

For example, one could perhaps replace the quantity t_2 with the inverse frequency of the beat wave $(\omega'')^{-1}$, which roughly measures the time two primary waves remain in phase and therefore interact strongly. Thus, one might conjecture that the number of fluid moments required for an accurate description of the nonlinear dynamics scales like $(k_\parallel'' v_t/\omega'')^2$. [This conjecture would be consistent with the results of MATTOR, 1992 confirmed here, that the nonlinear response of a few-moment fluid model is poor in the large $k_\parallel'' v_t/\omega''$ limit.] On the other hand, for $k_\parallel'' v_t/\omega'' = \mathcal{O}(1)$, one might expect to be able to show analytically that the agreement between the few-moment-fluid and kinetic results would be reasonable. This conjecture could be checked quantitatively using the expansions for the nonlinear fluid response given above.

Finally, note that the $k_\parallel v_t/\omega \to \infty$ limit is probably not a relevant limit in the presence of weak collisions. Because Coulomb interactions in real space lead to velocity-space diffusion, the sharply resonant denominators in Eq. (5.29) would be wiped out in the presence of collisional dissipation characterized by a collision frequency ν in a time $t \sim (k_\parallel v_t)^{-2/3}\nu^{-1/3}$ [STIX, 1992]. Thus, one might expect that the appropriate number of moments N needed to model the physical phenomena might scale like $N \sim (k_\parallel v_t/\nu)^{2/3}$.

Chapter 6

Numerical Integration Scheme

EQS. (2.63–2.69) WERE DERIVED WITH AN EYE toward numerical applications. In this chapter, the algorithms that were chosen for the `ITG` code are presented, and issues such as boundary conditions and the aspect ratios of the simulation domain (a right parallelepiped) are discussed.

`ITG` is a flexible Fortran code that presently runs on several platforms, including Sun workstations, Vaxes, and the National Energy Research Supercomputer Center (NERSC) Crays. Only the maximum system size is fixed at compile time; all other decisions are deferred until run time. The choices then available include the dimensions and resolution of the simulation domain, the boundary conditions, the physical parameters (such as L_n/L_T, L_n/L_s, *etc.*), the number of moments evolved, the time-stepping algorithm, the FLR model employed, spatial filtering options, and whether or not to produce color movies for later viewing. The nonlinear terms may be ignored if desired (for linear benchmark studies) and an X-window interface written by Q. P. Liu may be invoked to provide real-time feedback and control. Restart capabilities from periodically saved datasets ensure that unforeseen or inadvertent operating events do not result in the complete loss of data from a given simulation. An example input file is provided in App. G.

6.1 Time-stepping Algorithm

The default time-integration algorithm used in the `ITG` code is a standard two-step Runge–Kutta method.[1] To integrate the model equation

$$\frac{d\rho}{dt} = f(\rho) \tag{6.1}$$

using this algorithm, one would solve first for ρ at the half time-step

$$\rho^{j+1/2} = \rho^j + \tfrac{1}{2}\Delta t\, f(\rho^j)$$

and then use this information to find ρ at the full time-step:

$$\rho^{j+1} = \rho^j + \Delta t\, f(\rho^{j+1/2}).$$

For example, if $f(\rho) = -i\omega_*\rho$, then

$$\rho^{j+1} = \rho^j - i\omega_*\,\Delta t\,\rho^j(1 - \tfrac{1}{2}i\omega_*\,\Delta t) = \left(1 - i\omega_*\Delta t - \tfrac{1}{2}(\omega_*\Delta t)^2\right)\rho^j.$$

Note that this is the second-order expansion of the exact solution $\rho^{j+1} = \rho^j e^{-i\omega_*\,\Delta t}$. For real ω_* the exact solution is oscillatory with $|\rho^{j+1}| = |\rho^j|$. However, the numerical approximation introduces spurious growth. The artificial amplification at each time step is

$$\frac{|\rho^{j+1}|^2}{|\rho^j|^2} = 1 + \tfrac{1}{4}(\omega_*\,\Delta t)^4,$$

corresponding to a spurious numerical growth rate $\gamma_{\rm N} = \omega_*^4(\Delta t)^3/8$. One must choose the time step and spatial grid so that this numerical growth is small compared to the physical growth rates in which one is interested. If $f(\rho) \sim \mathbf{v}_E \cdot \nabla\rho$, this condition is related to the Courant condition $\Delta t\,\mathbf{v}_E/\Delta x < 1$. In our runs, we typically adjust Δt at each time step, requiring

$$\Delta t\,\mathrm{Max}[\mathrm{Max}(v_{Ex}/\Delta x), \mathrm{Max}(v_{Ey}/\Delta y)] < 0.025.$$

[1] Other second-order accurate schemes exist that are stable. It may be worth investigating improvements in the time-stepping algorithms I use at present. In addition to the method presented here, I have tried a first-order accurate semi-implicit scheme. However, no results using this scheme are presented in this thesis so I will not discuss it further.

6.2 Pseudospectral Representation

At various points in the time-stepping algorithm, the potential and the moments are represented in real space (evaluating nonlinear terms), spectrally (evaluating derivatives perpendicular to the magnetic field $\propto k_x, k_y$) and in mixed form (evaluating derivatives parallel to the magnetic field $\propto xk_y$). This general technique [ORSZAG, 1971], often referred to as the pseudospectral or collocation spectral method, reduces numerical diffusion associated with finite-difference methods and is faster than direct convolutions for large systems. The clearest and consequently most useful description of this method in the literature I searched was CROTINGER, 1989.

Our implementation of the pseudospectral technique varies somewhat from the standard fluid implementations because of the appearance of the parallel derivatives (including the Landau-damping terms) that are most easily evaluated in the mixed-form space. The mixed-form representation (the default representation in the code) is (for a field W):

$$W(x,y,z,t) = \sum_n \sum_{m\geq 0} \left[W_c(x,m,n,t) \cos\left(\frac{2\pi my}{L_y} - \frac{2\pi nz}{L_z}\right) \right.$$

$$\left. + W_s(x,m,n,t) \sin\left(\frac{2\pi my}{L_y} - \frac{2\pi nz}{L_z}\right) \right].$$

Equations for $W_c(x,m,n,t)$ and $W_s(x,m,n,t)$ are advanced in time as follows:

$W(x,k_y,k_z)$	Beginning of time step.
$\Downarrow$	
$W(k_x,k_y,k_z)$	$\partial/\partial x, \partial/\partial y$ terms evaluated.
$\Downarrow$	
$W(x,y,z)$	Nonlinear terms evaluated.
$\Downarrow$	
$W(k_x,k_y,k_z)$	Nonlinear terms dealiased.
$\Downarrow$	
$W(x,k_y,k_z)$	$k_\parallel$ terms evaluated and time step taken.
$\Downarrow$	
$W(k_x,k_y,k_z)$	Quasineutrality constraint equation solved for Φ.
$\Downarrow$	
$W(x,k_y,k_z)$	End of time step.

From this diagram, it is clear that improvements are available. For example, one could begin each time step in the transform space and eliminate two sets of Fast

Fourier transforms. In general, de-aliasing in a given direction is accomplished by keeping twice as many grid points in real space in that direction as Fourier modes whenever the real-space representation is used.[2]

6.3 Geometric Effects

ITG modes are naturally localized around a rational surface in this geometry because they are damped for $k_\parallel v_t \gg \omega_*$. Thus, if the driving temperature gradient relaxes nonlinearly in the vicinity of the rational surface, the instability is effectively stabilized. Because two-dimensional sheared-slab simulations have only a single rational surface, this stabilization mechanism plays an especially important role in single-helicity simulations, as noted previously [HORTON *et al.*, 1980; DIMITS *et al.*, 1991].

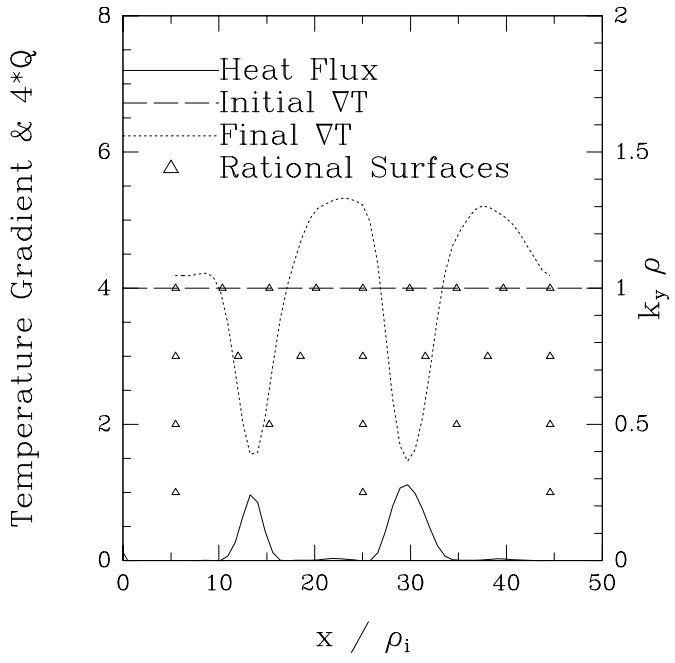

Figure 6.1: Heat flux *vs.* x for a simulation with rational surfaces spread too thinly.

[2]One may avoid aliasing errors with only 1.5 times as many grid points in real space in a given direction as associated Fourier modes. Thus, there is room for an improvement of about a factor of two ($1/5^3$) in the speed of `ITG`.

In a realistic plasma, the relaxation of the temperature gradient around one rational surface leads to a steeper gradient at another nearby rational surface. It is important to include this effect in three-dimensional simulations. That is, if the rational surfaces corresponding to unstable modes occupy a small region of the simulation domain, or if they are spaced too far apart, the transport rate predicted may be significantly misleading.

Consider the simulation in Fig. (6.1). The parameters are $L_x = 40\rho_i$, $L_y = 25\rho_i$, $L_z = 52L_n$, $\eta_i = 4$, $L_s/L_n = 40$, and $T_i = T_e$. The nonlinear terms were evaluated on a grid with $(n_x, n_y, n_z) = (64, 16, 16)$ grid points. The linear terms are advanced in (x, k_y, k_z) space with $k_y = 2\pi m/L_y$, $m = 0, 1, \ldots, M$, $M = 4$ and $k_z = 2\pi n/L_z$, $n = 0, \pm 1, \ldots, \pm N$, $N = 4$. Radially periodic boundary conditions were used, as described in Sec. 6.4.

A fair amount of information is included in this figure. First, the flux-surface-averaged, time-averaged heat flux

$$\langle\langle \bar{Q} \rangle\rangle \equiv \frac{1}{T L_y L_z} \int dy\, dz\, dt\, Q$$

is measured by the scale on the left axis and is shown as a solid line at the bottom of the figure. The quantity Q is defined in App. B. The time average is taken only over the nonlinear phase. Next, the imposed background temperature gradient (normalized to the density gradient) is shown as a dashed line at a constant value of $\eta_i = 4$. The dotted line is the temperature gradient averaged over the nonlinear phase of the simulation. Finally, the triangles represent the positions of the rational surfaces located within the simulation domain, with the corresponding $k_y\rho_i$ on the right axis.

The paucity of rational surfaces (and hence unstable modes) in this example allows the temperature gradient to flatten until $\eta_i \simeq 2$ at two points in the box without causing significant steepening at the neighboring rational surfaces. A volume-averaged thermal diffusivity χ [defined by Eq. (B.2)] would be misleading in this case, since the thermal flux is actually confined to a small region of the simulation domain and the driving temperature gradient varies widely over the box. In this example, a significant amount of perpendicular (y) rotation is occuring as well (not shown). Few conclusions can be drawn from such a simulation, since the resolution is simply inadequate. The lesson to be learned is that even though the

average temperature gradient across the entire box remains fixed at $\eta_i = 4$, as it should, the flux is suppressed because of local modifications of the temperature gradient. Hence, a prediction of χ based on such a low-resolution simulation should not be trusted. Nothing prevents this behavior from also occurring in low-resolution particle simulations (even if the multiple-scale expansion [LEE, 1983] is used).

The same problem occurs in the simulation shown in Fig. (6.2), but for different reasons. In part, the problem is again the spacing of the rational surfaces, as the outer regions of the simulation domain have no rational surfaces. This follows directly from the choice of L_z, the size of which causes the rational surfaces to be confined to the center of the box. Because this case is also an example of the effect of the boundary conditions, it is discussed further in the next section.

6.4 Boundary Conditions

The usual sheared-slab simulation domain is periodic in y and z. The radial (x) boundary condition has been treated in several ways in the past. The most common approach is to require all perturbed quantities ($n, u_\parallel, \Phi$, *etc.*) to be zero at the edges of the box (with reflecting boundary conditions for particles in kinetic simulations). This approach is followed in kinetic and gyrokinetic simulations if the entire distribution function is being evolved, with strong gradients ($\rho/L_T \sim 1/10$) across the radial direction. A multiple-scale expansion technique [LEE, 1983] is employed to separate the evolution of the background gradient from the simulation scales. With the advent of "partially linearized" [DIMITS and LEE, 1993] or δf techniques [KOTSCHENREUTHER, 1990; PARKER and LEE, 1992], it is possible to separate the background and fluctuating scales asymptotically in particle simulations by scaling δf and Φ as in Eqs. (2.61). Fluid simulations have long made this separation by using scaled fluid quantities [HORTON *et al.*, 1980] that make use of the ordering $\rho \ll L$.[3]

[3] I have not investigated the question of the evolution of the $\vec{K} = 0$ mode. While conservation of total energy, momentum, and density place constraints on the evolution of this mode, it is not implausible to assume that higher moments could evolve or that the background parallel and perpendicular temperatures could become different. If the latter possibility were observed, the fundamental equations would need to be rederived, since it was assumed in the derivation of Eq. (2.1) that $T_{\parallel 0} = T_{\perp 0}$ (see App. C).

One must treat the $(k_y = 0, k_z = 0)$ mode with care in any case. Because the gyrokinetic ordering allows $\nabla_\perp F_1 \sim \nabla_\perp F_0$, the fluctuating quantities generate gradients in the $(k_y = 0, k_z = 0)$ mode that can effectively cancel the driving background gradients and help to saturate the turbulence. This is a physical saturation mechanism that should be included in a microturbulence simulation; however, if the $(k_y = 0, k_z = 0)$ component of the pressure is handled inappropriately [as in Fig. (6.1), where there were too few rational surfaces], this mechanism can completely dominate the dynamics, which is probably not physical. Conversely, if the $(k_y = 0, k_z = 0)$ modes are simply removed from the system, an important source of stabilization may be lost.

In particular, $(F_1, \Phi) = 0$ radial boundary conditions do not adequately model the effects of heat sources and sinks that give rise to the overall gradient. For these boundary conditions, heat is not allowed to cross the radial boundaries of the box, and the background temperature gradient is gradually steepened near the edges of the box where the drive is intrinsically reduced by the boundary conditions. As in a low-resolution simulation, the gradients in the bulk of the simulation domain can relax, reducing the predicted thermal flux nonphysically. Fig. (6.2) shows the heat flux *vs.* x and the background temperature gradients for a nonlinear run with this geometry. The parameters for this run were chosen to compare with the weak-shear case of SYDORA *et al.*, 1990. Hence $L_x = 64\rho_i$, $L_y = 126\rho_i$, $L_z = 1257L_n$, $\eta_i = 4$, $L_s/L_n = 20$, and $T_i = T_e$. The time at the end of the simulation corresponds to a point just beyond the initial nonlinear saturation. The nonlinear terms were evaluated on a grid with $(n_x, n_y, n_z) = (64, 128, 32)$ grid points. In this run, the nonlinear phase-mixing terms were included and $\nu = 0.01\, v_t/L_n$. A Gaussian filter $\exp(-\beta^2 k_\perp^2 \rho^2)$ with $\beta = 1.2$ was included in Poisson's equation to simulate the effect of finite-sized particles. For the purposes of comparison, the adiabatic electron response of $n_e = e\Phi/T_e$ was used in the quasineutrality constraint (allowing nonphysical electron particle transport, as described in Ch. 8).

The curves are the time- and flux-surface averaged quantities obtained from the gyrofluid simulation. Several features can be noted. First, even though many rational surfaces are included, their distribution is uneven. In addition, the role of the boundary conditions is evident; despite the fact that nonlinear saturation is just occurring, the temperature gradients are strongly modified; steepening is evident

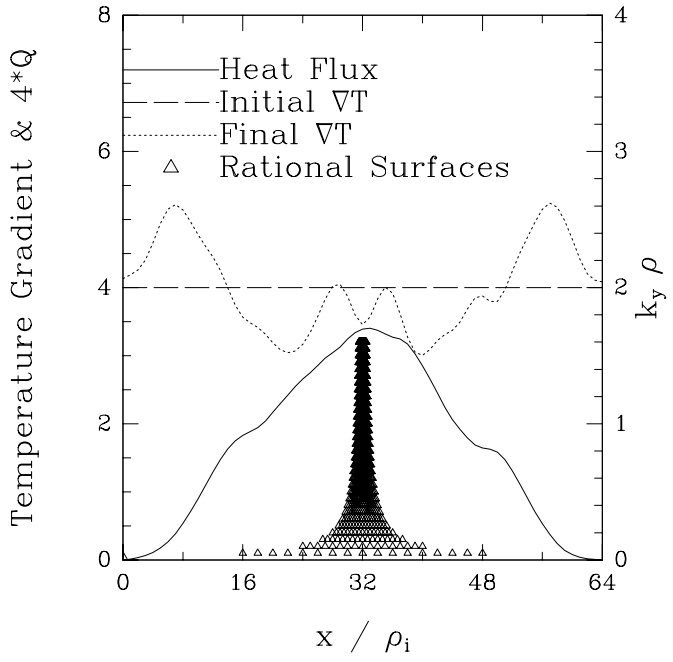

Figure 6.2: Heat flux, ∇T_0, and rational surfaces *vs.* x using $\Phi = 0$ radial boundary conditions.

near the boundaries where the flux is forced to zero, and flattening is evident in the center of the domain. The χ predicted from the simulation is difficult to interpret on these grounds, and an improved gyrofluid simulation will be shown after a discussion of radial periodicity conditions. (In the strong shear cases of SYDORA *et al.*, 1990, this effect is more pronounced and is under further investigation [SYDORA, 1993].) The volume-averaged peak (because this is soon after nonlinear saturation) heat flux within this simulation domain implies $\chi_i \sim 0.09\rho_i^2 v_t/L_n$, yet the value at the center of the domain is two times higher. SYDORA *et al.*, 1990 found a peak $\chi_i \sim 0.06\rho_i^2 v_t/L_n$ for these parameters and with this same simulation domain.

A boundary condition that removes this uncertainty and models the heat sources and sinks naturally is periodicity in the radial direction, which maintains the average temperature gradient everywhere in the simulation domain. Heat that flows out of the cold side re-enters on the warm side, mimicking a heat source. Because the simulation domain is typically very much smaller than the background gradients, the actual temperature and density differences between the edges of the domain are negligible. The difficulty lies in how to handle the sheared magnetic

field lines.

Because of the fast parallel motion of particles and the strong ion Landau damping that occurs if $k_{\|}$ is too large, the turbulent structures are highly elongated along the field line and thus tend to be aligned with the pitch of the local magnetic field. It is not sufficient simply to enforce periodicity by requiring any variable W to satisfy

$$W(x + L_x, y, z) = W(x, y, z)$$

as a result. For example, Fig. (6.3a) shows the electrostatic potential from a typical simulation in the linear phase in the $y - z$ plane at $\tilde{x} = 0$. The effect of the sheared magnetic field is clearly evident, especially when compared to Fig. (6.3b), which shows the potential at the other side of the box (after periodicity has been enforced as described below). The periodicity constraint used here is first to untwist the magnetic field so as to take into account the geometric effect, and then to enforce periodicity.

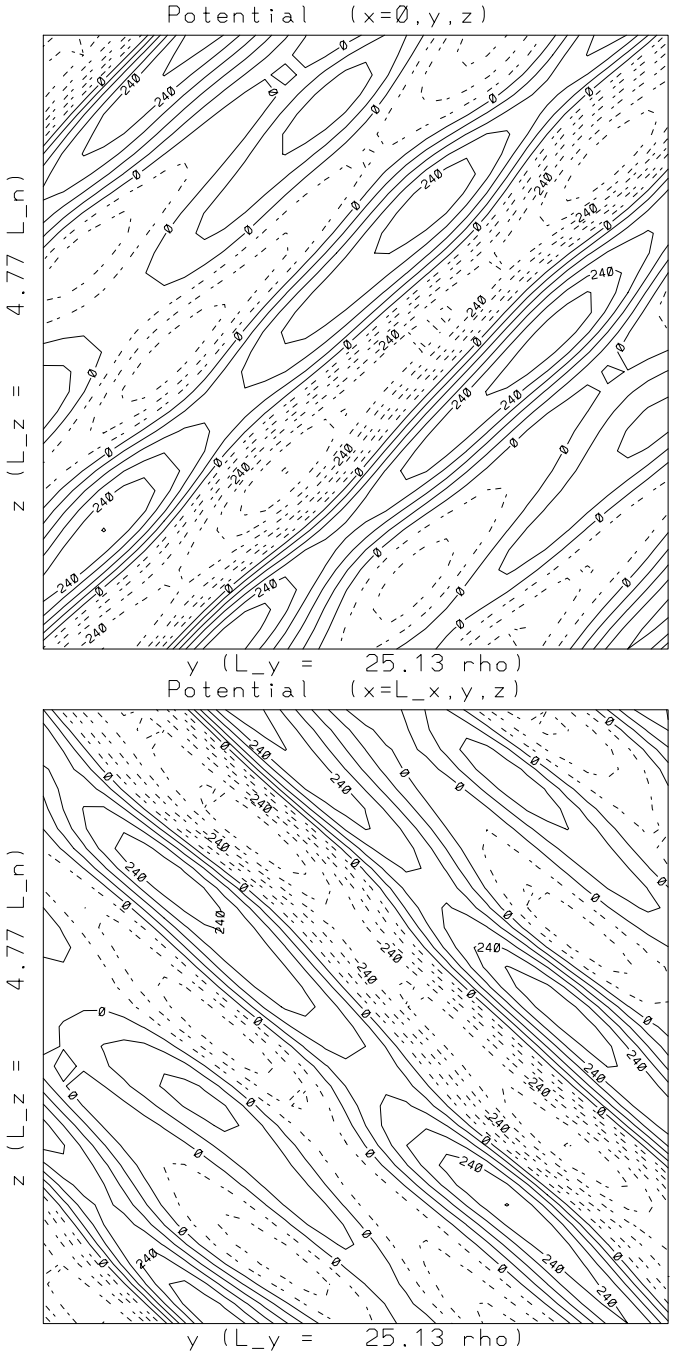

Figure 6.3: Φ in the $y-z$ plane at (a) $\tilde{x}=0$ and (b) $\tilde{x}=L_x$.

Mathematically, one transforms the periodic variables to a new coordinate system (x', y', z') that is aligned with the magnetic field. These twisting coordinates [ROBERTS and TAYLOR, 1965; COWLEY *et al.*, 1991] are given by

$$x' = x,$$

$$y' = y - sxz,$$

$$z' = z,$$

so that (x', y') labels a field line and z' measures the distance along a field line. In the new coordinates, the periodicity constraint is stated as

$$W'(x' + L_x, y', z') = W'(x', y', z'). \tag{6.2}$$

One then maps Eq. (6.2) back into the untwisted coordinates [using $W'(x', y', z') = W(x', y' + sx'z', z')$, then dropping the primes] to find

$$W\,(x + L_x,\, y + s(x + L_x)z,\, z) = W(x,\, y + sxz,\, z).$$

Upon Fourier-transforming in the y and z directions according to

$$W(x, y, z) = \sum_{m,n} W_{mn}(x) e^{ik_y y + ik_z z}$$

and using the definitions of k_y and k_z from above, one is led to

$$\sum_{mn} W_{mn}(x + L_x) \exp\left(i2\pi \left\{ \frac{m}{L_y}[y + s(x + L_x)z] + z\frac{n}{L_z} \right\}\right)$$

$$= \sum_{mn} W_{mn}(x) \exp\left\{ i2\pi \left[\frac{m}{L_y}(y + sxz) + z\frac{n}{L_z} \right] \right\}.$$

Upon shifting and matching the indices one is led to the twisting periodicity condition (similar to that first used by KOTSCHENREUTHER, 1991):

$$W_{m,n+2n_{\rm rat}}(x + L_x) = W_{m,n}(x), \tag{6.3}$$

where

$$n_{\rm rat}(m) \equiv \frac{m}{2}\frac{L_x L_z}{L_y}\frac{L_n}{L_s}$$

is constrained to be an integer. One of the dimensions of the simulation domain is quantized by the magnitude of the magnetic shear and the number of twists enclosed in the box. Also, many rational surfaces are forced to lie at the edge of the simulation domain to allow their periodic continuation elsewhere. For example, the position $x_{\rm rat}(m,n)$ of the rational surface of the (m,n) mode lies where $\hat{\mathbf{b}}\cdot\nabla = 0$. This may be written as

$$x_{\rm rat}(m,n) = (1 - \frac{n}{n_{\rm rat}})\frac{L_x}{2}\rho_i,$$

using Eq. (2.62). The rational surfaces of modes with $n = \pm n_{\rm rat}$ lie exactly at the edge of the box.

Returning to the simulations, I now show an example with the same physical parameters as the simulation of Fig. (6.2), but with periodic boundary conditions and the correct adiabatic electron constraint [i.e., Eq. (2.69)]. The nonlinear resolution is given by (64,32,32), and the box dimensions are $(38\rho_i, 38\rho_i, 38L_n)$. The artificial dissipation parameter $\nu = 0.005$. As a result of the periodic boundary

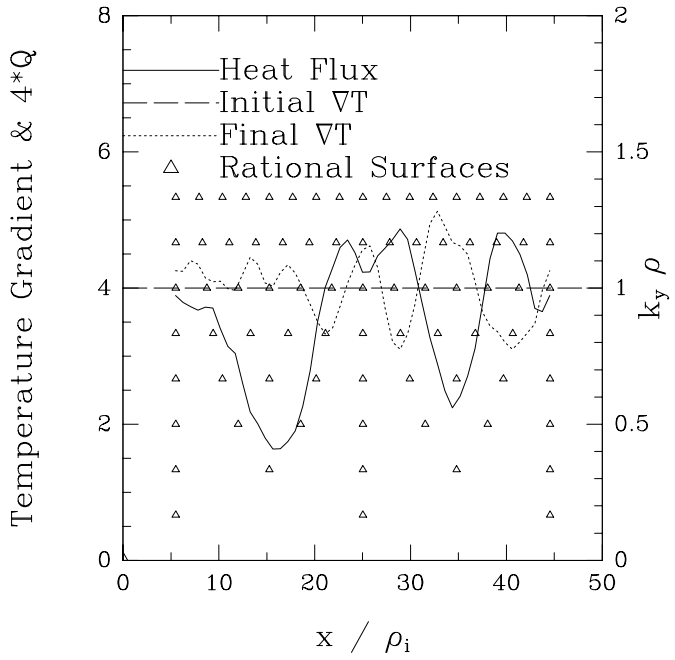

Figure 6.4: Heat flux *vs.* x for a simulation with periodic boundary conditions and reasonable resolution.

conditions, the temperature gradients are now roughly constant across the box.

While there remains a region of reduced thermal flux, there is no clear correlation of this region with the edge or with a region of low resolution. The predicted χ_i from this simulation is $0.18\rho_i^2 v_t/L_n$, in agreement with the mixing-length estimate[4] $\chi_{\rm ML} \sim (\gamma/k_\perp^2)_{\rm max} \sim 0.22\rho_i^2 v_t/L_n$ and without the ambiguity caused by the parameters used in Fig. (6.2). In passing, note that the addition of toroidal drive would increase the heat flux, perhaps to experimentally observed values.

[4]For these parameters, the stated maximum of $(\gamma/k_\perp^2)$ occurs around $k_y\rho = 0.4$. The maximum growth rate is found around $k_y\rho = 0.6$ but for this mode the mixing-length estimate is smaller: $(\gamma/k_\perp^2) = 0.11$.

Chapter 7

Comparisons with Gyrokinetic Particle Simulations

ULTIMATELY, ONE IS INTERESTED in a reduced description of plasma turbulence to the extent that it is economical and accurate. Accuracy affords one predictive power. Equally importantly, a computational tool that allows one to test many ideas quickly and inexpensively allows rapid innovation; the resulting physical and numerical insights can be widely beneficial. Developed over the last decade, gyrokinetic particle-simulation techniques [Lee, 1983; Lee, 1987] representing a tremendous improvement over full-dynamics descriptions for tokamak microturbulence research have made possible increasingly realistic kinetic simulations of tokamak discharges [Parker and Lee, 1992; Parker *et al.*, 1993]. Nevertheless, the computational demands inherent in the kinetic approach remain very high. The economy inherent in gyrofluid simulations makes possible about an order of magnitude increase in productivity [depending upon the physical system under consideration, it may be possible to realize much more, as discussed in Sec. (7.3)], given equal computational resources. Already, the impact of this increase in "tinkering time" has affected the plasma-simulation community positively. In this chapter, I address the question of accuracy by showing that the gyrofluid description outlined in the foregoing chapters retains sufficient physics content to allow excellent agreement with gyrokinetic particle simulations for three-dimensional microturbulence characteristic of existing magnetic confinement fusion devices. Though I have tackled neither the complicated question of electromagnetic disturbances nor the difficult problem of including toroidal effects, that a convincing

comparison may be made in the three-dimensional, sheared-slab geometry stands as one of the most important contributions in this thesis.

7.1 Three-Mode Coupling

In general, fully developed ITG turbulence is difficult to describe analytically. In the absence of analytic insights, it is difficult to know how well one's numerical code is performing, especially when the number of lines of code is large. One may employ energy conservation diagnostics, various spectral plots, and so on to ensure that one's code is behaving at least reasonably, but one would like to have more confidence in the accuracy of the results. When this problem was first tackled with pioneering gyrokinetic particle-simulation techniques [Lee and Tang, 1988], a highly simplified test problem was designed to test the numerical nonlinear coupling and saturation. This problem may be described as follows. Parameters were found (no magnetic shear, large η_i, conducting walls in the x direction, and a single $k_\parallel$) for which long-wavelength instabilities existed. By carefully choosing the simulation domain so that only two allowed complex Fourier modes with $\pm k_y$ were unstable, Lee and Tang, 1988 could then focus on the nonlinear coupling of these two modes to the background gradient. The theory they developed features two linearly unstable Fourier harmonics that couple together to relax the driving temperature gradient, resulting in a nonlinearly saturated state. This simple system is not turbulent and does not test many features of one's code or, in my case, of my model. Nevertheless, it is a excellent place to begin.

Linear analytic studies have shown that the kinetic models employed in the gyrofluid equations should perform well [Hammett and Perkins, 1990; Dorland and Hammett, 1993]. The linear performance of the `ITG` code is also reasonable and has been documented in Chaps. 3 and 4 [Dorland and Hammett, 1993]. Below, I investigate the three-mode-coupling problem with `ITG`, comparing the results with both analytic theory [Parker, 1993] and gyrokinetic particle simulations [Santoro and Lee, 1990]. I also compare the transient heat flux generated during the saturation process in each simulation, finding that better agreement between the fluid and particle codes is obtained with two-temperature ($T_\parallel, T_\perp$) model equations rather than the usual single-temperature approach, despite the fact that FLR

effects are very weak. First, however, the three-mode-coupling (TMC) theory using the gyrofluid equations first carried out by PARKER, 1993 is presented.

7.1.1 Three-Mode-Coupling Theory

I begin with Eqs. (2.69, 2.70–2.72) in the long-wavelength limit. Thus, FLR effects are completely unaccounted for. Furthermore, I shall consider a two-dimensional, radially bounded system in which the allowed[1] unstable modes are the longest wavelengths in the simulation domain. The beginning equations are therefore

$$\tau\frac{\partial\Phi}{\partial t}+\nabla_\parallel u_\parallel+\frac{\partial\Phi}{\partial y}=0, \tag{7.1}$$

$$\frac{du_\parallel}{dt}+\nabla_\parallel\left[T_\parallel+(\tau+1)\Phi\right]=0, \tag{7.2}$$

$$\frac{dT_\parallel}{dt}+2\nabla_\parallel u_\parallel+\eta_i\frac{\partial\Phi}{\partial y}+\sqrt{\frac{8}{\pi}}|k_\parallel|T_\parallel=0. \tag{7.3}$$

In this section, $k_\parallel L_n$ is taken to be proportional to $k_y\rho$; the constant of proportionality is $\tilde{\theta}\equiv\theta L_n/\rho$, where $\theta\equiv k_\parallel/k_y=B_y/B_z$ is the notation used in LEE and TANG, 1988. Note that I have used the $b=0$ limit of the quasineutrality constraint ($n_i=\tau\Phi$) to eliminate the ion density from the equations and that the FLR corrections to the nonlinear terms have also been dropped. In this limit, the polarization drift drops out, and the continuity equation is thus linear. I tested the effect of retaining the polarization drift in the simulations and found that for these parameters its effect was quite small.

Following LEE and TANG, 1988 and PARKER, 1993, I assume no-flux boundary conditions in x (equivalent to assuming conducting walls exist at $x=0$ and $x=L_x$) and periodicity in the y direction. One may then expand the fields into Fourier components

$$\Phi(x,y)=\sum_{\vec{K}}\Phi_{\vec{k}}\sin\left(K_x x\right)e^{iK_y y} \tag{7.4}$$

using the definitions

$$\vec{K}=(K_x,K_y)=(mk_x,nk_y)=(\frac{\pi m}{L_x},\frac{2\pi n}{L_y}),$$

[1]The Fourier representation for the electrostatic potential will be truncated beyond the longest wavelength in the box.

for $m = \pm 1, \pm 2, \ldots$ and $n = 0, \pm 1, \pm 2, \ldots$. There is no $m = 0$ mode since the sine terms vanish and the cosine terms are excluded to satisfy the boundary conditions. Furthermore, the $\pm m$ modes are not linearly independent since $\sin(-mx) = -\sin(mx)$. One may determine the $m < 0$ modes from the symmetry

$$\Phi_{-m,n} = -\Phi_{m,n}.$$

In this basis, the reality condition leads to the additional symmetry condition

$$\Phi_{m,-n} = \Phi^*_{m,n}.$$

The complex modes with $(m > 0, n \geq 0)$ are the fundamental modes and the rest may determined from the symmetry conditions. Eq. (7.4) may rewritten in terms of the conventional $e^{iK_x x} e^{iK_y y}$ basis,

$$\begin{aligned} \Phi(x,y) &= \sum_{\vec{K}} \Phi_{\vec{K}} \left(\frac{e^{iK_x x} - e^{-iK_x x}}{2i} \right) e^{iK_y y}, \\ &= -i \sum_{\vec{K}} \Phi_{\vec{K}}\, e^{i\vec{K}\cdot\vec{x}}, \end{aligned} \tag{7.5}$$

using the $\Phi_{-m,n} = -\Phi_{m,n}$ symmetry assumption. Note that there is factor of $-i$ difference from the conventional form of the Fourier expansion.

Using this same $-i$ convention in the Fourier expansion of the fields, the $\mathbf{E} \times \mathbf{B}$ nonlinearity may be written as

$$\frac{du_\parallel}{dt} \rightarrow -i\frac{\partial u_\parallel}{\partial t} + \sum_{\vec{K}=\vec{K}'+\vec{K}''} \left(K'_x K''_y - K'_y K''_x\right) \Phi_{\vec{K}'} u_{\parallel \vec{K}''}.$$

The $\Phi(2,0)$ mode is ignored in the analysis and systematically removed from the simulations (preventing self-generated perpendicular velocity-shear flows) following Lee and Tang, 1988. Since the $(1,1)$ mode (and its symmetric counterparts) have the dominant linear growth rates, the focus is on the nonlinear coupling among these modes and the modes they generate directly.

The reduced equations describing the evolution of the $(1,1)$ mode (denoted by the subscript "1") may therefore be written

$$\tau \frac{\partial \Phi_1}{\partial t} + ik_\parallel u_1 + ik_y \Phi_1 = 0, \tag{7.6}$$

$$\frac{\partial u_1}{\partial t} + ik_\parallel[T_1 + (\tau+1)\Phi_1] + 2ik_xk_y\Phi_1 u_0 = 0, \tag{7.7}$$

$$\frac{\partial T_1}{\partial t} + 2ik_\parallel u_1 + \eta_i ik_y\Phi_1 + \sqrt{\frac{8}{\pi}}|k_\parallel|T_1 + 2ik_xk_y\Phi_1 T_0 = 0. \tag{7.8}$$

Because the modes with $(m > 0, n \geq 0)$ are the fundamental modes and $k_\parallel$ is intrinsically positive for these modes, one may drop the absolute value that appears in Eq. (7.8). The "0" subscripts refer to the $(2,0)$ modes whose evolution corresponds to the relaxation of the driving background gradients. They evolve according to

$$\frac{\partial u_0}{\partial t} = 4k_xk_y\mathrm{Im}(\Phi_1^* u_1), \tag{7.9}$$

$$\frac{\partial T_0}{\partial t} = 4k_xk_y\mathrm{Im}(\Phi_1^* T_1). \tag{7.10}$$

Note that here n_0 is identically zero. In keeping with the physical intuition behind this model, I will first calculate the linear dispersion relation for the unstable modes. I will then find the amount of relaxation generated by the nonlinear interaction of these two modes. Finally, I will substitute this expression into the evolution equations of the linearly unstable modes to find the level of Φ necessary to turn off the linear growth. This "quasilinear" level (so called because linear solutions are substituted into the evolution equations for the nonlinear terms to get an approximate nonlinear dispersion relation) will then be compared to the simulation results.

Linear Growth. The linear dispersion relation in this limit is the $b = 0$ limit of Eq. (3.1) with $Z_4(\zeta)$ replaced by $Z_3(\zeta)$. The quantity $Z_3(\zeta)$ is defined in Eq. (5.12). I will refer to the linear frequency obtained from this dispersion relation with the notation $\omega = \omega_\ell + i\gamma_\ell$.

Nonlinear Relaxation. Some properties of the nonlinearly driven $(2,0)$ mode may be estimated by inserting the linear expressions for u_1 and T_1 into the latter evolution equations:

$$\frac{\partial u_0}{\partial t} = 4k_xk_y\mathrm{Im}\left[\Phi_1^*\left(\frac{\tau\omega_\ell + i\tau\gamma_\ell - k_y}{k_\parallel}\right)\Phi_1\right]$$

$$= 4\frac{k_xk_y}{k_\parallel}|\Phi_1|^2\tau\gamma_\ell,$$

since only the imaginary part of the expression in square brackets contributes. One may go one step further and get

$$u_0 = \tau \frac{k_\times^2}{k_\parallel} |\Phi_1|^2$$

where $k_\times^2 \equiv 2k_x k_y$, and the time dependence of Φ_1 allows one to cancel the linear growth rate with the contribution from the time derivative. Similarly,

$$T_0 = \frac{k_\times^2}{k_\parallel} \left(\frac{2\tau\omega_\ell}{k_\parallel} - \frac{k_y}{k_\parallel} \right) |\Phi_1|^2.$$

Self-Quenching. Combining the results from the previous two sections allows one to find a nonlinear dispersion relation involving the real parts of the linear (ω_ℓ) and nonlinear ($\omega_{\rm NL}$) frequencies:

$$2\tau \frac{\omega_{\rm NL}}{k_\parallel} + (\eta_i - 2)\frac{k_y}{k_\parallel} + \frac{k_\times^4}{k_\parallel^2} \frac{2\tau\omega_\ell - k_y}{k_\parallel} |\Phi_1|^2$$

$$= (\frac{\omega_{\rm NL}}{k_\parallel} + i\sqrt{\frac{8}{\pi}}) \left[\frac{\omega_{\rm NL}^2 \tau - \omega_{\rm NL} k_y}{k_\parallel^2} - (1+\tau) - \frac{\tau k_\times^4}{k_\parallel^2} |\Phi_1|^2 \right].$$

At the time of nonlinear saturation, the imaginary part of the nonlinear frequency must vanish. Thus, the coefficient in square brackets on the right-hand side must be identically zero, allowing one to find an expression for the initial saturation level,[2]

$$|\Phi_1|^2 = \frac{\omega_{\rm NL}^2 \tau - \omega_{\rm NL} k_y - (1+\tau) k_\parallel^2}{\tau k_\times^4}.$$

Note that the factor of $i\sqrt{8/\pi}$, which is critical to the determination of the linear frequency and therefore of the saturation level, comes directly from the Landau-damping model. Finally, upon substituting this expression into the real part of the nonlinear dispersion relation, one can solve for the nonlinear frequency, completing the calculation.

[2] In the later comparisons of this analysis with the numerically obtained saturation level, I have ignored the difference between the initial saturation level and the steady-state level.

7.1.2 Three-Mode-Coupling Simulations

Overview

Before proceeding to the actual comparisons, it is useful to outline exactly what is to be compared and what can be learned from each comparison. I will compare four descriptions of this simple system:

I. The three-moment quasilinear TMC theory outlined in Sec. 7.1.1,

II. Numerical simulations of the three-moment, three-mode gyrofluid model used in the TMC theory [Eqs. (7.6–7.10)],

III. Numerical simulations of more complete gyrofluid models [*e.g.,* Eqs. (2.63–2.69)], and

IV. Gyrokinetic (and drift-kinetic) particle simulations.

The level of agreement obtained between the first two items will be a measure of the validity of the quasilinear estimate presented in Sec. 7.1.1 but can provide no evidence regarding the validity of the Landau-damping model used in the original equations. Comparing I, II, and III allows one to understand the role additional moments play in a simple nonlinear problem, just as comparing the linear response function for different fluid models [see Figs. (2.1) and (2.2)] allows one to understand their role in the linear dynamics. Items III and IV contain three essential elements missing from I and II: (1) FLR effects, which should be weak since the instabilities being studied have $k_\perp \rho \ll 1$ but which could drive sheared velocity flows in the y direction if the $\Phi(x, k_y = 0)$ mode were not suppressed, (2) anisotropic temperature fluctuations, which should not affect the predictions of the TMC theory (since $k_\perp \rho \ll 1$) but which may dramatically alter the heat transport characteristics, and (3) a more complete Fourier representation for the moments/distribution function. The last point is potentially important, and should be explained carefully.

The TMC theory allows only the $(2, 0)$ Fourier component of the temperature to evolve. This places a limit on the amount of flattening of the background gradients that can occur. On the other hand, both the gyrokinetic particle simulations and the full gyrofluid simulations allow higher Fourier harmonics to appear in their respective descriptions of the perturbed distribution function. This allows, for example, the temperature gradient to flatten over a wider region of the simulation

domain. [This behavior is observed in both simulations.] At low resolution, the resolution of the grid in the x direction determines the maximum extent of this flattening, since the boundaries are felt by the plasma throughout the simulation domain. The nonlinear interactions that couple the potential to the $(m, 0)$ component of the temperature involve the $(m-1, 0)$ component of the temperature and the $(1, 1)$ component of Φ and are therefore not forbidden by the truncation of the Fourier representation of Φ. Because the amplitude of the $(2, 0)$ Fourier component of the temperature partially determines the saturation level in the TMC theory, it would not be surprising to see discrepancies arise between I and III or I and IV.

Good agreement between I and IV would constitute a demonstration of the validity of the Landau-damping model in at least one nonlinear scenario. Finally, agreement between the full gyrofluid simulation (III) and the gyrokinetic particle simulation would lend some credence to future results obtained using the kinetic models presented here (and to those produced by the `ITG` code in particular).

Results

For the simulations carried out to compare the fluid and particle codes to the theory, the basic parameters were $k_x\rho_i = k_y\rho_i = 0.1$, $\eta_i = 10$, $\tau = 1$, and $k_\parallel L_n = k_y\rho_i$. A scan of θ ($k_\parallel L_n$ at fixed $k_y\rho_i$) was also performed. The gyrofluid simulations[3] were performed on de-aliased $(n_x, n_y) = (32, 32)$ grids with $(L_x, L_y) = (31.4\rho_i, 62.8\rho_i)$.

[3]Because of the potential for confusion in comparing different simulation results, I describe here three ways to implement zero-flux boundary conditions. In the first method, one performs a simulation with a box width of L_x. However, one finds that in order to make use of standard FFT's one must double the real-space box length (and the number of real-space grid points) whenever a Fourier transform is to be evaluated. If a quantity $f(x)$ defined from $0 \le x < L_x$ is continued into the interval $L_x \le x < 2L_x$ with odd symmetry,

$$f(x + L_x) = -f(L_x - x), \tag{7.11}$$

the Fourier transform of the extended function is the desired sine transform. This method is often used in particle simulations (along with a reflection condition for the particles).

A second method is to simulate a domain twice as large, $L_x' = 2L_x$, with the odd symmetry condition enforced as in Eq. (7.11). In this case, one should distinguish between the physical simulation domain L_x and the simulation box width L_x'. Finally, one may also use the conventional Fourier decomposition [Eq. (7.5) without the factor of $-i$] in a simulation domain of width L_x and force all the fields to be zero at the edge. For large enough systems, I have found that these three methods yield the same result.

In this section, I used the first method.

In each case, all but the longest-wavelength Fourier components of the electrostatic potential were suppressed at every time step. Also, $\Phi(x, k_y = 0)$ was suppressed (as in the theory).

According to the preceding analysis, the linear frequency should be $\omega L_n/v_t = -0.11 + 0.075i$. Note that this implies that the Landau resonance is important, since $\zeta \sim 1$. The predicted saturation level is $|\Phi_1| = 6.4$ and the nonlinear frequency is predicted to shift 30% to $\omega L_n/v_t = -0.15$.

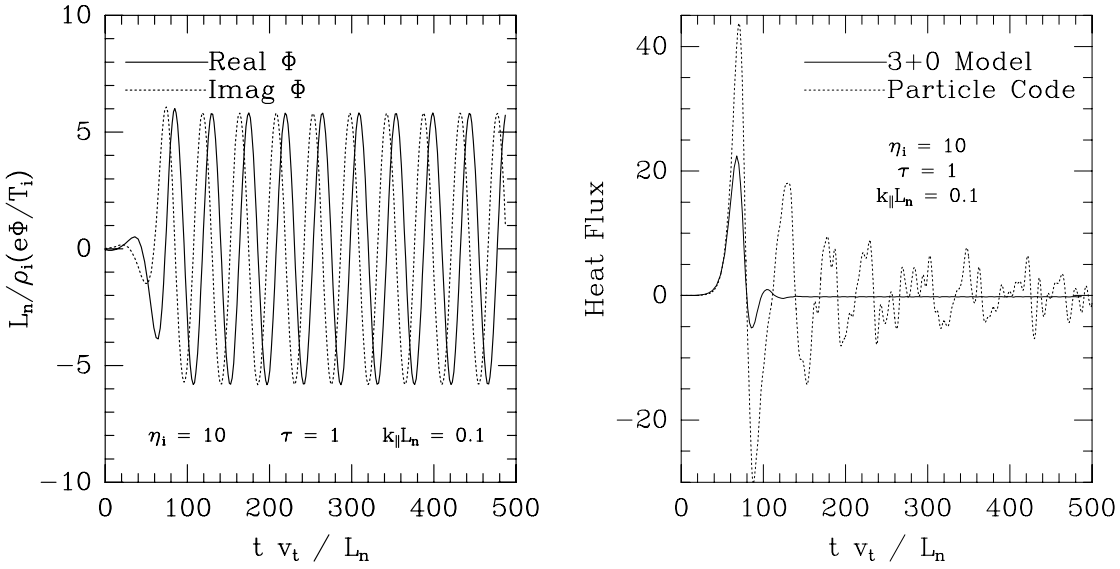

Figure 7.1: 3+0 three-mode simulation results (without FLR effects) for the three-mode-coupling calculation. Shown are (a) $\Phi_1(k_x\rho_i = 0.1, k_y\rho_i = 0.1)$ *vs.* time; and (b) the volume-averaged thermal flux *vs.* time for the parameters $\eta_i = 10$, $L_s = \infty$, $\tau = 1$, and $k_\parallel L_n = 0.1$.

Results from a three-mode, three-moment fluid simulation of Eqs. (7.1–7.3) are shown in Fig. (7.1). Only the Fourier modes retained in the TMC theory were kept in this simulation. The saturation level ($|\Phi| \sim 5.8$) and the nonlinear frequency shift $\omega = -0.14$ agree reasonably well with the estimates from the TMC theory (though the saturation predicted by the numerical code is smaller than expected). Thus, one can have some confidence that the TMC theory contains an element of the nonlinear dynamics in the most basic system. The volume-averaged radial heat flux [defined[4] in Eq. (B.1)] is shown in Fig. (7.1b) for comparison with more

[4]Actually, because the perpendicular temperature is not evolved in this simplest model, I have

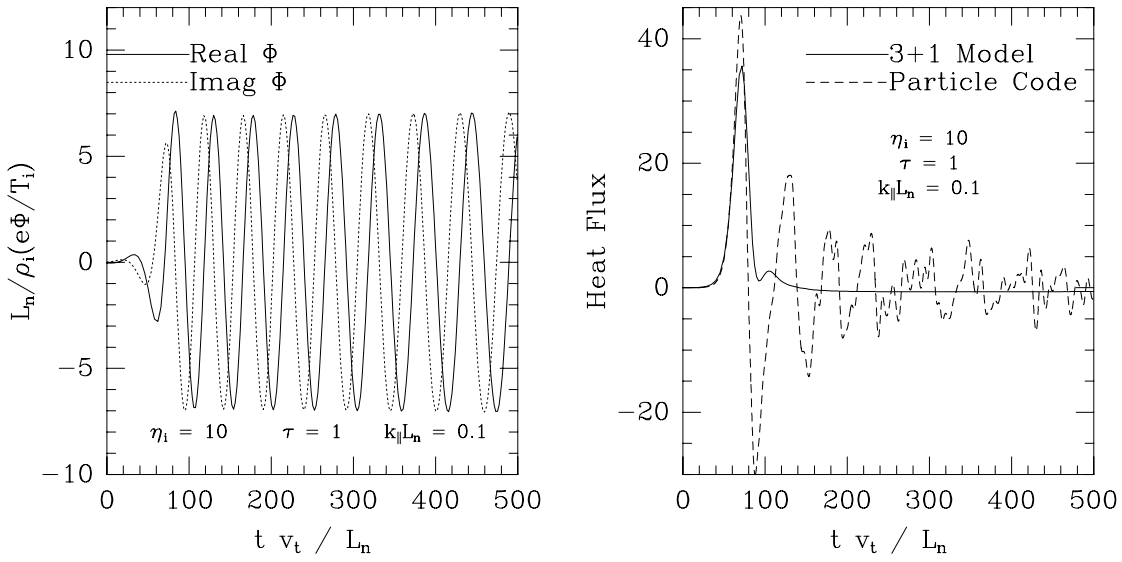

Figure 7.2: 3+1 gyrofluid simulation results (with full FLR effects) for the three-mode-coupling problem. Shown are (a) $\Phi_1(k_x\rho_i = 0.1, k_y\rho_i = 0.1)$ *vs.* time; and (b) the volume-averaged thermal flux *vs.* time for the parameters $\eta_i = 10$, $L_s = \infty$, $\tau = 1$, and $k_\parallel L_n = 0.1$.

complete models below. It clearly does not agree very well with the particle-code result shown in the same panel. More sophisticated simulations of the same physical system are now discussed to put into perspective the effects of the various kinetic models.

Saturation level. In Fig. (7.2) I show the results from a 3+1 gyrofluid simulation of Eqs. (2.70–2.73) for the same physical parameters and simulation domain as the previous case. There are three important differences between this model and Eqs. (7.6–7.10): FLR effects, anisotropic temperature fluctuations, and a larger Fourier basis set for the moments. As expected, the greatest impact on the initial saturation level was generated by the latter addition. Including additional Fourier modes in the moments retained caused the saturation amplitude to rise $\sim 25\%$, increasing to $|\Phi| \sim 7.2$ if the full resolution of the basic simulation domain is retained for the moments. Doubling the grid resolution in each direction to $(n_x, n_y) = (64, 64)$ resulted in no further shift. Including additional moments, FLR effects, and the

taken $Q_{3+0} = 3Q$ to account for the full temperature.

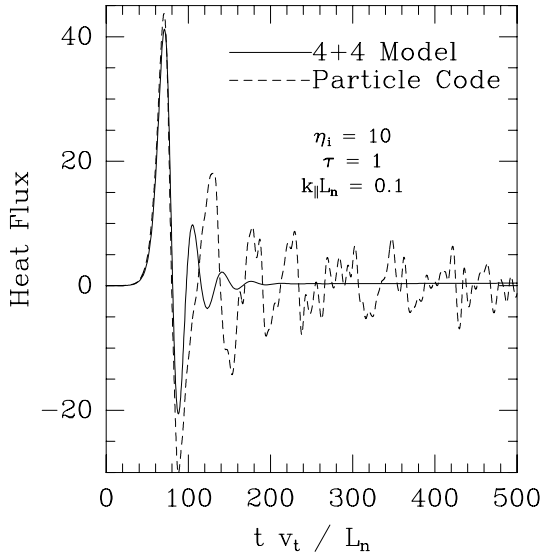

Figure 7.3: 4+4 gyrofluid simulation results for the three-mode coupling problem. Shown is the volume-averaged thermal flux.

NLPM models caused no significant changes in the saturation amplitude.

Thermal flux. As one employs increasingly complicated gyrofluid models, the dominant corrections to the thermal flux come from retaining the perpendicular moments ($T_\perp, q_\perp, etc.$). For example, one observes from Fig. (7.2) that retaining an equation for $T_\perp$ gives somewhat better agreement in the volume-averaged heat flux. The further improvement observable in Fig. (7.3) may be attributed entirely to the additional moments and confirms that retaining additional moments allows one to mimic the kinetic result more closely. Nevertheless, the gyrofluid thermal flux damps out more rapidly than the gyrokinetic thermal flux. I tried reducing the time step by a factor of two in both simulations and got the same answers. The particle-simulation flux appears to be getting noisy after $tv_t/L_n \sim 150$, but the low-frequency oscillations in the flux remain clearly discernible.

Complete gyrofluid model. The thermal flux predicted by full gyrofluid model results (item III above) are shown in Fig. (7.3). The 4+4 gyrofluid run shown here used the $\Gamma_0^{(1/2)}$ FLR model and included all of the Fourier modes in the moments. The NLPM model was used in this run, but its effect is very small since the dominant

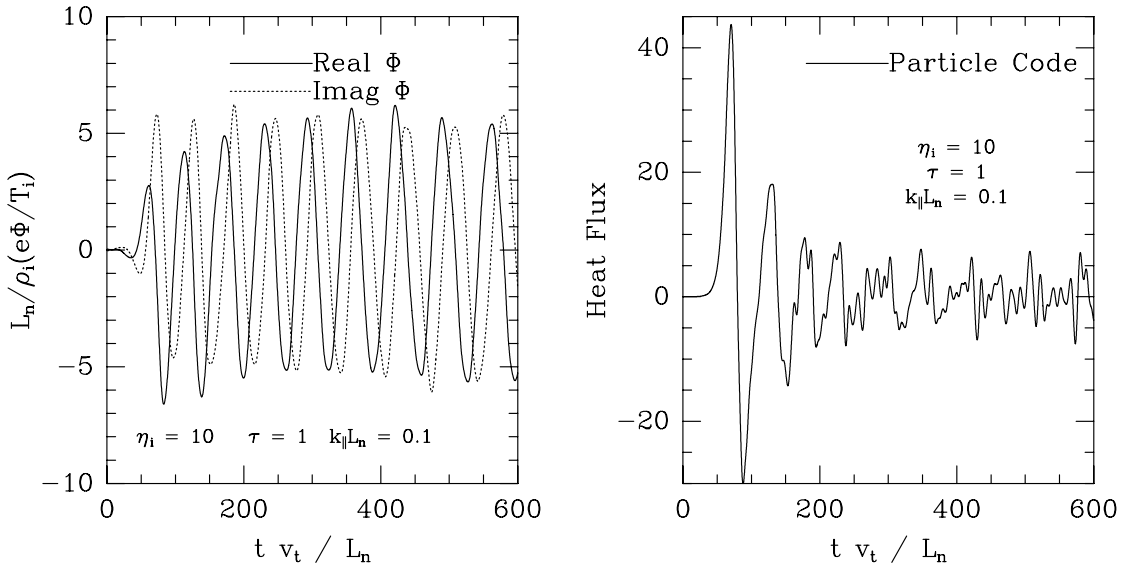

Figure 7.4: Gyrokinetic particle-simulation results for the three-mode-coupling calculation. Shown are (a) $\Phi_1(k_x\rho_i = 0.1, k_y\rho_i = 0.1)$ *vs.* time; and (b) the volume-averaged thermal flux *vs.* time for the parameters $\eta_i = 10$, $L_s = \infty$, $\tau = 1$, and $k_\parallel L_n = 0.1$.

modes are long-wavelength modes. The nonlinear frequency shift persists at a lower level in the full gyrofluid simulations: $\omega_{\rm NL} = -0.13$. The fact that the addition of FLR effects and anisotropic temperature fluctuations did not change the saturation amplitude or the frequency significantly compared to the three-mode, three-moment fluid model is easily understood, since the dominant modes are long-wavelength modes ($k_\perp\rho \sim 0.14$) and are therefore unaffected by the order $(k_\perp\rho)^2$ corrections.

Gyrokinetic particle simulation. Nonlinear particle-code results (representing the most fundamental and complete approach tried in this study for this problem) are shown in Fig. (7.4). The saturation level[5] $|\Phi| \sim 5$ is smaller than the numerically-obtained obtained TMC result [Fig. (7.1a)]. On the strength of the gyrofluid results, one might have expected to find a level 25% higher, since no filtering of the perturbed distribution function is undertaken in the particle simulation. The nonlinear frequency shift is small or non-existent. However, one may observe non-

[5]The gyrofluid and gyrokinetic simulations use opposite conventions for forward Fourier transforms, causing the real and imaginary parts of Φ to be reversed, as may be seen by comparing Figs. (7.4) and (7.1a).

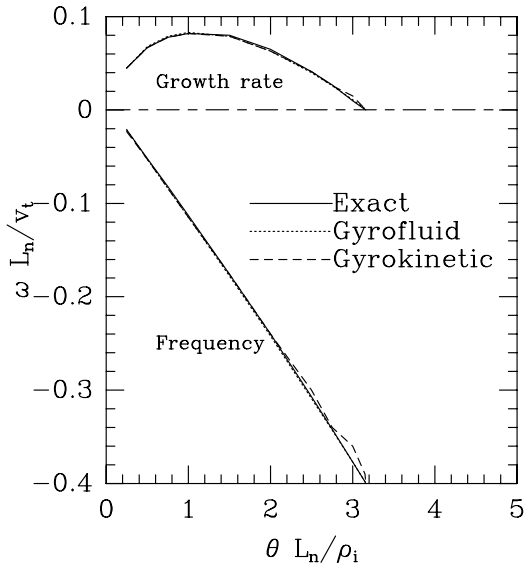

Figure 7.5: Linear frequencies and growth rates predicted by various models for the three-mode-coupling problem as a function of $k_\parallel/k_y$ with $\eta_i = 10$, $T_i = T_e$, and $k_x\rho_i = k_y\rho_i = 0.1$.

linearly generated beat waves in the particle simulation with frequencies comparable to the $\mathbf{E}\times\mathbf{B}$ rotation frequency that are not observed in the gyrofluid simulations.

Based on this comparison, one might conclude that the three-moment Landau-damping model performs adequately in this very simple nonlinear system, capturing at least enough information to estimate the saturation level within a factor of two despite the fact that $\zeta \sim 1$. However, in the next section, I show that the agreement between the gyrofluid and the gyrokinetic simulations is not as good as these results suggest for this highly simplified problem.

An Important Discrepancy?

Here, a possibly important shortcoming of the gyrofluid model is emphasized. A scan of $\theta = k_\parallel/k_y$ was undertaken to check the scaling of the saturation level with the amount of Landau damping compared to the linear drive. All other parameters remained the same as in the basic case. No FLR effects were retained in any of the simulations completed for this scan. Four different methods were used to obtain results: (1) the analytic TMC theory, (2) numerical simulations of the TMC

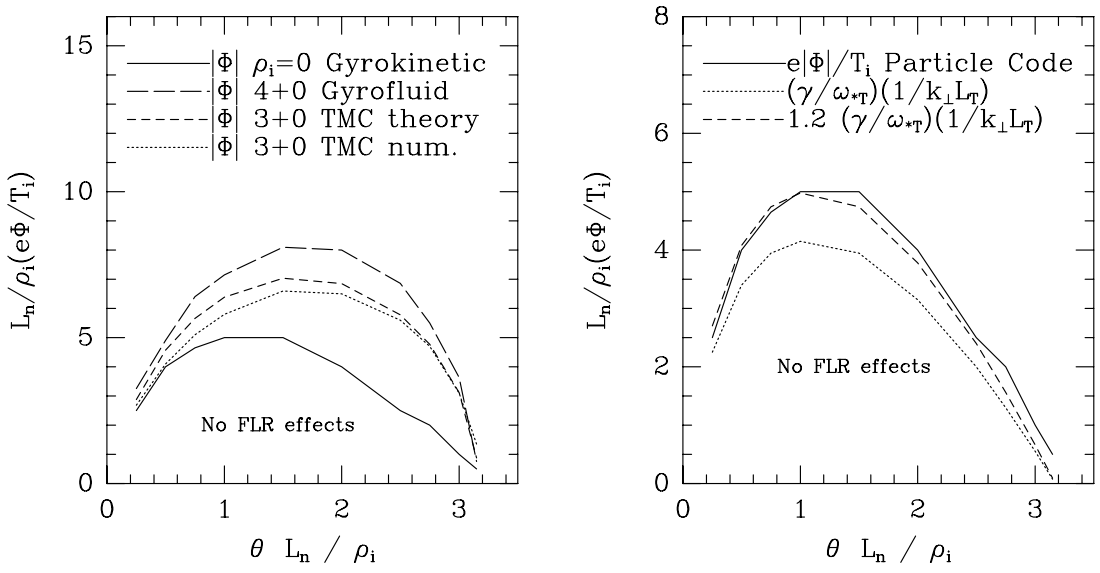

Figure 7.6: (a) Time-averaged saturation amplitude of $|\Phi_1(k_x\rho_i = 0.1, k_y\rho_i = 0.1)|$ *vs.* $k_\parallel/k_y$ for several different models of the three-mode-coupling problem with $\eta_i = 10$, $T_i = T_e$, and $k_x\rho_i = k_y\rho_i = 0.1$. (b) Simple quasilinear estimate for the saturation level observed in the particle simulations.

equations, (3) 4+0 gyrofluid numerical simulations, and (4) gyrokinetic particle simulations in the zero-gyroradius limit. The most important difference between (2) and (3) is again the number of Fourier components kept for the description of the distribution function/moments. The linear frequencies and growth rates predicted by these methods are shown in Fig. (7.5). The agreement is generally very good. Each of the models predicts that the most unstable modes have moderate $k_\parallel L_n$ and that the marginal stability point for modes with a short parallel wavelength is roughly $k_\parallel L_n = 3.15$. The nonlinear results shown in Fig. (7.6a) do not agree as well.

From this figure, one may see that the simple TMC theory agrees with the numerical solutions of Eqs. (7.6)–(7.10) for a range of values of $k_\parallel$. Recall that the TMC calculation of the saturation level was based upon the notion that the nonlinear flattening of the driving temperature gradient would serve to saturate the linear mode. The discrepancy between the curve labeled "4+0" and the curve labeled "3+0 TMC num." may be accounted for almost entirely by the fact the 4+0 simulations included a more complete Fourier description of the moments.

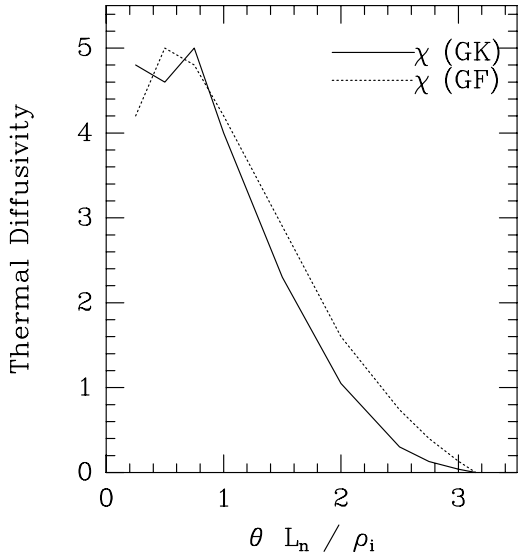

Figure 7.7: Peak thermal diffusivity *vs.* $k_\parallel/k_y$ for 4+4 gyrofluid and gyrokinetic simulations for the three-mode-coupling problem with $\eta_i = 10$, $T_i = T_e$, and $k_x\rho_i = k_y\rho_i = 0.1$. The thermal diffusivities agree better than the saturation levels of Φ.

That is, the effect of including the $\dot{q}_\parallel$ equation is small. Thus, the TMC theory appears to describe the fluid simulation results reasonably well. However, there is a discrepancy between the gyrofluid and particle-simulation results that is possibly important. For large enough $k_\parallel L_n$, each of the methods correctly predicts that the saturation amplitude decreases with the linear growth rate, yet for $\theta L_n/\rho > 1$, the particle code predicts a lower saturation level than both the TMC theory and the fluid simulation.

In Fig. (7.6b) I show an interesting result related to the particle-code saturation level. It appears that the variation of the saturation amplitude with $k_\parallel$ may be described by the simple formula (involving only linear quantities),

$$\frac{e|\Phi|}{T_i} \propto \frac{\gamma}{\omega_{*T}} \frac{1}{k_\perp L_T},$$

where $\omega_{*T} = \eta_i \omega_*$ and the constant of proportionality is roughly 1.2. The TMC theory presented in Sec. 7.1.1 fails to predict this scaling, since the TMC prediction for the saturation level does not depend on the linear growth rate. It is surprising that such a simple relation describes the nonlinear saturation level so well since the nonlinear behavior observed in the particle-code simulations appears complicated.

Physically, one could interpret this formula as implying that nonlinear saturation occurs in the particle code when the eddy turnover time $\omega_{\rm E}$ is comparable to the linear growth rate, or

$$k_\perp^2 \Phi \sim \gamma$$

in the dimensionless units used throughout this thesis. [A similar relation has been noted previously by LEE *et al.*, 1984 for the related electron drift-wave problem.] This interpretation is consistent with observed large-amplitude nonlinear oscillations of the electrostatic potential with $\omega_{\rm NL} \sim \omega_{\rm E}$. If this interpretation is correct, then one must conclude that the particle and fluid simulations have different nonlinear saturation mechanisms for this highly constrained case.

Although this is not a turbulent problem, it is possible that the discrepancy is related to the failings of few-moment gyrofluid models noted by MATTOR, 1992. Because $\gamma \ll \omega$ and $\omega \sim k_\parallel v_t$ in this region of parameter space, one might expect a few-moment fluid model to predict the saturation level poorly. That is, when the growth rate of the instability is slow compared to the frequency, information travels up the fluid hierarchy rapidly and feels the effects of the closure more strongly. This can result in a distortion of the slower nonlinear dynamics [HAMMETT *et al.*, 1993]. [One way to investigate this problem further would be to utilize the n-moment closures (where n is large) of SMITH and HAMMETT, 1993. Because there are no complicating FLR effects in this simple problem, one would need only to add the $\mathbf{E} \times \mathbf{B}$ nonlinearities and the driving terms to the equations of SMITH and HAMMETT, 1993 to proceed.] However, MATTOR, 1992 also noted that the heat flux predicted by the gyrofluid equations differed from the kinetic prediction by a factor of $(\omega/\sqrt{2}k_\parallel v_t)^2$ in the problem he was investigating. In the present problem, one may see from Fig. (7.5) that $|\omega| \sim k_\parallel v_t$ for the entire range of $k_\parallel$ considered in this scan. Thus, one might expect the thermal diffusivities observed in the two simulations to be in better agreement than the saturation level. This is in fact the case, as may be seen in Fig. (7.7). The initial[6] peak thermal diffusivities observed for different values of θ are shown here. The simulations used for this figure included FLR effects; the gyrofluid model used was the 4+4 model without NLPM terms. As before, the saturation levels do not change if one includes the FLR effects for these parameters because $k_\perp \rho = 0.14$ for the dominant modes. Including the

[6] As in the cases shown in Figs. (7.3), the gyrofluid thermal flux decays more rapidly than is observed in the particle simulation for these parameters.

perpendicular moments does change the thermal flux significantly for the reasons outlined above.

The overall impact of the discrepancy noted in Fig. (7.6a) may be smaller in a (more realistic) three-dimensional setting for four reasons. First, in this highly constrained problem there is only one eddy in the simulation domain. In a strongly turbulent problem, eddies are formed and destroyed rapidly so that particles are unlikely to become trapped long enough to significantly affect the dynamics. Second, there is a much stronger nonlinear saturation mechanism available if one allows the $k_\parallel = 0$ component of the potential to evolve, as discussed in Chap. 8. Neither quasilinear profile flattening nor particle trapping is likely to be relevant if velocity shear is allowed to develop naturally. Third, the (more interesting) heat flux predicted by the two simulations agrees reasonably well even though the saturation mechanisms are apparently different. Finally, the modes likely to dominate in a system with a range of parallel wavenumbers are the modes with the largest growth rates and the largest saturation amplitudes. For the parameters used here, the agreement between the fluid and particle simulations is not bad in the region around $\theta \sim 1$, where the growth rate is largest. In particular, the predicted heat flux agrees well. The gyrofluid model overestimates the saturation level in general, but correctly predicts stabilization above $k_\parallel L_n \simeq 3$.

Overall, the agreement found between the particle-code simulation and the full gyrofluid simulations is encouraging. I now turn to a more turbulent, sheared system.

7.2 Sheared Slab, Single Helicity

To date, published results from sheared-slab particle simulations have not employed radially periodic boundary conditions, although Kotschenreuther has described this scheme publicly [Kotschenreuther, 1991]. Thus, an important factor in determining the character of the saturated state of these simulations is the coupling of the pressure fluctuations to the background gradients, as discussed above. For the reasons outlined in Chap. 1, the coupling of the potential fluctuations to the background electric field is usually suppressed, so that the comparable dynamics involving gradients in the electric field are not present. In the interest of compari-

son I adopt these conventions, and extend the comparison to include the effects of magnetic shear.

Basic Parameters. The basic gyrofluid run for these comparisons used the following parameters: $\eta_i = 4, L_s/L_n = 4, \tau = 1, L_x = 25.6\rho_i, L_y = 12.8\rho_i$. The nonlinear terms were evaluated on a grid with $(n_x, n_y) = (64, 32)$ grid points. The linear terms were advanced in (x, k_y) space with lower resolution in k_y (because of the de-aliasing described in Chap. 6). They were calculated with $k_y = 2\pi m/L_y$, $m = 0, 1, \ldots, M$, $M = 8$. Sine transforms were used in the x direction whenever no-flux boundary conditions were employed [$\Phi(x = 0) = \Phi(x = L_x) = 0$]. They were implemented by using a box of width $2L_x$ along with Eq. (7.11) to evaluate the FFT's. The highest k_x retained (not suppressed[7]) was $n_x\pi/(2L_x)$. In accordance with the particle simulations, $\Phi(x, k_y = 0) = 0$ was enforced. The time step was $\Delta t = 0.05L_n/v_t$, and the equations were advanced explicitly in time. No special action was taken with respect to the $(x, k_y = 0)$ component of the pressure, which was consequently allowed to relax. The nonlinear phase-mixing model was employed, and numerical dissipation (when noted) was introduced into the equations by letting

$$\frac{dW}{dt} \to \frac{\partial W}{\partial t} + \mathbf{v}_\Psi \cdot \nabla W - \nu \nabla_\perp^2 W$$

in each equation except for the density, where the added term is taken to be $-\nu\nabla_\perp^4 n$ to reflect the fact that there is no particle diffusion introduced by classical collisions between like particles. Typically, for two- and three-dimensional runs, $\nu = 0.005 v_t/L_n$.

The particle code [SANTORO and LEE, 1990] is a partially linearized, or δf gyrokinetic code. The physical parameters $(\eta_i, L_n/L_s, \tau)$ and the simulation domain (L_x, L_y) were chosen to match the fluid code. The grid used was $(n_x, n_y) = (64, 32)$ grid points. The potential Φ was filtered exactly as in the fluid code. That is, during the field solve, Fourier components of Φ that correspond to $k_x > n_x\pi/(2L_x)$ or $k_y > 2M\pi/L_y$, $(M = 8)$ were zeroed out. The grid spacing, time step, and boundary

[7] Zeroing the highest k_x's of the grid (de-aliasing) is described in more detail in Chap. 6 and is carried out for all of the fields. Note that this implies that higher radial grid resolution would be required in the gyrofluid simulation to do a rigorous comparison, since the particle simulation distribution function is not filtered at every time step. To check this, I did some runs with twice the resolution using the gyrofluid code and obtained similar (though quieter) results. For more details, see App. B.

conditions were exactly as in the fluid code. Also, $\Phi(x, k_y = 0) = 0$ was enforced. Gaussian-shaped finite-size particles were tried, but slowed the convergence in the number of particles. This may be related to the fact that the linear eigenmodes for these physical parameters are highly localized around the rational surface; see Fig. (7.8). The linear eigenmodes in transform space are therefore broad. One needs good resolution above $k_x\rho = 1$ to resolve the linear physics and a filter of the form $\exp\{-(k_\perp a)^n\}$ makes this difficult. Nonlinearly, the $\Phi^2(k_\perp)$ spectrum is narrower but still non-negligible for $k_\perp\rho \gtrsim 1$. For these parameters, I found that 512K particles yielded a reliable answer (no discernible difference in the heat flux from a 2M particle run) with eight-point averaging [Lee, 1987]. More than thirty runs were carried out to test the convergence of the particle simulation in the number of particles, radial resolution (determined by the particle shaping for the given number of grid points), and the time step. Neither the aspect ratio (L_x/L_y) of the simulation domain, nor the resolution in the y direction, nor the number of radial grid points was altered for this study.

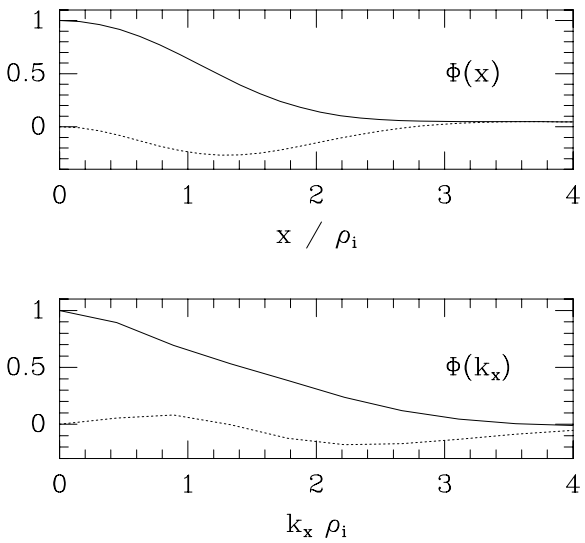

Figure 7.8: (a) Fastest-growing linear eigenmode for the physical parameters $\eta_i = 4.0$, $k_y\rho_i = 0.5$, $\tau = 1$, $L_s = 4L_n$. Because the mode is localized in x space, the Fourier transformed potential is broad in $k_x\rho$.

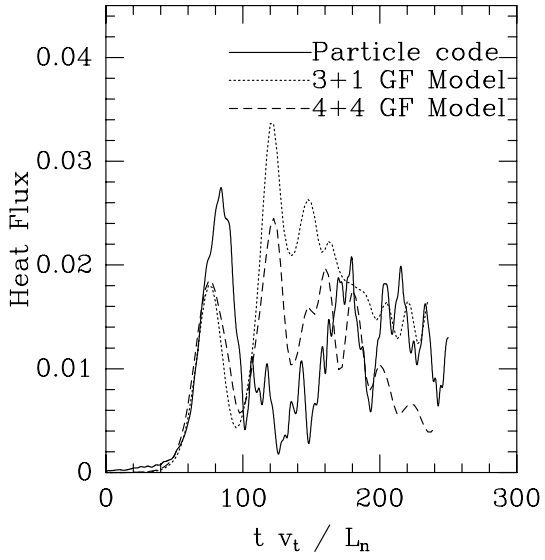

Figure 7.9: Thermal flux for single-helicity simulations with $\eta_i = 4$, $\tau = 1$, $L_s = 4L_n$. Particle simulation compared to 3+1 and 4+4 gyrofluid simulations with $\nu = 0.005$.

Results. Qualitatively, the results from the particle and fluid simulations are similar. Fig. (7.9) compares the time traces of the volume-integrated heat fluxes (defined below) from the two codes. The units between the two codes are consistent with the normalizations and units used throughout this thesis. [I took $\rho_i = L_n$ in the partially linearized particle code, effectively changing the usual (Ω_c) time normalization used in particle simulations to my (v_t/L_n).] Both codes show phases of exponential growth and saturation. Although the gyrofluid models fail to recover the initial peak in the thermal flux, the average thermal fluxes are generally the same level.

The initial peak is an artifact of the resolution used in the x direction, and is indicative of a nonlinear process that occurs at high $k_x\rho$. Support for this claim is provided by Figs. (7.8) and (7.10). The former figure indicates that the linear physics for these parameters may be described with a maximum $k_x\rho$ of at least 3. Thus, further increases in resolution should not change the linear results. On the other hand, the latter figure indicates that as one increases the resolution in the x direction by a factor of four, from a mesh with $(k_x\rho)_{\rm Max} = 3.9$ to a mesh with $(k_x\rho)_{\rm Max} = 15.7$, the initial peak disappears. The nonlinear process responsible for the saturation in this case in the flattening of the background temperature gradient

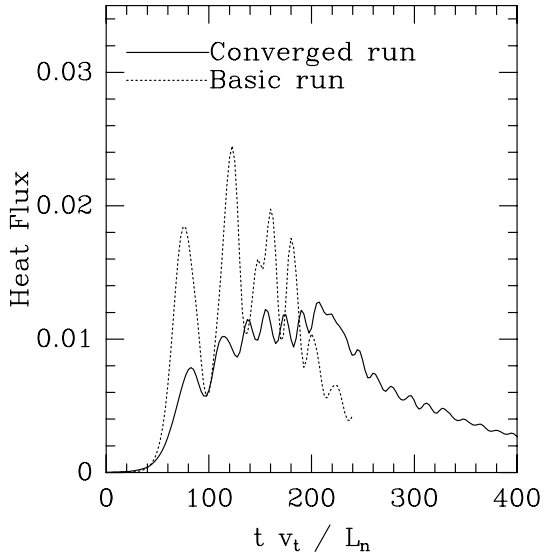

Figure 7.10: Thermal flux for single-helicity simulations with $\mathrm{Max}(k_x\rho) = 4$ ("Basic run") and $\mathrm{Max}(k_x\rho) = 15$ ("Converged run"). 4+4 Gyrofluid model with $\eta_i = 4$, $\tau = 1$, $L_s = 4L_n$, and $\nu = 0.005$.

through the evolution of the $T_{\parallel,\perp}(x, k_y = 0)$ modes, first in the region of the rational surface and later across the majority of the simulation domain. The high-resolution mesh allows the gradient to flatten more rapidly in the region of the rational surface, reducing the initial peak. The resultant steepening of the gradient near the edges of the domain[8] does not destabilize the system since there are no rational surfaces in this region. Because the dynamics of this system are dominated by the effects of the relaxation of the temperature profile (as argued in more detail below), comparisons of the heat flux *vs.* time are difficult to interpret. More detailed comparisons of the profile-relaxation dynamics should instead measure the time-integrated heat flux *vs.* time.

The level of thermal flux observed after the initial transient eventually falls to approximately zero in the gyrofluid simulation. I did not investigate the final state of the gyrokinetic particle simulation because of time constraints. For reference, the particle result (through $t = 250L_n/v_t$) used 2.5 hours on the NERSC C-90 Cray A-machine, while the equal-resolution 4+4 gyrofluid run (through $t = 500L_n/v_t$)

[8] As in Chap. (6), the average temperature gradient is not observed to change, although the local temperature gradient does vary.

required 15.5 CPU minutes on the same machine (approximately 20 times faster).

Allowing the background profiles to relax thus allows for "quasilinear" saturation (though this is potentially confusing nomenclature, it is the standard way of referring to the relaxation of the driving gradients and possibly can be traced back to GALEEV and SAGDEEV, 1984), rather than "nonlinear" saturation. While this argument is borne out by more detailed diagnostics in the gyrofluid simulation, the easiest way to show the impact of the quasilinear flattening is to force the $(x, k_y = 0, k_z = 0)$ components of each of the moments to be zero at every time step. For these parameters, one finds that the thermal flux reaches a steady-state level approximately fifty times larger than if the temperature profiles are allowed to relax, as shown in the next section.

7.3 Single Helicity, Turbulent Saturation

The fluid representation allows one to model the effects of strong sinks and sources trivially. For example, if one assumes that the heat source is strong enough to keep the background gradient fixed, then one can mimic this effect by suppressing the $(x, k_y = 0, k_z = 0)$ component of the pressure at every time step [HAMAGUCHI and HORTON, 1990]. To be consistent, one should also suppress the $(x, k_y = 0, k_z = 0)$ component of the remaining fields as well. Surprisingly,[9] one is thus able to recover the saturation level and thermal diffusivity predictions of a three-dimensional simulation *without* retaining multiple rational surfaces. The implications of this finding are perhaps profound and certainly useful. First, however, I present some evidence for this claim. There is one important caveat: the results of this section are very recent and consequently not as well documented as the results in the remainder of this thesis, nor as well understood. More investigation in this area is needed, especially in light of the possible savings in computational resources.

Simulation parameters. The physical parameters used in the basic simulation were $\eta_i = 4$, $L_n/L_s = 0.25$, and $T_i = T_e$. Runs with two different grids are shown here. The first (lower resolution) grid was $(n_x, n_y) = (64, 32)$ and the second

[9] It is surprising in the sense that it is a simple and powerful finding that to my knowledge has not been reported in the literature.

(higher resolution) grid was $(64, 128)$. The simulation domains had dimensions $(L_x/\rho, L_y/\rho) = (12.8, 50.2)$ and $(12.8, 69.1)$ respectively. The maximum $k_y\rho$ components of Φ retained were $k_y\rho = 1.0, 2.9$ respectively. The maximum $k_x\rho$ components of Φ retained were $k_x\rho = 7.9$ in each case. Sine transforms with 128 grid points were used over the $2L_x$ domain whenever Fourier transforms were utilized in the radial direction. No-flux boundary conditions were used. Finally, the 3+1 model was used with and without the NLPM terms, and the numerical diffusion coefficient was $\nu = 0.005$.

The particle simulation used a three-dimensional grid with $(n_x, n_y, n_z) = (128, 128, 64)$ and 4M particles. Four-point averaging [LEE, 1987] was utilized. The simulation domain had dimensions $(L_x/\rho, L_y/\rho, L_z/L_n) = (51.2, 51.2, 25.6)$. The highest $k_x\rho$ components of Φ retained were those with $k_x\rho \sim 1.5$.

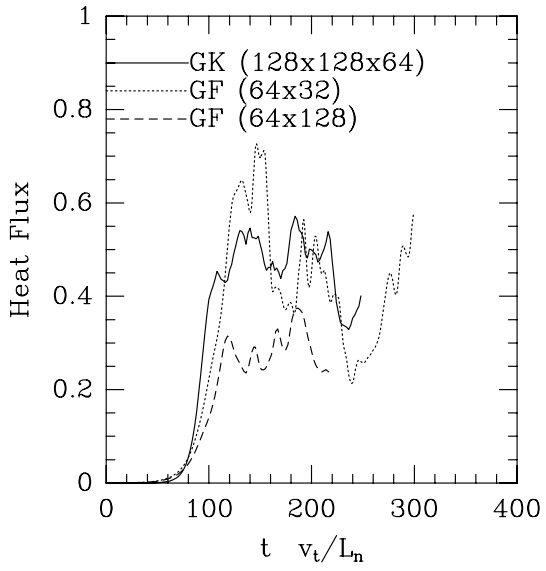

Figure 7.11: Thermal flux *vs.* time for 3D gyrokinetic and 2D (3+1) gyrofluid simulations with $\eta_i = 4$, $\tau = 1$, $L_s = 4L_n$. In the gyrofluid simulations, the $(k_y = 0)$ components of *all* fields were suppressed to prevent flattening of the background gradients. In the gyrokinetic simulation, the $(k_y = 0, k_z = 0)$ component of the electrostatic potential was suppressed.

In the 2D gyrofluid simulation, the steady state is characterized by $\mathbf{E} \times \mathbf{B}$ coupling of unstable modes to modes stabilized by Landau damping (large $k_\parallel L_n$), since the relaxation of the background gradients is explicitly prohibited. The ther-

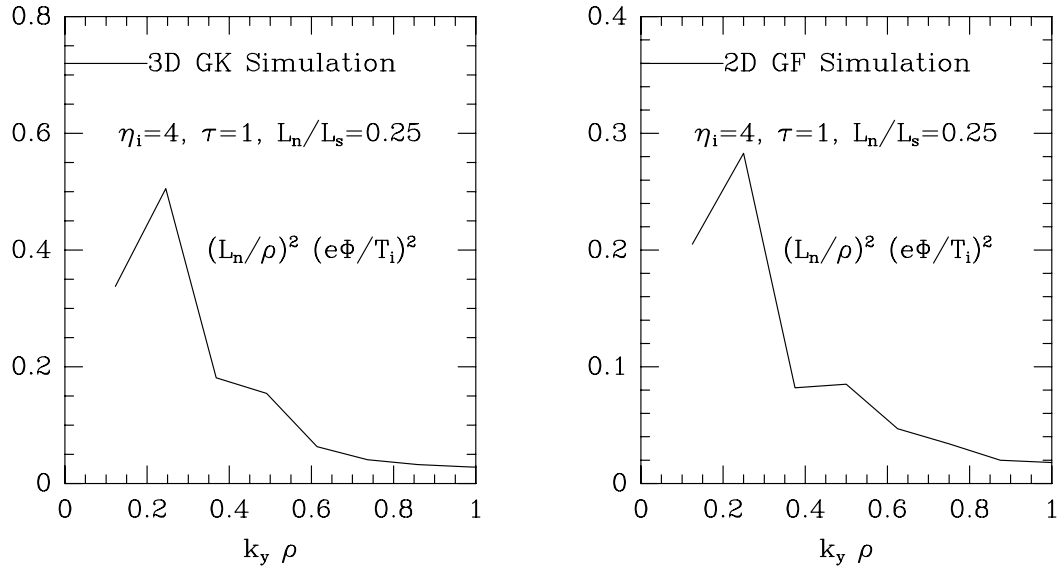

Figure 7.12: A comparison of the spectra of Φ^2 from a 2D, 3+1 gyrofluid simulation (with the $k_y = 0$ components of *all* fields suppressed to prevent flattening of the background gradients.) and a 3D, gyrokinetic simulation with the same physical parameters and with the $(k_y = 0, k_z = 0)$ component of the electrostatic potential suppressed. The fastest-growing modes have $k_y\rho = 0.5$ and are responsible for the "knee" visible in the spectrum. Note the difference in the overall level.

mal flux predicted by the different simulations is shown in Fig. (7.11). There is a factor of two difference in the thermal flux level between the two gyrofluid simulations, attributable to the difference in y resolution. Thus, one should take these results with a grain of salt until full convergence studies are shown. In addition to the resolution in the y direction, there are difficulties of interpretation in the x direction. That is, since there is only a single rational surface with a band of turbulence that does not extend indefinitely, one can make the volume-averaged heat flux as small as one wishes simply by taking the simulation domain to be very large in the x direction. It does not appear to be true, however, that one can make the fluxes larger by making the simulation domain smaller; there is an upper limit to the thermal flux transported across the rational surface, realized for a box size comparable to the linear mode widths for the parameters one is investigating.

In Fig. (7.13a) I show the scaling of the 2D thermal diffusivity with the shear parameter L_n/L_s. The error bars indicate the range of values I have obtained. I

have not rigorously shown that the 2D simulations converge as the resolution is increased. That the trend is comparable to that shown in Fig. (7.14) below is encouraging, however.

These results [summarized in Fig. (7.13b)] indicate that the principal difference between conventional two- and three-dimensional sheared-slab simulations of ITG turbulence is in the nonlinear saturation mechanism, and that one may recover three-dimensional results with a two-dimensional simulation by disallowing quasilinear flattening of the driving gradients. That is, ITG turbulence in a sheared magnetic field (without curvature) is perhaps fundamentally two-dimensional. If a similar result holds in a curved magnetic geometry, one could conceivably simulate a tokamak discharge with an order of magnitude less computational resources than presently estimated. However, there are reasons to doubt that this will come to pass. Most importantly, the effects of local modifications to the background gradients are important to the determination of the evolution of sheared flows, which may be an important source of stabilization in a toroidal configuration [Beer *et al.*, 1992].

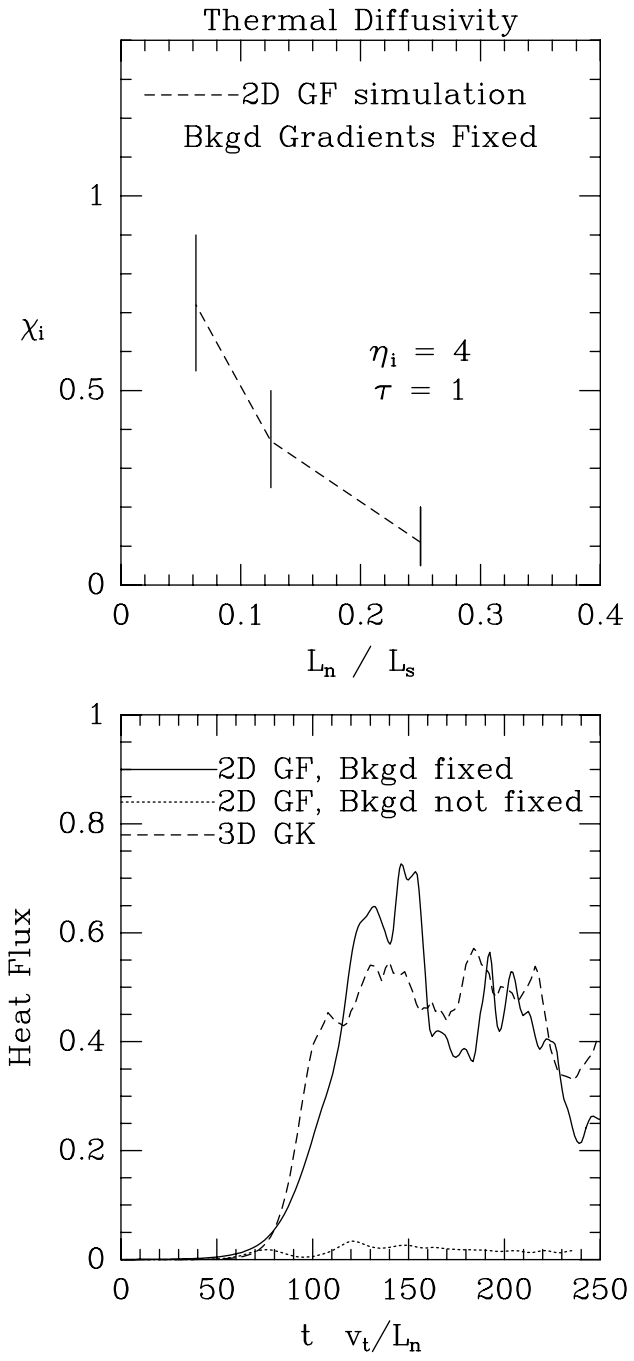

Figure 7.13: (a) Thermal diffusivity χ from 2D, 3+1 gyrofluid simulations with $\eta_i = 4$, $\tau = 1$, $L_s = 4L_n$. The $k_y = 0$ components of *all* fields suppressed to prevent flattening of the background gradients. (b) Thermal flux of 2D and 3D simulations compared.

7.4 Sheared Slab, Multiple Helicity

The most relevant benchmark presented in this chapter is the nonlinear, fully three-dimensional, sheared-slab comparison below. Two-dimensional simulations with and without magnetic shear are quickly saturated by quasilinear flattening of the driving gradients unless sources and sinks are included. While this is a relevant local effect, it is not characteristic of the evolution of tokamak plasmas in general. That is, one does not observe flattening of the pressure profile across the entire minor radius of a tokamak discharge in the presence of (what may be) ITG turbulence. With enough rational surfaces to fill one's simulation domain, one can begin to simulate the more realistic features of the turbulence problem. As noted in Chap. 6, one may enforce radial periodicity to overcome the problems associated with profile modifications that extend across the entire simulation domain. Here, this refinement is not pursued. Measurements of the diffusivities are taken before significant flattening across the majority of the domain occurs. Furthermore, sheared-velocity flows are suppressed. Nevertheless, the results are indicative of general convergence in the physical description of turbulent saturation. Three-dimensional simulations of more relevant geometries have been undertaken, [Beer *et al.*, 1992; Hammett *et al.*, 1993; Waltz, 1993; Parker *et al.*, 1993] but the question of the accuracy of the gyrofluid techniques in strongly turbulent settings remains unanswered. Here I present the first concrete evidence of the relevance of gyrofluid simulations of tokamak microturbulence.

The physical parameters used for these comparisons are $\eta_i = 4$, $\tau = 1$, and a varying magnetic shear length. The gyrokinetic simulation used $(n_x, n_y, n_z) = (128, 128, 64)$ with $(L_x/\rho_i, L_y/\rho_i, L_z/L_n) = (51.2, 51.2, 25.6)$. Fourier harmonics of the electrostatic potential characterized by $k_y\rho_i > 1$ or $k_x\rho_i > 1.5$ were suppressed along with the $(x, k_y = 0, k_z = 0)$ component. No-flux boundary conditions were used, and sine transforms (with $2n_x$ grid points) over a domain of width $2L_x$ were employed in the x direction. The time step was $\Delta t v_t/L_n = 0.125$.

Nonlinear terms in the gyrofluid simulations were evaluated on a grid with $(n_x, n_y, n_z) = (128, 32, 64)$. The lower resolution in the y direction should not be important, since there is little fluctuation energy above $k_y\rho \sim 1$, and since the potential is resolved equally well in the two simulations. The physical dimensions of the box, filters for Φ, and boundary conditions were the same as used for the

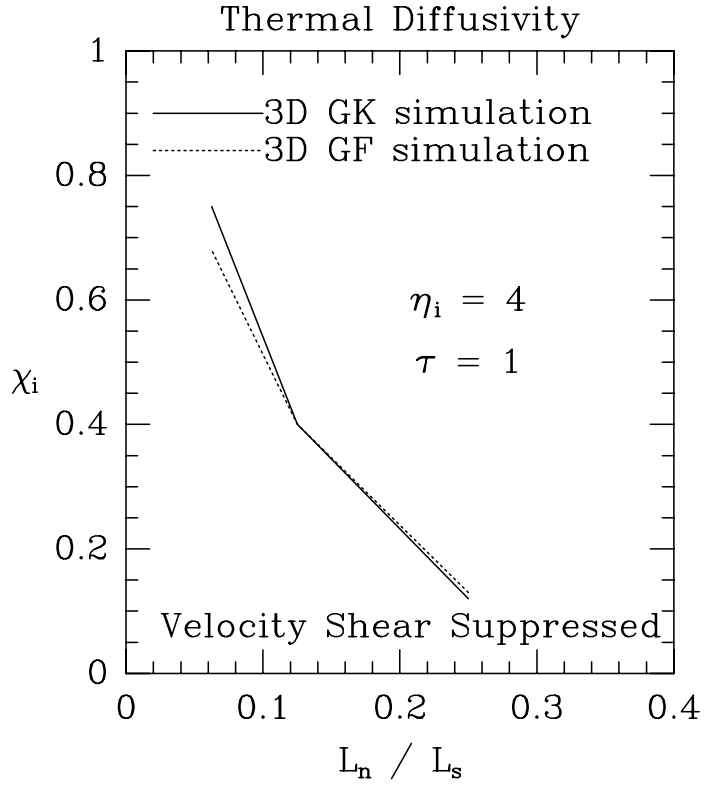

Figure 7.14: Comparison of χ from 3+1 gyrofluid and particle simulations with $\eta_i = 4$ and $\tau = 1$. (Each simulation with the $(k_y = 0, k_z = 0)$ components of Φ suppressed to prevent velocity-shear damping.)

particle simulation. The average nonlinear time step was $\Delta t v_t/L_n = 0.04$. The 3+1, $\Gamma_0^{1/2}$ model was used for all of the 3D simulations. For these runs, $\nu = 0.005$.

In Fig. (7.14) I compare the predicted thermal diffusivity (χ_i) from the two simulations as the magnetic shear length is changed. The agreement is excellent despite the fact that $\langle k_\parallel v_t/\omega\rangle \sim 1$, $\langle k_\perp \rho\rangle \sim 1$ and $(L_n/\rho)e\Phi/T \sim 1$. Either of the first two conditions is considered sufficient to render the straightforward fluid approach inapplicable. The final two conditions imply that the nonlinear phase-mixing terms may be significant; however, if they are ignored the resulting predictions for χ differ only by <10% [see Fig. (7.15)]. This may be attributed to the strong filtering of the potential at each time step. In an unfiltered system, nonlinear phase-mixing reduces the high-$k_\perp\rho$ oscillations most strongly. There is somewhat less noise when the NLPM terms are retained (as expected) but it is not clear from these comparisons if the additional time required to compute the NLPM terms is cost-effective

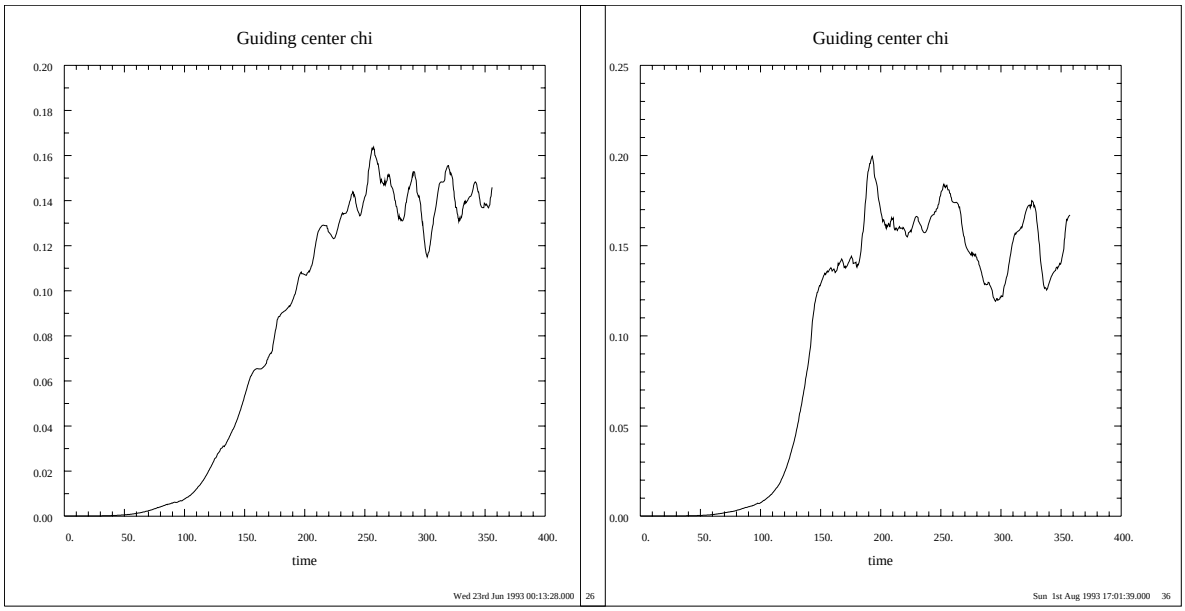

Figure 7.15: Gyrofluid thermal diffusivity (a) with NLPM and (b) without NLPM *vs.* time for filtered multiple-helicity simulations with $\eta_i = 4$, $\tau = 1$, $L_s = 4L_n$.

in this setting. In particular, the scaling of the thermal heat flux with the magnetic shear length does not appear to depend strongly on the NLPM terms. The thermal diffusivity varies by a factor of seven as the shear length varies between $L_n/L_s = 0.25$ and $L_n/L_s = 0.0625$. This variation is recovered by both simulations.

The spectra of the potential fluctuations are shown in Fig. (7.17). Note that the peak in the spectrum occurs for $k_y\rho_i \sim .2$, even though the fastest-growing mode is located at $k_y\rho = 0.5$. For longer simulations, one may find that the peak of the spectrum shifts to the longest "poloidal" wavelength ($k_y\rho_i = 0.13$ in this case) in the box. As a function of $k_x\rho$, the fluctuations in general have shorter wavelengths, as may be seen from Fig. (7.18). Some contour plots of the fields at the end of the weak-shear ($L_n/L_s = 0.0625$) gyrofluid run are shown in Figs. (7.19)–(7.21). One may see evidence of flattening of the temperature gradient across the system from Fig. (7.21), indicating that one should consider periodic boundary conditions.

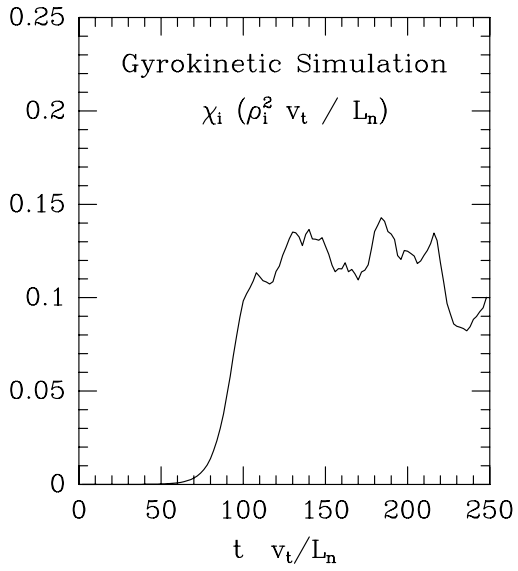

Figure 7.16: Gyrokinetic thermal diffusivity *vs.* time for multiple-helicity simulation with $\eta_i = 4$, $\tau = 1$, $L_s = 4L_n$.

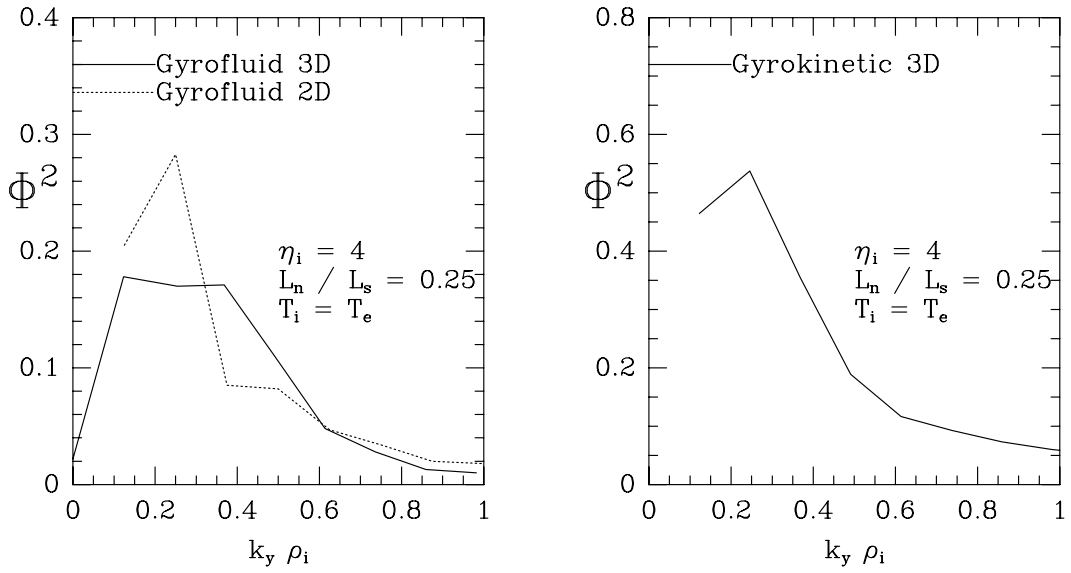

Figure 7.17: $\Phi^2(k_y\rho_i)$ for multiple-helicity simulations with $\eta_i = 4$, $\tau = 1$, $L_s = 4L_n$. Shown are gyrofluid and gyrokinetic simulation results with the $(k_y = 0, k_z = 0)$ components of Φ suppressed to prevent velocity-shear damping. In each case, the time average was performed over the nonlinear phase of the simulation. Note the difference in overall level.

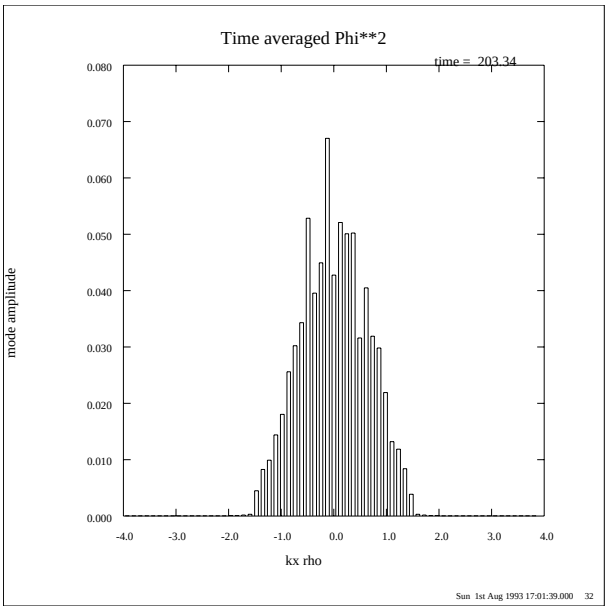

Figure 7.18: $\Phi^2(k_x\rho_i)$ from the gyrofluid simulation with $\eta_i = 4$, $\tau = 1$, $L_s = 4L_n$. The truncation of the potential above $k_x\rho_i = 1.5$ may be clearly seen.

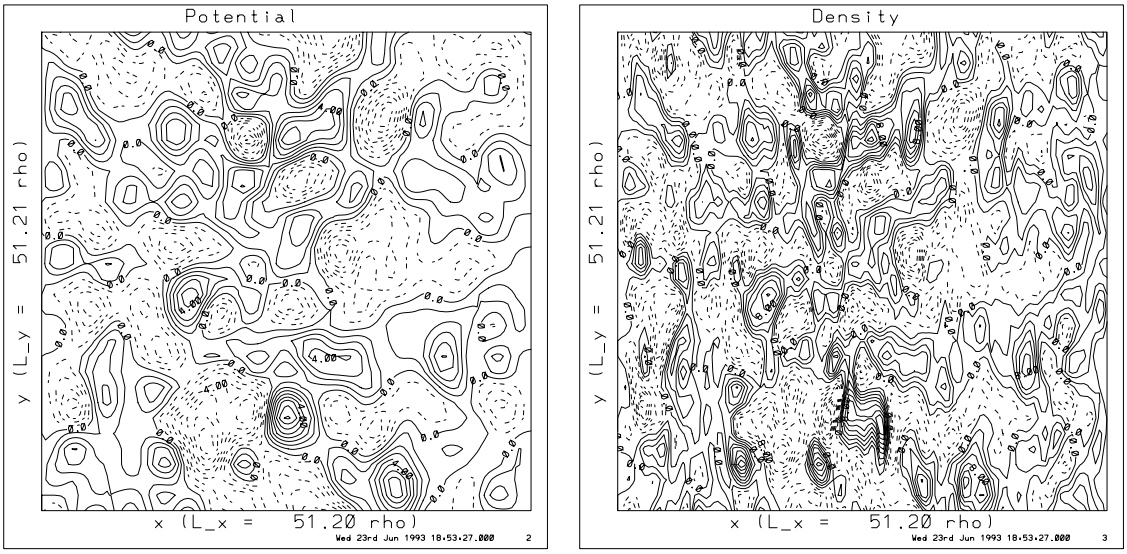

Figure 7.19: Contours of (a) Φ and (b) density for multiple-helicity simulation with $\eta_i = 4$, $\tau = 1$, $L_s = 16L_n$. From a 3+1 gyrofluid simulation with the $(k_y = 0, k_z = 0)$ component of Φ suppressed to prevent velocity-shear damping.

Figure 7.20: Contours of $u_\parallel$ for multiple-helicity simulation with $\eta_i = 4$, $\tau = 1$, $L_s = 16L_n$. From a 3+1 gyrofluid simulation with the $(k_y = 0, k_z = 0)$ component of Φ suppressed to prevent velocity-shear damping.

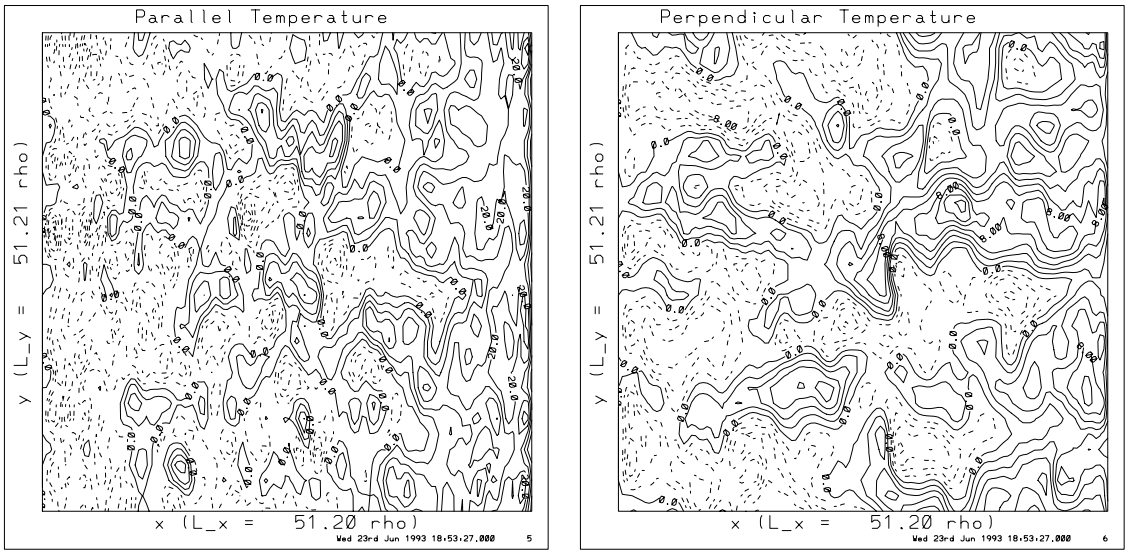

Figure 7.21: Contours of (a) $T_\parallel$ and (b) $T_\perp$ for multiple-helicity simulation with $\eta_i = 4$, $\tau = 1$, $L_s = 16L_n$. From a 3+1 gyrofluid simulation with the $(k_y = 0, k_z = 0)$ component of Φ suppressed to prevent velocity-shear damping.

Chapter 8

Nonlinearly Generated Velocity Shear

THAT PLASMA TURBULENCE may generate sheared flows that tend to be stabilizing is not a new concept.[1] However, the simulation results presented in this chapter (and previously [DORLAND *et al.*, 1992b]) were among the first [BEER *et al.*, 1992; DIMITS, 1992] to show that turbulence characteristic of the core (as opposed to the edge) of a tokamak discharge could likely behave in this way. Before showing the results, a short description of correct treatment of the quasineutrality constraint is presented (including the likely ramifications).

8.1 Adiabatic Electrons

An adiabatic electron response of the form $n_{e1} = n_0 e\Phi/T_e$ is often assumed for many types of tokamak instabilities [DIMITS and LEE, 1993]. This form is usually incorrect for the $(k_y = 0, k_z = 0)$ component of the fluctuations, which can make a big difference in nonlinear simulations. The adiabatic electron response is derived from the linearized parallel-force-balance equation for electrons, which in the $k_\| v_{te} \gg \omega$ limit is $\nabla_\|(p_{\|1} - en_0\Phi) = 0$. Upon assuming that the electrons are isothermal (so that $p_{\|1} = n_{e1}T_{e0}$), one finds

$$\nabla_\| n_{e1} = n_0 \nabla_\| \frac{e\Phi}{T_{e0}}. \tag{8.1}$$

[1] I have reviewed some of the relevant literature in Chap. 1.

Thus, only the parallel gradient of the electron density is determined; the constant of integration in

$$n_{e1} = C + n_0 \frac{e\Phi}{T_e} \tag{8.2}$$

must be determined from some other constraint. In the usual case of electrostatic waves in a plasma with good magnetic flux surfaces, there is no net radial transport of particles if the electrons are exactly adiabatic (the radial particle flux $n_e v_{Ex} \propto n_e \partial\Phi/\partial y$ vanishes when averaged over a flux surface). This means that the number of electrons on each flux surface must be constant, thus determining the constant of integration in Eq. (8.2),

$$n_{e1} = n_0 \frac{e}{T_e} \left(\Phi - \langle\langle \Phi \rangle\rangle \right), \tag{8.3}$$

so that the flux-surface-average $\langle\langle n_{e1} \rangle\rangle = 0$. For convenience, I will also use the notation $\langle\langle \Phi \rangle\rangle = \delta_m \delta_n \Phi$, where $\delta_m \delta_n$ is an operator in Fourier wave-number space that is unity for the $m = 0, n = 0$ component and zero for all other Fourier components. To demonstrate the importance of this, consider the solution of Eq. (2.69) for Ψ,

$$\Psi = \frac{\bar{n}_i}{\tau(1 - \delta_m \delta_n) + 1 - \Gamma_0}, \tag{8.4}$$

where $\bar{n}_i$ is the non-polarization part of the ion density, i.e., the first term on the right-hand side of Eq. (2.69). Upon expanding the Bessel function in the long-wavelength limit, one may reduce this expression to

$$\Psi = \frac{\bar{n}_i}{\tau(1 - \delta_m \delta_n) + k_\perp^2 \rho_i^2}. \tag{8.5}$$

For $m \neq 0$ or $n \neq 0$, this gives the familiar form $\Psi = \bar{n}_i/(\tau + k_\perp^2 \rho_i^2)$. But for the $m = n = 0$ component (the part representing poloidal flows $\propto \partial\Psi_{0,0}/\partial x$), this gives

$$\Psi_{0,0} = \frac{\bar{n}_{i0,0}}{k_x^2 \rho_i^2}, \tag{8.6}$$

which at long wavelengths ($k_x^2 \rho_i^2 \ll 1$) gives a very large enhancement in the poloidal flow over the usual formula that ignores the $\delta_m \delta_n$ term. In physical terms, the usual $n_{e1} = n_0 e\Phi/T_e$ formula allows electrons to move radially across flux surfaces and short out the radial electric field responsible for the poloidal flow, while the expression $n_{e1} = n_0 e(\Phi - \langle\langle \Phi \rangle\rangle)/T_e$ prevents this radial current. (Actually, it should

be pointed out that the usual form may be acceptable if the magnetic field lines are fully stochastic and space-filling rather than forming good flux surfaces. Radial electric fields will then have a component parallel to this stochastic magnetic field, allowing the electrons to flow radially as well. However, in the more conventional case where good flux surfaces are assumed, one should include the $\langle\langle\phi\rangle\rangle$ term so that the electrons do not respond to a potential that is constant along a field line.) Finally, note that this effect will continue to be important even if weak non-adiabatic effects (such as collisions or trapped electrons) are included. As long as the electron response is still close to adiabatic, the adiabatic component should not respond to a potential that is constant along a field line. These considerations apply equally to particle and fluid simulations when the electrons are modeled adiabatically.

8.2 Simple Theoretical Aspects of Flow Evolution

Having clarified the role of the adiabatic electron constraint, we may make a (guiding-center) correspondence with Diamond's physical picture [Diamond and Kim, 1986] of the turbulent momentum flux driving the mean shear flow. In the long-wavelength limit, the quasineutrality constraint (Eq. (2.69)) is approximately

$$\tau(\Phi - \langle\langle\Phi\rangle\rangle) = (1 + \frac{1}{2}\nabla_\perp^2)n + \frac{1}{2}\nabla_\perp^2 T_\perp + \nabla_\perp^2\Phi.$$

The flux-surface average of this equation produces an equation for the perpendicular velocity shear flow (since the left-hand side vanishes):

$$E_x' = \langle\langle -\nabla_\perp^2\Phi\rangle\rangle = \langle\langle n + \frac{1}{2}\nabla_\perp^2(n + T_\perp)\rangle\rangle$$

Upon employing this identity [and neglecting terms of order $(k_\perp\rho)^4$], one may write down an equation for the time evolution of the sheared perpendicular flow (ignoring the nonlinear phase mixing for the moment):

$$\begin{aligned}\frac{\partial E_x'}{\partial t} &= -\langle\langle\left[(1 + \tfrac{1}{2}\nabla_\perp^2)\mathbf{v}_\Psi\right]\cdot\nabla n + \left[\nabla_\perp^2\mathbf{v}_\Psi\right]\cdot\nabla T_\perp\rangle\rangle \\ &= -\langle\langle\left[(1 - \tfrac{1}{2}\nabla_\perp^2)\mathbf{v}_\Psi\right]\cdot\nabla n\rangle\rangle - \langle\langle\left[\nabla_\perp^2\mathbf{v}_\Psi\right]\cdot\nabla p_\perp\rangle\rangle.\end{aligned}$$

Diamond and Kim, 1986 discuss the general momentum-evolution equation, identifying the Reynold's stress or turbulent momentum flux as the drive for sheared

flows. Because I am using guiding-center variables, the corrections due to the polarization and diamagnetic drifts are more visible. However, the underlying idea is the same. Typically, the two terms on the right-hand side are the same size. *Via* the polarization drift, the local transport of guiding centers and of the guiding-center perpendicular pressure drives a mean sheared flow. Angular momentum is conserved in this process, as can be seen by integrating this expression over the x direction; the right-hand side vanishes. The important qualitative point is that this mean sheared flow can suppress the linear growth rates, as shown in App. D, and thereby reduce the thermal flux in the region around the rational surface (where the ITG mode is localized by Landau damping). The flows need not have a large radial extent to impact the turbulence significantly, since the most unstable modes are typically only several to a few tens of gyroradii in radial extent. Nor need the flux be large to begin to have an effect, since the velocity gradients that stabilize the linear modes are only $(v_y/v_t)(L_T/L_v) \sim L_T/L_s$.

From this simple picture, it is clear that the velocity shear and the nonlinear thermal flux are intimately related. To simply suppress the $k_\parallel = 0$ component of Φ at every time step without a solid rationale for doing so is probably inadvisable. Furthermore, most simulations to date have taken no special action with regard to the $k_\parallel = 0$ components of pressure, momentum, *etc.*; singling out the potential for different treatment is inconsistent.

If the resulting shear flows were tied to the box size (always largest for the longest x wavelengths, for example), the implications for the scaling of the turbulence would be quite important; one need not expect to find gyro-Bohm scaling. On the other hand, if the shear flows were strongly related to the grid resolution (through the thermal transport due to the relatively widely spaced low-order rational surfaces) for constant box-size, the effect could be spurious, and may not be observed in a physical system with densely packed rational surfaces. More study is called for in this regard. Two examples are shown in Figs. (8.2) and (8.4). In the first case, there are probably not enough rational surfaces in the simulation domain, because the dominant wavelength of the sheared flow in the x direction is comparable to the box size. In the second case, with much higher resolution, the dominant wavelength of the sheared flow is much smaller than the simulation domain. The peak values in the two cases are comparable. These examples suggest

that the shear flow effect is real.

One might argue for the practice of suppressing sheared flows in simulations by noting that in the limit of densely packed rational surfaces, it is unlikely that significant gradients in the electric field could build up. That is, with a very large number of modes in the box, each at a given time driving a sheared flow with arbitrary sign, the mean field should be very close to zero. According to this argument, the observation of mean sheared flows in simulations is a relic of the small number of modes. To address this argument, one should increase the resolution of one's simulation to the computational limit in such a way as to increase the density of rational surfaces while keeping their distribution as even as possible, and look for changes in the answers. There is no obvious reason to assume that the answer one gets from a highly resolved simulation will be the same as if one continues low-resolution runs, selectively removing a few Fourier components of electrostatic potential.[2]

8.3 Simulation Results

Here I show the importance of the self-generated velocity shear in the gyrofluid simulations. The parameters for the run shown in Figs. 8.1–8.3 were $L_x = 20\rho_i$, $L_y = 25\rho_i$, $L_z = 64L_n$, nonlinear resolution $(x, y, z) = (64, 16, 32)$, $L_n/L_s = 0.025$, $\eta_i = 4.0$, $T_i = T_e$, $\nu = 0.1$, no nonlinear phase-mixing, and twisting periodicity in the radial direction. Thus, this is a low-resolution simulation with a high value for ν. Fig. (8.1) shows χ_i *vs.* tv_t/L_n. The initial peak is quickly quenched by the nonlinearly generated sheared perpendicular flow whose time-averaged radial profile is shown in Fig. (8.2). In Fig. 8.3, the kinetic energy $\left\langle\left\langle u_\parallel^2 + (\nabla_\perp \Phi)^2\right\rangle\right\rangle$ for each (k_y, k_z) pair is plotted *vs.* tv_t/L_n. The mode that is dominant over most of the time of the simulation is the $(k_y = 0, k_z = 0)$ mode. This mode has no linear drive, and hence is a product of $(k_x, k_y, k_z) + (k_x', -k_y, -k_z)$ types of terms from the $\mathbf{E} \times \mathbf{B}$ nonlinearities. The only direct damping it sees in this simulation is $\propto \nu\nabla_\perp^4$, since the nonlinear phase-mixing terms are not included. Since $\nu \sim 0.1$ and the dominant wavelength ($\lambda \sim 10$) implies $k_x\rho_i \sim 0.4$, one would expect a damping

[2] To be fair, it seems that a very similar argument is correct with respect to quasilinear flattening of the driving pressure gradient. As shown in Chap. 7.3, one observes the same thermal flux in a 2D simulation with the gradient fixed as is obtained from a large, 3D simulation with closely packed rational surfaces.

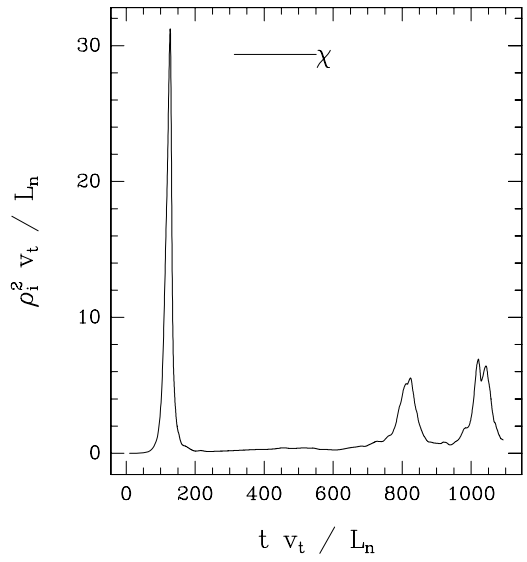

Figure 8.1: Heat flux *vs.* tv_t/L_n for a simulation with proper adiabatic electron response and with artificially large viscous damping.

rate $\gamma \sim 2.5 \times 10^{-3}$. This is consistent with the kinetic energy, which falls roughly $3.5e$-foldings between $tv_t/L_n = 200$ and 800.

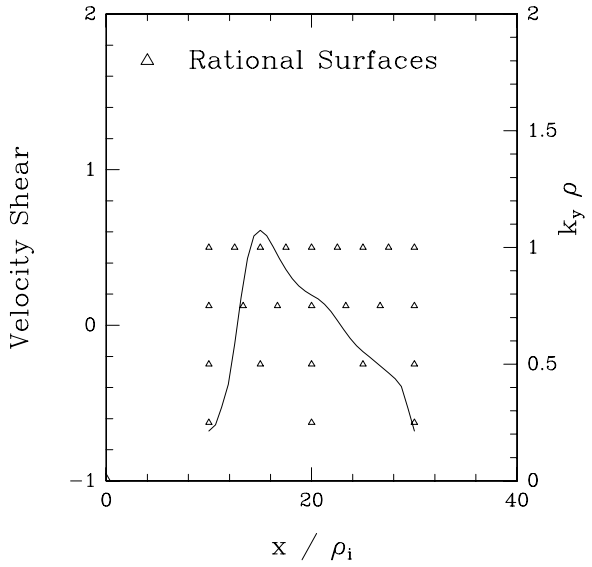

Figure 8.2: Time-averaged perpendicular velocity shear.

Figure 8.3: Kinetic energy for each (k_y, k_z) pair *vs.* tv_t/L_n. The dominant mode is $(k_y = 0, k_z = 0)$.

When the $(k_y = 0, k_z = 0)$ mode is sufficiently damped, the remaining modes begin to grow again, driving the perpendicular rotation that again damps all competing modes. This recurring process shows no sign of diminishing over very long times. If ν is taken to be small, the $(k_y = 0, k_z = 0)$ mode does not decay significantly, and the turbulent heat flux is usually eventually suppressed to very low levels, even for η_i large.

This may be seen in the simulation shown in Figs. (8.4)–(8.6). The parameters for this simulation were $L_x = 40\rho_i, L_y = 51.2\rho_i, L_z = 81.9L_n$, nonlinear resolution $(n_x, n_y, n_z) = (128, 32, 64)$, $L_n/L_s = 0.0625$, $\eta_i = 4.0$, $T_i = T_e$, $\nu = 0.005$, no nonlinear phase-mixing, and twisting periodicity in the radial direction.

Fig. (8.4a) shows the arrangement of the rational surfaces and their relative importance. The vertical axis is the mode number m for $k_y\rho_i = 2\pi m/L_y$. The horizontal axis is the radial position (measured in units of ρ_i). There are four vertical lines that mark the boundaries of the "real" simulation domain and of the total simulation domain. The real simulation domain is the domain over which the twisting periodicity conditions outlined in Chap. 6 are enforced, and is bounded by the inner two vertical lines, which intersect the x axis at $x = 5.6\rho_i$ and $x = 44.4\rho_i$. Because `ITG` is a spectral code for the purposes of evaulating derivatives in the x direction, it is necessary to include a few extra grid points on the edges of the periodic domain. That is, before each time step, a small strip of data between $x = 5.6\rho_i$ and $x = 11.2\rho_i$ is copied into the region between $x = 44.4\rho_i$ and $x = 51.2\rho_i$ according to the twisting periodicity condition, Eq. (6.3). Similarly, a strip of data between $x = 38.8\rho_i$ and $x = 44.4\rho_i$ is copied into the region between $x = 0$ and $x = 5.6\rho_i$. The Fourier transforms are then continuous across the boundaries of the periodic domain, and do not cause noise problems there. After calculating the x derivatives, the data in the edge regions is thrown away. The height of each oval is proportional to the logarithm of the amplitude of the mode at the end of the simulation. The width is proportional to the quantity Δ_x, defined in Eq. (4.1).

It is apparent from this figure that many of the modes have rational surfaces that lie outside the periodic domain. They are therefore strongly damped inside the domain, and provide a source of stability. Most of the modes have rational surfaces inside the domain. The modes fill the domain as uniformly as possible. Nevertheless, in the long-time limit of this simulation, a region of strong sheared

flows (with substantial curvature) forms on the left-hand side of the periodic domain, as may be seen in Fig. (8.4b). From Fig. (8.5) one may observe that the thermal flux is very small through this region, and the temperature gradient is steepening significantly. The average temperature gradient remains fixed at $\eta_i = 4$, but there are some regions where it is less than $\eta_i = 2$ and other regions where it is greater than $\eta_i = 5$. The thermal diffusivity reaches a peak value of $\chi = 0.35$ in the early stage of the simulation (not shown), and then steadily decreases as the gradients in the radial electric field act on the turbulence. In the final state, the diffusivity is very small, $\chi = 0.05$ [Fig. (8.6)].

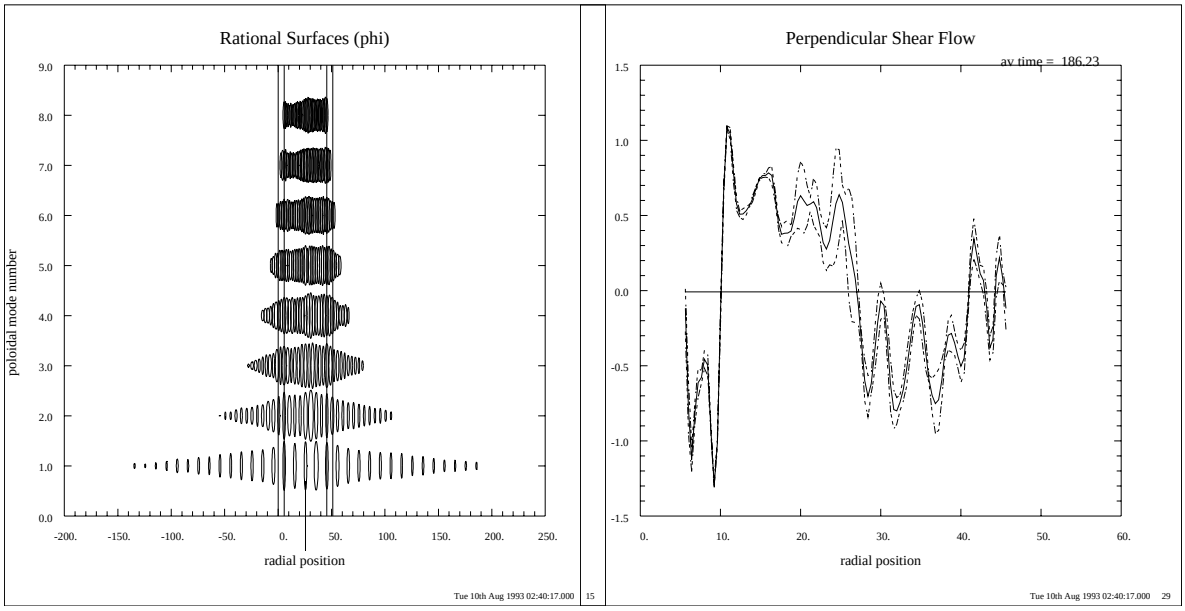

Figure 8.4: Despite (a) a dense arrangement of rational surfaces, one observes (b) sheared flows ($\partial E_x/\partial x$) that quench the thermal transport. The dashed lines represent one standard deviation in the time-average of the sheared flow.

In Fig. (8.7) I show results from a run in which the velocity shear does not quench the turbulence. The parameters for this run were $L_x = 40\rho_i, L_y = 51.2\rho_i, L_z = 10.2L_n$, nonlinear resolution $(n_x, n_y, n_z) = (128, 32, 32)$, $L_n/L_s = 0.25$, $\eta_i = 4.0$, $T_i = T_e$, $\nu = 0.005$, no nonlinear phase-mixing, and twisting periodicity in the radial direction. These parameters are comparable to the parameters used in the 3D comparisons with the particle simulations presented in Chap. (7). Note that the thermal diffusivity predicted is a factor of two smaller in this case ($\chi_i = 0.05\rho_i^2 v_t/L_n$). The drop may be attributed to the correct treatment of the adiabatic

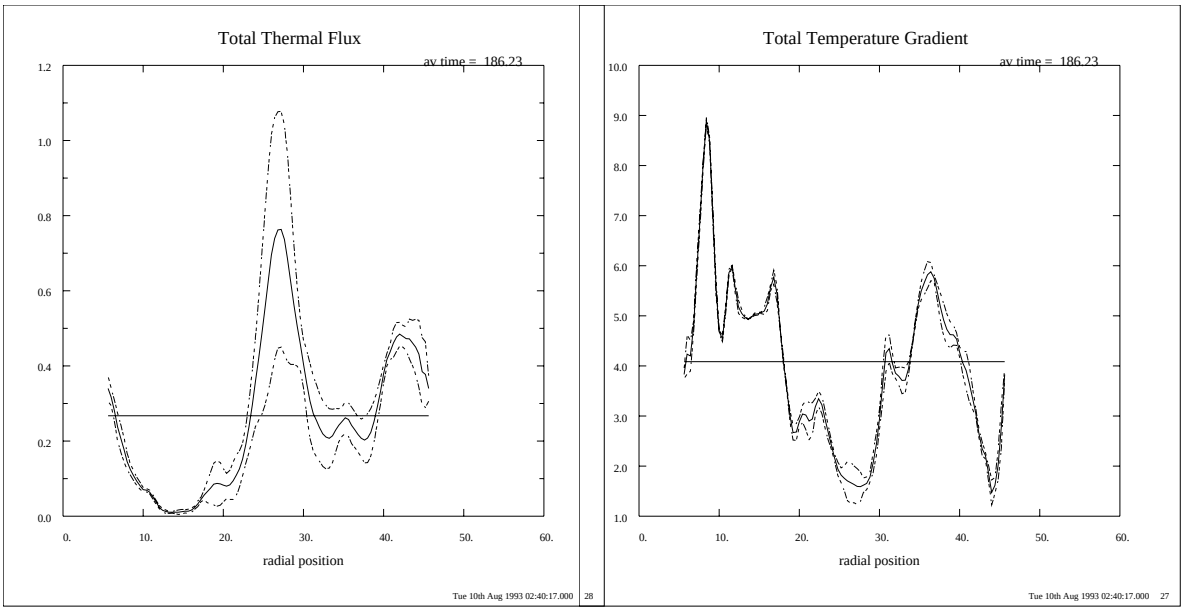

Figure 8.5: Time-averaged (a) thermal flux and (b) total temperature gradient.

electron response, and was confirmed by the gyrokinetic particle simulation (results from the particle simulation not shown).

The controlling difference between the run shown in Figs. (8.4)–(8.6) and this run is the level of magnetic shear. As the shear length L_s increases, the linear modes are wider radially. [Typical linear results that show this trend are shown in Figs. (4.4) and (7.8).] Wide modes are more easily stabilized by sheared flows than are narrow modes. Thus, simulations with lower magnetic shear are observed to be stabilized by velocity shear more easily.

The diminishing effects of these flows in the sheared-slab geometry are sufficiently pervasive as to render parameter scans quite boring. In a toroidal configuration, there are physical effects that limit the shear flows, and therefore control the transport according to this model. In future work, one should include these effects in simulations such as the ones shown here to systematically map out the thermal transport properties of the nonlinear ITG mode.

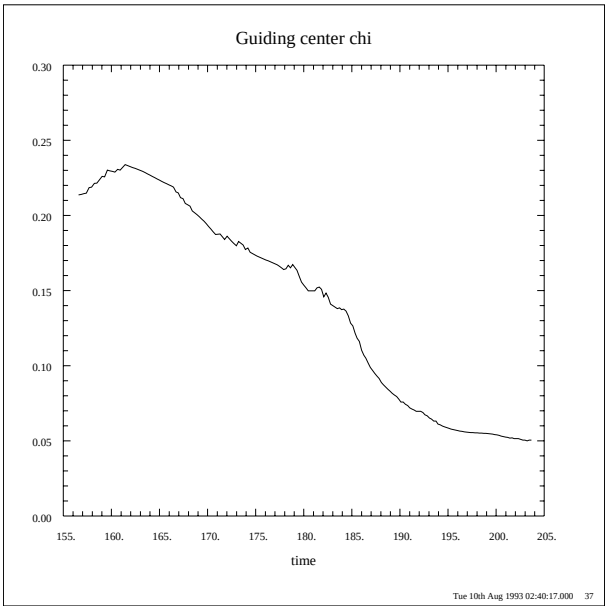

Figure 8.6: Thermal diffusivity is small in final state compared to peak value of $\chi_i = 0.35$ (not shown), for the parameters of Figs (8.4) and (8.5).

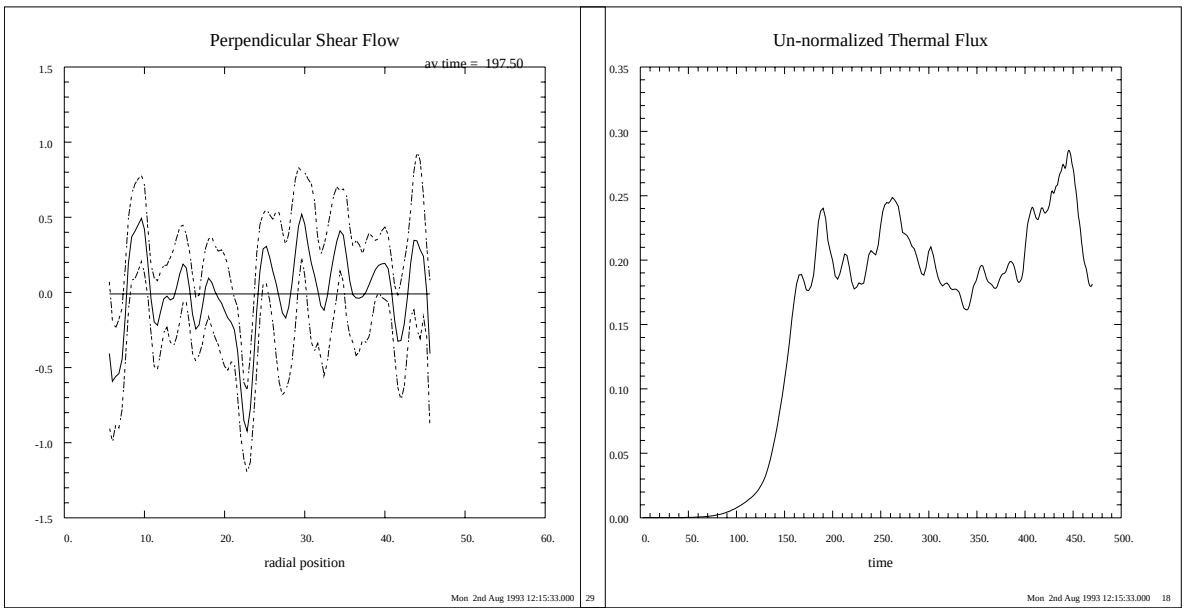

Figure 8.7: (a) Time-averaged perpendicular velocity shear and (b) volume-averaged thermal flux observed in high-shear simulation.

Chapter 9

Conclusions

MY GOAL HAS BEEN to derive a fluid description of plasma that retains as much of the unique kinetic physics as possible, to benchmark the model equations and numerical codes with existing, well-developed gyrokinetic theory, and to investigate the role of ion-temperature-gradient driven turbulence in a sheared slab. Within the extended "gyrofluid" paradigm, I have developed a three-dimensional plasma microturbulence simulation program (`ITG`) that successfully reproduces linear and nonlinear gyrokinetic particle-simulation predictions for thermal transport characteristics of thermonuclear plasma embedded in a strong, sheared magnetic field. Gyrofluid simulations complement gyrokinetic particle simulations, which are more fundamental and potentially more accurate, by providing a relatively inexpensive but physically relevant computational tool. For example, `ITG` is both fast enough to run in a workstation environment and flexible enough to permit the addition of realistic toroidal effects. Nonlinear gyrofluid simulations on a 64^3 grid can be completed in one or two hours of Cray C-90 CPU time (on a single processor) without introducing significant filtering; that is, with a large range of the spectrum accurately simulated.

On a general note, the fluid approach, while certainly not appropriate for all problems, is probably adequate for the investigation of tokamak turbulence, since (1) the nonlinear fluid equations express fundamental conservation laws that the turbulence must satisfy (conservation of particles, parallel momentum, parallel and perpendicular energy, and more if higher moments are retained); (2) they contain fairly accurate multipole Padé models of the kinetic linear propagator, and are

able to produce the proper linear frequency and wavenumber spectra; and (3) they contain the dominant nonlinearities ($\mathbf{E}\times\mathbf{B}$ and the related FLR nonlinearities) that couple these linear modes together to provide the nonlinear saturation mechanism for the turbulent, nonlinear system.

9.1 Highlights from this Thesis

Several issues were addressed as the results of HAMMETT and PERKINS, 1990 were extended from the shearless, drift-kinetic limit [their Eqs. (11ff)] to the sheared slab, gyrokinetic limit. First, the previous Landau-damping closure was generalized to include new perpendicular-velocity moment equations. I derived eight guiding-center moment equations (for n, $u_\parallel$, $T_\parallel$, $q_\parallel$, $T_\perp$, $q_\perp$, $r_\perp$, and $s_\perp$) and showed how to reduce them to as few as may be needed for a particular application. It was shown that for the ITG instability, a 3+1 model (n, $u_\parallel$, $T_\parallel$ and $T_\perp$) is sufficient to recover the linear eigenmodes and eigenfrequencies [LINSKER, 1981] with reasonable accuracy in the sheared-slab limit.

Second, I discussed how to approximate the velocity-space averages of gyro-averaged quantities. The usual Taylor-series approximations to these terms are inappropriate for numerical studies of ITG turbulence, as the radial grid spacing required to resolve the dynamics intrinsically involves modes with $k_\perp\rho > 1$, for which the Taylor-series approximations are inadequate. I presented several FLR models of varying complexity and utility. All except the 3+0 and 4+0 models are second-order accurate in $k_\perp\rho$ and well-behaved for $k_\perp\rho \gg 1$.

The most satisfactory model presented, the $\Gamma_0^{1/2}$ model, is linearly exact in the absence of magnetic shear if an equal number of parallel and perpendicular moments are kept. It can be easily implemented in existing spectral codes, as it requires only simple modifications of the perpendicular Laplacians and of Poisson's equation. These modifications also reduce the stiffness of the system, as the modified Laplacian operators are bounded by ~ 0.5 as $k_\perp\rho \to \infty$. With this FLR model in the gyrofluid equations, good agreement is found with the linear gyrokinetic predictions [LINSKER, 1981; DONG *et al.*, 1987] of frequencies, growth rates and mode structures even near marginal stability, where the ITG mode is known to be strongly affected by kinetic effects.

I also outlined an FLR model more suitable for finite-difference applications, the Padé model. This model reproduces the kinetic growth rates to within only $\sim 25\%$ accuracy in the regime in which we benchmarked its performance. However, I showed that with it one may recover linear gyrokinetic eigenmodes with good accuracy. Like the $\Gamma_0^{1/2}$ model, the Padé model reduces the stiffness of the system.

Next, I described a new nonlinear, FLR phase-mixing effect. This perpendicular phase-mixing process is analogous to parallel phase mixing, deriving from the $\nabla \cdot (J_0 \mathbf{v}_E F_1)$ term of Eq. (2.1) just as Landau damping derives from the $\nabla_\parallel (v_\parallel F_1)$ term. It may be as important as the Hasegawa–Mima [Hasegawa and Mima, 1977] polarization-drift nonlinearity when $T_i = T_e$, as it is $\propto k_\perp^2 |\Phi_{\vec{k}} \vec{k} \times \vec{k'}|$. It provides an FLR-induced hyperviscosity-like sink of turbulent energy for $k_\perp \rho \geq 1$ in a fluid description. A gyrofluid model that captures the qualitative features of the resulting nonlinear gyrokinetic response was presented, though it was noted that it is a difficult effect to model accurately with fluid equations. I noted that this effect tends to reduce the noise in nonlinear gyrofluid simulations, and can reduce the thermal diffusivity if the spectrum is not truncated around $k_\perp \rho \sim 1$.

In carrying out the derivation of the new nonlinear gyrofluid terms, I showed a fairly general way to proceed when trying to model kinetic effects with fluid equations. For example, using the same method one could find fluid models of the precessional drift resonance, cyclotron resonances, or the toroidal drift resonance. The latter has already been accomplished [Waltz *et al.*, 1992; Beer and Hammett, 1992]. Additional physics effects (such as non-adiabatic electrons, sheared equilibrium flows, and multiple species of ions), which may have important impacts for experimental parameter regimes, have been added to this model (and to the `ITG` code) with no significant complications and are discussed in the appendices.

I showed a few of the many linear, numerical benchmarks I have carried out. Utilizing the kinetic models described above, excellent agreement with linear gyrokinetic theory was found. Previous fluid estimates of the linear frequencies and mode widths were generally too large by factors of ~ 2 and overestimated the nonlinear thermal flux by a factor of ten [Kotschenreuther *et al.*, 1991]. Nonlinear simulations using the full gyrofluid models showed very good agreement with particle simulations. From the evidence presented here, one may conclude that the 3+1, $\Gamma_0^{1/2}$ model is probably sufficiently accurate for the study of ITG

turbulence. In any event, I showed that our gyrofluid systems that retain more moments do become more accurate. Thus, one may (for example) use the 4+2 model to check nonlinear results obtained from the 3+1 model for consistency.

While comparing the linear performance of the `ITG` code with linear gyrokinetic theory, I pointed out that concentrating on a single radial eigenmode is likely to be misleading. I noted that mixing-length estimates can vary widely depending upon which mode is selected, making such estimates (which loosely represent only an upper bound on the transport) uncertain unless a reliable selection criterion can be developed.

A weak-turbulence analysis of electron drift-wave turbulence was carried through to show the correspondence between the gyrofluid and gyrokinetic descriptions of the nonlinear physics. The FLR and Landau-damping models derived here and elsewhere [Hammett and Perkins, 1990] allow one to find a gyrofluid wave-kinetic equation that is an excellent approximation to the gyrokinetic wave-kinetic equation in the drift-wave limit. In particular, both the beat-wave-resonance damping and the sharp reduction of ion Compton scattering in the long-wavelength limit were reproduced for the first time using fluid equations. [Mattor, 1992 independently noted the former with a simpler set of fluid equations but did not emphasize the degree of agreement with kinetic theory.] As noted by Mattor, 1992, very near marginal stability, the 3+1 gyrofluid equations fail to recover the kinetic ion Compton-scattering rate. This conclusion is true also for all gyrofluid models described here, *i.e.,* up to the 4+4 model. It was conjectured that a larger system of fluid equations closed with the generalized many-moment Landau-damping closures of Smith and Hammett, 1993 and Hammett *et al.*, 1993 would perform better in this limit. Some numerical evidence was presented in support of this claim, but more work is needed to understand this limit better.

Nonlinear results from `ITG` were benchmarked with gyrokinetic particle simulations and three-mode-coupling theory. In general, excellent agreement was found, even in regimes where $\omega \sim k_\parallel v_t$, $k_\perp \rho_i \sim 1$, and the nonlinear terms were order unity. This level of agreement has never before been shown between fluid and particle simulations, and is a principal result of this thesis. Three problems were investigated: (1) the unsheared, single-$k_\parallel$, local limit; (2) the sheared, 2D system (with a single rational surface); and (3) the 3D sheared-slab with no allowed perpendicular shear

flows. The nonlinear saturation mechanism for each case was described. It was argued that in cases (1) and (2), quasilinear flattening of the background gradient was responsible for the nonlinear saturation. For case (1), a theory was presented [PARKER, 1993] to support this claim, and for case (2), numerical evidence was presented. Finally, the 3D simulations were sufficiently large to allow turbulent saturation, although some flattening of the temperature gradient in the bulk of the simulation domain was observed.

In light of these findings, a novel 2D simulation scheme was presented and shown to produce reasonable results in a small fraction of the time required by 3D simulations. By freezing all of the $k_\parallel = 0$ components of the moments and of the potential with strong sources and sinks [numerically equivalent to suppressing the $(x, k_y = 0, k_z = 0)$ components at every time step [HAMAGUCHI and HORTON, 1990]] I showed that it is possible to regard ITG turbulence as otherwise two-dimensional.

The role of the aspect ratio of one's simulation domain was discussed in connection with the rapid roll-over of thermal flux often previously reported. In particular, it was noted that if one does not choose one's domain so that rational surfaces are distributed evenly and densely throughout the entire domain, rapid local flattening of the driving gradient can reduce the nonlinear heat flux. Difficulties associated with boundary effects can be overcome by allowing for periodicity in each direction. A scheme for implementing radial periodicity in the presence of magnetic shear was outlined.

The correct adiabatic-electron response (for a magnetic configuration with good flux surfaces) was shown and its effect on the nonlinear turbulence described. On a more mundane level, numerical convergence of `ITG` was demonstrated in the appendices for an interesting set of physical parameters. The roles of spatial and temporal resolution, the number of moments, and artificial dissipation were discussed.

Having established that the physics is largely correctly described and that `ITG` is working properly, I presented the principal result to date from nonlinear gyrofluid sheared-slab simulations: the observation of self-generation of sheared velocity flows that strongly reduce the turbulent heat flux. Because there are no natural damping mechanisms for this rotation in a collisionless sheared-slab, one

finds that the thermal transport perpendicular to the magnetic field is much weaker than expected. This illuminates the very interesting possibility that toroidally-induced sheared-flow damping could control anomalous transport by acting as a "valve" for the thermal diffusivity, even far from the edge.

9.2 Future Work

FLR effects play a critical role in the development of low-frequency microturbulence since the ion gyroradius provides the fundamental small-scale length for collisionless, electrostatic systems. Along with Landau damping, FLR effects determine the linear mode structure and localize the mode around the rational surface. Because the most unstable modes typically have perpendicular wavelengths such that $k_\perp \rho \sim 1$, one will always need FLR models such as those developed here if one wishes to perform direct numerical simulations of microturbulence using fluid equations. In addition to FLR effects, the ultimate gyrofluid model would include models to account for toroidicity, multiple species, non-adiabatic (bounce-averaged) electrons, collisions, and possibly electromagnetic effects. Progress has already been made on several of these fronts; further development and the task of integration remain.

The most interesting follow-up to the work presented here is well underway [Beer *et al.*, 1992; Hammett *et al.*, 1992a; Waltz, 1993; Beer *et al.*, 1993; Hammett *et al.*, 1993]. That is, a careful nonlinear investigation of the ITG instability in toroidal geometry including self-generated sheared flows could possibly be extremely relevant to magnetic confinement fusion experiments. If it can be determined that the interaction of sheared flows and turbulent fluctuations continues to be important to the evolution of the ITG instability in the core region of the tokamak, one could then perhaps follow the lead of Diamond [Diamond and Liang, 1993] and LeBoeuf [Leboeuf *et al.*, 1993] and reduce the problem to a simpler predator-prey paradigm. However, one would require comprehensive simulations to determine the proper parameters for such a reduced description. Even if a reduced predator-prey model is not sufficiently accurate, this thesis has established the importance of turbulence-generated sheared flows and shown that it is important to model the generation and damping mechanisms accurately. In particular, with the inclusion of toroidicity, neoclassical damping mechanisms may introduce poloidal

field dependence into the scaling for χ_i through the self-generated $\mathbf{E} \times \mathbf{B}$ flows.

In addition to toroidal effects, one should consider the role of impurities and possibly of non-adiabatic electrons in ITG turbulence. For different reasons (discussed in the appendices), each might play a role in the generation or dissipation of sheared flows, or in the linear stability of the mode [KOTSCHENREUTHER, 1993]. Of more interest, however, might be the effect of full ITG turbulence on these components of the plasma [COWLEY, 1993]. One might discover signatures of sheared flows or of microturbulence in the dynamics of the minority species that could be exploited to understand the dynamics of the plasma as a whole. More optimistically, one might find a convenient "knob" with which one could affect the turbulence. Along these lines, HASSAM, 1993 has suggested using off-axis neutral-beam injection to drive differential poloidal rotation to reduce microturbulence. One would hope to be able to simulate such ideas numerically within the gyrofluid paradigm.

One might include the effects of trapped electrons with fluid moments of a bounce-averaged kinetic equation [PERKINS and HAMMETT, 1991]. With the proper precession-resonance model, one could then recover the collisionless trapped-electron mode. With the further inclusion of collisional models [CHANG and CALLEN, 1992a; CHANG and CALLEN, 1992b] one could include turbulence due to the dissipative trapped-electron mode and the effects of classical diffusion. If simulations with this level of complexity fail to explain the observed anomalous transport, one could incorporate electromagnetic effects [CHANG and CALLEN, 1992a; CHANG and CALLEN, 1992b; HEDRICK and LEBOEUF, 1992].

More far-reaching applications of the methods and models developed here might include a reduced description of electron transport in semiconductor lattices [FREY, 1991]. Presently, if one wishes to know the details of the electron distribution function in a semiconductor, one employs a semi-classical approximation to describe the possible energy levels that the electrons may occupy, and particle simulations (or more general Monte-Carlo methods) to describe the dynamics. Because the conduction electrons interact weakly with the lattice and with one another, fluid equations have been considered inapplicable. However, FREY, 1991 uses a fluid model similar to that of CHANG and CALLEN, 1992a to describe the motion of the electrons with good success. It would be interesting to investigate such phenomena further utilizing the insights found in this thesis.

General problems for which the present method might provide useful results include many-body problems in which the interactions among the bodies are too weak to validate the traditional fluid equations. For example, one might contemplate astrophysical applications such as the dynamics of galaxy formation or the evolution of the universe. In the latter case, one recent study [CEN *et al.*, 1990] utilized particle simulation methods to describe the cold dark matter component of the universe. It may be possible to improve upon this scheme using collisionless fluid closures.

Final Thought

Rarely is one interested in the fine-scale details of a thermodynamic system. More often one would be satisfied with a gross model accounting only for a few observable, low-order-average quantities. In this context, one should strive to reduce one's description of the dynamics to reflect one's interests to the greatest extent possible without significantly compromising the integrity of the resulting predictions. Insight is much easier to come by in a familiar setting.

Appendix A

4+4 Gyrofluid Model

IN THIS APPENDIX, I present the nonlinear 4+4 ($n, u_\parallel, T_\parallel, q_\parallel, T_\perp, q_\perp, r_\perp$ and $s_\perp$) gyrofluid model for completeness. While most problems probably do not require the accuracy afforded by this model, it is nevertheless useful to show that the closure schemes improve as more moments are retained. Also provided is the complete set of real and imaginary parts of each moment for the fastest growing linear mode for the parameters $\eta_i = 2, L_s = 40L_n, k_y\rho_i = 0.707$ and $\tau = 1$, in case the interested reader wishes to benchmark a code that solves these equations with the code used to produce the results in this thesis. The 4+4 model equations are

$$\frac{dn}{dt} + \left[\tfrac{1}{2}\hat{\nabla}_\perp^2 \mathbf{v}_\Psi\right] \cdot \nabla T_\perp + \mathcal{N}_{21} T_\perp + \hat{\mathbf{b}} \cdot \nabla u_\parallel + \left[1 + \eta_{i\perp} \tfrac{1}{2}\hat{\nabla}_\perp^2\right] \frac{\partial \Psi}{\partial y} = 0, \tag{A.1}$$

$$\frac{du_\parallel}{dt} + \left[\tfrac{1}{2}\hat{\nabla}_\perp^2 \mathbf{v}_\Psi\right] \cdot \nabla q_\perp + \mathcal{N}_{21} q_\perp + \hat{\mathbf{b}} \cdot \nabla \left(T_\parallel + n + \Psi\right) = 0, \tag{A.2}$$

$$\frac{dT_\parallel}{dt} + \left[\tfrac{1}{2}\hat{\nabla}_\perp^2 \mathbf{v}_\Psi\right] \cdot \nabla r_\perp + \mathcal{N}_{21} r_\perp + \hat{\mathbf{b}} \cdot \nabla (2u_\parallel + q_\parallel) + \eta_{i\parallel} \frac{\partial \Psi}{\partial y} = 0, \tag{A.3}$$

$$\frac{dq_\parallel}{dt} + \left[\tfrac{1}{2}\hat{\nabla}_\perp^2 \mathbf{v}_\Psi\right] \cdot \nabla s_\perp + \mathcal{N}_{21} s_\perp + \hat{\mathbf{b}} \cdot \nabla (3 + \beta_\parallel) T_\parallel + \sqrt{2}|k_\parallel|\, D_\parallel q_\parallel = 0, \tag{A.4}$$

$$\begin{aligned} \frac{dT_\perp}{dt} + \left[\tfrac{1}{2}\hat{\nabla}_\perp^2 \mathbf{v}_\Psi\right] \cdot \nabla n + \left[\hat{\hat{\nabla}}_\perp^2 \mathbf{v}_\Psi\right] \cdot \nabla T_\perp + \mathcal{N}_{22} T_\perp \\ + \hat{\mathbf{b}} \cdot \nabla q_\perp + \left[\tfrac{1}{2}\hat{\nabla}_\perp^2 + \eta_{i\perp}(1 + \hat{\hat{\nabla}}_\perp^2)\right] \frac{\partial \Psi}{\partial y} = 0, \end{aligned} \tag{A.5}$$

$$\frac{dq_\perp}{dt} + \left[\tfrac{1}{2}\hat{\nabla}_\perp^2 \mathbf{v}_\Psi\right] \cdot \nabla u_\parallel + \left[\hat{\hat{\nabla}}_\perp^2 \mathbf{v}_\Psi\right] \cdot \nabla q_\perp + \mathcal{N}_{22} q_\perp$$

$$+\hat{\mathbf{b}}\cdot\nabla\left(r_\perp + T_\perp + \tfrac{1}{2}\hat{\nabla}_\perp^2\Psi\right) = 0, \tag{A.6}$$

$$\frac{dr_\perp}{dt} + \left[\tfrac{1}{2}\hat{\nabla}_\perp^2\mathbf{v}_\Psi\right]\cdot\nabla T_\parallel + \left[\hat{\nabla}_\perp^2\mathbf{v}_\Psi\right]\cdot\nabla r_\perp + \mathcal{N}_{22}r_\perp$$
$$+\hat{\mathbf{b}}\cdot\nabla(2q_\perp + s_\perp) + \eta_{i\parallel}\tfrac{1}{2}\hat{\nabla}_\perp^2\frac{\partial\Psi}{\partial y} = 0, \tag{A.7}$$

$$\frac{ds_\perp}{dt} + \left[\tfrac{1}{2}\hat{\nabla}_\perp^2\mathbf{v}_\Psi\right]\cdot\nabla q_\parallel + \left[\hat{\nabla}_\perp^2\mathbf{v}_\Psi\right]\cdot\nabla s_\perp + \mathcal{N}_{22}s_\perp$$
$$+\hat{\mathbf{b}}\cdot\nabla(3+\beta_\parallel)r_\perp + \sqrt{2}|k_\parallel|\,D_\parallel s_\perp = 0. \tag{A.8}$$

In dimensional units, the quantity $r_\perp$ is defined by the relation:

$$r_\perp \equiv \frac{R_\perp}{T_\perp}$$

(so that when linearized and written in non-dimensional form, $r_{\perp 1} = R_{\perp 1} - T_{\perp 1}$). Poisson's equation [Eq. (2.69)] is unaffected by the additional moments. Figs. A.2

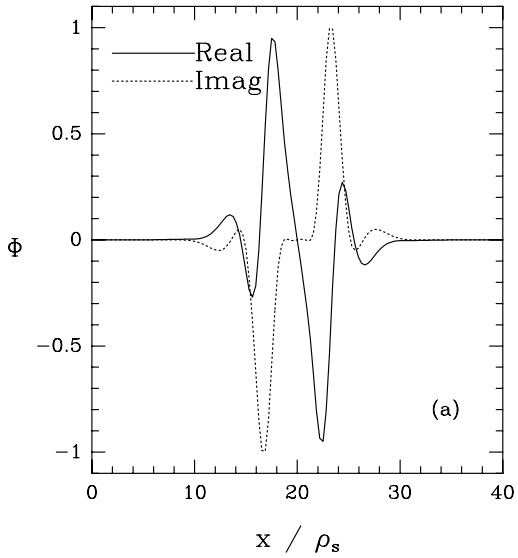

Figure A.1: Electrostatic potential (arbitrary units) of the fastest growing mode for $\eta_i = 2$, $L_s/L_n = 40$, $k_y\rho_i = 0.707$, and $\tau = 1$ using the 4+4 model.

and A.3 show the eight moments associated with the electrostatic potential of Fig. A.1.

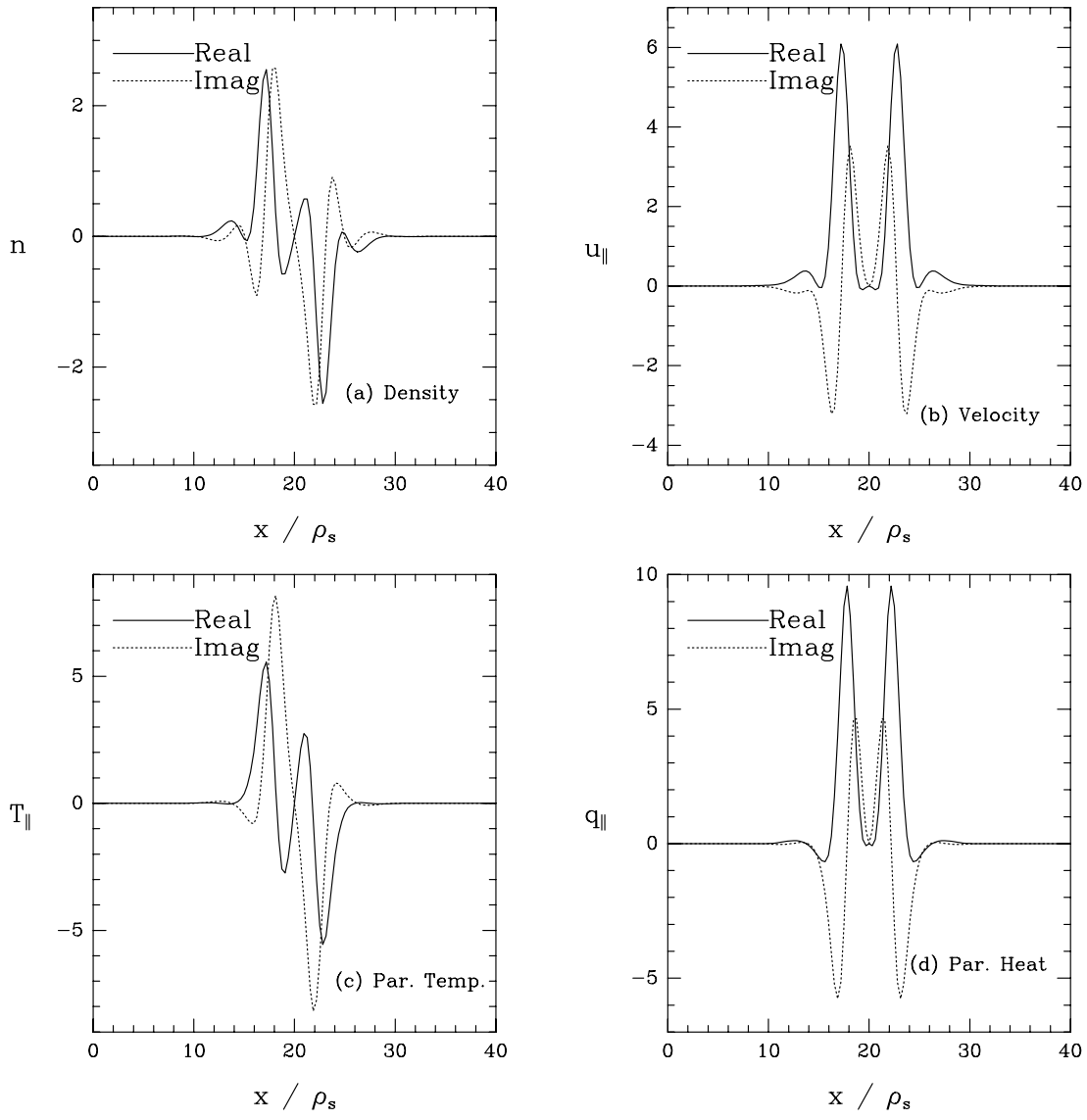

Figure A.2: Parallel moments (arbitrary units) of the fastest growing mode for $\eta_i = 2$, $L_s/L_n = 40$, $k_y\rho_i = 0.707$, and $\tau = 1$.

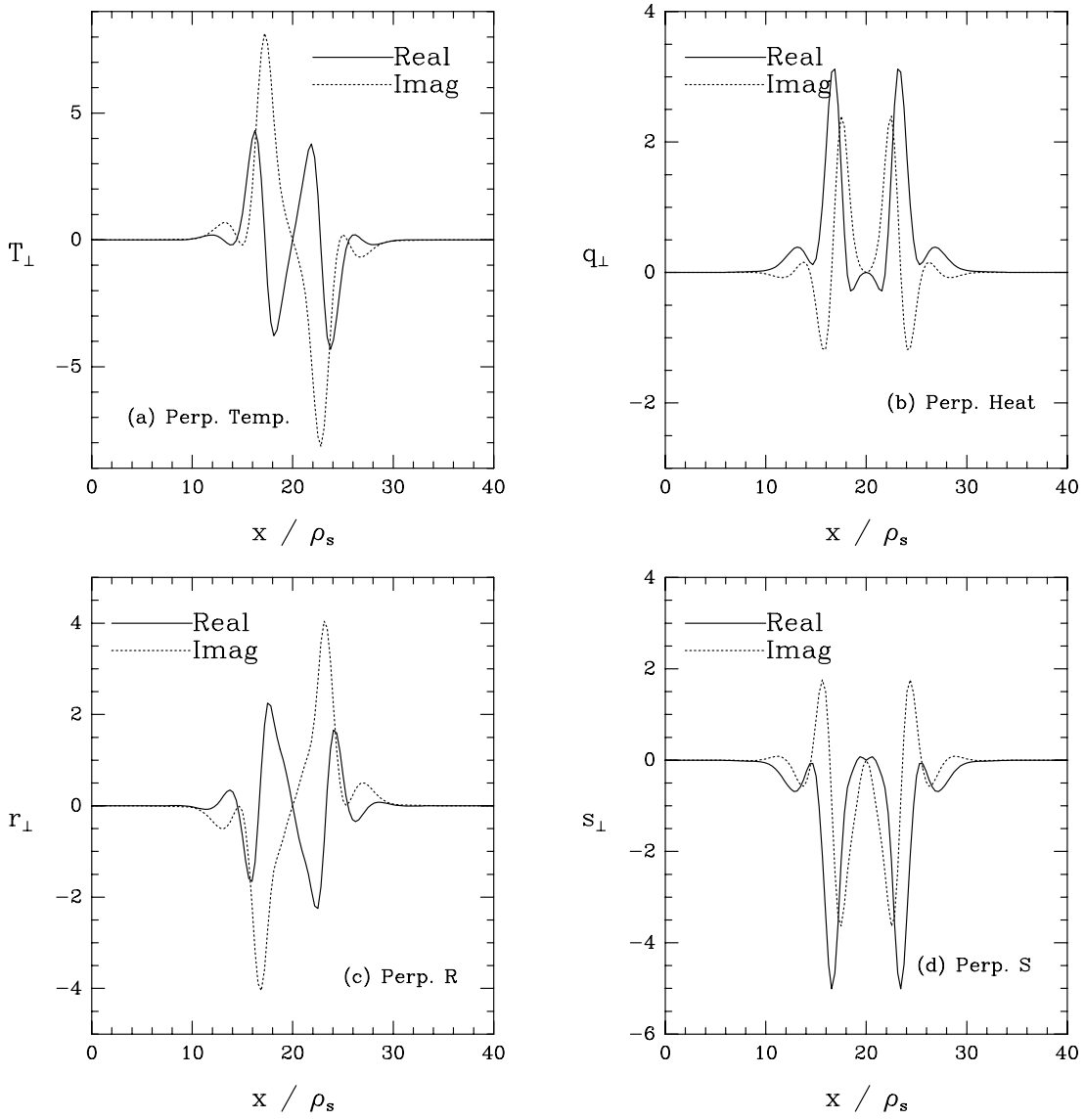

Figure A.3: Perpendicular moments (arbitrary units) of the fastest growing mode for $\eta_i = 2$, $L_s/L_n = 40$, $k_y\rho_i = 0.707$, and $\tau = 1$.

Appendix B

Numerical Convergence

HERE I study the convergence properties of `ITG` with respect to the spatial resolution, artificial numerical dissipation (when present), and the number of moments retained. The latter item is nice, since many fluid theories and most fluid simulations are not systematically extended to include higher moments. That the nonlinear results obtained do not depend strongly on the number of moments retained is evidence that the essential aspects of the nonlinear dynamics are well-represented by the most basic model advocated here. The parameters for the convergence studies presented below were chosen to match a set of gyrokinetic particle-code runs provided by R. A. Santoro [SANTORO and LEE, 1990; LEE, 1987] and are the same as the basic 2D case described in Sec. 7.2. The examples shown in this Appendix are primarily from single-helicity simulations, chosen for reasons of economy. I have carried out careful three-dimensional convergence studies in grid resolution for a set of parameters agreed upon by the Numerical Tokamak Working Group ($\eta = 4, \tau = 1, L_s = 4L_n$). In these studies, changing the number of grid points in each direction by factors of two to four (up to $64 \times 64 \times 64$ gridpoints), and reducing the time step resulted in no significant change in the time-averaged thermal flux or spectrum.

In general, numerical convergence should be shown in at least five dimensions:

(1) Spatial resolution {grid points/number of modes};

(2) temporal resolution {time step};

(3) dissipation parameter(s) {spatial filtering/particle size and added numerical (hyper)viscosity};

(4) number of moments/particles;

(5) and the FLR model {n-point averaging/different $\langle J_0 \rangle$ gyrofluid models}

before a result can be considered meaningful. Since it is impractical to carry out such a test for every run, here I explicitly show that `ITG` converges for a specific case in dimensions (1), (3), and (4) for a set of parameters that, aside from being two-dimensional, are close to the parameters of experimental interest. [Item (2) was tested here by halving the time step; all the diagnostic time traces in Fig. (B.2) were almost exactly the same.] I have not carefully tested the different nonlinear FLR models (such as discussed in Sec. 2.4.4). Note, however, that the linear behavior of the FLR models has been carefully investigated and that the comparisons with the gyrokinetic particle code shown in Chap. 7 indicate at least that nothing terribly wrong is occurring nonlinearly. Finally, I also showed the importance of the nonlinear phase-mixing model in the course of the direct comparisons to the particle simulations, Chap. 7.

B.1 Diagnostics

Several diagnostics are used to interpret the voluminous data that the code produces. Linear results are interpreted by time-series plots of the instantaneous complex frequency at a single point located slightly away from the center of the simulation domain (so that odd-parity modes centered in the box are not neglected), allowing one to know at a glance whether the fastest-growing (or least damped) eigenmode has dominated the initial transient phenomena, by the Fourier transform of this series (sometimes useful for distinguishing two roots with very similar growth rates), and by the final ($t = t_{\rm end}$) spatial states of the various fields. `ITG` was linearly benchmarked primarily against Linsker's fully gyrokinetic integral eigenvalue code [Linsker, 1981]. Recently, Q. P. Liu's [Liu and Cheng, 1992] nonlinear, 5-dimensional gyrokinetic Vlasov code has allowed simpler comparisons. That is, since both codes are initial-value codes, one does not have to iterate between codes to find the roots. Also, Liu's code includes toroidal effects comparable to the toroidal effects of Beer *et al.*, 1992. Thus, comparisons with the slab limit of his code pave

the way for benchmarks of more realistic systems later. Fig. (B.1) shows a comparison (in k_x space) of the fastest-growing even-parity eigenmodes obtained with the gyrofluid and the gyrokinetic Vlasov codes for the parameters $\eta_i = 2$, $L_s/L_n = 40$, $k_y\rho_i = 0.5$, and $\tau = 1$. The frequency obtained by Liu's code matched the prediction from the Linsker [LINSKER, 1981] code, $\omega L_n/v_t = -0.050 + 0.028i$. The 3+3 gyrofluid model obtained $\omega L_n/v_t = -0.047 + 0.026i$. Note that even though the magnetic shear is weak, the linear mode is not negligible $k_x\rho_i > 1$.

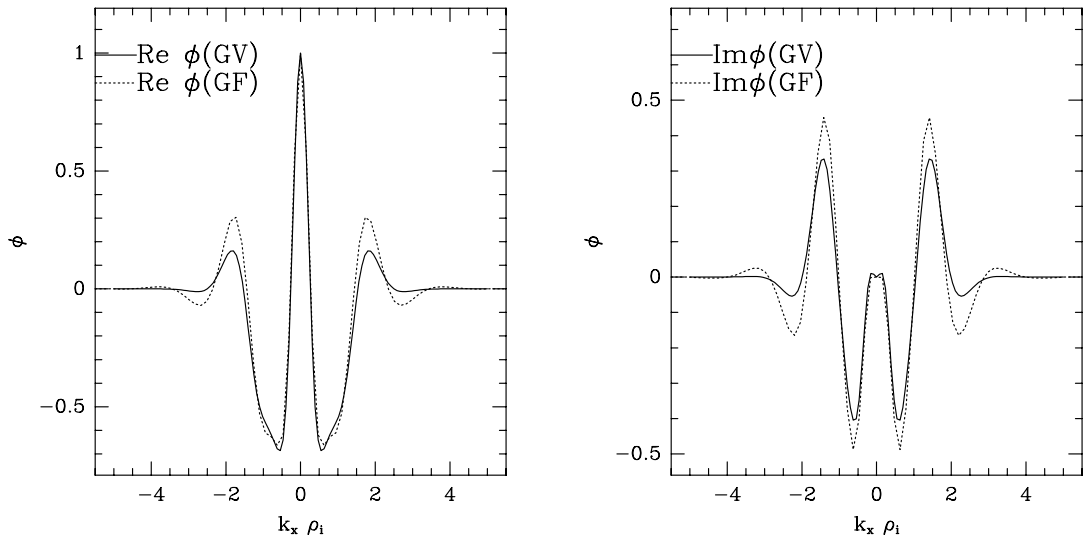

Figure B.1: Electrostatic potential (arbitrary units) of the fastest growing even-parity mode for $\eta_i = 2$, $L_s/L_n = 40$, $k_y\rho_s = 0.5$, and $\tau = 1$ using the 3+3 model (GF) and a gyrokinetic Vlasov code (GV).

Nonlinearly, the situation is more complex. Presently, at run time I save the shear flows, modifications to the background gradients [through the evolution of the $(x, k_y = 0, k_z = 0)$ modes], the time step, global growth rate, average spectral mode widths, average mode spread, the radially integrated pressure, heat flux and kinetic energy for each (k_y, k_z) mode, the volume-integrated electrostatic and total energy, and $\Phi(k_x, k_y)$, each as a function of time. If desired, movies of selected fields may be generated with the National Center for Supercomputer Applications' Hierarchical Data Format library routines. Finally, if desired, $\Phi(x, k_y, k_z, t)$ may be saved separately (this is a large file!). G. Valencia (a visiting Princeton Plasma Physics Laboratory summer student) has written a particle code that pushes particles in the turbulent fields thus saved, making available a wide range of studies that have not yet been pursued.

The principal diagnostic used to compare the various runs is the heat flux *vs.* time, integrated over the entire simulation domain. The heat flux, with the proper FLR corrections,[1] is defined by

$$Q = Q_0 + Q_{\rm NLPM}, \tag{B.1}$$

where for the 3+1 model

$$Q_0 \equiv -\frac{1}{L_x L_y L_z}\int d^3x \left[\frac{\partial\Psi}{\partial y}(p_\parallel/2 + p_\perp) + \frac{\partial(\frac{1}{2}\hat{\nabla}_\perp^2\Psi)}{\partial y}p_\perp + \frac{\partial(\frac{1}{4}\hat{\nabla}_\perp^2\Psi)}{\partial y}T_\perp + \frac{\partial(\hat{\hat{\nabla}}_\perp^2\Psi)}{\partial y}T_\perp\right],$$

and $p_\perp$ and $p_\parallel$ are defined by Eqs. (2.7). The heat flux associated with the dissipative part of a given nonlinear phase-mixing term may be calculated from Eq. (2.60). For example, the heat flux Q_1 associated with the dissipative part of the nonlinear phase-mixing term in Eq. (2.72) is given by

$$Q_1\{\tfrac{1}{2}\nu_1\hat{\nabla}_\perp^2\Psi, T_\parallel\} = \frac{\nu_1}{L_x L_y L_z}\int d^3x\, |\tfrac{1}{2}\hat{\nabla}_\perp^2\frac{\partial\Psi}{\partial y}|\frac{1}{|k_x|}\frac{\partial T_\parallel}{\partial x}$$

The total expression for the 3+3 $Q_{\rm NLPM}$ is

$$Q_{\rm NLPM} = \frac{\nu_2}{32}Q_1\{\hat{\nabla}_\perp^4\Psi, 3T_\perp + r_\parallel\} + \frac{\nu_2}{2}Q_1\{\hat{\nabla}_\perp^2\Psi, T_\perp\}$$

[1] If the $r_\parallel$ moment is evolved, there is an additional term that comes from the $T_\parallel$ equation not shown here.

$$+\frac{\lambda_2}{L_x L_y L_z}\int d^3x\,\left[\tfrac{1}{32}\hat{\nabla}_\perp^4\frac{\partial\Psi}{\partial y}(3T_\perp+r_\parallel)-\tfrac{1}{2}\hat{\nabla}_\perp^2\frac{\partial\Psi}{\partial y}T_\perp\right].$$

This definition may be shown to be in accord with the usual definition of the cross-flux-surface heat flux,

$$\frac{3}{2}\langle\!\langle\frac{\partial nT_{\rm tot}}{\partial t}\rangle\!\rangle=\frac{\partial}{\partial x}\langle\!\langle n\chi\frac{\partial T_{\rm tot}}{\partial x}\rangle\!\rangle=-\frac{\partial}{\partial x}\langle\!\langle Q\rangle\!\rangle,$$

where $T_{\rm tot}=1/3(T_\parallel+2T_\perp)$, and is also in accord with the kinetic description used in many gyrokinetic particle codes,

$$Q=-\frac{1}{L_xL_yL_z}\int d^3x\int dv\,[J_0(k_\perp v_\perp/\Omega)\frac{\partial\Phi}{\partial y}]\frac{m(v_\parallel^2+v_\perp^2)}{2v_t^2}\delta f.$$

The thermal flux defined here and in Eq. (B.1) is the guiding-center heat flux. There is another contribution from the gyrophase-dependent part of the distribution function [Eq. (2.2)] due to the variation of the distribution function around a gyro-orbit. While there may be a transient difference between the guiding-center heat flux and the total heat flux, the time-averaged, steady-state values should be the same in a turbulent system. In the dimensionless units used throughout this thesis [given in Eqs. (2.61) and (2.62)], the thermal diffusivity χ_i is simply related to the heat flux,

$$\chi_i=\langle\!\langle Q\rangle\!\rangle/\eta_i. \tag{B.2}$$

The thermal diffusivity calculated in this way is in units of $\rho_i^2 v_t/L_n$. (Care must be taken to define derived quantities such as these, since disparate conventions allow differences of order unity that may be misleading in a detailed comparison.)

Also compared are the time-averaged spectral characteristics of the electrostatic potential. Time averages are performed after nonlinear saturation has occurred. Since in all cases I retain the full dynamics (no filtering or dealiasing) for $k_\perp\rho_i\leq 3-4$, the spectral information is much less sensitive than the heat flux to the changes in the numerical quantities studied here, and is therefore not emphasized below. That is, unless extreme filtering is employed, so that the filter widths are comparable to the natural cutoffs in the wavenumber spectrum from the FLR effects, the spectral characteristics of the result are not affected. This is not surprising; what is perhaps important to realize, however, [as may be seen from Fig. (B.1)] is that the linear eigenmodes contain information for $k_\perp\rho_i>1$. From these figures, a reasonable filter would seem to be one that does not appreciably affect the dynamics until $k_\perp\rho_i\sim 4$.

B.2 Moment Convergence Study

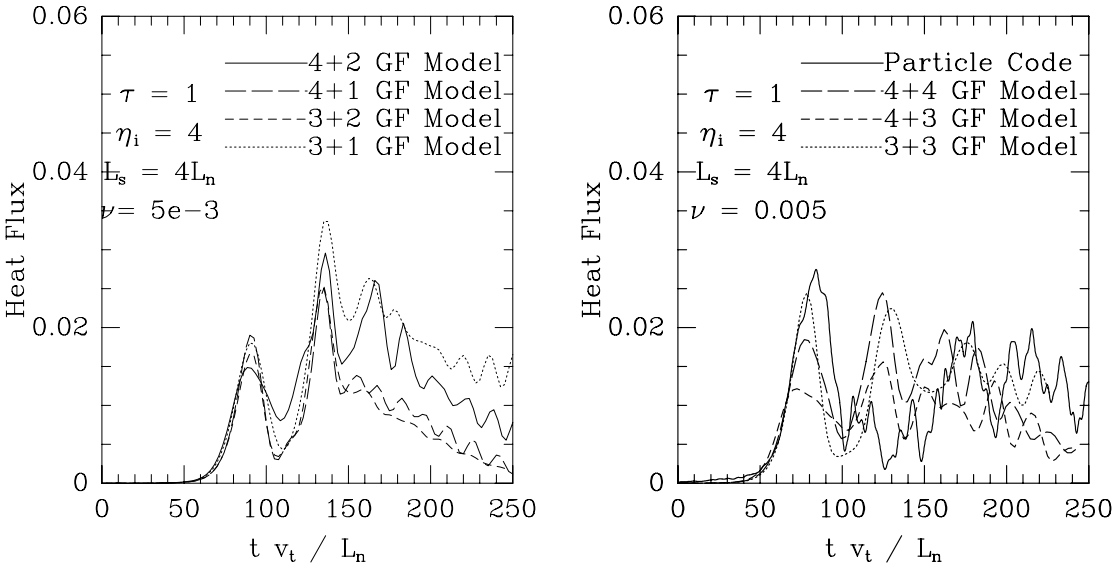

Figure B.2: Thermal flux *vs.* time for different numbers of moments.

Fig. (B.2) shows the heat flux *vs.* time for different numbers of moments retained, along with the results from the standard particle run. The fluid simulations have $\nu = 0.005 v_t/L_n$ and keep $k_x\rho \leq 2$. The fluid models agree reasonably well with the particle-simulation prediction and with one another (though the higher-moment models do not recover the initial peak). Even for the 3+1 model the agreement is probably acceptable. A more revealing study would compare time-averaged quantities in a steady state characterized by turbulent saturation, rather than the quasi-linear saturation found here.

B.3 Spatial and Temporal Convergence

Fig. (B.3) shows the heat flux *vs.* time for the 4+4 model as the number of grid points in the radial direction is increased. Here, the dissipation parameter $\nu = 0.001 v_t/L_n$, except in the "converged run", which had 256 grid points and $\nu = 0$, and the standard particle run (described in Chap. 7.2). Otherwise, the parameters are the same as for the "basic run" defined in Chap. 7.2. As expected, the lower resolution runs are noisier. On the basis of this plot, one could argue (from the large initial

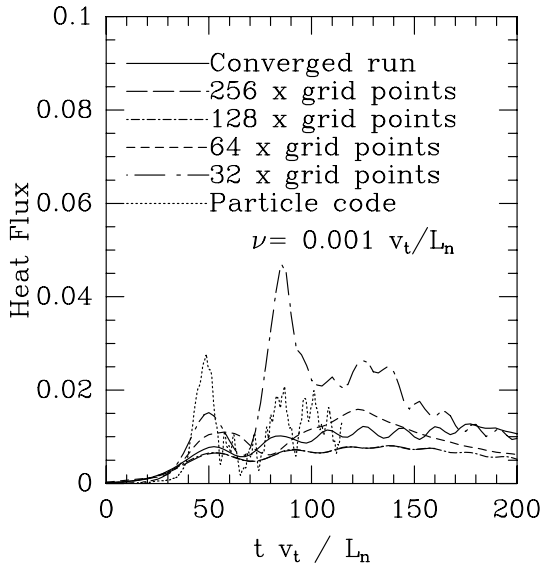

Figure B.3: Heat flux *vs.* time as the radial grid resolution is increased, holding everything else fixed.

peak) that higher resolution in the radial grid was called for in the particle run. Fig. (B.4) shows the heat flux *vs.* time for the 4+4 model, with the dissipation parameter $\nu = 0.001 v_t/L_n$, as the resolution in k_y is increased. Despite the very k_y poor resolution of the standard parameters, the results compare well for these parameters. Note that the modes with $k_y\rho \geq 1$ are at most very weakly growing, so that the plethora of high-k_y modes in the standard case have little effect here. Before they can grow to significant values, the pressure profile is relaxed.

B.4 Nonlinear Phase Mixing

The nonlinear phase-mixing model described in Chap. 2.5 has little effect if one truncates the Fourier components of the potential for $k_\perp\rho \sim 1$. This was shown in Chap. 7.4. However, if one does not use a low-resolution grid and does not filter the potential, one finds that the NLPM model can significantly reduce the thermal flux. At the same time, one observes an attenuation of the high-$k_\perp\rho$ part of the fluctuation spectrum. In general, the NLPM model reduces the thermal diffusivity by as much as a factor of two for grids with sufficient resolution to be considered converged. However, I have found that unless one keeps the same number of parallel

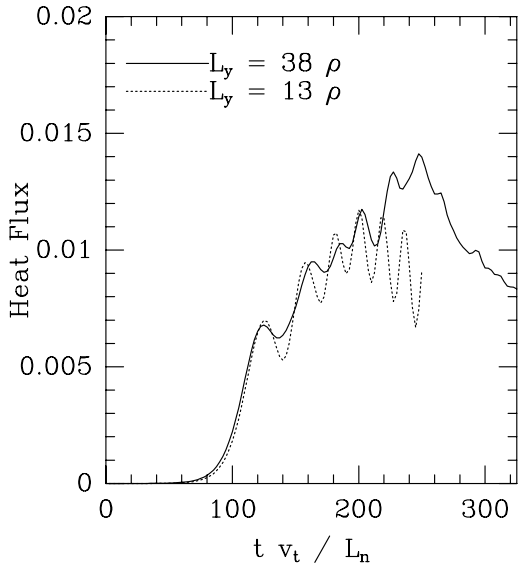

Figure B.4: Heat flux *vs.* time with increasing resolution in $k_y\rho$.

and perpendicular moments, the model fails to damp high-$k_\perp\rho$ fluctuations, and instead can lead to a nonlinear instability that causes `ITG` to crash in some cases.

The effect of nonlinear phase-mixing on the thermal heat flux in this 2D setting is shown by Fig. (B.5). Here $\nu = 0$. The result is quieter, and the overall level is reduced by a factor of two. Note that this result implies that one should not filter out modes with $k_\perp\rho > 1$ [*e.g.,* see Fig. (7.18)], since the answer can change as a result. This is not surprising; if one were interested in drift-kinetic results, one could abandon the gyrokinetic equation altogether.

B.5 Added Dissipative Effects

Fig. (B.6) shows the heat flux *vs.* the parameter ν for the 3+1 model. For these runs, I used the 2D model with the $(x, k_y = 0, k_z = 0)$ components of the moments and of Φ suppressed. The physical parameters were $\eta_i = 4$, $\tau = 1$, and $L_n/L_s = 0.25$. Modes with $k_x\rho \leq 7.9$, $k_y\rho \leq 1$ were retained for this figure. I usually run the code with $\nu \leq 0.005$ so that the dependence is expected to be relatively unimportant. [A small amount of damping reduces the noise at the shortest wavelengths in the box.] The dependence is never completely neglible, however, since the terms introduced

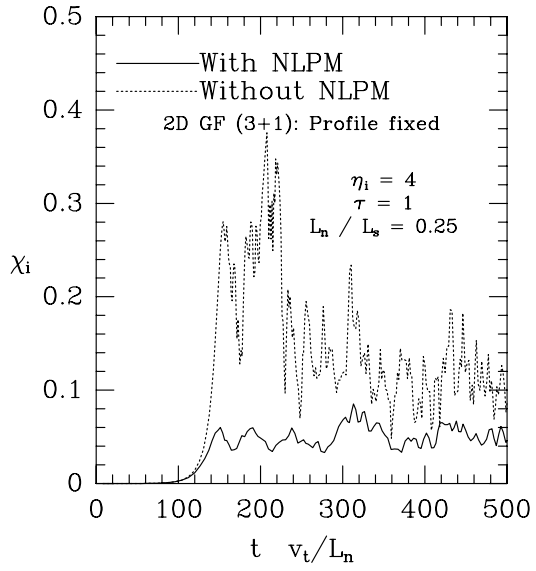

Figure B.5: The effect of nonlinear phase-mixing (in 2D) on the thermal heat flux.

here (or in the Krook model) are the only terms in this geometry that directly damp the $k_\parallel = 0$ modes, which in turn are often crucial to the saturation level in the 3D simulations. The situation is much different in toroidal geometry, where a variety of physical effects (such as transit-time magnetic pumping) can interact with these modes.

B.6 Krook Collision Terms

A simple density-, momentum-, and energy-conserving collision model derived by taking moments of the density-, momentum-, and energy-conserving Krook collision operator and ignoring FLR corrections when transforming the collision operator from particle to guiding-center coordinates was also introduced (and found to have little effect in the sheared slab for small ν_{ii}). This collision model changes the 4+2 gyrofluid model [Eqs. (2.63–2.69)] by including the following terms

$$\left(\frac{\partial T_\parallel}{\partial t}\right)_{\rm coll} = -(2\nu_{ii}/3)(T_\parallel - T_\perp),$$

$$\left(\frac{\partial T_\perp}{\partial t}\right)_{\rm coll} = -(\nu_{ii}/3)(T_\perp - T_\parallel),$$

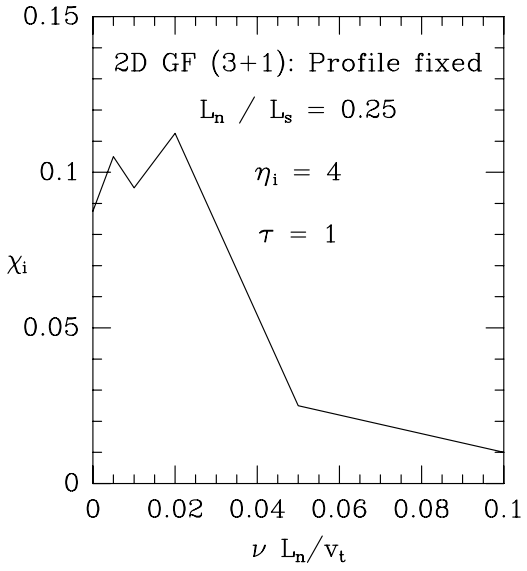

Figure B.6: Scaling of the (single helicity) average heat flux *vs.* the dissipation parameter ν, using the 3+1 model.

$$\left(\frac{\partial q_\parallel}{\partial t}\right)_{\rm coll} = -\nu_{ii} q_\parallel,$$

$$\left(\frac{\partial q_\perp}{\partial t}\right)_{\rm coll} = -\nu_{ii} q_\perp,$$

on the right-hand sides of the respective equations. In this simple model, ν_{ii} is independent of velocity. A collision operator of this form would recover neoclassical transport in a toroidal system but would not recover classical diffusion (because of the incomplete guiding-center transformation).

Appendix C

Gyrokinetic-Poisson System

HERE I PROVIDE a brief derivation of the nonlinear electrostatic gyrokinetic equation [Frieman and Chen, 1982; Lee, 1983; Dubin *et al.*, 1983; Lee, 1987] in a sheared slab, along with the associated quasineutrality constraint. There are no new contributions to the literature to be found in this appendix. The derivation is presented to clarify the role of the gyrokinetic ordering [Frieman and Chen, 1982] used extensively throughout this thesis and to justify the neglect of nonlinear terms often retained in Poisson's equation [Dubin *et al.*, 1983; Lee, 1983].

C.1 Gyrokinetic Equation

One begins with the familiar Vlasov equation, which describes the evolution of the one-particle distribution function in phase space:

$$\frac{\partial \mathcal{F}}{\partial t} + \vec{v} \cdot \frac{\partial \mathcal{F}}{\partial \vec{x}} + \frac{e}{m}\left(\vec{E} + \frac{\vec{v} \times \vec{B}}{c}\right) \cdot \frac{\partial \mathcal{F}}{\partial \vec{v}} = 0. \tag{C.1}$$

Here, $\mathcal{F}(\vec{x}, \vec{v}, t)$ is the distribution function, $\vec{x}$ and $\vec{v}$ are the position and velocity vectors in real space, and the remainder of the symbols are the usual physical constants and electromagnetic fields. One wishes to find an equation that can easily describe the slow dynamics of the guiding-center motion while ignoring the fast dynamics of the cyclotron motion. The Vlasov equation is complete (it contains all of the collisionless dynamics) but does not easily treat the disparate time scales.

The first task is to change the phase-space variables from $(\vec{x},\vec{v})$ to guiding-center variables $(\vec{R},\mu,v_\parallel,\alpha)$. Here, $\vec{R}$ is the position of the guiding center of the particle, μ is its magnetic moment, $v_\parallel$ is the parallel velocity of the particle, and α is the gyrophase angle.

Upon changing variables

$$\mathcal{F}(\vec{x},\vec{v},t)\rightarrow F(\vec{R},\mu,v_\parallel,\alpha,t),$$

where $\vec{\rho}=\vec{x}-\vec{R}$, $\hat{e}_1$ and $\hat{e}_2$ are local orthogonal unit vectors such that $\hat{\mathbf{b}}=\hat{e}_1\times\hat{e}_2$, $\vec{v}_\perp=v_\perp(\cos\alpha\hat{e}_1+\sin\alpha\hat{e}_2)$, and $\vec{\rho}=\vec{v}_\perp/\Omega$, one is led to

$$\frac{\partial F}{\partial t}+\vec{v}\cdot\left(\nabla\vec{R}\cdot\nabla_R F+\nabla\mu\frac{\partial F}{\partial\mu}+\nabla v_\parallel\frac{\partial F}{\partial v_\parallel}+\nabla\alpha\frac{\partial F}{\partial\alpha}\right)$$

$$+\frac{e}{m}\left(\vec{E}+\frac{\vec{v}\times\vec{B}}{c}\right)\cdot\left(\nabla_v\vec{R}\cdot\nabla_R F+\nabla_v\mu\frac{\partial F}{\partial\mu}+\nabla_v v_\parallel\frac{\partial F}{\partial v_\parallel}+\nabla_v\alpha\frac{\partial F}{\partial\alpha}\right)=0.$$

Here, unless otherwise noted $\nabla=\nabla_x$. This expression may be simplified upon employing several identities:

$$\vec{v}\cdot\nabla\vec{R}=\vec{v}-\vec{v}\cdot\nabla\vec{\rho},\qquad \nabla\mu=-\tfrac{\mu}{B}\nabla B-\tfrac{v_\parallel}{B}(\nabla\hat{\mathbf{b}})\cdot\vec{v}_\perp,$$

$$\nabla\vec{v}=0,\qquad \nabla\alpha=\nabla\hat{e}_2\cdot\hat{e}_1+\tfrac{v_\parallel}{v_\perp^2}(\nabla\hat{\mathbf{b}})\cdot\left(\vec{v}_\perp\times\hat{\mathbf{b}}\right),$$

$$\nabla_v\vec{R}=-\tfrac{\mathsf{I}\times\hat{\mathbf{b}}}{\Omega},\qquad \nabla_v\mu=\tfrac{\vec{v}_\perp}{B},$$

$$\nabla_v v_\parallel=\hat{\mathbf{b}}\qquad \nabla_v\alpha=\tfrac{1}{v_\perp^2}\left(\hat{\mathbf{b}}\times\vec{v}\right),$$

where $\Omega=eB/mc$ is the cyclotron frequency, and I is a unit tensor. The result is

$$\frac{\partial F}{\partial t}+\left(\vec{v}_\parallel+\frac{e}{m}\vec{E}\times\hat{\mathbf{b}}\right)\cdot\nabla_R F-\Omega\frac{\partial F}{\partial\alpha}$$

$$+\vec{v}\cdot\left\{(\nabla_x\vec{\rho})\cdot\nabla_R F-\frac{\mu}{B}\nabla_x B\frac{\partial F}{\partial\mu}-\left[\frac{v_\parallel}{B}\frac{\partial F}{\partial\mu}-\frac{\partial F}{\partial v_\parallel}\right](\nabla_x\hat{\mathbf{b}})\cdot\vec{v}_\perp\right.$$

$$\left.+\left[(\nabla_x\hat{e}_2)\cdot\hat{e}_1+\frac{v_\parallel}{v_\perp^2}\nabla_x\hat{\mathbf{b}}\cdot(v_\perp\times\hat{\mathbf{b}})\right]\frac{\partial F}{\partial\alpha}\right\}+\frac{e\vec{E}}{m}\cdot\left(\frac{\vec{v}_\perp}{B}\frac{\partial F}{\partial\mu}+\hat{\mathbf{b}}\frac{\partial F}{\partial v_\parallel}+\frac{\hat{\mathbf{b}}\times\vec{v}_\perp}{v_\perp^2}\frac{\partial F}{\partial\alpha}\right)=0. \tag{C.2}$$

In a sheared slab, the term proportional to $\nabla_x B$ may be dropped. Upon adopting the gyrokinetic ordering [FRIEMAN and CHEN, 1982] $\omega/\Omega \sim \rho/L \sim k_\parallel \rho \sim F_1/F_0 \sim e\Phi/T_e \sim \varepsilon \ll 1$ and $k_\perp \rho \sim 1$, where ω is a typical frequency of the fluctuation spectrum, ρ is the ion Larmor radius, L is a typical scale length of the system, $k_\parallel$ and $k_\perp$ are typical parallel and perpendicular wavenumbers of the fluctuation spectrum, and Φ is the electrostatic potential, one proceeds order by order to find an equation describing the time evolution of the gyrophase-independent part of F_1.

The largest term in Eq. (C.2) is $\Omega\,\partial F/\partial\alpha$. One finds therefore that the equilibrium distribution function must be independent of the gyrophase,

$$\frac{\partial F_0}{\partial \alpha} = 0, \qquad\qquad F = F_0 + F_1(\alpha).$$

At next order one may assume the equilibrium distribution is Maxwellian (with $T_{\parallel 0} = T_{\perp 0}$) to eliminate the term proportional to $(v_\parallel/B)\,\partial F/\partial\mu - \partial F/\partial v_\parallel$. One finds that the equilibrium distribution function must satisfy

$$\vec{v}_\parallel \cdot \nabla_R F_0 = 0,$$

and the perturbed distribution function satisfies

$$F_1 = \frac{e}{mB}\left(\Phi - \langle\Phi\rangle\right)\frac{\partial F_0}{\partial \mu} + g \equiv \tilde{f} + g \tag{C.3}$$

where g is the gyrophase-independent part of the perturbed distribution function, $\tilde{f}$ is the gyrophase-dependent part of the distribution function, and $\langle\ldots\rangle$ represents the gyrophase-averaging operation.

At order ε^2, one finds a dynamical equation for the total perturbed distribution function,

$$\frac{\partial F_1}{\partial t} + \vec{v}_\parallel \cdot \nabla F_1 + \frac{e}{m}\left(\vec{E}\times\hat{\mathbf{b}}\right)\cdot\nabla\left(F_0+F_1\right) + \vec{v}\cdot\left\{\left(\nabla_x\vec{\rho}\right)\cdot\nabla_R(F_0+F_1)\right.$$

$$\left. - \left[\frac{v_\parallel}{B}\frac{\partial F_1}{\partial\mu} - \frac{\partial F_1}{\partial v_\parallel}\right]\left(\nabla_x\hat{\mathbf{b}}\right)\cdot\vec{v}_\perp + \left[\left(\nabla_x\hat{e}_2\right)\cdot\hat{e}_1 + \frac{v_\parallel}{v_\perp^2}\nabla_x\hat{\mathbf{b}}\cdot\left(v_\perp\times\hat{\mathbf{b}}\right)\right]\frac{\partial F_1}{\partial\alpha}\right\}$$

$$+\frac{e\vec{E}}{m}\cdot\left(\frac{\vec{v}_\perp}{B}\frac{\partial F_1}{\partial\mu} + \hat{\mathbf{b}}\frac{\partial F_0}{\partial v_\parallel} + \frac{\hat{\mathbf{b}}\times\vec{v}_\perp}{v_\perp^2}\frac{\partial F_1}{\partial\alpha}\right) = 0.$$

Upon gyrophase-averaging this equation, one is led to the desired gyrokinetic equation for the time evolution of g,

$$\frac{\partial g}{\partial t} + v_\parallel \hat{\mathbf{b}} \cdot \nabla g + \frac{e}{m}\left(\left\langle \vec{E} \right\rangle \times \hat{\mathbf{b}}\right) \cdot \nabla \left(F_0 + g\right) + \frac{e\left\langle \vec{E} \right\rangle}{m} \cdot \hat{\mathbf{b}} \frac{\partial F_0}{\partial v_\parallel} = 0.$$

Upon adding back in the small terms $\partial F_0/\partial t$, $v_\parallel\, \hat{\mathbf{b}} \cdot \nabla F_0$ and $(e/m)\left\langle \vec{E} \right\rangle \cdot \hat{\mathbf{b}}\, \partial g/\partial v_\parallel$, one can find Eq. (2.1). The quantity F that appears in Eq. (2.1) corresponds to the quantity $(F_0 + g)$ here. Also, in Eq. (2.1), I chose to write out the gyrophase-averaging operator as a Bessel function as discussed in Chap. 2.

C.2 Quasineutrality Constraint

To find the quasineutrality constraint [Eq. (2.4)] one begins with Poisson's equation,

$$\nabla^2 \Phi = -4\pi \sum_{\mathrm{s}} \int d^3v\, q_{\mathrm{s}} \mathcal{F}_{\mathrm{s}}, \tag{C.4}$$

where the indicated sum is over species. Here, I consider the case of a pure hydrogen plasma. The ion distribution function that appears in Eq. (2.1) is the distribution of guiding centers. One must therefore be careful in evaluating Eq. (C.4), since the integral is to be taken at fixed particle position ($\vec{x}$) rather than at fixed guiding-center position ($\vec{R}$). (The guiding-center transformation mixes configuration- and velocity-space variables since $\vec{R}$ is a function of velocity.) The resulting corrections to the integral are of order $(k_\perp \rho_i)^2$, as may be seen by expanding the distribution function in a Taylor series and gyroaveraging:

$$\mathcal{F}(\vec{R}) = \mathcal{F}(\vec{x} - \vec{\rho}) \simeq \mathcal{F}(\vec{x}) - \vec{\rho} \cdot \nabla_{\vec{\rho}} \mathcal{F}(\vec{x}) + \frac{1}{2} \vec{\rho}\vec{\rho} : \nabla_{\vec{\rho}} \nabla_{\vec{\rho}} \mathcal{F}(\vec{x}),$$

$$\left\langle \mathcal{F}(\vec{R}) \right\rangle \simeq \mathcal{F}(\vec{R}) - \frac{1}{2} k_\perp^2 \rho^2 \mathcal{F}(\vec{R}).$$

Because $\rho_e/\rho_i \propto \sqrt{m_e/m_i} \ll 1$, corrections to the electron distribution function are of higher order and may be neglected.

Thus, Eq. (C.4) may be written as

$$\nabla^2 \Phi = -4\pi |e| \left(\int d^3v \left|_{\vec{x}}\, \mathcal{F}_{\mathrm{i}} - n_e \right.\right). \tag{C.5}$$

In the previous section, the distribution function through $O(\varepsilon)$ was found:

$$\mathcal{F}(\vec{x},\vec{v},t) = F(\vec{R},\mu,v_\parallel,\alpha,t) = F_0(\vec{R},\mu,v_\parallel,t)+\tilde{f}(\vec{R},\mu,v_\parallel,\alpha,t)+g(\vec{R},\mu,v_\parallel,t)+O(\varepsilon^2).$$

With the aid of this expression, one may evaluate the integral in Eq. (C.5):

$$\int d^3v \,\Big|_{\vec{x}}\, \mathcal{F}_{\rm i} = \int d^3v \,\Big|_{\vec{x}}\, \Big(F_0+\tilde{f}+g\Big) = n_0 + [1-\Gamma_0(b)]\,\frac{n_0 e\Phi}{T_i} + \bar{n}_1.$$

Poisson's equation is therefore

$$\nabla^2\Phi = -4\pi|e|\left(n_0 + [1-\Gamma_0(b)]\,\frac{e\Phi}{T_i} + \bar{n}_1\right) - n_e$$

To order ε^0, the dominant terms are the background densities of ion and electrons; hence $n_{i0} = n_{e0}$. At order ε^1, one may compare the magnitude of the term on the left-hand side to the term proportional to Φ on the right-hand side,

$$\frac{\nabla^2\Phi}{(4\pi n_0 e^2/T_i)\rho_i^2\nabla_\perp^2\Phi} \sim \frac{\lambda_D^2}{\rho_i^2} \ll 1,$$

where I have taken the small $k_\perp\rho$ limit of the latter term for simplicity. Upon neglecting the left-hand side, one is led to Eq. (2.4). Finally, note that the nonlinear terms retained in some simulations (*e.g.*, [Lee, 1987]) that scale like

$$\nabla_\perp(\frac{n_1}{n_0}\nabla_\perp\frac{e\Phi}{T_e})$$

are smaller than the terms retained in Eq. (2.4) by a factor of ε.

Appendix D

Velocity-Gradient Effects

RECENTLY, THERE HAS BEEN much interest in the effect of gradients in the velocity profile on microturbulence [DIAMOND and KIM, 1986] and on ITG turbulence in particular [ARTUN and TANG, 1992; HAMAGUCHI and HORTON, 1992a; MATTOR and DIAMOND, 1988; GROEBNER *et al.*, 1990; DORLAND *et al.*, 1992b]. Here, I show that the `ITG` code can describe the effects of imposed velocity shear and discuss its effects on the linear dynamics. Because we find the nonlinearly self-generated sheared flows to be important to ITG turbulence [DORLAND *et al.*, 1993b; BEER *et al.*, 1992; HAMMETT *et al.*, 1993], this point is an important one to confirm. The new contributions contained in this appendix are modest. The long-wavelength linear analysis of ARTUN and TANG, 1992 is extended to the $k_\perp \rho_i \sim 1$ limit. It is found that short-wavelength fluctuations ($k_\perp \rho \sim 10$) are the last modes to be stabilized by perpendicular velocity shear. An estimate of the amount of shear necessary to stabilize the linear ITG instability is made and compared to the numerical result for a given set of parameters.

D.1 Gyrofluid Equations

It is easy to include the effects of an imposed external velocity shear in the gyrofluid model. One may always shift to the frame of reference moving with the bulk velocity of the plasma; however, if there are imposed gradients in that velocity the equations must be modified. Velocity gradients in the direction parallel to the magnetic field cause a new term to appear in the parallel momentum and perpendicular heat-flux

equations, as well as a Doppler shift in every equation. Velocity gradients in the direction perpendicular to both the density gradient and the magnetic field contribute only to the Doppler shift. Thus, one may redefine the total time derivative of a field to be

$$\frac{d}{dt} \equiv \frac{\partial}{\partial t} + \mathbf{v}_\Psi \cdot \nabla + \mathbf{v}_0 \cdot \nabla, \tag{D.1}$$

in which $\mathbf{v}_0 \cdot \nabla = v_y' x \partial/\partial y + v_z' x \partial/\partial z$. The nonlinear 4+2 gyrofluid model that includes these gradients is then given by

$$\frac{dn}{dt} + \left[\tfrac{1}{2}\hat{\nabla}_\perp^2 \mathbf{v}_\Psi\right] \cdot \nabla T_\perp + \mathcal{N}_{21} T_\perp + \hat{\mathbf{b}} \cdot \nabla u_\parallel + \left[1 + \eta_{i\perp} \tfrac{1}{2}\hat{\nabla}_\perp^2\right] \frac{\partial \Psi}{\partial y} = 0, \tag{D.2}$$

$$\frac{du_\parallel}{dt} + \left[\tfrac{1}{2}\hat{\nabla}_\perp^2 \mathbf{v}_\Psi\right] \cdot \nabla q_\perp + \mathcal{N}_{21} q_\perp + \hat{\mathbf{b}} \cdot \nabla \left(T_\parallel + n + \Psi\right) - v_z' \frac{\partial \Psi}{\partial y} = 0, \tag{D.3}$$

$$\frac{dT_\parallel}{dt} + \mathcal{N}_1 T_\parallel + \hat{\mathbf{b}} \cdot \nabla (2u_\parallel + q_\parallel) + \eta_{i\parallel} \frac{\partial \Psi}{\partial y} = 0, \tag{D.4}$$

$$\frac{dq_\parallel}{dt} + \mathcal{N}_1 q_\parallel + \hat{\mathbf{b}} \cdot \nabla (3 + \beta_\parallel) T_\parallel + \sqrt{2}|k_\parallel|\, D_\parallel q_\parallel = 0, \tag{D.5}$$

$$\begin{aligned} \frac{dT_\perp}{dt} + \left[\tfrac{1}{2}\hat{\nabla}_\perp^2 \mathbf{v}_\Psi\right] \cdot \nabla n + \left[\hat{\hat{\nabla}}_\perp^2 \mathbf{v}_\Psi\right] \cdot \nabla T_\perp + \mathcal{N}_{22} T_\perp \\ + \hat{\mathbf{b}} \cdot \nabla q_\perp + \left[\tfrac{1}{2}\hat{\nabla}_\perp^2 + \eta_{i\perp}(1 + \hat{\hat{\nabla}}_\perp^2)\right] \frac{\partial \Psi}{\partial y} = 0, \end{aligned} \tag{D.6}$$

$$\begin{aligned} \frac{dq_\perp}{dt} + \left[\tfrac{1}{2}\hat{\nabla}_\perp^2 \mathbf{v}_\Psi\right] \cdot \nabla u_\parallel + \left[\hat{\hat{\nabla}}_\perp^2 \mathbf{v}_\Psi\right] \cdot \nabla q_\perp + \mathcal{N}_{22} q_\perp \\ + \hat{\mathbf{b}} \cdot \nabla (T_\perp + \tfrac{1}{2}\hat{\nabla}_\perp^2 \Psi) - \tfrac{1}{2} v_z' \hat{\nabla}_\perp^2 \frac{\partial \Psi}{\partial y} + \sqrt{2}|k_\parallel|\, D_\perp q_\perp = 0. \end{aligned} \tag{D.7}$$

The quasineutrality constraint equation is unchanged by the imposed velocity shear.

D.2 Linear Eigenmodes

The effect of velocity shear on the linear ITG eigenmodes has been discussed in detail in the literature [Artun and Tang, 1992; Dong, 1993; Artun *et al.*, 1993]. I have previously confirmed the importance of the relative signs of the gradients in the parallel and perpendicular flows in trends noted in Artun and Tang, 1992 with the `ITG` code [Dorland *et al.*, 1992a]. Here, I show only an example eigenmode for

the purposes of discussion. The 4+4, $\Gamma_0^{1/2}$ gyrofluid equations were used throughout this appendix.

The fastest-growing linear eigenmode for the parameters $\eta_i = 4$, $L_s/L_n = 16.0$, $k_y\rho_i = 0.6$, and $T_i = T_e$ is shown in Fig. (D.1a). The frequency predicted by the gyrofluid model is $\omega = -0.26{+}0.086i$. In Fig. (D.1b), I show the eigenmode obtained with the same parameters in the presence of moderate perpendicular velocity shear, $v_y/v_t(L_T/L_v) = -0.02$. The eigenmode no longer has a definite parity and is shifted away from the rational surface (located at $x = 30\rho_i$). The frequency of this modified mode is $\omega = -0.056 + 0.13i$. Thus, for these parameters the sheared background flow destabilizes the mode. Note also that the modified mode is broader, with a longer average x wavelength. A mixing-length estimate based upon these properties would suggest that moderate perpendicular-velocity shear modes might have more dangerous transport properties. As the gradient in the electric field is increased the mode is shifted further from the rational surface. Stabilization occurs when the mode amplitude at the rational surface becomes negligible.

These properties are summarized in Fig. (D.2). Note that the fastest-growing mode for these parameters is for different values of the sheared-velocity parameter on different branches of the linear dispersion relation as the jumps in the real frequency observable in Fig. (D.2a) at $\omega v_t/L_n = 0.12, 0.35$ indicate. Also, one may note the initially destabilizing effect of the sheared flow and the ultimate stabilization. As $|(v_y/v_t)(L_T/L_v)|$ increases, the mode is at first broader and then much narrower, as may be seen in Fig. (D.2b). Around $(v_y/v_t)(L_T/L_v) = -0.04$, the average $k_x\rho$ in $|\Phi^2|$ is of order 10 and the FLR effects effectively damp the mode to very low growth rates.

The amount of sheared perpendicular flow required to stabilize the mode may be roughly estimated by finding the value for which the rate of (linear) radial decorrelation is comparable to the growth rate. Upon using the expression for $\mathbf{v}_0\cdot\nabla$ found immediately after Eq. (D.1) and assuming the mode has a width Δ_x, one is led to

$$\frac{v_y}{L_v}\Delta_x\frac{\partial}{\partial y} \sim \omega \sim \langle k_\parallel \rangle\, v_t.$$

The latter relation has been noted by Kotschenreuther [KOTSCHENREUTHER, 1991] and has been found to reasonably accurate for a wide range of parameter space in

my own investigations. The critical shear-flow value is then given by

$$\left(\frac{v_y}{v_t}\frac{L_T}{L_v}\right)_{\rm crit} \sim \frac{L_T}{L_s}.$$

For the parameters shown in Fig. (D.2), this quantity is $v'_{y\rm crit} \sim 0.016$; the numerically obtained value is $v'_{y\rm crit} \sim 0.04$. The discrepancy is not important in light of the fact that this parameter is often about unity in the nonlinear simulations presented in Chap. 8. The important point is that stabilization does occur, and that the gyrofluid equations recover this behavior. Magnetic shear determines the planes along which $\mathbf{E}\times\mathbf{B}$ flows exist. In the shearless limit, one finds that sheared flows give way to convective cells [Cheng and Okuda, 1977], which are observed to increase transport. Thus, understanding the $L_s \to \infty$ limit is non-trivial.

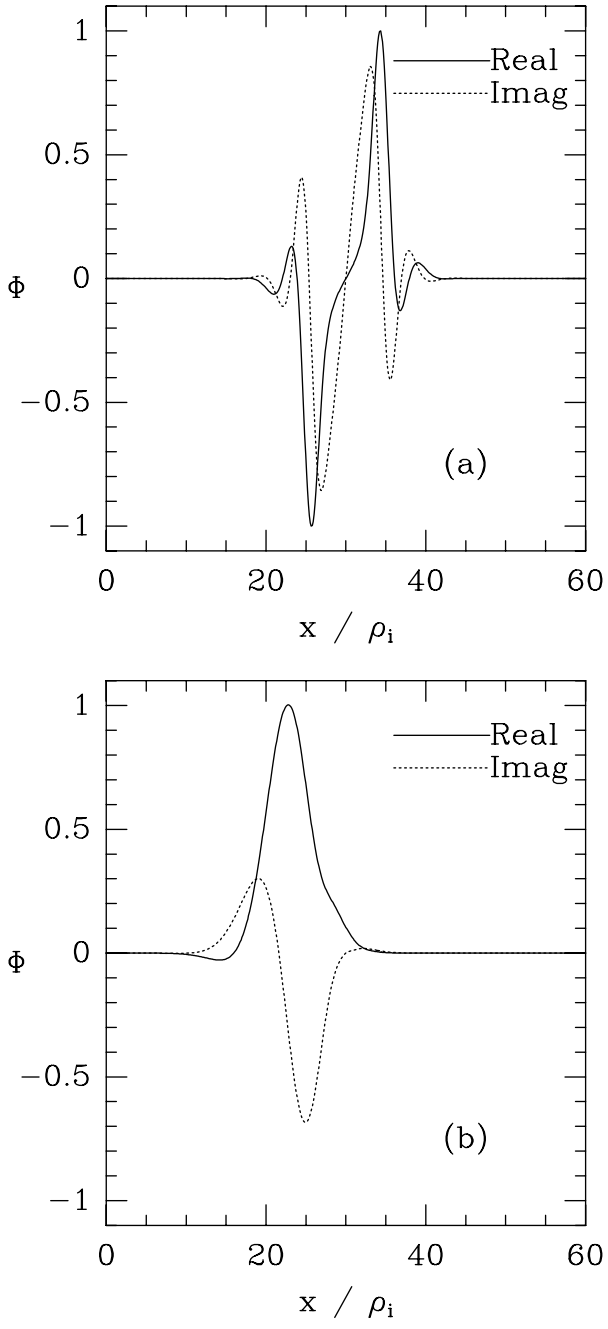

Figure D.1: Most unstable linear eigenmodes for the parameters $\eta_i = 4$, $L_s/L_n = 16.0$, $k_y\rho_i = 0.6$, $T_i = T_e$, and (a) $v_y' = 0$, (b) $(v_y/v_t)(L_T/L_v) = -0.02$.

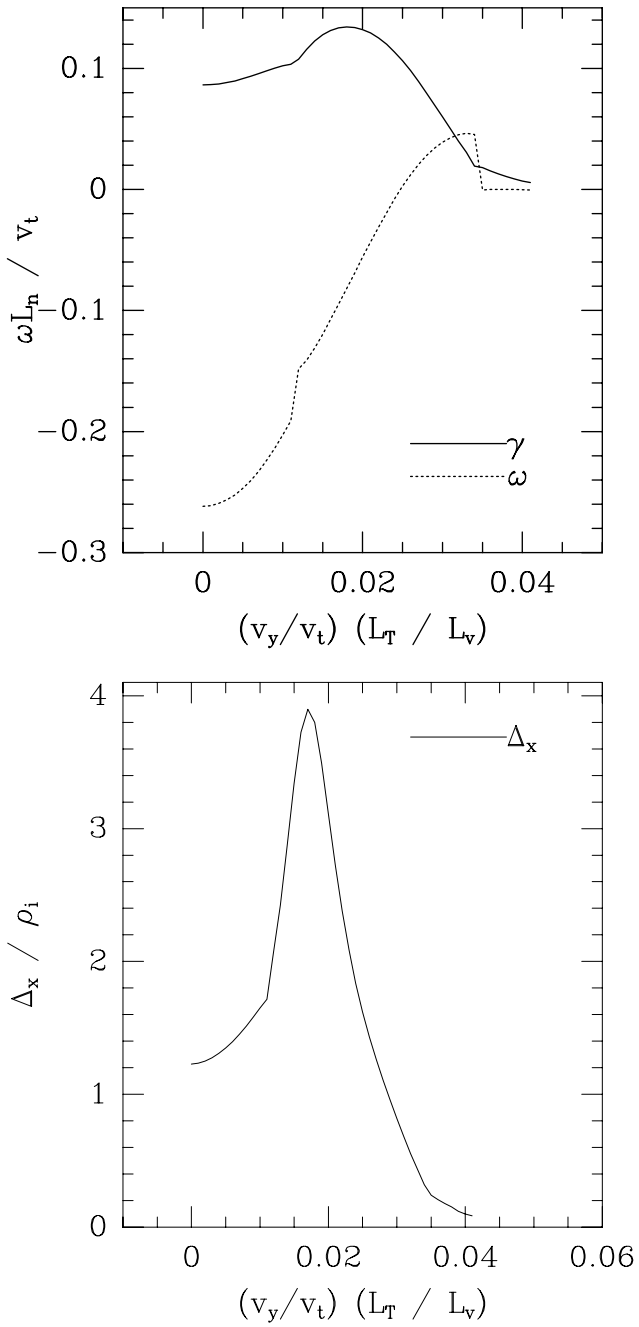

Figure D.2: The most unstable linear eigenmodes for the parameters $\eta_i = 4$, $L_s/L_n = 16.0$, $k_y\rho_i = 0.6$, and $T_i = T_e$. Shown are (a) the frequencies and (b) the average radial (x) mode width Δ_x/ρ_i.

Appendix E

Multi-Species Effects

THE ADDITION of impurities, alpha particles, or hot ion populations (from an RF heating scheme or neutral-beam injection, for example) to the gyrofluid framework is straightforward if each species is modelled as approximately Maxwellian at the appropriate temperature. Recently, Kotschenreuther [KOTSCHENREUTHER, 1993] has emphasized the role of impurities on the stability of the ITG mode. Presently, the code outlined in this thesis handles an arbitrary number of such species, with all of the physics and model options available to the majority species. The parameters that must be specified for each additional species are the charge (Z_s), mass, (M_s), temperature (T_s), gradients (η_s) and concentration (c_s). The additional equations are closed with the closures described in Chap. 2. Thus, the physics of a strongly non-Maxwellian component may be poorly represented. Upgrading the closure to reflect non-Maxwellian distributions has not been investigated here, but would be an interesting and useful exercise.

It is convenient to express the atomic number, mass, and temperature of each impurity species relative to the majority ion species. That is, $\mu_s \equiv M_s/M_i$, $T_s \equiv T_s/T_i$, and $Z_s \equiv q_s/q_i$, where M_s is the mass of the impurity ion, T_s is the temperature of the impurity ions, and so on. The normalized gyroradius and normalized thermal velocity are then defined by

$$\rho_s \equiv \frac{\sqrt{\tau_s \mu_s}}{Z_s}, \qquad\qquad v_{ts} \equiv \sqrt{\frac{\tau_s}{\mu_s}}.$$

Upon using these definitions and making the additional assumption that $L_{ns} = L_{ni}$ (constant Z_{eff} profile) one finds that the dynamical equations assume a simple form.

The latter assumption should be relaxed in the future. The major modification is in the normalization of the perpendicular derivatives, where $k_\perp \rho_s$ replaces $k_\perp \rho_i$ in the arguments of the gyroaveraging operators.

$$\frac{dn_s}{dt} + \left[\tfrac{1}{2}\rho_s^2 \hat{\nabla}_\perp^2 \mathbf{v}_{\Psi_s}\right] \cdot \nabla T_{\perp s} + \mathcal{N}_{21} T_{\perp s} + \hat{\mathbf{b}} \cdot \nabla u_{\parallel s} + \left[1 + \eta_{s\perp} \tfrac{1}{2}\rho_s^2 \hat{\nabla}_\perp^2\right] \frac{\partial \Psi_s}{\partial y} = 0, \quad \text{(E.1)}$$

$$\frac{du_{\parallel s}}{dt} + \left[\tfrac{1}{2}\rho_s^2 \hat{\nabla}_\perp^2 \mathbf{v}_{\Psi_s}\right] \cdot \nabla q_{\perp s} + \mathcal{N}_{21} q_{\perp s} + v_s^2 \, \hat{\mathbf{b}} \cdot \nabla \left(T_{\parallel s} + n + \frac{Z_s}{\tau_s}\Psi_s\right) = 0, \quad \text{(E.2)}$$

$$\frac{dT_{\parallel s}}{dt} + \left[\tfrac{1}{2}\rho_s^2 \hat{\nabla}_\perp^2 \mathbf{v}_{\Psi_s}\right] \cdot \nabla r_{\perp s} + \mathcal{N}_{21} r_{\perp s} + \hat{\mathbf{b}} \cdot \nabla (2u_{\parallel s} + q_{\perp s}) + \eta_{s\parallel} \frac{\partial \Psi_s}{\partial y} = 0, \quad \text{(E.3)}$$

$$\frac{dq_{\parallel s}}{dt} + \left[\tfrac{1}{2}\rho_s^2 \hat{\nabla}_\perp^2 \mathbf{v}_{\Psi_s}\right] \cdot \nabla s_\perp + \mathcal{N}_{21} s_\perp + v_s^2 \, \hat{\mathbf{b}} \cdot \nabla (3 + \beta_\parallel) T_{\parallel s} + \sqrt{2} v_s |k_\parallel| \, D_\parallel q_{\parallel s} = 0, \quad \text{(E.4)}$$

$$\frac{dT_{\perp s}}{dt} + \left[\tfrac{1}{2}\rho_s^2 \hat{\nabla}_\perp^2 \mathbf{v}_{\Psi_s}\right] \cdot \nabla n_s + \rho_s^2 \left[\hat{\hat{\nabla}}_\perp^2 \mathbf{v}_{\Psi_s}\right] \cdot \nabla T_{\perp s} + \mathcal{N}_{22} T_{\perp s}$$
$$+ \hat{\mathbf{b}} \cdot \nabla q_{\perp s} + \left[\tfrac{1}{2}\rho_s^2 \hat{\nabla}_\perp^2 + \eta_{s\perp}(1 + \rho_s^2 \hat{\hat{\nabla}}_\perp^2)\right] \frac{\partial \Psi_s}{\partial y} = 0, \quad \text{(E.5)}$$

$$\frac{dq_{\perp s}}{dt} + \left[\tfrac{1}{2}\rho_s^2 \hat{\nabla}_\perp^2 \mathbf{v}_{\Psi_s}\right] \cdot \nabla u_{\parallel s} + \rho_s^2 \left[\hat{\hat{\nabla}}_\perp^2 \mathbf{v}_{\Psi_s}\right] \cdot \nabla q_{\perp s} + \mathcal{N}_{22} q_{\perp s}$$
$$+ v_s^2 \hat{\mathbf{b}} \cdot \nabla \left(r_{\perp s} + T_{\perp s} + \frac{Z_s}{\tau_s} \tfrac{1}{2}\rho_s^2 \hat{\nabla}_\perp^2 \Psi_s\right) = 0, \quad \text{(E.6)}$$

$$\frac{dr_{\perp s}}{dt} + \left[\tfrac{1}{2}\rho_s^2 \hat{\nabla}_\perp^2 \mathbf{v}_{\Psi_s}\right] \cdot \nabla T_{\parallel s} + \mathcal{N}_{22} r_{\perp s} + \rho_s^2 \left[\hat{\hat{\nabla}}_\perp^2 \mathbf{v}_{\Psi_s}\right] \cdot \nabla r_{\perp s}$$
$$+ \hat{\mathbf{b}} \cdot \nabla (2q_{\perp s} + s_{\perp s}) + \eta_{s\parallel} \tfrac{1}{2}\rho_s^2 \hat{\nabla}_\perp^2 \frac{\partial \Psi_s}{\partial y} = 0, \quad \text{(E.7)}$$

$$\frac{ds_{\perp s}}{dt} + \left[\tfrac{1}{2}\rho_s^2 \hat{\nabla}_\perp^2 \mathbf{v}_{\Psi_s}\right] \cdot \nabla q_{\parallel s} + \mathcal{N}_{22} s_\perp + \rho_s^2 \left[\hat{\hat{\nabla}}_\perp^2 \mathbf{v}_{\Psi_s}\right] \cdot \nabla s_{\perp s}$$
$$+ v_s^2 \, \hat{\mathbf{b}} \cdot \nabla (3 + \beta_\parallel) r_{\perp s} + \sqrt{2} v_s |k_\parallel| \, D_\parallel s_{\perp s} = 0. \quad \text{(E.8)}$$

Poisson's equation [Eq. (2.69)] must also be modified to reflect the additional species. The generalization is

$$\tau(\Phi - \langle\langle \Phi \rangle\rangle) = \sum_s Z_s c_s \left[\bar{n}_s + (\Gamma_{0s} - 1)\frac{Z_s}{\tau_s}\Phi\right],$$

where $c_s \equiv n_{0s}/n_{0e}$ and

$$\bar{n}_s \equiv \frac{\Gamma_{0s}^{1/2}}{D_s}\left[N_s n_s + \tfrac{1}{2}\rho_s^2 \hat{\nabla}_\perp^2 T_{\perp s}\right].$$

The normalizations used are

$$\left(\frac{n_{s1}}{n_0}, \frac{u_{\parallel s1}}{v_{ti}}, \frac{T_{\parallel s1}}{T_{0s}}, \frac{q_{\parallel s1}}{v_{ti}p_{0s}}, \frac{T_{\perp s1}}{T_{0s}}, \frac{q_{\perp s1}}{v_{ti}p_{0s}}, \frac{r_{\perp s1}}{n_{0s}T_{0s}^2}, \frac{s_{\perp s1}}{v_{ti}T_{0s}^2}\right)$$

$$= \frac{\rho_i}{L_n}(\tilde{n}_s, \tilde{u}_{\parallel s}, \tilde{T}_{\parallel s}, \tilde{q}_{\parallel s}, \tilde{T}_{\perp s}, \tilde{q}_{\perp s}, \tilde{r}_{\perp s}, \tilde{s}_{\perp s}). \qquad \text{(E.9)}$$

The effect of impurities on sheared rotation may be roughly estimated by looking at the flux-surface averaged quasineutrality constraint in the long-wavelength limit:

$$0 = \langle\!\langle \sum_s Z_s c_s \left[\bar{n}_s + (\nabla_\perp^2 \rho_s^2)\frac{Z_s}{\tau_s}\Phi\right]\rangle\!\rangle,$$

$$\sum_s Z_s c_s \langle\!\langle \bar{n}_s \rangle\!\rangle = \left(\sum_s \mu_s c_s\right) \langle\!\langle \frac{\partial E_x}{\partial x}\rangle\!\rangle.$$

The term in parentheses on the right-hand side of this expression is the effective mass of the ions. Unless the plasma is dominated by impurities, then, the impurities will likely have only a small effect on the rotation. The self-generated shear flow is somewhat weaker (and therefore less stabilizing) in the presence of massive impurities. From the point of view of the conservation of angular momentum, this makes sense, since the greater the mass of the plasma, the more difficult it should be to spin. Slower rotation corresponds to weaker differential rotation effects.

On the other hand, the presence of the charge on the left-hand side indicates that the greater the charge of a given impurity species, the greater the corresponding contribution to the shear flow. Again, this is a weak effect unless the plasma is dominated by impurities. The effect of the rotation on the impurities might be interesting, however, and deserves futher investigation.

Appendix F

Non-adiabatic Electron Model

BECAUSE $\rho_e/\rho_i \propto \sqrt{m_e/m_i} \ll 1$, the drift-kinetic equation is adequate to describe the electron dynamics in the low-frequency limit considered here. Consequently, the electron fluid equations may be recovered from the derivation of the ion equations by taking the $k_\perp \rho_e \ll 1$ limit (and noting the change of the sign of the charge). The neglect of the FLR effects results in considerable simplification. First, perpendicular moments (such as $T_\perp, q_\perp$, *etc.*) are completely decoupled from the parallel moments; they are needed to describe the evolution of the perpendicular temperature perturbations, important (for example) in the case of magnetically trapped electrons. Second, nonlinear phase-mixing, fundamentally related to the differential drifts of particles with different Larmor radii, is not significant for the electrons. Finally, the remainder of the linear and nonlinear terms ($\propto \nabla_\perp^2$) that are necessary to describe the ion FLR dynamics do not appear in the electron equations. Electron collisions could be modeled using a Krook model, with the same kind of modifications suggested for the ions in App. B.6.

The normalizations for the electron density, momentum, *etc.* are given by

$$\left(\frac{n_{e1}}{n_0}, \frac{u_{e1}}{v_{ti}}, \frac{T_{\parallel e1}}{T_e}, \frac{q_{\parallel e1}}{v_{ti} n_0 T_e}, \frac{T_{\perp e1}}{T_e}, \frac{q_{\perp e1}}{v_{ti} n_0 T_e} \right) = \frac{\rho_i}{L_n} (\tilde{n}_e, \tilde{u}_e, \tilde{T}_{\parallel e}, \tilde{q}_{\parallel e}, \tilde{T}_{\perp e}, \tilde{q}_{\perp e}). \quad \text{(F.1)}$$

Upon introducing the ratio of thermal velocities parameter $v_e \equiv v_{te}/v_{ti}$, one finds that the equations are

$$\frac{dn_e}{dt} + \hat{\mathbf{b}} \cdot \nabla u_e + \frac{\partial \Phi}{\partial y} = 0, \quad \text{(F.2)}$$

$$\frac{du_e}{dt} + v_e^2 \hat{\mathbf{b}} \cdot \nabla \left(T_{\parallel e} + n_e - \tau \Phi \right) = 0, \tag{F.3}$$

$$\frac{dT_{\parallel e}}{dt} + \hat{\mathbf{b}} \cdot \nabla (2u_e + q_{\parallel e}) + \eta_{e\parallel} \frac{\partial \Phi}{\partial y} = 0, \tag{F.4}$$

$$\frac{dq_{\parallel e}}{dt} + v_e^2 \hat{\mathbf{b}} \cdot \nabla (3 + \beta_\parallel) T_{\parallel e} + \sqrt{2} v_e |k_\parallel| \, D_\parallel q_{\parallel e} = 0, \tag{F.5}$$

$$\frac{dT_{\perp e}}{dt} + \hat{\mathbf{b}} \cdot \nabla q_{\perp e} + \eta_{\perp e} \frac{\partial \Phi}{\partial y} = 0, \tag{F.6}$$

$$\frac{dq_{\perp e}}{dt} + v_e^2 \hat{\mathbf{b}} \cdot \nabla T_{\perp e} + \sqrt{\frac{\pi}{2}} v_e |k_\parallel| \, q_{\perp e} = 0. \tag{F.7}$$

Unlike the ions, which are convected by the gyro-averaged potential, electrons see the local potential. Hence, the total time derivative becomes

$$\frac{d}{dt} = \frac{\partial}{\partial t} + \mathbf{v}_E \cdot \nabla.$$

Note that if one wishes to use fewer equations to describe the electron response, one may find the proper closure coefficients using the moment-reduction scheme outline in Chap. 2.3.3. One should use Eq. (2.4) in place of Eq. (2.69) when the electron dynamics are retained.

Presently, the electron equations are advanced implicitly to allow reasonable time steps. However, the implicit scheme I am using is not unconditionally stable. Consequently, for realistic mass ratios, the time step tends to be smaller by a factor of 10–20. While this is an improvement over the factor of 40–60 expected for an explicit scheme (for hydrogen or deuterium plasmas), I have not pursued this avenue of research in detail as a result. Furthermore, one would expect the nonadiabatic electron response to be a weak effect in a sheared-slab setting, since an appreciable electron response occurs only very near rational surfaces. I have developed this model in anticipation of simulating more complex geometries.

Appendix G

Sample Input File for ITG

This input namelist file re-creates the run used for Fig. (B.1). It is provided to give the reader a feel for the actual ITG code.

```
! input namelist for itg.
$wdat
!
!---------------------Make a note about this run-------------------
!
note='This message appears on the first page of the output.'
!
!----------------------Specify Grid Details----------------------

ldb=64          ! # of gridpoints in the x (radial) direction
                ! ldb should be of the form (2^n * 3^m * 5^p)

md=-1           ! number of modes in the +y direction
                ! (and thus only half of the total y modes)
                ! md should be of the form (2^n * 3^m * 5^p) + 1
                ! for nonlinear runs [e.g., md=2,3,4,5,6,7,9 etc.]

                ! LINEAR RUNS ONLY:
                ! md=-1 allows you to specify mlow and mhi
```

```
mlow=1          ! mmin for each n
mhi=1           ! mmax for each n

nd=1            ! number of modes in the z direction: should be odd
                ! and of the form (2^n * 3^m * 5^p) + 1
                ! nd=-1 implies 1 mode with n=1
                ! (for shearless cases)

x0=40.00        ! Box width Lx in the x direction (units of rho_i)
y0=2.0          ! ky = m / (y0 rho_i);   Ly = 2 pi y0 rho_i
z0=10.00        ! kz = n / (z0 Ln, L_T); Lz = 2 pi z0 Ln (or L_T)

iperiod=0       ! iperiod = 0 -> 0 radial b.c.'s
                ! iperiod = 1 -> periodic radial b.c.'s
                ! iperiod = 2 -> twisted periodic radial b.c.'s

nrat=0          ! If iperiod=2, m=1,n=nrat determines z0 by
                ! requiring the (1,nrat) rational surface to lie
                ! on the edge of the periodic domain.
                !
xp=0.           ! If iperiod=2, xp is roughly the distance the
                ! computational box is extended (radially) in
                ! one direction beyond the (1,nrat) rational
                ! surface. The exact value is determined by the
                ! nearest grid point.  That is, the physical Lx is
                ! Lx = x0 - 2 r(ld*xp/x0).
                ! The code enforces (xp .le. x0 / 3.)
!
!----------------------Physics parameters-------------------------
!
norm=0          ! Normalize to L_n or L_T.  Default is L_n.
                ! norm = 0 -> L_n,  norm = 1 -> L_T
shr=0.025       ! shear parameter s=Ln/Ls or eta_s=L_T/L_s
                ! depending on the value of norm.
```

```
etai=2.0        ! L_n/L_T_perp.  If norm=1, etai=0 is a bad value
                ! and etaipar=etai regardless of the next line.
etaipar=2.0     ! L_n/L_T_||. Default is to set etaipar = etai.
                !
vy=0.0          ! vy/Lv (imposed sheared perpendicular flow)
vz=0.0          ! vz/Lv (imposed sheared parallel flow)
                ! Both flows are normalized to L_T / v_t
                ! regardless of the value of norm.
tiovte=1.0      ! Ti/Te
                !
nspecies=1      ! number of ion species (if nspecies > 1,
                ! change cnstnts.f to reflect the charges,
                ! masses and concentrations of the ions).

ilx=0           ! 0 -> adiabatic electrons,
                ! 1 -> full electron equations
etae=2.0        ! L_n/L_T (for the electrons)
rmime=1837.0    ! m_i / m_e

!
!---------------------Specify time step--------------------------
!

idt=1           ! idt=1 -> adjustable time step. idt=0 -> dt=dt0
                ! Time step adjusts only for nonlinear runs.
                ! Default: idt=1
dt0=1.0         ! maximum (and initial) time step allowed
                ! (in units of Ln/v_t or L_T/v_t depending on norm)
nstp=1000       ! Total # of time steps to take
nprnt=10        ! Keep intermediate results every nprnt steps
implicit=0      ! Take an implicit time step if istep=1.

!
!------------------Choose number of moments to keep--------------
```

```
!

nparmom=3      ! number of parallel moments (3,4).  Default
               ! value is 4.

nperpmom=3     ! number of perpendicular moments (1-4).  Default
               ! value is 2.

!
!--------------------Choose FLR model----------------------------
!

iflr=3         ! Select a model for <J_0>:
               ! 1=1/(1+b/2)
               ! 2=not an option (for debugging)
               ! 3=Gamma_0^(1/2) (Default)
               ! 4=exp(-b/2)
               ! 5=1-b/2
               ! 6=No Linsker effect (3 or 4 + 0 models)
               ! 7=Real space Taylor series equations
               ! 8=No FLR effects at all.

beta=0.0       ! filter width for particle shapes (see iflr)
               ! phi = Exp[-beta^2 k^2]*n_i etc.
               ! Set beta=0. for no shaping.

!
!-------------------Choose damping model-----------------------
!
               ! Always use Hammett-Perkins linear Landau damping
               ! model.Select perpendicular damping models
               ! for nonlinear cases:
               !
inlpm=0        ! 1->Use nonlinear phase mixing model
```

```
               ! ikx=2 is necessary for this option to work.
               !
ifilter=0      ! 0 -> no moment filters
               ! 1 -> filter each moment at every time step
               !      with an implicit viscosity, hyperviscosity,
               !      etc., determined by nuii. For example,
               !      n -> n/(1 + dt*nuii*b**2).
               !      v -> v/(1 + dt*nuii*b).
               !
nuii=0.000     ! damping coefficient in filter and/or
               ! Krook collision operator
               !
krook=0        ! 1 -> Use the Krook operator with
               ! coefficient nuii.
               !
!
!------------------------Miscellaneous-----------------------
!

lin=1          ! 0= nonlinear  1=linear
               !
nsafe=0        ! # of intermediate save files
               ! (for emergency restarts)
               !
ikx=2          ! 1 -> finite difference for d/dx in NL terms
               ! 2 -> spectral (i*kx) for d/dx in NL terms
               !
iodd=2         ! 1 -> odd modes initialized
               ! 2 -> even modes initialized
               ! 0 -> both initialized  -- (Default is iodd = 0)

igradon=0      ! 2=Remove the (m=0,n=0) component of all moments
               ! 1=Constant bkgd pressure gradient, no (m=0,n=0)
               ! mode in parallel or perpendicular pressure.
```

```
                ! 0=Keep the (m=0,n=0) modes

 iphi00=2       ! 0 -> set phi(ky=0,kz=0)=0
                ! iphi00=2 (presently the default) uses Hamaguchi's
                ! method, which allows non-physical electron
                ! transport.
                ! iphi00=2 (presently the default) uses Hammett's
                ! method which ensures that there is no cross-field
                ! particle transport when adiabatic electrons
                ! are assumed.

 nread=0        ! initial conditions 0=set by code 1=read from file
                ! 0=initialized by the code using PMAG (below).
                ! 1=read initial conditions from the file ITG.RESP,
                ! which is a copy of the results file ITG.RES from a
                ! previous run of ITG.  This option is used to start
                ! where a previous run finished.

 pmag=1.e-20    ! initial magnitudes of perturbations
 ntrace=1       !(0,1) -> (off,on) (watch time steps go by)
 movieon=90000  ! Begin filming (NCSA-HDF) on this time step
 ninterv=10     ! Make a movie frame every ninterv time step.
 ihdf=1         ! 1->hdf,0->phi(x,y) is written into itg.fields
                ! for time steps after MOVIEON
                ! and at intervals NINTERV.  Default is ihdf=1.
 $end
 $xstuff
 xgrafix=0      ! 1 -> Use Peter Liu's X-windows interface
 phi_v_time=0   ! 1 -> Open Phi vs. time window
 phi_v_x=0      ! 1 -> Open Phi vs x animation
 energy_v_time=0! 1 -> Open energy vs. time window
 gamma_v_time=0 ! 1 -> Open growth rate vs. time window
 $end
```

Appendix H

Symbolic Algebra Script for Gyrofluid Dispersion Relation

For reference, I obtained the following six roots upon running *Maple* V.2 with this script: $\omega_1 = -0.2110988258 - 0.1621487371i$, $\omega_2 = -0.1416719426 + 0.07129201067i$, $\omega_3 = -0.06831743085 - 0.06998323722i$, $\omega_4 = 0.06151314904 - 0.2032132654i$, $\omega_5 = 0.06977519789 - 0.06771730455i$, and $\omega_6 = 0.2572503397 - 0.04542318297i$. The unstable root ($\omega_2$) falls on the 4+2 curve shown in Fig. (3.1b).

```
# *************   Maple input file   *************
#
# This routine generates the 4+2 gyrofluid dispersion
# relation for arbitrary forms of the FLR approximations for
# <J_0> and <J_0^2>.  <J_0^2> enters only in the quasineutrality
# constraint.  The starting equations may be found in Dorland
# and Hammett, Phys. Fl. B, Vol. 5, (812) 1993, Eqs. 56-62
# (linearized).
#*************************************************************
# Choose an approximation to <J_0>.

j0 := proc(b) BesselI(0,b)^(1/2)*exp(-b/2) end:
#j0 := proc(b) 1/(1+b/2) end:
#j0 := proc(b) exp(-b/2) end:
```

```
# Choose an approximation to <J_0^2>.

g0 := proc(b) BesselI(0,b)*exp(-b) end:
#g0 := proc(b) 1/(1+b) end:
#************************************************************
#
# The 4+2 gyrofluid equations in the local linear limit
# are given by e1 -- e6.  The notation used is transparent, with
# the possible exception of skpar, which represents the sign
# of kpar.
#

e1 := -I*w*n + I*kpar*v + (1+eta*b*diff(log(j0(b)),b))*I*ky*psi = 0:
e2 := -I*w*v + I*kpar*(n+tpar) + I*kpar*psi = 0:
e3 := -I*w*tpar + I*kpar*(2*v+qpar) + I*ky*psi*eta = 0:
e4 := -I*w*qpar + I*kpar*(3+beta)*tpar + skpar*kpar*D1*qpar = 0:
e5 := -I*w*tperp + I*kpar*qperp + I*ky*psi*(b*diff(log(j0(b)),b)
       + eta*(1+b*diff(j0(b)+b*diff(j0(b),b),b)/j0(b))) = 0:
e6 := -I*w*qperp + I*kpar*(tperp + b*diff(log(j0(b)),b)*psi)
       + skpar*kpar*D2*qperp = 0:

# The quasineutrality constraint is given by e7.

e7 := (tau + (1 - g0(b)))*psi =j0(b)^2/
        (1+b*diff(j0(b)+b*diff(j0(b),b),b)/j0(b)
        -(b*diff(log(j0(b)),b))^2)
        *((1+b*diff(j0(b)+b*diff(j0(b),b),b)/j0(b)
        -2*(b*diff(log(j0(b)),b))^2)*n
        +b*diff(log(j0(b)),b)*tperp):

# Now solve for the dispersion relation, substituting
# the values of the closure coefficients along the way:
```

```
e8  := solve({e1,e2,e3,e4,e5,e6},{n,v,tpar,qpar,tperp,qperp}):
e9  := subs(e8,e7):
e10 := subs({psi=1,D2=sqrt(Pi/2)},e9):
e11 := subs({beta=(32-9*Pi)/(3*Pi-8),D1=2*sqrt(2*Pi)/(3*Pi-8)},e10):
e12 := subs({skpar=1},e11):
e13 := denom(rhs(e12)):
e14 := numer(rhs(e12)):
e15 := e13*lhs(e12) - e14 = 0:

# Evaluate the dispersion relation for some specific parameters:

numdr := evalf(subs(kpar=.1,b=ky**2,eta=2,tau=1,e15)):
fsolve(evalf(subs(ky=1.0,numdr)),w,complex);

# ************  end of Maple input file   *************
```

Bibliography

Artun, M., Reynders, J. V. W., and Tang, W. M. (1993). Integral Eigenmode Analysis of Ion Temperature Gradient Modes in the Presence of Sheared Flows. Accepted for publication by Phys. Fluids B.

Artun, M. and Tang, W. M. (1992). Gyrokinetic Analysis of Ion Temperature Gradient Modes in the Presence of Sheared Flows. *Phys. Fluids B* **4**, 1102.

Aydemir, A. Y. (1991). Linear Studies of $m = 1$ Modes in High-Temperature Plasmas with a Four-Field Model. *Phys. Fluids B* **3**, 3025.

Bakshi, P., Bellew, W., Ganguli, G., and Satyanarayana, P. (1977). Presented at the 1977 Sherwood Theory Conference.

Beer, M. A. and Hammett, G. W. (1992). Private communication.

Beer, M. A., Hammett, G. W., Dorland, W., and Cowley, S. C. (1992). Nonlinear Ballooning Gyrofluid Simulations of Toroidal ITG Turbulence. *Bull. Am. Phys. Soc.* **37**, 1478.

Beer, M. A., Hammett, G. W., Dorland, W., and Cowley, S. C. (1993). Nonlinear Gyrofluid Simulations of Toroidal ITG Turbulence. Presented at the 1993 Sherwood Theory Conference.

Bell, M. G., Arunasalam, V., Barnes, C. W., Bitter, M., Bosch, H.-S., L.Bretz, N., Budny, R., Bush, C. E., Cavallo, A., Chu, T. K., Cohen, S. A., Colestock, P. L., Davis, S. L., Dimock, D. L., Dylla, H. F., Efthimion, P. C., Ehrhardt, A. B., Fonck, R. J., Frederickson, E. D., Furth, H. P., Gammel, G., Goldston, R. J., Greene, G. J., Grek, B., Grisham, L. R., Hammett, G. W., Hawryluk, R. J., Hendel, H. W., Hill, K. W., Hinnov, E., Hosea, J. C., Howell, R. B., Hsuan, H., Hulse, R. A., Jaehnig, K. P., Janos, A. C., Jassby, D. L., Jobes,

F. C., Johnson, D. W., Johnson, L. C., Kaita, R., Kieras-Phillips, C., Kilpatrick, S. J., Krupin, V. A., LaMarche, P. H., Langer, W. D., LeBlanc, B., Little, R., Lysojvan, A. I., Manos, D. M., Mansfield, D. K., Mazzucato, E., McCann, R. T., McCarthy, M. P., McCune, D. C., McGuire, K. M., McNeill, D. H., Meade, D. M., Medley, S. S., R.Mikkelsen, D., Motley, R. W., Mueller, D., Murakami, Y., Murphy, J. A., Nieschmidt, E. B., Roquemore, A. L., Rutherford, P. H., Saito, T., Sauthoff, N. R., Schilling, G., Schivell, J., Schmidt, G. L., Scott, S. D., Sinnis, J. C., Stevens, J. E., Stodiek, W., Stratton, B. C., Tait, G. D., Taylor, G., Timberlake, J. R., Towner, H. H., Ulrickson, M., von Goeler, S., Wieland, R. M., Williams, M. D., Wilson, J. R., Wong, K.-L., Yoshikawa, S., Young, K. M., Zarnstorff, M. C., and Zweben, S. J. (1989). An Overview of TFTR Confinement with Intense Neutral Beam Heating. In *Plasma Physics and Controlled Nuclear Fusion Research, 1988*, volume 1, page 27, International Atomic Energy Agency, Vienna.

Bender, C. M. and Orszag, S. A. (1978). *Advanced Mathematical Methods for Scientists and Engineers*. McGraw-Hill Book Company, New York.

Bowman, J. C. (1992). *Realizable Markovian Statistical Closures: General Theory and Application to Drift-Wave Turbulence*. PhD thesis, Princeton University.

Brizard, A. (1992). Nonlinear Gyrofluid Description of Turbulent Magnetized Plasmas. *Phys. Fluids B* **4**, 1213.

Callen, J. D., Carreras, B. A., and Stambaugh, R. D. (January, 1992). Stability and Transport Processes in Tokamak Plasmas. *Physics Today* , 34.

Carreras, B. A. and Lynch, V. E. (1991). Electron Diamagnetic Effects on the Resistive Pressure-Gradient-Driven Turbulence and Flow Generation. *Phys. Fluids B* **3**, 1438.

Cen, R. Y., Jameson, A., Liu, F., and Ostriker, J. P. (1990). The Universe in a Box: Thermal Effects in the Standard Cold Dark Matter Scenario. *Astro. J.* **362**, L41.

CHANG, Z. and CALLEN, J. D. (1992a). Unified Fluid/Kinetic Description of Plasma Microinstabilities. Part I: Basic Equations in a Sheared Slab Geometry. *Phys. Fluids B* **4**, 1167.

CHANG, Z. and CALLEN, J. D. (1992b). Unified Fluid/Kinetic Description of Plasma Microinstabilities. Part II: Applications. *Phys. Fluids B* **4**, 1182.

CHAR, B. W., GEDDES, K. O., GONNET, G. H., LEONG, B. L., MONAGAN, M. B., and WATT, S. M. (1991). *Maple V Language Reference Manual.* Springer-Verlag, Toronto.

CHEN, L., BERGER, R. L., LOMINADZE, J. G., ROSENBLUTH, M. N., and RUTHERFORD, P. H. (1977). Nonlinear Saturation of the Dissipative Trapped-Electron Instability. *Phys. Rev. Lett.* **39**, 754.

CHENG, C. Z. and OKUDA, H. (1977). Formation of Convective Cells, Anomalous Diffusion, and Strong Plasma Turbulence Due to Drift Instabilities. *Phys. Rev. Lett.* **38**, 708.

CHENG, C. Z. and OKUDA, H. (1978a). Numerical Simulation of Trapped-Electron Instabilities in Toroidal Geometry. *Phys. Rev. Lett.* **14**, 1116.

CHENG, C. Z. and OKUDA, H. (1978b). Theory and Numerical Simulations on Collisionless Drift Instabilities in Three Dimensions. *Nucl. Fusion* **18**, 587.

CHEW, G. F., GOLDBERGER, M. L., and LOW, F. E. (1956). Boltzmann Equation and the One-Fluid Hydrodynamic Equations in the Absence of Particle Collisions. *Proc. Roy. Soc.* **A236**, 112.

CHING, H. C. (1973). Large-Amplitude Stabilization of the Drift Instability. *Phys. Fluids* **16**, 130.

COPPI, B., ROSENBLUTH, M. N., and SAGDEEV, R. Z. (1967). Instabilities Due to Temperature Gradients in Complex Magnetic Field Geometries. *Phys. Fluids* **10**, 582.

CORDEY, J. G., GOLDSTON, R. J., and PARKER, R. R. (January, 1992). Progress Toward a Tokamak Fusion Reactor. *Physics Today* , 22.

COWLEY, S. C. (1993). Private communication.

COWLEY, S. C., KULSRUD, R. M., and SUDAN, R. (1991). Considerations of Ion-Temperature-Gradient-Driven Turbulence. *Phys. Fluids B* **3**, 2767.

CROTINGER, J. A. (1989). *Simulation of Drift-Wave Turbulence: Trapped Structures and a New Nonadiabatic Electron Model.* PhD thesis, Massachusetts Institute of Technology.

DAVIDSON, R. C. (1972). *Nonlinear Plasma Theory.* Academic Press, New York.

DIAMOND, P. H. and KIM, Y.-B. (1986). Theory of Mean Poloidal Flow Generation by Turbulence. *Phys. Fluids* **29**, 3291.

DIAMOND, P. H. and LIANG, Y. (1993). An Analytical Model of Coupled Fluctuation and Flow Dynamics in Self-Regulating Turbulence. Presented at the 1993 Sherwood Theory Conference.

DIMITS, A. (1992). Supplemental paper presented at the APS-DPP meeting.

DIMITS, A., DRAKE, J. F., GUZDAR, P. N., and HASSAM, A. B. (1991). Ion-Temperature-Gradient-Driven Turbulence and Transport in a Sheared Magnetic Field. *Phys. Fluids B* **3**, 620.

DIMITS, A. M. and LEE, W. W. (1993). Partially Linearized Algorithms in Gyrokinetic Particle Simulations. *J. Comput. Phys.* **107**, 309.

DONG, J. Q. (1993). Presented at the 1993 Sherwood Theory Conference.

DONG, J. Q., GUZDAR, P. N., and LEE, Y. C. (1987). Finite Beta Effects on Ion Temperature Gradient Driven Modes. *Phys. Fluids* **30**, 2694.

DORLAND, W. and HAMMETT, G. W. (1991). 3D Gyrofluid Simulations of Electrostatic Ion Temperature Gradient Turbulence in a Sheared Slab. *14^{th} International Conference on the Numerical Simulation of Plasmas* , PWA6.

DORLAND, W. and HAMMETT, G. W. (1993). Gyrofluid Turbulence Models with Kinetic Effects. *Phys. Fluids B* **5**, 812.

DORLAND, W., HAMMETT, G. W., BEER, M. A., and HAHM, T. S. (1993a). Nonlinear Gyrofluid Simulations and Analysis: ITG Turbulence. Presented at the 1993 Sherwood Theory Conference.

DORLAND, W., HAMMETT, G. W., CHEN, L., PARK, W., COWLEY, S. C., HAMAGUCHI, S., and HORTON, W. (1990). Numerical Simulations of Nonlinear 3-D ITG Fluid Turbulence with an Improved Landau Damping Model. *Bull. Am. Phys. Soc.* **35**, 2005.

Dorland, W., Hammett, G. W., and Hahm, T. S. (1992a). Nonlinear Gyrofluid Simulation and Analysis. Presented at the 1992 Sherwood Theory Conference.

Dorland, W., Hammett, G. W., Hahm, T. S., and Beer, M. A. (1992b). Nonlinear and Linear FLR Effects in Gyrofluid Turbulence Simulations. *Bull. Am. Phys. Soc.* **37**, 1478.

Dorland, W., Hammett, G. W., Hahm, T. S., and Beer, M. A. (1993b). Nonlinear Gyrofluid Model of ITG Turbulence. In Horton, W., Wakatani, M., and Wootton, A., editors, *Ion Temperature Gradient Driven Turbulent Transport*. American Institute of Physics, New York.

Dorland, W., Hammett, G. W., Reynders, J. V. W., and Santoro, R. A. (1992c). Nonlinear Gyrofluid Simulations of ITG Turbulence in a Sheared Slab. *Bull. Am. Phys. Soc.* **36**, 2281.

Drummond, W. E. and Pines, D. (1962). *Nucl. Fusion Suppl. Pt. 3* , 1049.

Dubin, D. H. E. and Krommes, J. A. (1983). Stochasticity, Superadiabaticity, and Adiabatic Invariants. In Horton, Jr., C. W., Reichl, L. E., and Szebehely, V. G., editors, *Long-Time Prediction in Dynamics*, page 257. John Wiley and Sons, New York.

Dubin, D. H. E., Krommes, J. A., Oberman, C., and Lee, W. W. (1983). Nonlinear Gyrokinetic Equations. *Phys. Fluids* **26**, 3524.

Dupree, T. H. and Tetreault, D. J. (1978). Renormalized Dielectric Function for Collisionless Drift Wave Turbulence. *Phys. Fluids* **21**, 425.

Frey, J. (1991). Numerical Simulation of Semiconductor Devices. *14^{th} International Conference on the Numerical Simulation of Plasmas* , SIT.

Fried, B. D. and Conte, S. D. (1961). *The Plasma Dispersion Function*. Academic Press, New York.

Frieman, E. A. and Chen, L. (1982). Nonlinear Gyrokinetic Equations for Low-Frequency Electromagnetic Waves in General Plasma Equilibria. *Phys. Fluids* **25**, 502–508.

Galeev, A. A., Oraevskii, V. N., and Sagdeev, R. Z. (1963). 'Universal' Instability of an Inhomogeneous Plasma in a Magnetic Field. *Soviet Physics*

JETP **17**, 615.

GALEEV, A. A. and SAGDEEV, R. Z. (1984). *Basic Plasma Physics I*, volume 1 of *Handbook of Plasma Physics*. North-Holland Physics Publishing, New York.

GROEBNER, R. J., BURRELL, K. H., and SERAYDARIAN, R. P. (1990). Role of Edge Electric Field and Poloidal Rotation in the L-H Transition. *Phys. Rev. Letters* **64**, 3015.

GUZDAR, P. N., DRAKE, J. F., MCCARTHY, D., HASSAM, A. B., and LIU, C. S. (1993). Submitted to Phys. Fluids B.

HAHM, T. S., LEE, W. W., and BRIZARD, A. (1988). Nonlinear Gyrokinetic Theory for Finite-Beta Plasmas. *Phys. Fluids* **31**, 1940.

HAHM, T. S. and TANG, W. M. (1990). Weak Turbulence Theory of Ion-Temperature-Gradient Modes for Inverted Density Plasmas. *Phys. Fluids B* **2**, 1815.

HAMAGUCHI, S. and HORTON, W. (1990). Fluctuation Spectrum and Transport from Ion Temperature Gradient Driven Modes in Sheared Magnetic Fields. *Phys. Fluids B* **2**, 1833–1851.

HAMAGUCHI, S. and HORTON, W. (1992a). Effects of Sheared Flows on Ion-Temperature-Gradient-Driven Turbulent Transport. *Phys. Fluids B* **4**, 319.

HAMAGUCHI, S. and HORTON, W. (1992b). Modeling of Drift Wave Turbulence with a Finite Ion Temperature Gradient. *Plasma Physics and Controlled Fusion* **34**, 203–233.

HAMMETT, G. W. (1993). Private communication.

HAMMETT, G. W., BEER, M. A., and DORLAND, W. (1993). Developments in the Gyrofluid Approach to Tokamak Turbulence Simulations. Technical Report PPPL-2918, Princeton Plasma Physics Laboratory. 1993 Sherwood theory conference invited talk.

HAMMETT, G. W. and DORLAND, W. (1991). Nonlinear Gyrofluid Equations for 3D Simulations of ITG Turbulence in a Sheared Slab. Presented at the 1991 Sherwood Theory Conference.

HAMMETT, G. W., DORLAND, W., BEER, M. A., and COWLEY, S. C. (1992a). Progress on Toroidal and Nonlinear Effects in Gyrofluid Simulations of Tokamak

Turbulence. *Bull. Am. Phys. Soc.* **37**, 1554.

Hammett, G. W., Dorland, W., and Perkins, F. W. (1992b). Fluid Models of Nonlinear Gyrokinetic Dynamics and Landau Damping. *Bull. Am. Phys. Soc.* **36**, 2454.

Hammett, G. W., Dorland, W., and Perkins, F. W. (1992c). Fluid Models of Phase Mixing, Landau Damping, and Nonlinear Gyrokinetic Dynamics. *Phys. Fluids B* **4**, 2052.

Hammett, G. W. and Perkins, F. W. (1990). Fluid Models for Landau Damping with Application to the Ion-Temperature-Gradient Instability. *Phys. Rev. Lett.* **64**, 3019–3022.

Hasegawa, A. and Mima, K. (1977). Stationary Spectrum of Strong Turbulence in Magnetized Nonuniform Plasma. *Phys. Rev. Lett.* **39**, 205.

Hasegawa, A. and Wakatani, M. (1987). Self-Organization of Electrostatic Turbulence in a Cylindrical Plasma. *Phys. Rev. Letters* **59**, 1581.

Hassam, A. B. (1993). Possibility of Driving Perpendicular Rotation in Core Plasma by Off-Axis Neutral Beam Injection to Suppress Microturbulence. Presented at the 1993 Sherwood Theory Conference.

Hawryluk, R. J., Arunsalam, V., Bell, M. G., Bitter, M., Blanchard, W. R., Bretz, N. L., Budny, R. V., Bush, C. E., Callen, J. D., Cohen, S. A., Combs, S. K., Davis, S. L., Dimock, D. L., Dylla, H. F., Efthimion, P. C., Emerson, L. C., England, A. C., Eubank, H. P., Fonck, R. J., Frederickson, E., Furth, H. P., Gammel, G., Goldston, R. J., Grek, B., Grisham, L. R., Hammett, G. W., Heidbrink, W. W., Hendel, H. W., Hill, K. W., Hinnov, E., Hiroe, S., Hsuan, H., Hulse, R. A., Jaehnig, K. P., Jassby, D. L., Jobes, F. C., Johnson, D. W., Johnson, L. C., Kaita, R., Kamperschroer, R., Kaye, S. M., Kilpatrick, S. J., Knize, R. J., Kugel, H., LaMarche, P. H., LeBlanc, B., Little, R., Ma, C. H., Manos, D. M., Mansfield, D. K., McCann, R. T., McCarthy, M. P., McCune, D. C., McGuire, K., McNeill, D. H., Meade, D. M., Medley, S. S., Mikkelsen, D. R., Milora, S. L., Morris, W., Mueller, D., Mukhovatov, V., Nieschmidt, E. B., O'Rourke, J., Owens, D. K., Park, H., Pomphrey, N., Prichard, B.,

Ramsey, A. T., Redi, M. H., Roquemore, A. L., Rutherford, P. H., Sauthoff, N. R., Schilling, G., Schivell, J., Schmidt, G. L., Scott, S. D., Sesnic, S., Sinnis, J. C., Stauffer, F. T., Stratton, B. C., Tait, G. D., Taylor, G., Timberlake, J. R., Towner, H. H., Ulrickson, M., Vershkov, V., Goeler, S. V., Wagner, F., Wieland, R., Wilgen, J. B., Williams, M., Wong, K. L., Yoshikawa, S., Yoshino, R., Young, K. M., Zarnstorff, M. C., Zaveryaev, V. S., and Zweben, S. J. (1987). TFTR Plasma Regimes. In *Plasma Physics and Controlled Nuclear Fusion Research, 1986*, volume 1, page 51, International Atomic Energy Agency, Vienna.

Hazeltine, R. D., Hsu, C. T., and Morrison, P. J. (1987). Hamiltonian Four-Field Model for Nonlinear Tokamak Dynamics. *Phys. Fluids* **30**, 3204.

Hedrick, C. H. and Leboeuf, J.-N. (1992). Landau Fluid Equations for Electromagnetic and Electrostatic Fluctuations. *Phys. Fluids B* **4**, 3915.

Heppenheimer, T. A. (1984). *The Man-Made Sun: The Quest for Fusion Power*. Little, Brown and Company, Boston.

Hirshman, S. P. (1980). Two-Dimensional Electrostatic $\mathbf{E} \times \mathbf{B}$ Trapping. *Phys. Fluids* **23**, 562.

Horton, W. (1984). Drift Wave Turbulence and Anomalous Transport. In *Basic Plasma Physics II*, volume 2 of *Handbook of Plasma Physics*. North-Holland Physics Publishing, New York.

Horton, W., Estes, R. D., and Biskamp, D. (1980). Fluid Simulation of Ion Pressure Gradient Driven Drift Modes. *Plasma Physics* **22**, 663.

Horton, W., Lindberg, D., Kim, J. Y., Dong, J. Q., Hammett, G. W., Scott, S. D., and Zarnstorff, M. C. (1992). Ion-Temperature-Gradient-Driven Transport in a Density Modification Experiment on the Tokamak Fusion Test Reactor. *Phys. Fluids B* **4**, 953.

Kadomtsev, B. B. (1965). *Plasma Turbulence*. Academic Press, Reading, Massachusetts. edited by M. G. Rusbridge, translated by L. C. Ronson.

Kadomtsev, B. B. and Pogutse, O. P. (1970). In Leontovich, M. A., editor, *Review of Plasma Physics*, page 249. Consultants Bureau, New York. Vol. 2, No. 69.

KADOMTSEV, B. B. and POGUTSE, O. P. (1985). Self-Consistent Transport Theory in Tokamak Plasmas. In *Plasma Physics and Controlled Nuclear Fusion Research, 1984*, volume 2, page 69, International Atomic Energy Agency, Vienna.

KOTSCHENREUTHER, M. (1990). Heat Transport Calculations due to η_i Microturbulence by Kinetic Simulation Using the Low-Noise δf Algorithm. *Bull. Am. Phys. Soc.* **35**, 2035.

KOTSCHENREUTHER, M. (1991). Continuing Development and Applications of the δf Algorithm for Tokamaks. *Bull. Am. Phys. Soc.* **36**, 2435.

KOTSCHENREUTHER, M. (1993). Impurity Effects on ITG Turbulence. In HORTON, W., WAKATANI, M., and WOOTTON, A., editors, *Ion Temperature Gradient Driven Turbulent Transport*. American Institute of Physics, New York.

KOTSCHENREUTHER, M., BERK, H. L., DENTON, R., HAMAGUCHI, S., HORTON, W., KIM, C.-B., LEBRUN, M., LYSTER, P., MAHAJAN, S., MINER, W. H., MORRISON, P. J., ROSS, D., TAJIMA, T., TAYLOR, J. B., VALANJU, P. M., WONG, H. V., XIAO, S. Y., and ZHANG, Y.-Z. (1991). Novel Computational Techniques to Predict Transport in Confinement Devices, and Applications to Ion-Temperature-Gradient Driven Turbulence. In *Plasma Physics and Controlled Nuclear Fusion Research, 1990*, volume 2, page 361, International Atomic Energy Agency, Vienna.

KROMMES, J. A. (1980). Renormalized Compton Scattering and Nonlinear Damping of Collisionless Drift Waves. *Phys. Fluids* **23**, 736.

KROMMES, J. A. (1993). Private communication.

LEBOEUF, J.-N., CHARLTON, L. A., and CARRERAS, B. A. (1993). Shear Flow Effects on the Nonlinear Evolution of Thermal Instabilities. *Phys. Fluids B* **5**, 2959.

LEE, G. S. and DIAMOND, P. H. (1986). Theory of Ion-Temperature-Gradient-Driven Turbulence in Tokamaks. *Phys. Fluids* **29**, 3291.

LEE, W. W. (1983). Gyrokinetic Approach in Particle Simulation. *Phys. Fluids* **26**, 556.

LEE, W. W. (1987). Gyrokinetic Particle Simulation Model. *J. Comput. Phys.* **72**, 243.

Lee, W. W., Hahm, T. S., Parker, S. E., Perkins, F. W., Rath, S., Rewoldt, G., Reynders, J. V. W., Santoro, R. A., and Tang, W. M. (1993). Kinetic Studies of Microinstabilities in Toroidal Plasmas: Simulation and Theory. In *Plasma Physics and Controlled Nuclear Fusion Research, 1992*, volume 2, pages IAEA–CN–56/D–4–18, International Atomic Energy Agency, Vienna.

Lee, W. W., Krommes, J. A., Oberman, C. R., and Smith, R. A. (1984). Nonlinear Evolution of Drift Instabilities. *Phys. Fluids* **27**, 2652.

Lee, W. W., Kuo, Y. Y., and Okuda, H. (1978). Numerical Simulation of Collisionless Drift Instabilities for Low-Density Plasmas. *Phys. Fluids* **21**, 617.

Lee, W. W. and Tang, W. M. (1988). Gyrokinetic Particle Simulation of Ion Temperature Gradient Drift Instabilities. *Phys. Fluids* **31**, 612.

Lee, W. W., Tang, W. M., and Okuda, H. (1980). Ion Temperature Drift Instabilities in a Sheared Magnetic Field. *Phys. Fluids* **23**, 2007.

Lehnert, B. (1989). Phase-Mixing by the Guiding-Centre Drifts of Charged Particles in a Plasma. *Plasma Physics and Controlled Fusion* **31**, 363–370.

Lidsky, L. M. (October, 1983). The Trouble with Fusion. *Technology Review* **86**, 32.

Linsker, R. (1981). Integral-Equation Formulation for Drift Eigenmodes Cylindrically Symmetric Systems. *Phys. Fluids* **24**, 1485–1491.

Liu, Q. P. and Cheng, C. Z. (1992). Numerical Solution of the Gyrokinetic Equation for Tokamak Microinstabilities. *Bull. Am. Phys. Soc.* **37**, 1364.

Mattor, N. (1992). Can Landau-Fluid Models Describe Nonlinear Landau Damping? *Phys. Fluids B* **4**, 3952.

Mattor, N. and Diamond, P. H. (1988). Momentum and Thermal Transport in Neutral-Beam-Heated Tokamaks. *Phys. Fluids* **31**, 1180.

Okuda, H. and Dawson, J. M. (1973). Theory and Numerical Simulation on Plasma Diffusion Across a Magnetic Field. *Phys. Fluids* **16**, 408.

Okuda, H., Dawson, J. M., Lin, A. T., and Lin, C. C. (1978). Quasi-neutral Particle Simulation Model with Application to Ion Sound Wave Propagation. *Phys. Fluids* **21**, 476.

O'NEIL, T. M. and GOULD, R. W. (1968). *Phys. Fluids* **11**, 134.

ORSZAG, S. A. (1971). *Stud. Appl. Math* **50**, 293.

PARKER, S. E. (1993). Private communication.

PARKER, S. E. and LEE, W. W. (1992). A Fully Nonlinear Characteristic Method for Gyrokinetic Simulation. *Phys. Fluids B* **5**, 77.

PARKER, S. E., LEE, W. W., and SANTORO, R. A. (1993). Gyrokinetic Simulation of Ion Temperature Gradient Driven Turbulence in 3D Toroidal Geometry. Technical Report PPPL-2904, Princeton Plasma Physics Laboratory.

PERKINS, F. W. and HAMMETT, G. W. (1991). Gyrofluid Equations for Toroidally-Trapped Particles. *Bull. Am. Phys. Soc.* **36**, 2277.

ROBERTS, K. V. and TAYLOR, J. B. (1965). Gravitational Resistive Instability of an Incompressible Plasma in a Sheared Magnetic Field. *Phys. Fluids* **8**, 315.

RUDAKOV, L. I. and SAGDEEV, R. Z. (1961). On the Instability of a Nonuniform and Rarefied Plasma in a Strong Magnetic Field. *Dokl. Akad. Nauk. SSSR* **138**, 415.

SAGDEEV, R. Z. and GALEEV, A. A. (1969). Nonlinear Plasma Theory. Benjamin, New York. T. M. O'Neil and D. L. Book, Eds.

SANTORO, R. A. and LEE, W. W. (1990). Gyrokinetic Particle Simulation of Impurity Particle Transport. *Bull. Am. Phys. Soc.* **35**, 2038.

SIMILON, P. (1981). *A Renormalized Theory of Drift-Wave Turbulence in Sheared Magnetic Fields.* PhD thesis, Princeton University.

SMITH, S. A. and HAMMETT, G. W. (1993). Manuscript in preparation.

STIX, T. H. (1992). *Waves in Plasmas.* American Institute of Physics, New York.

STRINGER, T. E. (1969). Diffusion in Toroidal Plasmas with Radial Electric Field. *Phys. Rev. Lett.* **22**, 770.

SYDORA, R. D. (1993). 3D Gyrokinetic Particle Simulations of Ion Temperature Gradient-Driven Turbulence and Transport. In HORTON, W., WAKATANI, M., and WOOTTON, A., editors, *Ion Temperature Gradient Driven Turbulent Transport.* American Institute of Physics, New York.

Sydora, R. D., Hahm, T. S., Lee, W. W., and Dawson, J. M. (1990). Fluctuations and Transport Due to Ion-Temperature-Gradient-Driven Instabilities. *Phys. Rev. Lett.* **64**, 2015–2018.

Waltz, R. E. (1993). Toroidal Turbulence Simulations with Gyro-Landau Fluid Models in a Nonlinear Ballooning Mode Representation. In Horton, W., Wakatani, M., and Wootton, A., editors, *Ion Temperature Gradient Driven Turbulent Transport*. American Institute of Physics, New York.

Waltz, R. E., Dominguez, R. R., and Hammett, G. W. (1992). Gyro-Landau Fluid Models for Toroidal Geometry. *Phys. Fluids B* **4**, 3138.

Wesson, J. (1987). *Tokamaks*. Clarendon Press, Oxford.

Winsor, N. K. (1969). *A Numerical Model for a Low-Pressure Plasma in a Toroidal Magnetic Field*. PhD thesis, Princeton University.

Wolfram, S. (1988). *Mathematica, A System for Doing Mathematics by Computer*. Addison-Wesley Publishing Co., New York.

Wong, H. V., Berk, H. L., and Jungwirth, K. (1991). Gyrokinetic Simulation of Toroidal η_i Modes. *Bull. Am. Phys. Soc.* **36**, 2435.

Zarnstorff, M. C., Barnes, C. W., Efthimion, P. C., Hammett, G. W., Horton, W., Hulse, R. A., Mansfield, D. K., Marmar, E. S., McGuire, K. M., Rewoldt, G., Stratton, B. C., Synakowski, E. J., Tang, W. M., Terry, J. L., Xu, X. Q., Bell, M. G., Bitter, M., Bretz, N. L., Budny, R. V., Bush, C. E., Diamond, P. H., Fonck, R. J., Frederickson, E. D., Furth, H. P., Goldston, R. J., Grek, B., Hawryluk, R. H., Hill, K. W., Hsuan, H., Johnson, D. W., McCune, D. C., Meade, D. M., Mueller, D., Owens, D. K., Park, H. K., Ramsey, A. T., Rosenbluth, M. N., Schivell, J., Schmidt, G. L., Scott, S. D., Taylor, G., and Wieland, R. M. (1991). Overview of Recent TFTR Results. In *Plasma Physics and Controlled Nuclear Fusion Research, 1990*, volume 1, page 109, International Atomic Energy Agency, Vienna.